FORM-FINDING FRAMEWORK FOR MONOCOQUE SANDWICH COMPOSITE BRIDGES

An optimisation tool for the preliminary design of bridges

TU Delft

OLA ÅSBØ

MSc. THESIS // August 2023

Page intentionally left without content.

Form-finding framework for monocoque sandwich composite bridges

An optimisation tool for the preliminary design of bridges

by

Ola Åsbø

To obtain the degree of Master of Science in Civil Engineering
track Structural Engineering
at Delft University of Technology,
Faculty of Civil Engineering (CiTG).

Student number: 5139961

GRADUATION COMMITTEE:

Prof. dr. Maria Nogal Macho	CiTG // Integral Design & Management, chair
Dr. Marko Pavlović	CiTG // Steel & Composite Structures
Ir. Angeliki Christoforidou	CiTG // Steel & Composite Structures

EXTERNAL SUPERVISOR:

Dr. Reidar Kvale Joki	FiReCo AS / JOKI Engineering AS

Keywords: fibre-reinforced polymer (FRP), parametric design, structural optimisation, sandwich panels, footbridges

Acknowledgements

I would like to express my heartfelt gratitude to all those who have supported and encouraged me throughout the journey of completing this Master's thesis.

First and foremost, I am immensely grateful to my thesis supervisors: Dr. Marko Pavlović, Ir. Angeliki Christoforidou and the chairman of my committee, Prof. Dr. Maria Nogal Macho. Furthermore, I would to express my gratitude towards Dr. Reidar Kvale Joki, who stepped in as an external supervisor. I am indebted to his input, which allowed me to formulate an optimisation problem based on a real case (tender) – the Klosterøy bridge in Skien, Norway.

Prior to initiating this work, I am grateful towards Professor Macho for suggesting to attend her classes in *Engineering Systems Optimisation*. This proved to be invaluable in the mathematical formulation of the optimisation problem expressed throughout this report, not to mention the comments and recommendations I received while working out these formulations.

I am grateful to Dr. Pavlović, who let me step in as a student assistant in the course *Fibre-reinforced Polymer (FRP) Structures*, which was an insightful and educational experience. The combined expertise of Dr. Pavlović, Ir. Christoforidou and Dr. Joki in fibre-reinforced polymer (FRP) and engineering has been crucial for this thesis work.

Overall, I am grateful to the supervisors and my sister for their unwavering guidance, invaluable insights, and patient mentoring. Their expertise and constructive feedback have been instrumental in shaping the direction and quality of this research. I am especially thankful for the patience I was given, which has allowed me to follow my career, though at the expense of the report's progress. Consequently, this journey has been considerably longer than initially anticipated.

My sincere thanks also go to my family and friends for their unwavering support, encouragement, and understanding throughout this challenging journey. Their belief in me has been a constant source of motivation and strength.

To all those mentioned and those unmentioned, I extend my deepest gratitude for being a part of my academic journey and making this thesis possible.

Ola Åsbø
Oslo, August 2023

Abstract

FRP is increasingly utilised in the built environment, following successful implementations in the aerospace and marine industry. However, it exhibits poor stiffness and stability compared to conventional materials such as steel, making it challenging to satisfy serviceability and comfort requirements. Optimising FRP to address these challenges will allow for lightweight solutions with long service lives which could contribute to a cost-efficient reduction of carbon footprint. To this end, an optimisation tool for the preliminary design of bridges using FRP is presented in this thesis report.

The research explores the feasibility of adopting FRP in the main load-carrying system of pedestrian bridges and develops a framework for the concurrent geometry and material architectural optimisation of said structures. The study aims to achieve significant cost- and carbon footprint reductions in monocoque FRP bridges by employing a numerical optimisation approach.

The optimisation tool utilizes the computer-aided geometric design (CAGD) software Rhino® and its parametric interface, Grasshopper®, to concurrently optimise the shape and material architecture of the bridges. Through the use of genetic algorithms, the framework overcomes FRP's poor stiffness and stability, and maximizes its unique advantages, including lightweight and high-strength properties, enabling free-form designs. This feat is achieved by implementing hybrid sandwich panels, comprising glass fibre-reinforced polymer (GFRP) and carbon fibre-reinforced polymer (CFRP) face sheets. Satisfactory stiffness is ensured by defining deflection constraints, whereas constraints on the fundamental frequency and critical buckling load factor ensure adequate stability.

The research demonstrates promising results, showing potential cost reductions of up to 17% and carbon footprint reductions of up to 27.4% compared to a real case design carried out by FiReCo. However, certain limitations and areas for improvement are acknowledged, including the required run-time and the complexity of the solution space. Suggestions for enhancing the framework's efficiency are proposed, including implementing orthotropic failure criteria and reducing the solution space through adjustments to ply thicknesses and foam core configurations.

Overall, the developed optimisation tool provides valuable insights and serves as a valuable resource for researchers and practitioners seeking sustainable and economically viable bridge designs. By embracing innovative solutions and eco-friendly materials, this study contributes to global efforts towards carbon neutrality and sustainable infrastructure development in the built environment.

Contents

List of Figures

List of Tables

Abbreviations

BREP boundary representation 56, 117, 122
CAD computer-aided design 47
CAGD computer-aided geometric design iii, 41, 44, 56, 88
CFRP carbon fibre-reinforced polymer iii, 37, 47, 58, 62, 63, 88, 91, 93, 94, 110
CLT classical lamination theory 21, 25, 26, 49, 61, 70, 92, 122
CSM chopped strand mat 58, 66, 105, 114–116, 119, 123, 124
DB double biased 112
EE embodied energy 62, 119
FE finite element 36, 38, 44, 47, 49–51, 61, 73, 74, 84, 86, 89
FEA finite element analysis 43
FEM finite element method 37, 44, 88
FPF first-ply failure 22, 26, 86
FRP fibre-reinforced polymer ii, iii, 2–4, 7, 10, 15, 26, 27, 30, 32, 35–41, 44, 50, 51, 65, 84, 88, 89, 91, 94, 112
GA genetic algorithm 42, 69, 72
GFRP glass fibre-reinforced polymer iii, 37, 46, 47, 58, 62, 63, 80, 88, 91–94, 110, 111, 113
GWP global warming potential 46, 47, 62, 66, 77, 78, 87, 109, 119
LCA life cycle assessment 46, 119
LP lamination parameter 36–38, 106, 107
LPF load proportionality factor 23, 24
OSD orthotropic steel deck 90
SA sensitivity analysis 42, 77, 78
SLS serviceability limit state 60, 91, 92, 113
UD unidirectional 16, 19, 21, 25, 28, 58, 93, 104–106, 114, 115, 123
UDL uniformly distributed load 60, 91
ULS ultimate limit state 60, 157
VARTM vacuum-assisted resin transfer moulding 4, 12, 13, 84, 119
WWFE world-wide failure exercise 26, 27

Symbols

Coordinates

X, Y, Z	axes in global coordinate frame	
x, y, z	axes in local coordinate frame	

Material-related symbols

ε_{f1}	in-plane strain limit in the 1 direction of UD plies	
ε_{f2}	in-plane strain limit in the 2 direction of UD plies	
ν_{12}	major Poisson's ratio UD plies	
ν_{21}	minor Poisson's ratio for UD plies	
ν_{f}	major Poisson's ratio fibre	
ν_{m}	major Poisson's ratio matrix/resin	
ν_{xy}	in-plane major Poisson's ratio for laminates	
ν_{yx}	in-plane minor Poisson's ratio for laminates	
γ_{f12}	in-plane shear strain limit	
ρ	material density	kg/m^3
θ	fibre orientation (Fig. 3.1)	$^\circ$
ζ	fibre mass portion of reinforcement mat	g/m^2
a_{ij}	entry in the compliance matrix (inverse of the **A** matrix)	
d_{ij}	entry in the compliance matrix (inverse of the **D** matrix)	
E_1	in-plane elastic modulus in the 1 direction of UD plies	N/mm^2
E_2	in-plane elastic modulus in the 2 direction of UD plies	N/mm^2
E_f	in-plane elastic modulus in the x-direction for fibres	N/mm^2
E_m	in-plane elastic modulus in the x-direction for matrix/resin	N/mm^2
E_x	in-plane elastic modulus in the x direction of laminates	N/mm^2
E_y	in-plane elastic modulus in the y direction of laminates	N/mm^2
f_E	exposure factor	
G_f	in-plane shear modulus for fibres	N/mm^2
G_m	in-plane shear modulus for matrix/resin	N/mm^2
G_{12}	in-plane elastic shear modulus of UD plies	N/mm^2
G_{xy}	in-plane elastic shear modulus of composite laminates/plies	N/mm^2
K	number of layers/plies	
t	thickness of ply; thickness of laminate	mm

V_f	fibre volume fraction (or content) of a ply or composite material	%
S_{12}	shear failure strength, 1-2-plane	N/mm^2
S_{13}	shear failure strength, 1-3-plane	N/mm^2
S_{23}	shear failure strength, 2-3-plane	N/mm^2
X_C	compressive failure strength, 1-direction	N/mm^2
X_T	tensile failure strength 1-direction	N/mm^2
Y_C	compressive failure strength, 2-direction	N/mm^2
Y_T	tensile failure strength, 2-direction	N/mm^2
Z_C	compressive failure strength, 3-direction	N/mm^2
Z_T	tensile failure strength, 3-direction	N/mm^2

Optimisation-related symbols

$\mathbf{x}$	optimisation variables
Φ	pseudo-objective function
$\mathbf{F}$	objective functions
g	constraint
m	total mass
n_c	number of constraints
P	penalty function
r_p	penalty factor
w	weighting factor

Conversion factors

η_c	total conversion factor
η_{cf}	conversion factor for fatigue effects
η_{cm}	conversion factor for moisture effects
η_{ct}	conversion factor for temperature effects
η_{cv}	conversion factor for creep effects

Other symbols

δ	deflection; displacement	mm
λ	buckling load factor	
λ_{cb}	critical buckling load factor	
WF	weighting factor	
Ω	frequency	Hz
Ω_0	fundamental frequency	Hz
φ_X, φ_Y, φ_Z	rotational degree of freedom in global coordinates	
φ_x, φ_y, φ_z	rotational degree of freedom in local coordinates	
q_fk	characteristic value of vertical loading on footpath	kN/m^2
u_X, u_Y, u_Z	translational degree of freedom in global coordinates	
u_x, u_y, u_z	translational degree of freedom in local coordinates	

1

INTRODUCTION AND RATIONALE

Chapter 1.1. Rationale

Chapter objectives

1. Introduce the reader to FRP, its applications, advantages and drawbacks
2. Introduce the challenges and opportunities regarding bridge construction
3. Formulate the rationale behind the study

1.1.1. Fibre-reinforced polymer: a brief introduction

Fibre-reinforced polymer (FRP) as a composite material has been used in the aerospace industry for several decades, while it is a rather novel material within the field of civil engineering. It has been successfully used in applications ranging from sports equipment, such as tennis rackets and hockey sticks, to boat hulls and wind turbine blades, where its light weight is of the essence. In such applications, the equipment is exposed to demanding requirements such as a corrosive environment and numerous load cycles, while a high stiffness is desired. These merits triggered research into the material to find suitable applications for using composites in the built environment.

Following the construction of the first European all-composite highway bridge in Bulgaria in 1982, FRP gained ever-increasing traction in the built environment [1, 2]. The resulting research has proved that it exhibits greater corrosion and fatigue resistance than traditional building materials, while at the same time having a lower weight. The anisotropy of composites introduces complex load paths requiring advanced computational methods, enabling tailorable layup (orientation, order and thickness of plies) for optimal strength and stiffness [3].

Due to the increased traffic loads in recent years, both in amplitude and frequency, numerous bridges have failed to meet their expected service life as the increased dynamic action accelerates deterioration processes [4]. These structures have been strengthened and retrofitted using externally bonded FRP composites, which was one of the first applications of FRP in civil engineering [5]. With these means, the flexural, compressional, and shear strength can be improved. Other operations involve replacing the steel reinforcement with composites, effectively decreasing the deck thickness and enabling the bridge to carry greater live loads. Similar effects can be achieved by replacing the deck in steel bridges with composite alternatives, greatly increasing the fatigue resistance of the girders.

In recent years, pedestrian bridges, bridge decks for new and rehabilitated structures, and other applications such as lock gates have been undertaken using FRP composite components [6]. This trend is expected to remain, as a modular approach with made-to-measure prefabrication may result in reduced construction times, improved quality and increased flexibility and economy [7].

1.1.2. Challenges, opportunities and motivation

The current state of numerical optimisation involves isotropic and homogenous materials to a great extent, whereas anisotropic materials are still an issue. Efficient designs in FRP can be achieved by shaping the structure's geometry and tailoring the material properties by its layers' number, orientation and stacking sequence. However, this introduces non-linear optimisation problems due to the numerous possible combinations of ply angles, ply thickness, and their stacking sequence [8]. The combined optimisation of member geometry and laminate design has been applied to the sizing (cross-sectional design) of standard linear shapes in two-dimensional panels. These methods are suitable for members intended for pultrusion but are lacking when exploring free-form solutions and lead to designs that make poor use of the in-plane strength and stiffness of FRP laminates [8].

Bridges play a crucial role in connecting communities and facilitating efficient transportation systems. However, conventional materials like steel and concrete often pose limitations in terms of weight, maintenance, and environmental impact. We are facing severe climate changes and resource depletion, increasing the need for sustainable infrastructure solutions. To this end, FRP serves as a promising solution with its lightweight, high strength and potential for low carbon footprints.

By exploiting the unique characteristics of FRP, such as its anisotropic properties and adaptability to complex geometries, it becomes possible to create structurally efficient and aesthetically pleasing bridges. Implementing numerical optimisation in the design process, with the ability to concurrently optimise the bridge's shape and material architecture, opens doors to cost-efficient solutions that surpass the limitations of traditional designs.

As governments and organizations strive to meet carbon neutrality targets, the construction sector has a pivotal role in embracing innovative and environmentally friendly materials. By developing an optimisation tool tailored specifically for FRP bridges, it is envisaged to encourage the widespread adoption of composite materials in civil engineering projects. The successful implementation of the herein proposed framework will not only contribute to reducing carbon footprints and construction costs but also pave the way for a more sustainable and resilient infrastructure that can withstand the challenges of the future. For these reasons, the focus of this thesis is on FRP.

Chapter 1.2. Question, aim and objectives

Chapter objectives

1. Formulate the research question of the MSc thesis project
2. Formulate the main aim
3. Formulate partial objectives necessary to fulfil the research question

1.2.1. Question

Following the optimisation complications concerning the design of composites, the research question of this master thesis:

> What is the potential cost- and carbon footprint reduction in monocoque FRP bridges when a numerical optimisation approach is adopted, and what is required for its implementation?

1.2.2. Aim

The study aims to investigate the feasibility of bridges using FRP in the main load-carrying system and to create a framework for the preliminary optimal design of these employing monocoque structures.

1.2.3. Objectives

A set of subquestions are formulated as the objectives of the thesis project, with the intention of structuring the report and providing the necessary means to answer the research question. The structure of the thesis is aligned with these objectives, defined for the respective chapters as:

Part 1. Literature review

Chapter 2: Fibre-reinforced composites and sandwich panels

O 2.1 What is a composite material?
O 2.2 What are the main constituents and properties of FRP?
O 2.3 What is a monocoque structure?
O 2.4 What is a sandwich structure?
O 2.5 What are the practical limitations concerning transportation and manufacturing?

Chapter 2 introduces FRP as a material, elaborating on its constituents, strengths and weaknesses. The main production methods will be clarified in conjunction with manufacturing and transportation limitations.

Chapter 3: Mechanical properties

O 3.1 How are the anisotropic intrinsic properties of FRP defined?
O 3.2 How can the properties and behaviour of a laminate be predicted?
O 3.3 What are FRP's failure mechanisms and failure modes, and how can these be predicted?

Chapter 3 describes the mechanical properties of FRP related to the meso-scale structure (layup). This includes laminate theory and failure criteria associated with the first-ply failure, such as the Tsai-Wu failure criterion.

Chapter 4: Structural optimisation and form-finding

O 4.1 What form-finding methods are available that are beneficial to FRP design, and what are their limitations?
O 4.2 What is structural optimisation, and how can it be used to solve the aforementioned limitations?

O 4.3 What specific challenges and potential solutions pertain to the numerical optimisation of FRP structures?

Chapter 4 covers the state-of-the-art in structural optimisation, showcasing the available methods for optimisation on FRP. It will be apparent that most algorithms are intended for isotropic material, thus expressing the need for a different approach when using more complex material compositions. The challenges posed by this type of problem will be identified, such as an increase in the number of design variables, non-linear constraints and the need for discrete variables.

Part 2. Optimisation tool

Chapter 5: Framework

O 5.1 What optimisation objectives can be efficiently adopted to reach an optimised design?
O 5.2 What are the necessary prerequisites for the optimisation of a structure?
O 5.3 What are the limitations and drawbacks of the framework

Chapter 5 implements theory from the literature review, enabling defining a framework for the preliminary optimal design of composite bridges. The optimisation objectives and the pertaining design constraints are defined alongside the adopted optimisation algorithm.

Part 3. Validation with real case and Post-Optimisation

In the third part, a case study will be conducted, with which the advantages and limitations of the framework will be exemplified. This part will also provide the results of the report, as it quantifies to what extent the optimisation objectives have been reached.

Discussions

The report's final chapter will answer the research question and reflect upon the relevant parts of the study. Finally, conclusions will be drawn on the proposed framework and the case study before recommending future work and investigations.

Chapter 1.3. Scope, methods and limitations

Chapter objectives

1. Identify the scope of the master thesis
2. Introduce the methods used in achieving the objectives of the study

1.3.1. Scope

Owing to the time constraints concerning this thesis work, the following omissions can be defined, which are also indicated in Chapter 1.3.2:

- Only FRP bridges are considered.
- The solution must be possible to produce using vacuum-assisted resin transfer moulding (VARTM).
- The proposed framework will only consider linear behaviour, thus disregarding progressive failure mechanisms and non-linear analyses.

1.3.2. Methods and Limitations

In order to attain information on FRP and optimisation, a literature study will be carried out. These findings illustrate approaches to optimising FRP structures and key approaches for defining their properties. The usefulness will be proved through a case study. With this, the reader will get insight into its applicability and limits. Comparing an optimised design with a non-optimised one will show how the framework helps reduce material consumption and costs.

The thesis will mainly focus on glass and carbon fibres, since these are the most commonly adopted fibres over the various industries using FRP. Pedestrian bridges are mainly considered, with a shell-type load-carrying system. The main analyses are limited to serviceability limit state (SLS) loads, used for deformation, linear buckling and natural frequency analyses. Running non-linear structural analyses for each iteration would complicate the procedure and be highly disadvantageous for the execution time.

1.3.3. Structure of the MSc thesis report

The thesis report is structured accordant with the established objectives, comprising three main parts, each divided accordant with the formulated objectives in Chapter 1.2.3. The outline is depicted below:

Introduction	Research question, aim and objectives, and the thesis' methodology
1. Literature review	1. Fibre-reinforced polymers 2. Mechanical properties 3. Structural optimisation and form-finding
2. Optimisation tool	Definition of the framework and preparation of the case study in the context of the framework
3. Validation with real case and Post-Optimisation	**Results** from the optimisation of the chosen case study and evaluation on the optimality of the solution; and **Post-processing**, discretising the structure to manufacturable components
Discussions	Answer to the research question, proposed future work, reflections

Figure 1.1: The outline of the report.

2

Fibre-reinforced polymers

The first chapter of the literature review will give an introduction to FRP as material, answering the *what* and the *why* of FRP composites. Namely, *what* is a composite material, and *why* one should consider using it instead of conventional materials. Additionally, the structural concepts of sandwich and monocoque structures are introduced, and the benefit of applying these concepts in the design of bridges. Finally, an account of construction processes is given, along with some of the practical limitations concerning this thesis.

The chapter aims to answer the following:

O 2.1 What is a composite material?
O 2.2 What are the main constituents and properties of FRP?
O 2.3 What is a monocoque structure?
O 2.4 What is a sandwich structure?
O 2.5 What are the practical limitations concerning transportation and manufacturing?

Chapter 2.1. Fibre-reinforced polymers

Chapter objectives

O 2.1 What is a composite material?
O 2.2 What are the main constituents and properties of FRP?

2.1.1. The what and why of FRP composites

Composite materials combine two or more natural or artificial distinct phases with different physical and chemical properties that are stronger as a team than individual players [9]. Wood, for instance, is a natural composite comprising cellulose fibres embedded in lignin [10]. Here, the fibres offer strength and tensile resistance, while the lignin keeps the fibres in position, preventing separation and adding to the compressive strength. Similarly, the poor tensile strength of concrete is countered by introducing steel reinforcement, resulting in a composite with high tensile and compressive resistance. This principle is the basis for the development of FRP, in which fibres are embedded in a polymer matrix to protect against environmental and external damage and transfer the load between the fibres (Fig. 2.1). The fibres provide strength and stiffness, helping to resist cracks and fractures in the continuous matrix phase [9]. With a wide range of constituent materials, some of which are discussed in Chapter 2.1.2 and Chapter 2.1.3, it naturally follows that the properties of the composite material depend on:

- the combination of fibre and matrix material and their respective properties;
- the adhesion at the interface between the constituents, decisive for their synergy; and
- the orientation of the fibres with respect to the load path(s).

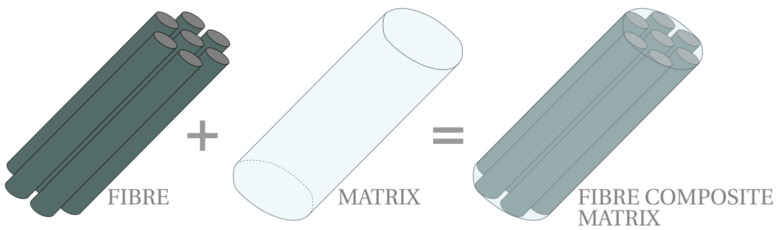

Figure 2.1: Fibres embedded in a matrix creates a composite utilising the strength of both constituents [9].

The benefits of adopting FRPs in design are many. It is worthwhile bearing in mind that one acquired property may negatively impact other desired properties; therefore, the material should merely have the required characteristics to perform its design task. Table 2.1 depicts some of the pros and cons concerning the use of FRP.

Table 2.1: Pros and cons of fibre-reinforced polymers [10, 11, 12, 13]

Advantages	**Disadvantages**
– High specific strength and stiffness yielding cost-effective lightweight structures	– Poor out-of-plane strength and impact resistance
– Ability to co-cure reduces assembly cost	– High fabrication and raw material costs
– Exceptional chemical- and water resistance reducing maintenance costs	– Difficult to repair (as opposed to weld repairment in steel)
– Tailorable layup for optimal strength and stiffness	– Susceptible to delamination in service and sensitive to temperature and fire
– Numerous production methods allowing free-form shapes	

2.1.2. Fibres

The fibres constitute the reinforcement of FRP composites, coming in a wide range of different forms and materials. First, these different forms are established before the commonly adopted fibre types are presented.

A *fibre* is a material having an aspect ratio (length to diameter) normally greater than 100. Similarly, *filaments* refer to the smallest unit of a fibrous material, synonymous with *fibre*, formed by a single hole in the spinning process. *Strands* are bundles or groups of untwisted filaments associated with glass fibres, while *tows* refer to the carbon fibre counterpart. When *strands* or *tows* are bundled together without twisting, the product is referred to as *roving*. Conversely, when these are twisted, it is considered *yarn*. These yarns or tows can be weaved together, making a *woven cloth*, usually providing reinforcement in the 0° and 90° direction [11]. While there is a wide range of fibre types, including coconut filaments, the following paragraphs focus on glass, carbon, and aramid.

Glass fibres

A variant of glass fibre, E-glass, is the most commonly used reinforcement material in load-bearing composites due to its good mechanical properties and environmental resistance at a low price. This type of fibre is susceptible to humidity, and alkaline attacks, which has triggered the creation of types with high chemical and alkaline resistance (AC-glass), often necessary for cement and concrete applications [14]. Even though numerous alternatives exist, R- and S-glass are the most prominent. The letter designation R refers to fibres having higher strength and acid corrosion resistance, while S refers to high-strength glass with high stiffness and greater temperature and corrosive resistance [15].

Carbon fibres

Carbon fibres offer greater stiffness, strength, and fatigue performance than other fibres and are mainly divided into high-strength (HS) fibres with very high tensile strength and relatively high failure strain; and high modulus (HM) fibres with very high stiffness. Apart from high costs, the drawbacks of these fibres tend to be brittleness, low impact resistance and a slightly negative thermal resistance, resulting in micro cracking of the matrix [15].

Aramid fibres

Aramid fibres exhibit strength and stiffness intermediate between carbon and glass fibres. These fibres are well known under the trade name Kevlar®, used in ballistic protection due to their extreme toughness and ability to absorb large amounts of energy during fracturing. The main advantage of aramid fibres is their ability to undergo plastic deformation in compression and defibrillate during tensile fracture, resulting in ductile failure, in contrast to glass and carbon. While aramid fibres have great wear resistance, they suffer from strength degradation by prolonged exposure to ultraviolet radiation. Although this can be a severe concern for exposed fibres in stay cables, it is not a significant problem because the resin matrix protects the fibres [11].

Some characteristic properties of the mentioned fibres are shown in Table 2.2 below.

Table 2.2: Typical properties of commonly used fibres.

Fibre type	Density [kg/m^3]	Tensile strength [MPa]	Young's Modulus [GPa]	Ultimate strain [%]
Glass [16]				
E-glass	2570	2750	73	3.8
R-glass	2520	3450	86	4.0
Carbon [16]				
High strength	1790	3600	238	1.5
High modulus	1880	4700	410	0.6
Aramid [17]				
Kevlar 49	1440	3600	124	2.9

Reinforcement

The flexibility of fibres offers a wide range of use-cases, owing to the wide variety of reinforcement forms. The choice of form and type of the fibres, i.e. the reinforcement, depends on the structural and environmental requirements and the manufacturing method. However, to maintain the form-freedom associated with the composite, it is necessary to have a drapable reinforcement. For instance, a tight weave or collection of strands translates into a stiff and impregnable reinforcement, impeding the production as wetting out the fibres and forming them on the contour/mould becomes troublesome [11].

After bundling the fibres into yarns (or strands), these can be woven together, forming a two-dimensional fabric offering reinforcement at 0° and 90°, or at +45° and −45°. An extension of such woven fabrics combines different types of fibres such as glass and carbon, utilising their benefits while saving on costs. Multiple layers of these two-dimensional weaves can be laminated together – forming a laminate. To obtain mats inheriting (close to) isotropic properties, the strands can be laid down in a swirl pattern or chopped to create chopped strand mat (CSM), held together by a resin binder. These principle reinforcement forms are visualised in Fig. 2.2.

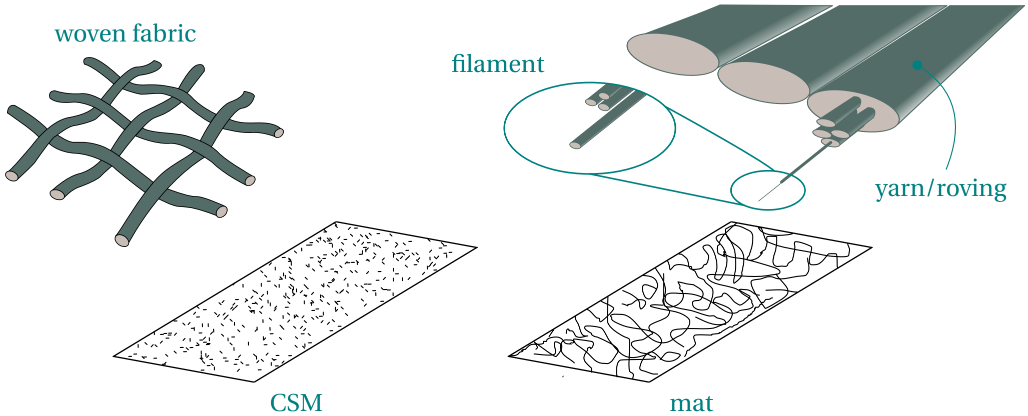

Figure 2.2: Some forms of reinforcements, adapted from [18].

2.1.3. Matrices

The family of polymeric composites are split into those that use thermosetting resins and those that use thermoplastic resins, differentiated by their intramolecular crosslinking – or lack thereof (Fig. 2.3). Polymers are formed from chemical processes in which small molecules (monomers) form covalent bonds to produce chainlike or network molecules through polymerisation [11, 19]. These polymer matrices provide the structural integrity of the composite and are responsible for:

- transferring loads between the fibres and keeping them in position;
- safeguarding the notch-sensitive fibres against abrasion, fire and impact;
- protecting the fibres from moisture, chemicals, UV radiation and oxidation; and
- providing the shear, transverse tensile and compression properties of the composite essential in preventing premature failure due to microfibre buckling.

Thermoset Polymers

Thermosets are extensively used in engineering applications as the molecules form an infusible and insoluble structure due to three-dimensional crosslinking between the molecules [11]. A thermoset goes from a low-viscosity liquid that solidifies through chemical crosslinking of a low-molecular-weight monomer and prepolymer into a high-weight polymer network, giving off heat in an exothermal and irreversible reaction [15]. Consequently, further heating beyond curing will considerably degrade the mechanical properties or cause it to char. To overcome the inherent brittleness and relatively poor toughness of these polymers due to the high crosslink density, thermoplastic additions can be introduced to the thermoset resin.

Thermoplastic Polymers

Thermoplastics are high molecular weight polymers that are not chemically crosslinked. However, their main chains are held together by relatively weak secondary bonds, meaning that an adequate amount of heat will melt, liquefy or soften the plastic enough to be processed. Thus, they may be subsequently reheated for forming or joining operations. Due to the quick curing time, thermoplastics account for about 80 % of all polymers produced. However, because of their inherent high viscosity and melting points, these processes normally require high temperatures and pressures[11, 15]. Although thermoplastics exhibit greater (impact) damage tolerance than thermosets, they are susceptible to creep at room temperature, require high processing temperatures, and can have poor solvent, fire and fluid resistance properties, which has prevented them from replacing thermosets in most structural applications [11].

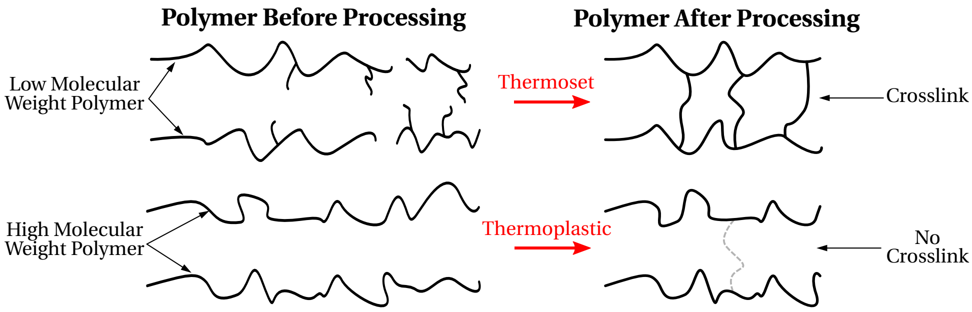

Figure 2.3: Thermoset and thermoplastic polymer structures [11].

The thermosets predominantly applied in structural applications include polyesters, vinylesters and epoxies. The latter is also used for adhesive purposes. See [11] for more comprehensive coverage on these and other resins.

Chapter 2.2. Monocoque structures

Chapter objectives

O 2.3 What is a monocoque structure?

The word monocoque stems from the Greek word *mono* (single) and the French word *coque* (shell), referring to a structural principle in which stresses are reacted by a thin load-bearing membrane or shell – a 'stressed skin' construction. Enabling free space internally and high bending resistance makes these structures ideal for weight-sensitive applications such as aeroplane fuselages and automobile chassis. However, monocoque shells suffer from structural instability due to the thin exterior as they tend to fail in buckling or crippling. Overcoming such issues requires some means of stiffening, which is often realised through an assembly of frames, bulkheads, stringers, and longerons in aeroplane designs. The introduced stiffening members add to the overall weight without compromising the light and stiff characteristics. This is, strictly speaking, not a load-bearing shell anymore; thus, the combination is referred to as a semi-monocoque structure [20], see Figure 2.4.

2.2.1. From aeroplanes to bridge design

From a structural point of view, the ideal shape of a monocoque structure is cylindrical, as the loads are reacted through hoop- and tangential stresses [20]. However, such designs are less beneficial for bridges, where the governing loads usually come from above, not as uniform pressure (as for aeroplanes). Moreover, a cylindrical superstructure would require excess material, amount to tall cross-sections, and introduce challenges when joining the deck with the superstructure. With the introduction of diaphragms (transverse and longitudinal stiffeners) and a modified shape, monocoque structures provide an efficient solution in the design of FRP bridges, where the tailored material can utilise the tensile strength of the fibres, especially so as the buckling sensitivity of these structures can be mitigated by introducing the most significant compressive forces in the deck.

Although closed sections have torsional rigidity superior to open sections, aiming to reduce the height of the cross-section will potentially increase the distortional effects due to eccentric loads on the deck. Fortunately, the accessibility and open space are of less importance in the bridge's interior, meaning that the stiffening of the structure does not have to run along its exterior, allowing to increase the torsional stiffness significantly through diaphragms. These internal stiffeners will also increase the local bending resistance of the deck.

The benefits of monocoque structures are not only structural, as the closed structure comes off as aesthetically pleasing and elegant, with a smooth shape. From a maintenance point of view, there will be less dirt accumulation, and the creation of bird nests is prevented [21].

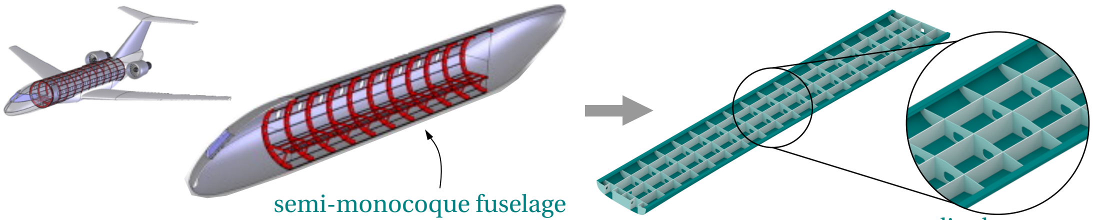

Figure 2.4: From aeroplane fuselage to semi-monocoque bridge design. Adapted from [20].

Chapter 2.3. Sandwich structures

Chapter objectives

O 2.4 What is a sandwich structure?

2.3.1. Definition of a Sandwich Element

A sandwich structure consists of three main parts: two thin, stiff, and strong face sheets separated by a thick, light, and weaker core. The faces act together to form a stress couple resisting the external moment, while the core resists shear and prevents the faces from buckling or wrinkling, in a similar fashion to how an I-beam operates [15].

The choice of face sheet and core material depends on the desired application and available manufacturing methods. For instance, commonly used face materials are aluminium, steel, timber veneer, and increasingly applied composite laminates. The appreciation of FRP facings comes from further weight reductions and form freedom, as it is challenging to manufacture sandwich elements from sheet metal with double curvature [15].

Core materials are usually divided into four groups: corrugated, honeycomb, balsa wood and foams, not to mention possible combinations of these concepts. Honeycomb cores offer the greatest shear strength and stiffness-to-weight ratios but necessitate adequate bonding to the faces and come at a substantially greater cost. Even though balsa offers inferior properties, it is used when the weight is not critical. Fig. 2.5 illustrates panels with foam- and honeycomb cores.

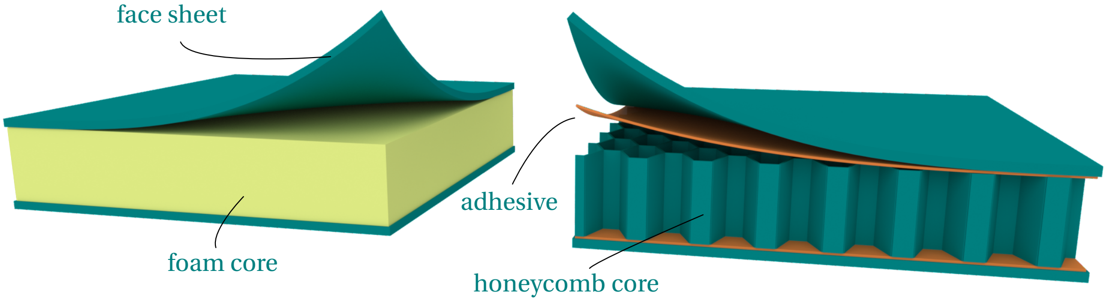

Figure 2.5: Foam core and honeycomb panel construction.

2.3.2. Why sandwich?

The primary advantages of these assemblies are their very high stiffness-to-weight ratio and high bending strength-to-weight ratio, overcoming the stiffness concerns regarding composites. For instance, by doubling the core thickness, the stiffness can be increased seven times with only a three per cent weight gain[11]. This means that the instability adhering to monocoque structures can efficiently be overcome through sandwich panels.

By using closed-mould production processes (see next section), face sheets and foam cores can be co-cured, providing good synergy between the components and cancelling the need for adhesives. As such, the assembly costs are significantly reduced, allowing producing large sheets with smooth areas without the use of rivets and bolts.

Chapter 2.4. Manufacturing processes

The choice of manufacturing processes depends on an intricate trade-off and consideration of tool costs, temperature, scale, surface quality, materials and size of the production series. Since the mould and other tools related to an assembly often are expensive non-recurring costs, it is preferable to create designs that repurpose these. Seemingly, the choice of the production process is driven by desires to achieve low component costs, improve recyclability and improve the work environment rather than the component's performance. There are mainly two types of production processes, namely open mould- and closed mould processes [11, 15, 18].

2.4.1. Open-mould processes

As the name suggests, these processes are open to the environment, meaning there may be an emission of volatile substances, potentially harmful to the manufacturers. The most common among these processes are spray-up and hand layup. The former involves spraying a mixture of chopped strands and resin onto a mould. In contrast, the latter consists in applying loose plies onto a mould and wetting them with a roller or brush. These processes are labour intensive but cost-effective for single series production. Dependent on the worker's skill, the resulting component is prone to having resin- and void-rich areas. An intermediate category of the open- and closed mould processes are the continuous pultrusion and filament winding processes. These allow for the creation of beam sections and cylindrical containers with great accuracy and high fibre contents.

2.4.2. Closed-mould processes

These processes differentiate from the open-mould methods as the production is sealed, either through multiple moulds, a covering sheet or a vacuum bag helping to provide a safe working environment. Although several techniques exist, vacuum infusion (or VARTM) is preferred in manufacturing large, integrated structures with short production series – such as bridges. This is especially true with the adoption of sandwich panels since vacuum infusion facilitates concurrently wetting out the fibres and co-curing the face sheets with the core in a single-step procedure. As schematised below, the face sheets and the intermediate core are placed into a mould and covered in a vacuum bag sealed off with sealant tape ('tacky tape'). When the set-up is air-tight, a vacuum is applied at several places, impregnating the panel as resin flows through the mould (see Fig. 2.6).

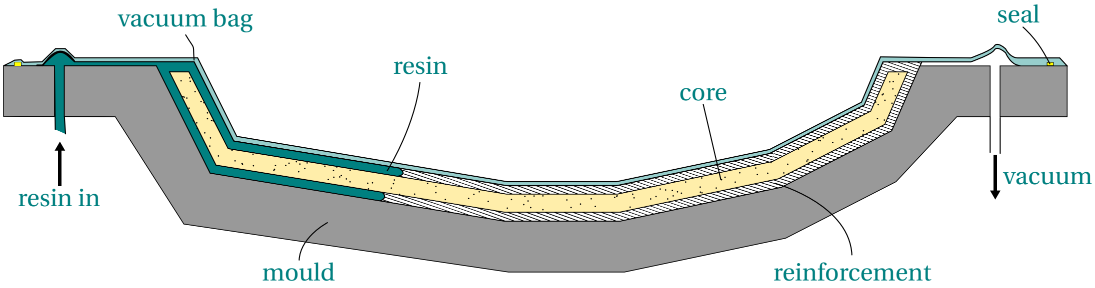

Figure 2.6: Schematic of vacuum infusion (VARTM) [15].

Although facilitating free-form structures with relatively good mechanical properties – up to fibre volume fractions of 55 %, the production is highly in favour of recurring use of the same moulds, as the initial costs are usually quite high. On the other hand, manufacturers such as FibreCore have developed piston technologies enabling numerous moulds at the click of a button. Even still, the quality of the end product requires careful handling of the flow of the resin, pressure, temperature and surface treatment. Showcasing the opportunities of vacuum infusion is the Pont y Ddraig ('Dragon Bridge') footbridge in Wales, comprising two bascule spans with complex plan and elevation geometry (Fig. 2.7).

Figure 2.7: The Pont y Ddraig (**left**) during manufacturing at AM Structures, Sandown, Isle of Wight and (**right**) in operation at Rhyl, Isle of Wight, UK, 2013. Courtesy of AM Structures [22].

Chapter 2.5. Practical limitations

Chapter objectives

O 2.5 What are the practical limitations concerning transportation and manufacturing?

The Dutch law limits the dimensions of vehicles on public roads to widths of 2.55 metres, heights of 4.00 metres, lengths of 18.75 metres, and a total mass of 50 tonnes, without considering case-specific exemptions [25]. As such, these metrics set the upper limit for the geometric boundaries of structures transported via roads. However, the scale of bridges realised in FRP (and their light weight) allow for pioneering transportation measures. Notably, these can be transported by barges on the water, flown in with a helicopter in remote areas, or even floated into position (Fig. 2.8).

An additional problem concerning lightweight structures is the possible damages during transportation, leading to minimum thickness requirements. The limitations set by the manufacturer steer the geometrical limitations for fabrication. For instance, the VARTM method used by FiberCore Europe ®, limits the height to approximately one metre due to the limits of the vacuum. However, the lengths and widths are theoretically unlimited but constrained by logistics. Due to difficulties in wetting the fibres, the maximum achievable thickness is around 30 mm. Nonetheless, one should aim for 20 mm as this saves costly material consumption and weight (FiberCore Europe®, personal communication).

Figure 2.8: The perks of installation with FRP. (**Top**) FRP bridge installed by helicopter in Scotland [23], and (**bottom**) FibreCore showcasing their lightweight, floating bridges [24].

Chapter 2.6. Conclusion

This chapter answers the following objectives:

O 2.1 What is a composite material?
O 2.2 What are the main constituents and properties of FRP?
O 2.3 What is a monocoque structure?
O 2.4 What is a sandwich structure?
O 2.5 What are the practical limitations concerning transportation and manufacturing?

Chapter 2 briefly introduces the *what* and *why* of FRP composites, describing their two main constituents: the fibres and the resin matrix. The proposed framework of this thesis will give an example of *how* this material can be implemented in designs, utilising its benefits.

The flexibility of fibrous composites enables the creation of fibres in many types and forms, responsible for the main load-bearing strength and stiffness of FRPs. The matrix provides the continuous phase of the composite, which is vital for the fibre's protection. Since thermoplastic polymers inherit poor creep and fatigue resistance, not to mention their thermal sensitivity, the polymers used in civil engineering structures are limited to thermosetting ones.

Sandwich structures are recognised by their three main parts, the two facesheets and the intermediate core structure. They significantly increase the bending stiffness of panels without compromising the low weight. These panels can be combined with monocoque structures to overcome the instability issues concerning these load-bearing shells. A combination of these principles allows for the introduction of cost-effective, low-weight structures with a low environmental impact, forming the basis of this thesis' framework.

The following chapter entails the material's mechanical properties, providing necessary details for *how* one can use it.

3

MECHANICAL PROPERTIES OF FRP

As introduced in the earlier chapters, the mechanical properties of FRP depend not only on its constituents, the fibre and the resin but on the volume and direction of the fibres. Following the defined material properties of the layers (commonly known as *plies* or *laminae*) comprising a laminate, the classical lamination theory (CLT) is used to predict the elastic properties and behaviour of laminates at a macroscopical level. The strength of the laminates can be predicted utilising several methods and theories. This chapter highlights some commonly adopted failure theories for unidirectional (UD) plies, such as the maximum stress criterion and the Tsai-Wu failure criterion, and how these theories apply when determining the resistance of multidirectional laminates.

The chapter aims to answer the following:

O 3.1 How are the anisotropic intrinsic properties of FRP defined?
O 3.2 How can the properties and behaviour of a laminate be predicted?
O 3.3 What are FRP's failure mechanisms and failure modes, and how can these be predicted?

Chapter 3.1. Anisotropic properties of FRP

Chapter objectives

O 3.1 How are the anisotropic intrinsic properties of FRP defined?

To describe the behaviour of a laminate, it is of great importance to understand the behaviour of its building blocks, the laminae. As such, this section will cover how the constitutive relations are defined for laminae and how these principles can be combined to define the stress-strain relation and stiffness of a laminate.

3.1.1. Lamina or Ply fundamentals

Convention and definition

Consider a convention depending on the right-hand coordinate system, where the z-axis denotes the plane normal. Then, the angle θ between the structural x-axis and the principal material 1-axis defines the fibre orientation angle, being positive when measured in a counterclockwise direction to the positive x-axis, as illustrated in Figure 3.1. Under plane-stress conditions, i.e. disregarding loads in the z-direction, the stresses in the material axes are denoted σ_{11}, σ_{22} and τ_{12}, with the corresponding strains denoted as ε_{11}, ε_{22} and γ_{12}.

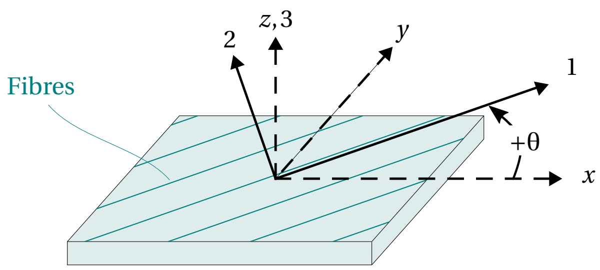

Figure 3.1: Sign convention for a lamina. 1,2 and 3 denote the material (local) axes, where 1 is parallel to the ply fibre direction. x, y and z denote structural axes.

For unidirectional (UD) composite orthotropic laminae under a state of plane stress, like the one in Figure 3.1, there are five independent material constants. E_1 is the longitudinal modulus, defining the stiffness in the direction parallel to the fibres, and E_2 is the transverse modulus, perpendicular to the direction of E_1. G_{12} is the in-plane shear modulus. ν_{12} is the major Poisson's ratio, specifying the contraction in the 2-direction due to tensile loads in the 1-direction, and ν_{21} is the minor Poisson's ratio for a contraction in the 1-direction due to tension in the 2-direction [11]. Suppose the properties of the UD lamina are unavailable. In that case, one can approximate these using the *Rule of Mixtures* or the more commonly adopted *Halpin-Tsai equations* introduced in Appendix A.

Following the established convention, it should be clear that the load-carrying capacity depends on the direction of the stresses. For instance, if a positive shear stress τ_{xy} is applied on a lamina with an orientation θ = 45° (Figure 3.2), the maximum tensile stress will be parallel to the main fibre direction, and thus reacted by σ_{11}, as seen in Figure 3.3. On the contrary, if τ_{xy} is negative, the stress must be reacted by the weaker matrix [11]. This illustrates one of the many complexities introduced when dealing with orthotropic materials, as opposed to isotropic materials, in which the direction of the shear stress is usually inconsequential.

Constitutive relations and transformation of stresses and strains

The introduced material constants can express the constitutive relation in the local coordinate frame as:

$$\bar{\boldsymbol{\sigma}} = \bar{\boldsymbol{Q}}\bar{\boldsymbol{\varepsilon}} \quad \text{or} \quad \begin{Bmatrix} \sigma_{11} \\ \sigma_{22} \\ \tau_{12} \end{Bmatrix} = \begin{bmatrix} \frac{E_1}{(1-\nu_{12}\nu_{21})} & \frac{\nu_{21}E_1}{(1-\nu_{12}\nu_{21})} & 0 \\ \frac{\nu_{21}E_1}{(1-\nu_{12}\nu_{21})} & \frac{E_2}{(1-\nu_{12}\nu_{21})} & 0 \\ 0 & 0 & G_{12} \end{bmatrix} \begin{Bmatrix} \varepsilon_{11} \\ \varepsilon_{22} \\ \gamma_{12} \end{Bmatrix} \tag{3.1}$$

where $\bar{\boldsymbol{\sigma}}$, $\bar{\boldsymbol{\varepsilon}}$, and $\bar{\boldsymbol{Q}}$ are the stresses, strains and the reduced stiffness matrix in the material coordinates, respectively; and $\nu_{21} = (\nu_{12}/E_1)E_2$. It follows from Eq. (3.1) that the strains can be expressed using the

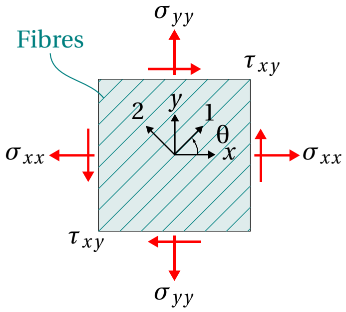

Figure 3.2: Orthotropic plane stress conditions and the shear stress state on 45° lamina.

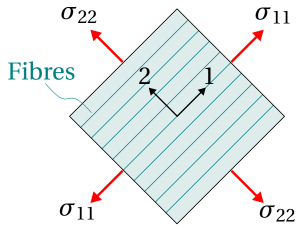

Figure 3.3: Positive shear stress on a 45° lamina is supported by the fibres.

reduced compliance matrix, $\bar{\boldsymbol{S}} = \bar{\boldsymbol{Q}}^{-1}$:

$$\bar{\boldsymbol{\varepsilon}} = \bar{\boldsymbol{S}}\boldsymbol{\sigma} \quad \text{or} \quad \begin{Bmatrix} \varepsilon_{11} \\ \varepsilon_{22} \\ \gamma_{12} \end{Bmatrix} = \begin{bmatrix} \frac{1}{E_1} & \frac{-\nu_{21}}{E_2} & 0 \\ \frac{-\nu_{12}}{E_1} & \frac{1}{E_2} & 0 \\ 0 & 0 & \frac{1}{G_{12}} \end{bmatrix} \begin{Bmatrix} \sigma_{11} \\ \sigma_{22} \\ \tau_{12} \end{Bmatrix} \tag{3.2}$$

To describe the behaviour of lamina, one must know the behaviour described in the structural coordinate system. The stresses in the material coordinate frame (σ_{11}, σ_{22} and τ_{12}) are transformed to stresses in the structural coordinate frame through the relation θ using:

$$\boldsymbol{\sigma} = \boldsymbol{T_\sigma}\bar{\boldsymbol{\sigma}} \quad \text{or} \quad \begin{Bmatrix} \sigma_{xx} \\ \sigma_{yy} \\ \tau_{xy} \end{Bmatrix} = \begin{bmatrix} \cos^2\theta & \sin^2\theta & -2\sin\theta\cos\theta \\ \sin^2\theta & \cos^2\theta & 2\sin\theta\cos\theta \\ \sin\theta\cos\theta & -\sin\theta\cos\theta & \cos^2\theta - \sin^2\theta \end{bmatrix} \begin{Bmatrix} \sigma_{11} \\ \sigma_{22} \\ \tau_{12} \end{Bmatrix} \tag{3.3}$$

where the overbar indicates quantities defined in the local coordinate frame and $\boldsymbol{T_\sigma}$ denotes the transformation matrix going from local to global stresses. Thus, with a contracted notation the relation can be expressed through the tensors and the transformation matrix: $\boldsymbol{\sigma} = \boldsymbol{T_\sigma} \cdot \bar{\boldsymbol{\sigma}}$. Similarly, transforming the stress from the structural axes to the material axes can be accomplished through: $\bar{\boldsymbol{\sigma}} = \boldsymbol{T_\sigma}^{-1} \cdot \boldsymbol{\sigma}$. A similar operation can be used to transform strains from structural to material axes:

$$\bar{\boldsymbol{\varepsilon}} = \boldsymbol{T_\varepsilon}\boldsymbol{\varepsilon} \quad \text{or} \quad \begin{Bmatrix} \varepsilon_{11} \\ \varepsilon_{22} \\ \gamma_{12} \end{Bmatrix} = \begin{bmatrix} \cos^2\theta & \sin^2\theta & \sin\theta\cos\theta \\ \sin^2\theta & \cos^2\theta & -\sin\theta\cos\theta \\ -2\sin\theta\cos\theta & 2\sin\theta\cos\theta & \cos^2\theta - \sin^2\theta \end{bmatrix} \begin{Bmatrix} \varepsilon_{xx} \\ \varepsilon_{yy} \\ \gamma_{xy} \end{Bmatrix} \tag{3.4}$$

where $\boldsymbol{T_\varepsilon} = \boldsymbol{T_\sigma}^T$ is the strain transformation matrix and superscript T denotes the transpose. The stress-strain relationship in the x-y coordinates can thus be defined using Equations (3.1), (3.3) and (3.4) and the global reduced stiffness matrix $\boldsymbol{Q}$ as:

$$\boldsymbol{\sigma} = \boldsymbol{T_\sigma}\bar{\boldsymbol{\sigma}} = \boldsymbol{T_\sigma}\bar{\boldsymbol{Q}}\boldsymbol{T_\varepsilon}\boldsymbol{\varepsilon} = \boldsymbol{Q}\boldsymbol{\varepsilon} \qquad \text{or} \qquad \begin{Bmatrix} \sigma_{xx} \\ \sigma_{yy} \\ \tau_{xy} \end{Bmatrix} = \begin{bmatrix} Q_{11} & Q_{12} & Q_{16} \\ Q_{12} & Q_{22} & Q_{26} \\ Q_{16} & Q_{26} & Q_{66} \end{bmatrix} \begin{Bmatrix} \varepsilon_{xx} \\ \varepsilon_{yy} \\ \gamma_{xy} \end{Bmatrix} \tag{3.5}$$

where the components of the $\boldsymbol{Q}$ matrix in the global coordinate frame are:

$$Q_{11} = \bar{Q}_{11}\cos^4\theta + \bar{Q}_{22}\sin^4\theta + 2\left(\bar{Q}_{12} + 2\bar{Q}_{66}\right)\sin^2\theta\cos^2\theta \tag{3.6a}$$

$$Q_{12} = \bar{Q}_{12}\left(\sin^4\theta + \cos^4\theta\right) + \left(\bar{Q}_{11} + \bar{Q}_{22} - 4\bar{Q}_{66}\right)\sin^2\theta\cos^2\theta \tag{3.6b}$$

$$Q_{16} = \left(\bar{Q}_{11} - \bar{Q}_{12} - 2\bar{Q}_{66}\right)\sin\theta\cos^3\theta + \left(\bar{Q}_{12} - \bar{Q}_{22} + 2\bar{Q}_{66}\right)\sin^3\theta\cos\theta \tag{3.6c}$$

$$Q_{22} = \bar{Q}_{11}\sin^4\theta + \bar{Q}_{22}\cos^4\theta + 2\left(\bar{Q}_{12} + 2\bar{Q}_{66}\right)\sin^2\theta\cos^2\theta \tag{3.6d}$$

$$Q_{26} = \left(\bar{Q}_{11} - \bar{Q}_{12} - 2\bar{Q}_{66}\right)\sin^3\theta\cos\theta + \left(\bar{Q}_{12} - \bar{Q}_{22} + 2\bar{Q}_{66}\right)\sin\theta\cos^3\theta \tag{3.6e}$$

$$Q_{66} = \left(\bar{Q}_{11} - \bar{Q}_{22} - 2\bar{Q}_{12}\right)\sin^2\theta\cos^2\theta + \bar{Q}_{66}\left(\cos\theta^2 - \sin\theta^2\right)^2 \tag{3.6f}$$

The relation in Eq. (3.5) is of great importance when more laminae are introduced to construct a laminate, as will be apparent in the following section.

Chapter 3.2. Classical Lamination Theory (CLT)

Chapter objectives

O 3.2 How can the properties and behaviour of a laminate be predicted?

Classical lamination theory (CLT) is applied to calculate the stresses, strains and curvature in each ply of a thin laminate, in addition to the determination of the overall elastic constants of the laminate. The assumptions hold for plates with thicknesses much smaller than the in-plane dimensions and constitute elements from the Kirchoff hypothesis for plates and are as follows [11, 19, 26] :

- Normals to the undeformed middle surface remain straight and normal to the deformed middle surface.
- Stress normal to the plate is negligible, consequently the strains $\varepsilon_{zz} = \gamma_{xz} = \gamma_{yz} = 0$.
- Vertical deflection does not vary through the thickness.
- The strains in the deformed plate are small compared to unity, limiting the theory to linear elasticity.
- The laminate consists of perfectly bonded laminae – without this assumption, we do not have a laminate. Thus, the theory cannot be used to assess delamination.

With the sign convention introduced in Figure 3.1, a coordinate system is established such that the x- and y-axes describe the middle surface of a laminate, with the z-axis normal to this plane. The value of z is negative below the middle surface. As illustrated in Figure 3.4, lamina k has the thickness t_k, defined by the distance $|z_k - z_{k-1}|$. Thus, a laminate comprising K plies has a total thickness t, with individual thicknesses t_1, t_2, and so forth.

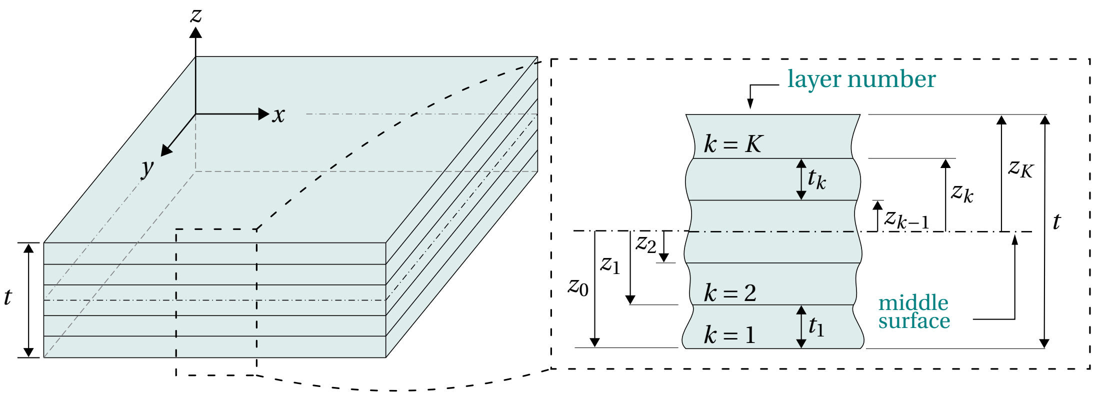

Figure 3.4: Laminate stacking sequence notation of a K-layered laminate [26].

By virtue of the Kirchoff hypothesis, the laminate strains are limited to ε_{xx}, ε_{yy} and γ_{xy}. These strains can be evaluated at any point through the thickness of the laminate, based on the middle surface strains ε^o_{xx}, ε^o_{yy} and γ^o_{xy} and the curvatures κ_{xx}, κ_{yy} and κ_{xy}. Followingly, the stresses in the k^{th} layer can be expressed by substituting the strain relations in Eq. (3.5) [26]:

$$\begin{Bmatrix} \sigma_{xx} \\ \sigma_{yy} \\ \tau_{xy} \end{Bmatrix}_k = \begin{bmatrix} Q_{11} & Q_{12} & Q_{16} \\ Q_{12} & Q_{22} & Q_{26} \\ Q_{16} & Q_{26} & Q_{66} \end{bmatrix}_k \left[\begin{Bmatrix} \varepsilon^o_{xx} \\ \varepsilon^o_{yy} \\ \gamma^o_{xy} \end{Bmatrix} + z \begin{Bmatrix} \kappa_{xx} \\ \kappa_{yy} \\ \kappa_{xy} \end{Bmatrix} \right] \tag{3.7}$$

Figure 3.5 illustrates the in-plane normal forces and moments per unit width acting on a flat laminate, which must be in equilibrium with the total internal ply forces. This relation is described through the $\boldsymbol{ABD}$-matrix, under the assumption that the stiffness matrix $\boldsymbol{Q}$ is constant through the thickness of each lamina:

$$\begin{Bmatrix} N_{xx} \\ N_{yy} \\ N_{xy} \\ M_{xx} \\ M_{yy} \\ M_{xy} \end{Bmatrix} = \begin{bmatrix} A_{11} & A_{12} & A_{16} & B_{11} & B_{12} & B_{16} \\ A_{12} & A_{22} & A_{26} & B_{12} & B_{22} & B_{26} \\ A_{16} & A_{26} & A_{66} & B_{16} & B_{26} & B_{66} \\ B_{11} & B_{12} & B_{16} & D_{11} & D_{12} & D_{16} \\ B_{12} & B_{22} & B_{26} & D_{12} & D_{22} & D_{26} \\ B_{16} & B_{26} & B_{66} & D_{16} & D_{26} & D_{66} \end{bmatrix} \begin{Bmatrix} \varepsilon^o_{xx} \\ \varepsilon^o_{yy} \\ \gamma^o_{xy} \\ \kappa_{xx} \\ \kappa_{yy} \\ \kappa_{xy} \end{Bmatrix} \tag{3.8}$$

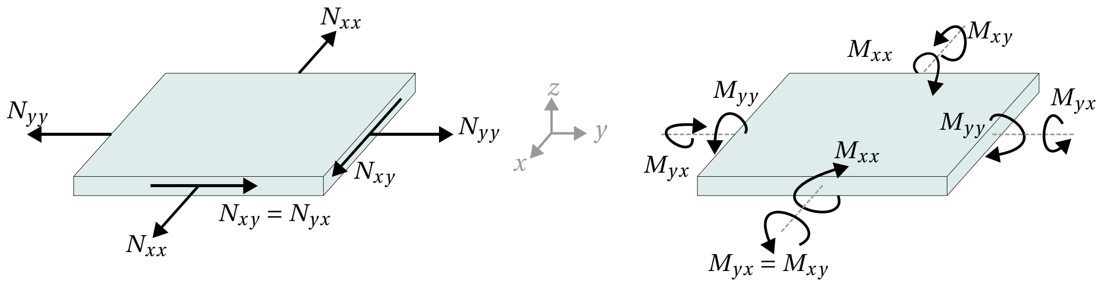

Figure 3.5: In-plane forces and moments acting on a laminate [11].

where $\boldsymbol{A}$ is the extensional stiffness matrix, $\boldsymbol{B}$ is the bending-extension coupling stiffness matrix and $\boldsymbol{D}$ is the bending stiffness matrix. The components of these matrices are calculated from:

$$A_{ij} = \sum_{k=1}^{K} \left(Q_{ij}\right)_k \left(z_k - z_{k-1}\right) \tag{3.9a}$$

$$B_{ij} = \frac{1}{2} \sum_{k=1}^{K} \left(Q_{ij}\right)_k \left(z_k^2 - z_{k-1}^2\right) \tag{3.9b}$$

$$D_{ij} = \frac{1}{3} \sum_{k=1}^{K} \left(Q_{ij}\right)_k \left(z_k^3 - z_{k-1}^3\right) \tag{3.9c}$$

where, referring to Figure 3.4:
z_k and z_{k-1} are the distances from the middle surface to the top and bottom of the k^{th} ply, respectively, and $(Q_{ij})_k$ is the element of the $\boldsymbol{Q}$ matrix of the k^{th} ply.

In-plane elastic constants

By considering the inverse of the resulting **ABD**-matrix – the compliance matrix – the equivalent elastic constants of the laminate can be defined. In this regard, it is important to point out the need for different properties when considering membrane elastic behaviour and bending behaviour, which are used in the calculations of global deflections and buckling verifications, respectively. Table 3.1 summarise these expressions, with a_{ij} referring to the inverse of **A** and d_{ij} to the inverse of **D**, and t being the laminate thickness.

Table 3.1: Membrane and bending equivalent elastic constants [19]

	Membrane elastic constants	**Bending elastic constants**
E_x	$1/(\mathrm{t} \cdot \mathrm{a}_{11})$	$12/(\mathrm{t}^3 \cdot \mathrm{d}_{11})$
E_y	$1/(\mathrm{t} \cdot \mathrm{a}_{22})$	$12/(\mathrm{t}^3 \cdot \mathrm{d}_{22})$
G_{xy}	$1/(\mathrm{t} \cdot \mathrm{a}_{66})$	$12/(\mathrm{t}^3 \cdot \mathrm{d}_{66})$
ν_{xy}	$-\mathrm{a}_{12}/\mathrm{a}_{11}$	$-\mathrm{d}_{12}/\mathrm{d}_{11}$
ν_{yx}	$-\mathrm{a}_{12}/\mathrm{a}_{11}$	$-\mathrm{d}_{12}/\mathrm{d}_{22}$

3.2.1. Laminates and laminate notations

The laminae can be arranged in numerous ways to form laminates. In this regard, we commonly distinguish between some important standard laminates and notations, some of which are illustrated in Fig. 3.6. The consequence of the respective configurations and how these affect the structural response are discussed in Chapter 3.2.2.

Unidirectional (UD) laminates

In a UD laminate, several layers of unidirectional plies are stacked together in the same direction to form a laminate with high axial stiffness, such as the zero-degree laminate [0°/0°/0°/0°] comprising four laminae.

Cross-ply laminates

Cross-ply laminates are characterised by the alternating layers of 0° and 90°, such as $[0°/90°]_3$, in which the subscript 3 implies that the pattern is repeated thrice: [0°/90°/0°/90°/0°/90°].

Angle-ply laminates

Similar to cross-ply laminates, angle-ply laminates comprise a repeating pattern of $+\theta/-\theta$. A commonly adopted configuration is $[+45°/-45°]_n$, or simply $[\pm45°]_n$, with n indicating the number of repetitions.

Symmetric laminates

In symmetric laminates, there is an identical ply (meaning with the same material, orientation and thickness) at an equal distance below the centerline of the laminate, forming a mirror image on both sides of the centerline. Consider for instance $[0°/45°/90°/-45°]_s$, where s indicates that the laminate is symmetrical, i.e. $[0°/45°/90°/-45°/-45°/90°/45°/0°]$.

Balanced laminates

In balanced laminates, there is an identical ply oriented in $-\theta$ for every ply of $+\theta$ orientation somewhere in the stacking sequence, such as $[\theta_1°/-\theta_1°/\theta_2°/-\theta_2°]$. Then by definition, the above presented $[0°/45°/90°/-45°]_s$ is both symmetric and balanced.

Quasi-isotropic laminates

Quasi-isotropic laminates exhibit an in-plane elastic response that is isotropic, which holds for laminates with $K \geq 3$ equal-thickness layers and K equal angles between the fibre orientations on each side of the middle surface. Thus, the angles between the layers is $\Delta\theta = \pi/\mathrm{K}$, which for an eight ($2K$) layered laminate result in $\Delta\theta = 45°$. Since neither the bending nor the strength of these laminates exhibits isotropic characteristics, they are called quasi-isotropic rather than isotropic [12].

Hybrid laminates

Hybrid laminates have two or more different materials, such as the commonly adopted carbon, c, and glass, g, fibre laminates. An example of such laminate is $[0^c/\pm45^g/-90^g]_s$ in which the 0° carbon ply is located away from the centerline to increase the bending stiffness of the laminate.

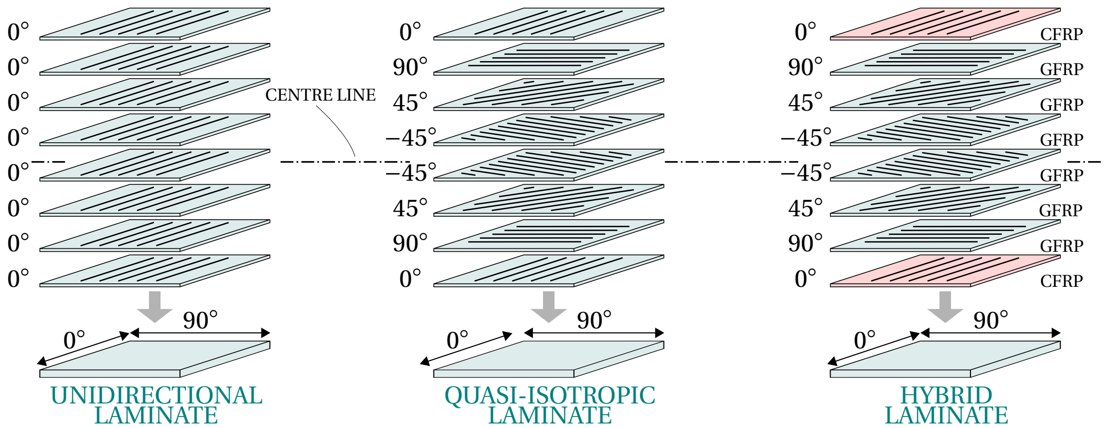

Figure 3.6: Typical laminate layups [11]

3.2.2. Behaviour of laminates

A laminate's response to the applied in-plane forces and moments depends on the present couplings. Based on specific terms of the **ABD**-matrix, it is possible to predict the behaviour. The following discussion explains the importance and influence of specific characteristics of the **ABD**-matrix, where reference will be made to Eq. (3.8). Although research suggests the presence of 24 unique couplings in laminates [27], the following will focus on the most commonly considered couplings.

A-matrix

The **A**-matrix represents the extensional stiffness of a laminate. From Eq. (3.9a), it is evident that this stiffness is not a function of a ply's relative distance to the middle surface; hence any stacking sequence of a prescribed set of plies will result in the same **A**-matrix. When the coupling between in-plane extensional and shear responses (see Fig. 3.7 (a)) is absent, the terms A_{16} and A_{26} are cancelled (=0). Such laminates are called specially orthotropic and can be achieved through balanced laminates.

B-matrix

The **B**-matrix represents the coupling stiffness matrix. Nonzero values in this matrix indicate that a normal force N_{xx} or bending moment M_{xx} will introduce extensional and shear deformations, in addition to bending-twisting curvatures. This warping of the laminate can be eliminated by having a symmetric layup, for which $\mathbf{B} = 0$, and all the couplings of this matrix are cancelled. Notably, balanced and symmetric laminates will ensure that $A_{16} = A_{26} = \mathbf{B} = 0$. Nonzero values of B_{11}, B_{12} and B_{22} introduce extension-bending coupling (see Fig. 3.7 (b)), while B_{16} and B_{26} introduce extension-twisting coupling (see Fig. 3.7 (c)), and B_{66} relate to the shearing-twisting coupling (see Fig. 3.7 (d)) [27].

D-matrix

The **D**-matrix represents the bending stiffness. The terms D_{16} and D_{26} introduce bending-twisting coupling (see Fig. 3.7 (e)) which can be cancelled with antisymmetric laminates, i.e. laminates in which for each $+\theta$ ply at a given distance above the middle surface, there is an identical ply oriented at $-\theta$ at the same distance below the middle surface. Such configurations are not symmetric, but the terms are zero for each 0° and 90° ply. Furthermore, when a large number of plies are oriented at $\pm\theta$, the terms become small and are usually insignificant for laminates comprising more than sixteen plies.

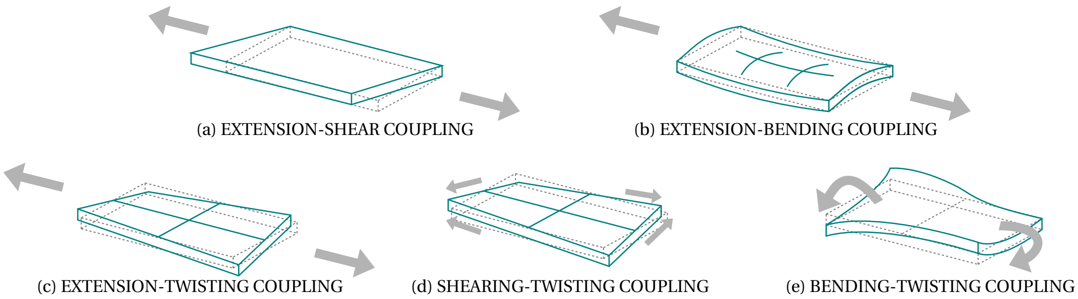

Figure 3.7: Relevant couplings in laminates that should be mitigated. (a) relate to A_{16} and A_{26}, (b) to B_{11}, B_{12} and B_{22} , (c) to B_{16} and B_{26}, (d) to B_{66}, and (e) relates to D_{16} and D_{26}.

3.2.3. Stress distributions in laminates

The stress state in a laminate is a function of the thickness, material and orientations of the layers that make up the laminate. Following the assumptions regarding classical lamination theory (CLT), the strain distribution will always be linear through the thickness, while the stress distribution is linear through each layer. Following Hooke's law, adjacent layers with different properties will generally result in stress jumps and a discontinuous stress distribution through the laminate thickness.

The below example (Fig. 3.8) illustrates the stress state in a [0°/60°/90°] laminate with arbitrary layer thicknesses subjected to uniaxial tension and bending. The resulting strains ε_x from the two load cases are transformed to stresses in the principal material coordinates of each layer according to Eqs. (3.3) and (3.5), evidently showing that the layers carry decreasing stresses as the orientation θ deviates from the load direction. The principal material axis 2 of the 90° layer coincides with the primary load direction, resulting in the most significant transverse stress at the bottom of this layer. Since UD plies generally exhibit poor tensile resistance in the 2-direction ($Y_T \approx 1/50\ X_T$), the critical layer of this configuration is the 90° ply, which will be apparent from Chapter 3.3.

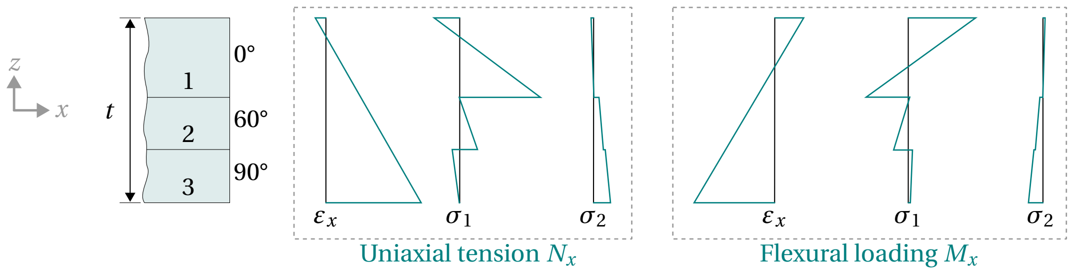

Figure 3.8: Laminate stress state of a 3-layered laminate, showcasing the relation between axial strains in the structural axis and the stresses in principal material axes.

Chapter 3.3. Failure in composites

Chapter objectives

O 3.3 What are FRP's failure mechanisms and failure modes, and how can these be predicted?

In structural design, failure starts with the weakest link, which for composite laminates is the matrix. Accounting for the redistribution of stresses within the laminate means that matrix failure usually does not lead to final failure. For this, the fibres must fail. While rupture of the fibres can be disastrous, the resin can often transfer the load around torn fibres through shear. These local failure modes are generally noncatastrophic on their own. However, simultaneous and interactive progression renders the prediction of failure in composites a complicated feat. Although a single ply can fail in several ways, the commonly distinguished modes are (Fig. 3.9):

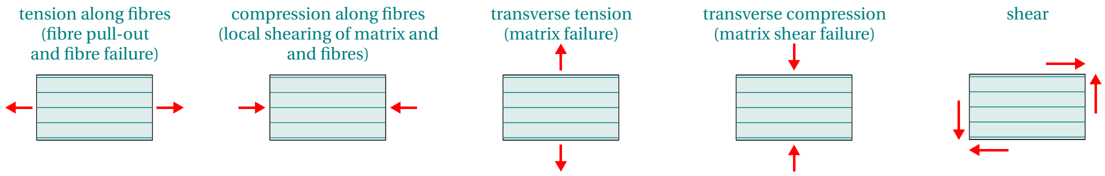

Figure 3.9: Failure modes of plies.

There seems to be no universal agreement on the nomenclature for the basic laminate strength properties. Therefore, to limit the confusion, this thesis will make use of the following notation concerning these strengths [12]:

$\mathbf{X_T}$: Tensile failure strength, 1-direction ($\sigma_1 > 0$) $\mathbf{X_C}$: Compressive failure strength, 1-direction ($\sigma_1 < 0$)
$\mathbf{Y_T}$: Tensile failure strength, 2-direction ($\sigma_2 > 0$) $\mathbf{Y_C}$: Compressive failure strength, 2-direction ($\sigma_2 < 0$)
$\mathbf{Z_T}$: Tensile failure strength, 3-direction ($\sigma_3 > 0$) $\mathbf{Z_C}$: Compressive failure strength, 3-direction ($\sigma_3 < 0$)
$\mathbf{S_{12}}$: Shear failure strength, 1-2-plane ($|\tau_{12}|$) $\mathbf{S_{13}}$: Shear failure strength, 1-3-plane ($|\tau_{13}|$)
$\mathbf{S_{23}}$: Shear failure strength, 2-3-plane ($|\tau_{23}|$)

Due to the complexity of determining laminate failure, most theories are limited to predicting first-ply failure (FPF), indicating the onset of failure. In some applications, this can progress to ultimate failure, while in others, the redistribution of stresses safeguards the structure. Therefore, the following theories are considered conservative and limited to plane stress situations. The reader is referred to [12, 28] for further investigation of the criteria in the 3D space.

3.3.1. Maximum stress criterion

The maximum stress failure criterion assumes that failure will occur whenever either of the stress components attains their limiting value, regardless of the value of others. Followingly, the condition for a "safe" lamina takes the form:

$$\begin{aligned} -X_C &< \sigma_1 < X_T \\ -Y_C &< \sigma_2 < Y_T \\ |\tau_{12}| &< S_{12} \end{aligned} \tag{3.10}$$

3.3.2. Maximum strain criterion

Analogous to the maximum stress criterion, the maximum strain theory states that failure occurs if any strain in the principal material axes is equal to or greater than the corresponding allowable strain. Following the linear relations between stresses and strains, admissable strains for a "safe" lamina can be expressed using the strength parameters of the respective lamina:

$$\begin{aligned} -\frac{X_C}{E_1} &< \varepsilon_1 < \frac{X_T}{E_1} \\ -\frac{Y_C}{E_2} &< \varepsilon_2 < \frac{Y_T}{E_2} \\ |\gamma_{12}| &< S_{12} \end{aligned} \tag{3.11a}$$

where the strains relate to principal stresses through:

$$
\begin{aligned}
\varepsilon_1 &= \frac{1}{E_1}\left(\sigma_1 - \nu_{12}\cdot\sigma_2\right)\\
\varepsilon_2 &= \frac{1}{E_2}\left(\sigma_2 - \nu_{12}\cdot\sigma_1\right)\\
\gamma_{12} &= \frac{\tau_{12}}{G_{12}}
\end{aligned} \tag{3.11b}
$$

3.3.3. Tsai-Wu failure criterion

Tsai and Wu (1971) [28] postulated that there exists a failure surface in the six-dimensional stress space in the form

$$F_i\sigma_i + F_{ij}\sigma_i\sigma_j = 1 \qquad i,j = 1,\cdots,6 \tag{3.12}$$

where the contracted stress notation is used ($\sigma_4 = \tau_{23}$, $\sigma_5 = \tau_{31}$ and $\sigma_6 = \tau_{12}$). Equation (3.12) is a lengthy expression. By limiting the scope to orthotropic laminae under plane stress conditions, it can be formulated as

$$\sigma_1\left(\frac{1}{X_T} - \frac{1}{X_C}\right) + \sigma_2\left(\frac{1}{Y_T} - \frac{1}{Y_C}\right) + \frac{\sigma_1^2}{X_T X_C} + \frac{\sigma_2^2}{Y_T Y_C} + \frac{\tau_{12}^2}{S_{12}^2} - \sigma_1\sigma_2\sqrt{\frac{1}{X_C X_T Y_C Y_T}} = 1 \tag{3.13}$$

3.3.4. Discussions on lamina failure criteria

Although the maximum strain and maximum stress criterion are conceptually simple to implement, the five inequalities related to the five failure modes (Fig. 3.9) render them computationally inconvenient. The coupling effects of the various stress components are not considered for the maximum stress criterion, while the maximum strain criterion only accounts for this through Poisson's ratio, which is the main difference between the criteria. Furthermore, the theories usually lead to an unrealistic prediction of low transverse tensile strength because the restraining effect of adjacent layers arresting matrix crack propagation is not incorporated [29]. The possibility of adopting wrong stresses if assuming a linear strain behaviour until failure may overestimate the strength, resulting in disastrous consequences (see Fig. 3.10). On the other hand, the Tsai-Wu criterion indirectly accounts for these effects through experimental curve fitting, making it an interactive criterion all evaluated against a single value. A comparison of the discussed failure theories is visualised through their respective failure envelopes (Fig. 3.11). A minor weakness regarding the Tsai-Wu criterion is the unconservative values in the third ($-\sigma_1$, $-\sigma_2$) quadrant [30].

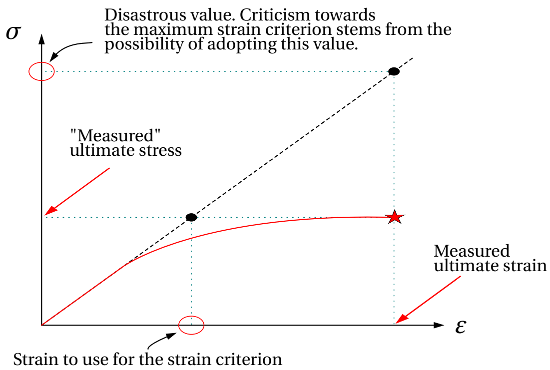

Figure 3.10: Criticism of the ultimate strain criterion: the possibility of adopting the wrong value of the stresses may lead to disastrous consequences.

Quantifying failure

While the introduced theories predict whether or not a lamina fails, the degree of utilisation is not clear. In this regard, the failure theories can be extended by introducing the load proportionality factor (LPF), or strength ratio, denoted by R, expressing a factor for the admissible increase of the loads (stress components) to reach failure. Naturally, the reciprocal of the LPF will return the utilisation of a lamina, expressed as the exposure factor $f_E = 1/R$. In case of the Tsai-Wu criterion, Eq. (3.13) is

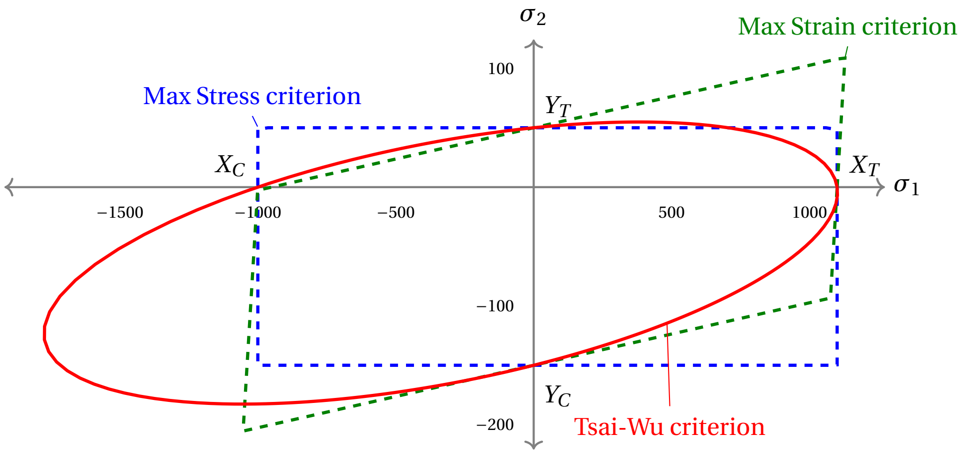

Figure 3.11: Failure envelopes for maximum strain criterion, maximum stress criterion and the Tsai-Wu failure criterion under combined normal stresses in directions parallel (σ_1) and perpendicular (σ_2) to the fibres. Material: E-glass/Vinylester.

adapted to take into account the LPF as a dimensionless parameter R. Solving the resulting quadratic equation for the LPF [31, 32]:

$$R^2\left(\frac{\sigma_1^2}{X_T X_C}+\frac{\sigma_2^2}{Y_T Y_C}+\frac{\tau_{12}^2}{S_{12}^2}-\sigma_1\sigma_2\sqrt{\frac{1}{X_C X_T Y_C Y_T}}\right)+R\left(\sigma_1\left(\frac{1}{X_T}-\frac{1}{X_C}\right)+\sigma_2\left(\frac{1}{Y_T}-\frac{1}{Y_C}\right)\right)=1 \quad (3.14a)$$

with

$$\begin{aligned} a &= \frac{\sigma_1^2}{X_T X_C}+\frac{\sigma_2^2}{Y_T Y_C}+\frac{\tau_{12}^2}{S_{12}^2}-\sigma_1\sigma_2\sqrt{\frac{1}{X_C X_T Y_C Y_T}} \\ b &= \frac{1}{X_T}-\frac{1}{X_C} \\ c &= -1 \end{aligned} \quad (3.14b)$$

and

$$R=\frac{-b+\sqrt{b^2-4ac}}{2a} \quad (3.14c)$$

from which the exposure factor corresponding to Tsai-Wu reads

$$f_{E,TW}=\frac{1}{R} \quad (3.15)$$

Note that R can take zero values, which must be counteracted by letting $f_{E,TW}=0$ when $R=0$. Similarly, the exposure factors for maximum stress and maximum strain can be defined as

$$f_{E,MS}=\max\left(-\frac{\sigma_1}{X_C},\frac{\sigma_1}{X_T},-\frac{\sigma_2}{Y_C},\frac{\sigma_2}{Y_T},\frac{|\tau|}{S_{12}}\right) \quad (3.16)$$

and

$$f_{E,ME}=\max\left(-\frac{\varepsilon_1}{X_C},\frac{\varepsilon_1}{X_T},-\frac{\varepsilon_2}{Y_C},\frac{\varepsilon_2}{Y_T},\frac{|\gamma_{12}|}{S_{12}}\right) \quad (3.17)$$

where $f_{E,MS}$ and $f_{E,ME}$ refer to the exposure factors relating to the maximum strain criterion and the maximum strain criterion, respectively.

Consider a $[0°/45°/90°/-45°]_s$ laminate of E-glass/Polyester (see Table 6.2) with ply thicknesses of 1 mm subjected to $N_x = 500 \quad N/\text{mm}$ and $M_x = 500 \quad N\text{mm}/\text{mm}$, resulting in the strains and stresses shown in Fig. 3.12. Since the 0° plies coincide with the global x-direction, the local- and global stresses are effectively the same in these plies. In the ±45° plies, it can seem like the absolute magnitude of the transverse- and shear stresses are equal. This is merely a coincidence: the shear strains coincide with the extension in the x-direction, causing relatively high shear (τ_{12}) stress. Yet, since the transverse stiffness of the ply is greater than the shear stiffness ($E_2 > G_{12}$), it carries more stresses giving the illusion that the stresses are equal. Owing to the Poisson's ratio, the axial extension causes transverse contraction, as can be seen from the negative values of σ_y and σ_1 for the 90° plies.

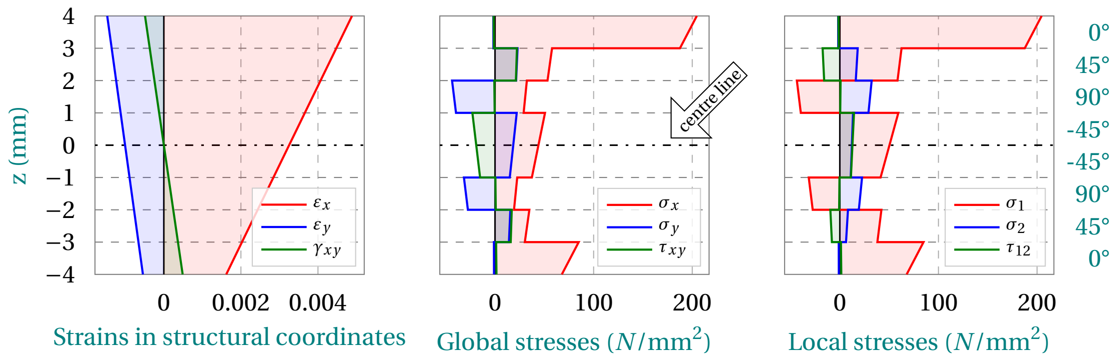

Figure 3.12: The stress-strain relationship in an 8-layered quasi-isotropic laminate subjected to $N_x = 500\ N/\text{mm}$ and $M_x = 500\ N\text{mm}/\text{mm}$.

The corresponding exposure factors (Eqs. (3.15)–(3.17)) at the top and bottom of each layer (see Fig. 3.13) reveal the inaccuracy of the maximum stress and the maximum strain theory for combined load cases and their disparities. The poor transverse tensile resistance of UD lamina, as mentioned in Chapter 3.2.3, result in relatively high exposure factors for 90° plies, with the most adverse effect in the third layer owing to the combined tensile stresses from bending and uniaxial extension. Having a detailed look at the applied stresses at the top of the third layer in relation to the failure envelopes, visualised in Fig. 3.14, confirms that strength ratio R is the least according to the maximum strain theory (remember that $f_E = \frac{1}{R}$). In the ±45° plies, a greater exposure factor is obtained according to Tsai-Wu, owing to its consideration of the interaction of stresses, whereas the remaining theories merely evaluate the adverse stresses due to σ_1, σ_2 and τ_{12}. Generally, the Tsai-Wu criterion reveals a greater utilisation (f_E) due to the interaction of the stresses, which amounts to approximately 60 % greater utilisation in the ±45° plies.

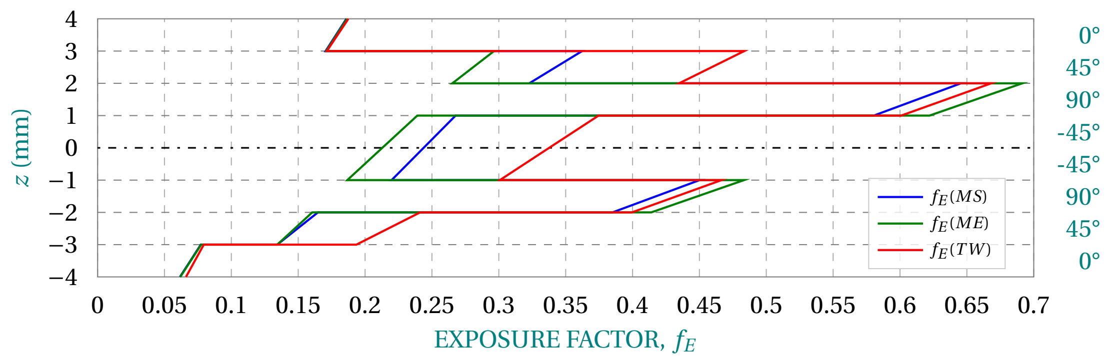

Figure 3.13: Exposure factors according to the maximum stress criterion (blue), maximum strain criterion (green) and the Tsai-Wu criterion (red) at the top and bottom of each layer in a laminate following the stress-strain relationship in Fig. 3.12.

3.3.5. Failure of laminates

The presented theories are by no means an exhaustive list of the available theories and simply present failure criteria related to UD fibre composites. The theories rely on the implementation of CLT, generally failing to include the build-up of large interlaminar stresses along the free boundary edges, strongly influencing failure delamination, which in reality can be coupled with the intralaminar failure.

Following in the footsteps of Tsai and Wu, numerous theories have been developed to best predict the failure modes in laminates and diminish the discrepancies between experimental results. In 1980, Hashin developed a failure-mode-based theory, stating that the available theories poorly predict fail-

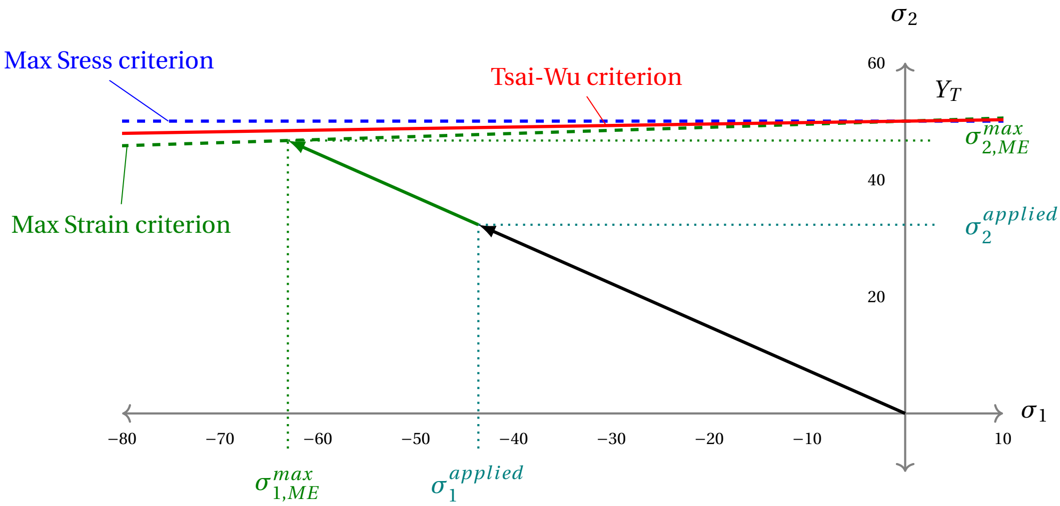

Figure 3.14: Stress at the top of layer 3 (90°) from Fig. 3.13 shown as a loading vector in black, and the strength ratio **R** corresponding to the maximum strain (ME) theory as a scaling factor in green. The applied stresses $\sigma_i^{applied}$ can be increased by a factor R before failure is estimated: $\sigma_{i,ME}^{max} = \sigma_i^{applied} \cdot R_{ME}$.

ure [mode] due to a specified stress state. The Hashin criterion accounts for four separate failure modes on a lamina level: tensile fibre failure, compressive fibre failure, tensile matrix failure and compressive matrix failure, resulting in a piece-wise smooth failure envelope [29, 33]. Discovering the poor predictive capabilities of Hashin's theory in the case of fibre or matrix compression, Puck (1998) improved and extended Hashin's theory [34], which is further improved with the introduction of the LaRC03 criterion [35]. The continuous efforts to improve the failure prediction of laminates introduce increasingly complex expressions, leaving only a few of them available in a form that can be readily utilised in practical applications. Therefore, with always room for improvement, the Tsai-Wu criterion remains the most popular theory.

Last ply failure

Designs utilising the concept of FPF are generally conservative and may inaccurately assume poor resistance of laminate that would have sufficient strength. The failed ply causes an increase of stresses and strains in the remainder of the laminate and a reduction in its stiffness. Although mathematically questionable, several available methods account for the failed ply and subsequent laminate behaviour. The *total discount method* assumes zero strength and stiffness in the failed ply in all directions. The *limited discount method* takes zero strength and stiffness for the transverse and shear modes if the failure occurs in the matrix. If fibre rupture causes ply failure, the *total discount method* is used. The *residual discount method* assigns residual strength and stiffness to the failed ply [11]. The progressive failure in a laminate involves the successive failure of plies in increasing order of strength in the loading direction. Generally, the transverse plies fail, followed by the off-axis angled plies, causing delamination followed by splitting of 0° plies and last ply failure.

More sophisticated analyses of the progressive failure of laminates require investigations not based on CLT, enabling more accurate modelling of the interlaminar behaviour – for instance, non-linear fracture mechanics analyses and detailed finite element analyses.

Takeaways from laminate failure

As mentioned, 'failure' in composites is not a unique event in most cases. Instead, the failure process will follow a gradual sequence of microcracking and delamination leading up to structural collapse. The famously known 'world-wide failure exercise (WWFE)', a comprehensive work attempting to expose the strengths and weaknesses of the then (2004) available theories, reveals a mindset every design practitioner should bear in mind when dealing with FRP. In declining to join this research, Prof. Hashin (famous for [33]) states :

> *My only work in this subject relates to failure criteria of unidirectional fibre composites, not to laminates. [...] I must say to you that I personally do not know how to predict the failure*

of a laminate (and furthermore, that I do not believe that anybody else does) [30].

The conclusion of the WWFE strengthens Hashin's view, seeing that none of the 19 theories could predict the final measured strength within ±50% accuracy in 85% of the load cases, at best [30].

3.3.6. Design guidelines – Rules of thumb

The discussion throughout the preceding chapters, in addition to some suggestions mentioned herein, can be conceptualised to formulate design guidelines for the robust and practical design of plastic composite structures. The following discussion introduces concepts that prove instrumental to the design and optimisation framework laid out in this thesis. Note that the presented recommendations certainly are not comprehensive but are intended as general guidance on the design of FRP load-bearing structures.

Firstly, we should consider the industry recommendations from Chapter 2.5, namely to limit the thickness of laminates to 20 mm, while ensuring a minimum thickness to overcome instability and transportation issues. In doing so, cost-effective designs with minimal manufacturing implications are achieved.

The layup of a laminate, i.e. the orientation, material and thicknesses of the plies, is instrumental for its structural response and behaviour, not to mention its behaviour during manufacturing. Chapter 3.2 introduce wanted and unwanted behaviour in composites. Notably, laminates should be symmetric to eliminate membrane/bending coupling ($\mathbf{B} = 0$). Moreover, balanced laminates should be achieved to eliminate extensional shear coupling ($A_{16} = A_{26} = 0$). Preferably, the bending-twisting coupling should be avoided through antisymmetric layups. However, such configurations violate the possibility of having symmetric laminates. Therefore, one should aim to minimise the terms D_{16} and D_{26} through grouping of $+\theta°$ and $-\theta°$ plies.

The bending, twisting and warping shown in Fig. 3.7 is not only a consequence of the applied loads and moments. In fact, unbalanced laminates tend to warp and twist due to thermal contraction during curing, in which case the laminate would have to be forced back into shape during assembly [11]. Hence, if not diminished through adequate design, these effects must be cautiously accounted for during production, much like the spring back effect in sheet metals.

An unexpected layup obtained through the optimisation procedure at an earlier stage of this thesis resulted in an axially tensioned laminate only comprising ±45° laminae. While this may satisfy the stiffness requirements, it proves to be problematic. Such configurations require that most of the stresses are transferred through interlaminar stresses that the resin must resist. This introduces considerable creep, not to mention a highly non-linear stress-strain behaviour. By adopting *the 10 % rule*, i.e. having at least 10 % of the fibres lined up with each of the principal directions: 0°, 45°, −45° and 90° [13], the stress-strain behaviour is linearised while the creep effects are reduced by ensuring a minimum stiffness in the main load direction. Due to the hybrid laminates adopted in this thesis, a slightly stricter *12.5 % rule* is implemented.

Chapter 3.4. Conclusion

This chapter answers the following objectives:

O 3.1 How are the anisotropic intrinsic properties of FRP defined?
O 3.2 How can the properties and behaviour of a laminate be predicted?
O 3.3 What are FRP's failure mechanisms and failure modes, and how can these be predicted?

Although designs comprising plastic composites offer significant advantages, it is essential to understand and define the necessary steps in the tailorable design process. First, the material properties are defined at a ply level for the UD laminae based on micromechanics using the *Rule of Mixtures* or the *Halpin-Tsai* method if test data is not available. Then these building blocks are combined to determine the in-plane properties in the structural coordinate of the laminate through classical lamination theory (CLT), which estimates the laminate's response to the applied loads and moments.

Establishing the laminate properties allows verifying whether it fulfils the strength requirements. These verifications are performed at the ply-level through intralaminar failure theories: the maximum stress criterion, the maximum strain criterion and the Tsai-Wu failure criterion. While both the maximum stress and maximum strain criterion are conceptually easy to implement, the Tsai-Wu criterion remains the most popular theory due to its efficient compromise between accuracy and ease of implementation. Although the maximum- strain and stress criterion generally are conservative, combined load cases may overestimate the strength leading to unconservative utilisation: a difference of 60 % was observed between the theories' estimations.

Finally, a set of design guidelines are derived based on the presented material, which provides the foundation for the optimisation framework presented in Chapters 5 and 6. The process for defining the laminate properties and the corresponding strengths of the laminates paves the way for the definition of the design criteria for any optimisation framework.

4

STRUCTURAL OPTIMISATION AND FORM-FINDING

With the advent of parametric and computational design, there has been an increasing interest in form-finding and structural optimisation of thin-walled structures. These concepts allow for numerical optimisation, exploring a vast amount of different design configurations. These principles are relatively old, but the cost savings and improved level of integrated design have sparked an interest among architects and engineers in this direction. Thus far, the potential benefits of these form-finding approaches incorporating the added benefits of FRP remain relatively uncharted territory.

This chapter aims to answer:

O 4.1 What form-finding methods are available that are beneficial to FRP design, and what are their limitations?

O 4.2 What is structural optimisation, and how can it be used to solve the aforementioned limitations?

O 4.3 What specific challenges and potential solutions pertain to the numerical optimisation of FRP structures?

Chapter 4.1. Form-finding

Chapter objectives

O 4.1 What form-finding methods are available that are beneficial to FRP design, and what are their limitations?

Traditional design methods through trial-and-error are not applicable for the design of shape-resistant structures. Instead, so-called form-finding or shape optimisation methods are required for their design. Historically based on experimental and increasingly diverse numerical approaches, form-finding has been successfully used in determining the optimal shapes of shell/membrane structures. Famous for their contribution to this topic is Gaudí with his inverse hanging chain models to create compression structures, later extended by Isler with his hanging membrane models (Fig. 4.1). Contrastingly, Frei Otto's soap film analogies (Fig. 4.2) present an approach to determine the shape of pre-stressed membranes and tents [36, 37]. An extension of these principles is the distended pneumatic membranes, i.e. structures supported by internal air pressure, presenting a set of minimal structures par excellence, as no cables or masts are required [38]. Although the application of pneumatic structures dates far back – used for hot air balloons and radar-proof 'radomes' for military use – Otto was the first to undertake academic investigations [39]. Otto used the pneumatic method to capitalise on the tensile capabilities of membranes. In contrast, Isler used the concept to generate concrete shells inheriting constant buckling stability at all points [40], see Fig. 4.4. However, due to high maintenance costs associated with these permanently insufflated structures, their application tends to stop as an idea at the drawing table – such as Otto's arctic city envelope (1971, Fig. 4.3).

Apart from being derived from innovative structural experiments, these concepts are based on the principle of *form follows force*, presenting shape-resistant structures which carry the design loads mainly through in-plane or membrane resultants acquired by shaping the material according to the applied loads. The mechanical equivalent is the minimisation of strain energy while restricting the total structural mass [36].

Minimising the strain energy U is analogous to maximising the stiffness. Furthermore, it diminishes the presence of bending stresses, resulting in a shape-resistant structure reacting the stresses through membrane stresses. As such, the resulting geometrical shape will follow the moment distribution, much like the concepts of hanging models. From Equation (4.1), it is evident that increasing the structural stiffness $[K]$ reduces the strain energy and that the strain energy contributed by the bending curvature and axial-bending coupling are quadratically and linearly proportional to the section thickness z, respectively [41]:

$$U = \frac{1}{2}\{R\}^T[K]^{-1}\{R\} = \frac{1}{2}\int_V \left(\{\varepsilon^0\}^{\mathrm{T}}[E]\{\varepsilon^0\} + 2z\{\kappa\}^{\mathrm{T}}[E]\{\varepsilon^0\} + z^2\{\kappa\}^{\mathrm{T}}[E]\{\kappa\}\right)\mathrm{d}V \tag{4.1}$$

where $\{R\}$ global nodal load vector and $[E]$ is the material stiffness (**ABD**).

The dynamic relaxation and the updated reference strategy techniques (soap film analogies); and the geometrical non-linear large-deformation analyses (simulating hanging models) represent the numerically developed equivalents to these experimental approaches. However, these numerical approaches inherit the limitations of the physical approaches they simulate. For instance, the hanging models are based on mirrored tensile structures, resulting in pure compression and buckling instabilities, while the soap film analogies can physically only be implemented on isotropic films [36, 40]. Since these methods mainly apply to isotropic materials maintaining the same material properties during the form-finding process, determining the optimal shapes of laminated FRP composite structures requires a different approach [42].

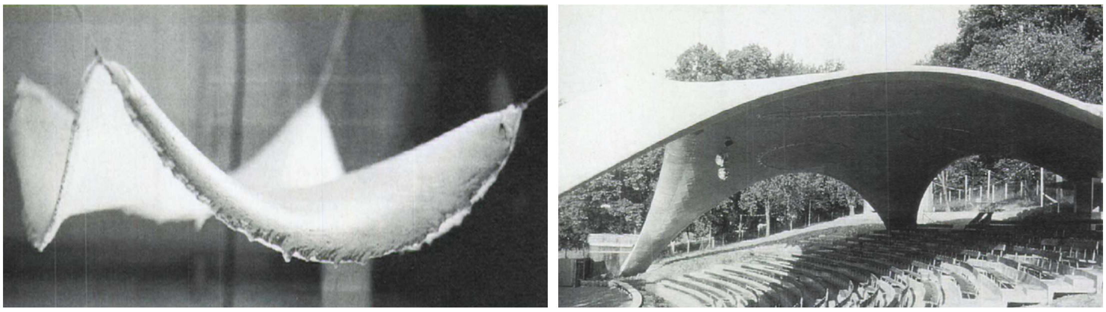

From hanging membranes . . . . . . to concrete shells.

Figure 4.1: Isler's hanging membrane approach to form-finding used to design the open-air theatre in Grõtzingen, Germany, 1977 [40].

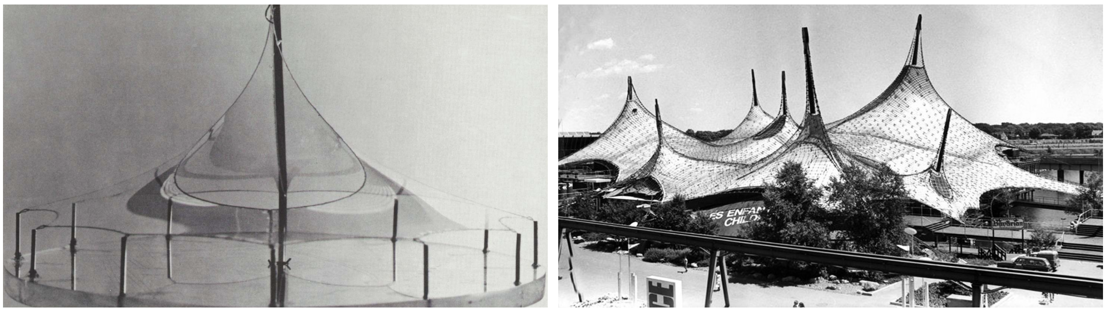

From soap film experiments . . . . . . to tent-like structures.

Figure 4.2: Otto's soap film analogies, used in the design of the German Pavillion in Montreal, Canada, 1967 [38].

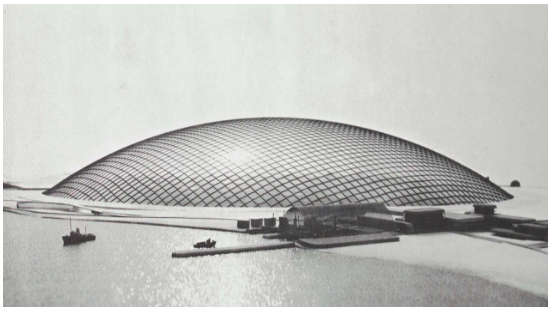

Figure 4.3: Otto's pneumatic membrane structures utilising the tensile capabilities of fabrics, 1971 [38].

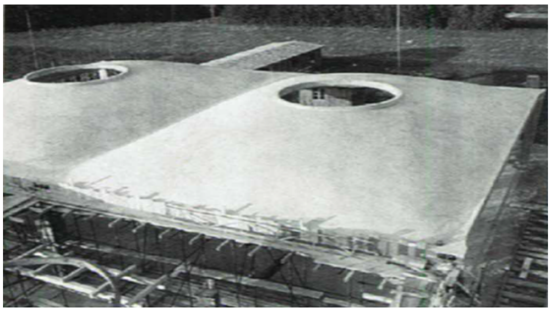

Figure 4.4: Isler's concrete shells based on pneumatic models, 1955 [40].

Chapter 4.2. Structural optimisation

Chapter objectives

O 4.2 What is structural optimisation, and how can it be used to solve the aforementioned limitations?

The basic idea of structural optimisation involves finding a solution to a structural problem that sustains the loads in the best way or fulfils any other criteria most optimally. Examples of such problems could be finding the lightest beam that resists the given loads (i.e. a weight minimisation problem) or the beam that provides the greatest stiffness (i.e. stiffness maximisation). These problems are generally pointless without defining some constraints to limit, for instance, the geometry, the stresses, the displacement or the mass of the structure. Without these constraints, we may find ourselves without a well-defined solution. Structural optimisation problems are divided into three categories: sizing, shape, and topology optimisation [43, 44].

Sizing optimisation

Sizing optimisation is similar to the design procedure familiar to all structural engineers: optimisation of the cross-section. This means that the design variables define the cross-section of one (or more) of the members without changing the end-nodes of the elements. These problems can, for instance, aim to find the optimal member area in a truss structure or the optimal thickness of an elastic plate.

Shape optimisation

Shape optimisation indicates problems where the design variables represent the form or contour of some part of the boundary of the structural domain. Typically, this means the position of the nodes within the design space can be varied, which ultimately alters the shape of the structure. Instead of playing with the definition of the nodes, mathematical functions can be used to define the shape – both for beam and shell-like structures (see Fig. 4.5).

Topological optimisation

Topology optimisation involves determining the number, shape and location of holes in a solid structure and the connectivity to the domain. In the case of a solid sheet, a binary representation of the material can be used – either it is present or absent. For discrete topological problems, such as a truss, the problem is an extension of sizing optimisation, as the cross-sectional area is allowed to be zero.

A schematisation of these different concepts is shown below (Fig. 4.5). Combinations of these concepts are possible – if not essential. Especially so for the concurrent optimisation of FRP structures and their material architecture, combining shape with a complex sizing optimisation.

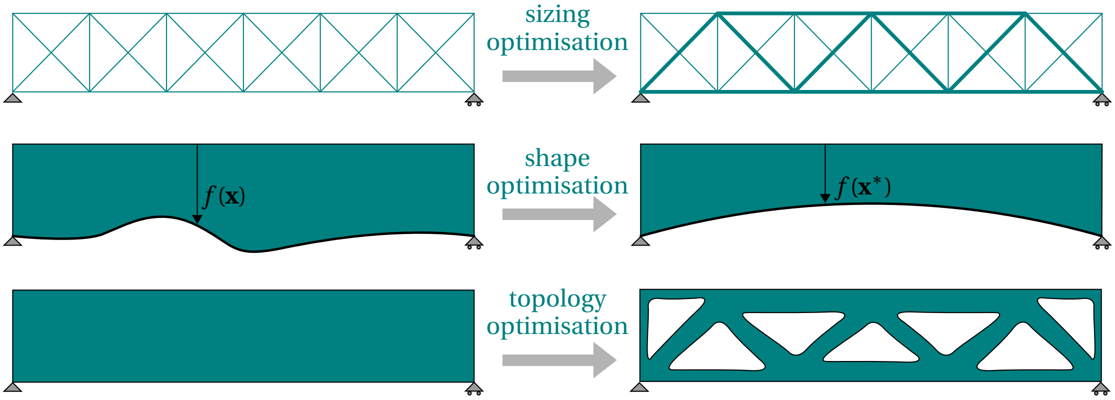

Figure 4.5: Categories of structural optimisation [43, 44]. $\mathbf{x}^*$ indicates the vector of design variables pertaining to the optimal solution.

In order to improve a design, one must first define the design problem, which may arguably be the most critical step of the procedure. The remainder of this section formulates both single and multi-objective optimisation problems and the means to reduce multi-objective problems capable of a single-valued scalar evaluation.

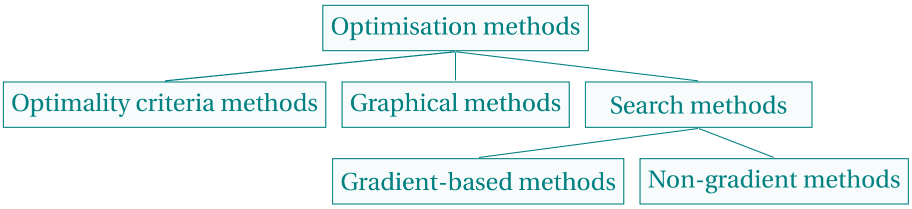

Figure 4.6: Classification of solution techniques for optimisation problems [45].

4.2.1. Solution techniques and problem classifications

The solution techniques for optimisation problems can be broadly divided as shown in Fig. 4.6. This thesis is concerned with the search methods using numerical algorithms, which may be subject to the following types of optimisation problems [43, 45, 46].

Discrete *versus* continuous optimisation problem:
If all the variables can take on any (or a set of) real values, it is a continuous optimisation problem. On the other hand, if the variables are discrete, the problem becomes a discrete one. Generally, continuous problems tend to be easier to solve owing to the smoothness of the function: the function values at a point $\mathbf{x}$ can be used to deduce information about points in the neighbourhood of $\mathbf{x}$. However, algorithms and computing technology advancements have significantly improved the efficiency of solving even increasingly complex discrete problems.

Local *versus* global optimisation problem:
Available algorithms can quite efficiently find local optimum points, i.e. a point where the function value is smaller (or greater) than or equal to the value at nearby points. If this local optimum is smaller than or equal to the value at all other feasible points, it is the global minimum. Due to the possible extreme number of local optima, obtaining the global optimum can be tremendously challenging. However, there is an important class of problems for which the local optimum is the global optimum, namely convex problems.

Direct *versus* gradient-based method:
Gradient-based solvers require continuous functions to calculate the gradient, used for determining the direction to possible stationary points. On the other hand, direct search methods solve the problem without any information about the gradient or higher derivatives, enabling solving functions that are not continuous or differentiable, such as discrete problems.

4.2.2. Single objective optimisation

Optimisation problems always include an objective function F, expressing the goal of the optimisation. It returns a numeric value indicating the goodness of the design, where lower values typically are favourable (a minimisation problem). The objective function is a function of the design variables $\mathbf{x}$, which typically can describe the geometry of a structure. These are limited to some lower and upper bounds, often referred to as side constraints, representing, e.g. a feasible range of the variables. Finally, constraints (can be introduced to) ensure that the structure's response adheres to the design criteria. Hence, a design problem can be presented in a mathematical form as

$$\text{Minimise } F(\mathbf{x}) \tag{4.2}$$

Subject to

$$g_i(\mathbf{x}) \leq 0, \qquad i = 1, \ldots, n \tag{4.2a}$$
$$h_i(\mathbf{x}) = 0, \qquad i = n+1, \ldots, n_c \tag{4.2b}$$
$$x_k^l \leq x_k \leq x_k^u, \qquad k = 1, \ldots, m \tag{4.2c}$$

where g and h are the inequality and equality constraints, respectively, n_c is the number of constraints, and the superscripts l and u indicate the lower- and upper bound of design variable k, respectively, with a total of m variables.

4.2.3. Multi-objective optimisation

More often than not, there is more than a singular objective, especially in the context of structural optimisation. Due to the unlikelihood that a single solution simultaneously optimises each objective, these problems introduce conflicts. Consider, for instance, concurrent stiffness maximisation and material minimisation. Obviously, the stiffness benefits from as much material as possible, defeating the goal of the second objective. Nevertheless, these problems can be mathematically formulated as

$$\text{Minimise } F_1(\mathbf{x}), F_2(\mathbf{x}), \ldots, F_q(\mathbf{x}) \qquad \text{or} \qquad \mathbf{F}(\mathbf{x}) \tag{4.3}$$

Subject to

$$g_i(\mathbf{x}) \leq 0, \qquad i = 1, \ldots, n \tag{4.3a}$$

$$h_i(\mathbf{x}) = 0, \qquad i = n+1, \ldots, n_c \tag{4.3b}$$

$$x_k^l \leq x_k \leq x_k^u, \qquad k = 1, \ldots, m \tag{4.3c}$$

where q is the number of objective functions. Considering that all objectives rarely can be optimised for the same $\mathbf{x}$, one normally tries to obtain the so-called Pareto optimal solutions [43, 45].

4.2.4. Pareto optimality

According to the principle of Pareto optimality, a solution is considered non-dominated (or non-inferior) if none of the objective functions can be improved in value without degrading the other objective function values. These Pareto optimal solutions are considered equally good if no other preference information exists. Hence, a point $\mathbf{x}^*$ in the feasible design space S is defined as Pareto optimal iff (if and only if) there does not exist another point $\mathbf{x} \in S$ such that $F_q(\mathbf{x}) \leq F_q(\mathbf{x}^*) \forall q$ and $F_q(\mathbf{x}) < F_q(\mathbf{x}^*)$ for at least one q [45].

Commonly, one obtains Pareto optimal points by introducing a weighted sum of the objectives, i.e.

$$\sum_{q=1}^{Q} w_q F_q(\mathbf{x}) \qquad \text{with} \qquad \sum_{q=1}^{Q} w_q = 1 \tag{4.4}$$

where Q is the number of objective functions. Considering a problem of two objectives (i.e. F_1 and F_2), one can map out the Pareto-front based on the non-dominated solutions corresponding to each $w_q \in [0, 1]$ (see Fig. 4.7).

Weak Pareto optimality

Similarly, in a case where one objective may be improved, without improving (or penalising) the others, it is considered a weak Pareto optimal point. This is the case for $\mathbf{x}^* \in S$ iff $\nexists$ (there does not exist) $\mathbf{x} \in S$ such that $F_q(\mathbf{x}) < F_q(\mathbf{x}^*) \forall q$. Figure 4.8 illustrates this concept. At the line A-B at the boundary of the feasible criterion space (i.e. $Z = \{F_q(\mathbf{x}) | \mathbf{x} \in S\}$), F_1 can be minimised without affecting F_2: there are several points $F_1(\mathbf{x}) < F_1(\mathbf{x}_E)$ and $F_2(\mathbf{x}) = F_2(\mathbf{x}_E)$.

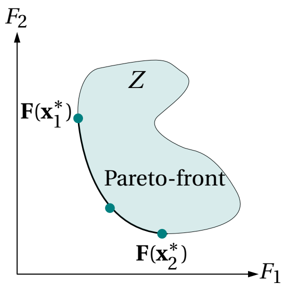

Figure 4.7: Pareto-front.

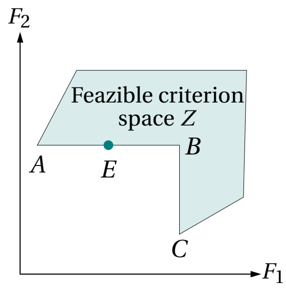

Figure 4.8: Weak Pareto optimality [45].

A priori and a posteriori articulation

The concept of Pareto optimality eventually leads to a point where one must articulate the preferences of the optimisation. With the information on all the different weights and corresponding values of the objectives, one can articulate the desired Pareto optimal out of the points on the Pareto-front – an example of a posteriori articulation. Since these preferences can be hard to articulate, or because one does not have a clear preference for the objectives, one can use some of the methods discussed in [45].

Mapping out the Pareto-front can be overly time-consuming for complex problems as it essentially requires running optimisations with numerous variations on the weights of the objectives. Therefore, especially useful if the designer has preferences on the relative importance of the objectives, one can make an a priori articulation of the preferences. Considering Eq. (4.4), one can define the relative importance of the objectives through their respective weights, culminating in a single optimisation problem:

$$\underset{\mathbf{x}\in S}{\text{Minimise}} \quad u(\mathbf{x}) = \sum_{q=1}^{Q} w_q F_q(\mathbf{x}) \tag{4.5}$$

where u represents the new objective.

4.2.5. Dealing with constraints

Constraints play an important role in optimisation, reducing the feasible solution space to a smaller one. The incorporation of these depends on the algorithm at hand, but for algorithms that evaluate a singular scalar (such as the Galapagos solver, Chapter 4.4.2), so-called death penalties or penalty functions are convenient [47]. Death penalties add a constant to the function value if one or more constraints are violated and may therefore cause premature stagnation. For this reason, exterior penalty functions are preferred, as these add a penalty relative to the constraint violation. Considering only inequality constraints (for brevity), a constrained optimisation problem can be formulated as a pseudo-objective function:

$$\text{Minimise} \quad \Phi(\mathbf{x}, r_p) = \mathbf{F}(\mathbf{x}) + r_p \cdot P(\mathbf{x}) \tag{4.6}$$

where $\mathbf{F}$ are the objective functions and the penalty function $P(\mathbf{x})$ is defined as:

$$P(\mathbf{x}) = \sum_{i=1}^{n_c} \left\{ \max\left(0, g_i(\mathbf{x})\right) \right\}^2 \tag{4.7}$$

with r_p being a multiplier that should be appropriately tuned to the problem. Having covered the fundamentals of optimisation, it is interesting to see how researchers have implemented these methods in optimising FRP structures, as will be introduced in the following sections.

Chapter 4.3. Structural optimisation in FRP

Chapter objectives

O 4.3 What specific challenges and potential solutions pertain to the numerical optimisation of FRP structures?

The advent of the computer and the proceeding development of numerical optimisation methods have enabled the formal exploration of thin-walled plates and exceedingly complex structures in FRP; however, the general literature seems to miss out on the benefits of FRP's form freedom. Typically limited to the optimisation of flat laminates (e.g. [48, 49, 50]), with a few examples of cylindrical shells (e.g. [49, 51, 52]) and sizing optimisations of girders (e.g. [53, 54]), the recurring objectives are to

- minimise the mass or material;
- minimise the cost (applicable for hybrid laminates);
- maximise the stiffness (equivalent to minimising the deflection); or
- maximise the buckling resistance or natural frequency.

Among the approaches to reach these goals, the recurring optimisation variables are

- the number of layers;
- the orientation of these;
- the thickness of these; and
- their stacking sequence within the laminates.

4.3.1. Brief historical overview

One of the earliest examples of structural optimisation in FRP traces its roots back to 1973, when Schmit and Farshi conducted a weight minimisation of a 4-layered laminate with predefined orientations, varying the layer thicknesses [55]. In what followed, optimisations were conducted considering both ply angles and layer thicknesses as continuous variables [53, 54, 56], arguably due to the then available algorithms limiting the implementation of discrete variables. Nevertheless, both [56] and [50] used continuous variables for the ply angles with genetic algorithms, though [50] designated ranges referring to specific orientations (e.g. $-90 \leq \alpha < 30$ represents $\theta = 0°$). Continued research into different algorithms (solvers) and their suitability for FRP-related problems, along with a matured confidence in the understanding and programming of FRP, have further increased the complexity of the problems. In [57], the authors investigate two cases: concurrent weight and deflection optimisation; and weight and cost optimisation of laminates using genetic algorithms, finite element analyses, and discrete ply orientations.

Lamination parameters (LPs)

Although the currently available algorithms solve these complex problems relatively fast, the large number of (discrete) variables require numerous function evaluations, resulting in time-consuming processes when incorporating finite element (FE) analyses. Therefore, lamination parameters (LPs) are used to create mathematical programming procedures which can be solved with gradient-based algorithms.

Tsai and Pagano's introduction of LPs [58] enable expressing symmetrical and balanced laminates and their stiffness matrix through four continuous LPs ($\xi_1^A, \xi_2^A, \xi_1^D, \xi_2^D$) and one laminate thickness (see Appendix B). With this concept, Fukunaga and Vanderplaats (1991) could perform a sequential design approach to (1) optimise the buckling resistance of cylindrical shells using only four variables, then (2) obtain these LPs using continuous orientations and ply thicknesses as variables [59]. Similar sequential design approaches using LPs remain popular, as the sandwich panel optimisation (2020) in [60] and the concurrent topology and stacking sequence optimisation (2021) in [61].

Paramount to the proper sequential procedure is an initial definition of the LPs based on the intended ply orientations of the laminates, which defines the feasible range (i.e. the constraints) of the LPs. An illustration of the feasible region for the in-plane lamination parameters are shown in Fig. 4.9(left). As elaborated on in Appendix B, the feasible region of the out-plane LPs depend on the current value of the point $P(\xi_1^A, \xi_2^A)$, resulting in the regions $I - IV$ (Fig. 4.9(right)).

Although these lamination parameters bypass discrete variables and provide a convex design space, the sequential design approaches lead to suboptimal solutions. One reason for this suboptimality

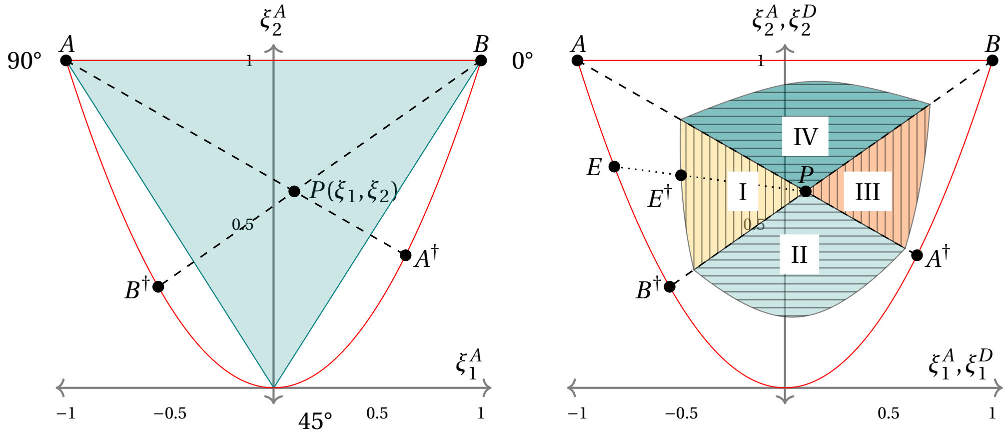

Figure 4.9: The relation between the in- and out-of-plane LPs for a laminate composed of 0°, 90° and ±45°. (**left**) The feasible region for the in-plane lamination parameters; and (**right**) the feasible region for the out-of-plane LPs for a specific point $P(\xi_1^A, \xi_2^A)$.

may be an inadequate definition of the feasible region of the LPs, seeing that the feasible region (i.e. the constraints one must adopt) should coincide with available layer orientations. Because of this, the minimisation of the discrepancy between the optimal LPs and those one seeks to obtain in the second step will leave significant errors. Moreover, practical laminate designs imply discrete parameters, meaning that a stacking sequence that exactly matches the optimal parameters sought does not always exist [41].

The presented literature reveals that there have been very few attempts to concurrently optimise the material architecture and the shape of FRP structures, meaning that the free-form advantages remain quite untouched in the world of numerical optimisation. Notably, some examples of concurrent sizing and stacking order optimisation exist [53, 54], focused on standard linear shapes with limited optimisation of thickness and/or ply orientations. Most examples in the literature adopt extremely small ply angles (1°, 2° etc.), seeking to obtain the most optimal solution from a theoretical point of view. This disregards practical manufacturing considerations and hand-layup, where even 30° angles are suggested against (FibreCore Europe, personal communication).

Optimisation through computer-aided design
In their thesis, Andersson and Good create their own finite element method (FEM) package for interaction with Rhino and Grasshopper to optimise the sandwich panels in a structure [62]. They find the panels for which the 0° GFRP layers are substituted by CFRP. This approach is not a shape optimisation procedure, as the initial geometry remains unchanged. However, it highlights the opportunities for higher-level sizing optimisation using computer-aided geometric design (CAGD).

The procedure involves evaluating the principal stresses of the elements, then those elements in which the axial stresses exceed a certain limit, CFRP is applied, see Fig. 4.10. Without changing the total amount of CFRP, but optimising its position and orientation, they efficiently reduce the deflection by 49 mm (-46%) and increase the fundamental frequency by 0.43 Hz (+18%).

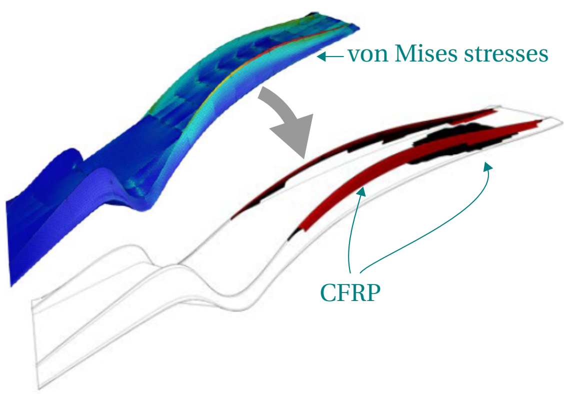

Figure 4.10: From von Mises stresses to carbon fibre placement. Adapted from [62]

4.3.2. Form-finding in FRP

As mentioned, the general literature does not incorporate form-finding in optimisation. However, the work of two authors stands out, in addition to some theses, which will be discussed in the following.

Two-level shape and laminate stacking sequence approach - Burgueño & Wu

Inspired by the approach of Fukunaga and Vanderplaats [59], Burgueño and Wu proposed a two-level approach for the sequential optimisation of FRP structures adopting FE analyses [8, 41]. As illustrated in Fig. 4.11, their approach entails:

Level-1 – Shape and lamination parameters optimisation, minimising the strain energy.
Level-2 – Stacking sequence optimisation: obtain the stacking sequence and ply orientations having the same stiffness properties as those in Level-1.

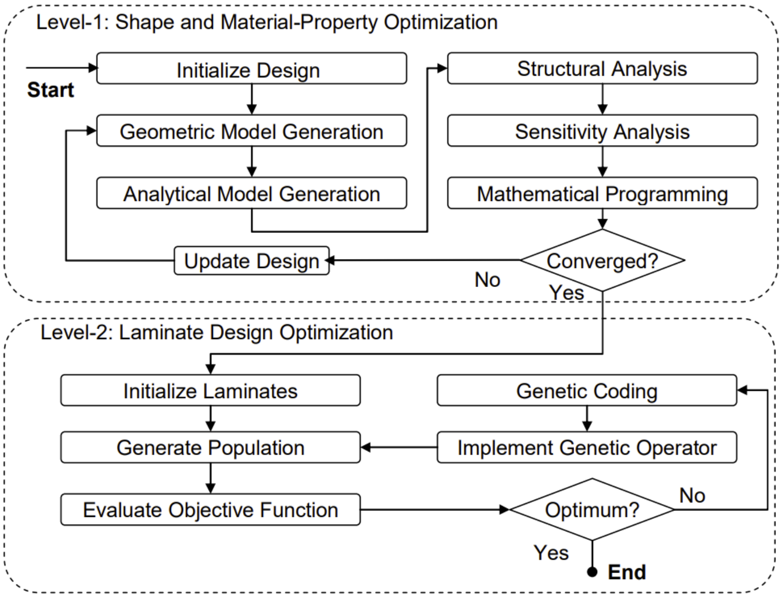

Figure 4.11: Burgueño and Wu's two-level approach to shape and laminate stacking sequence [63].

Their approach entails describing the geometry through a set of key geometrical points, plus four lamination parameters, which amounts to the total number of variables for the Level-1 optimisation. Verifying their approach, they analysed different bridge structure concepts, such as the composite membrane beam (CMB) bridge system in Fig. 4.12. For the Level-2 optimisation, a single laminate configuration is assumed for the entire structure. Then, the discrepancy between the optimal LPs ($\overline{V}_i$) and the LPs evaluated by the design variables of fibre orientations (V_i) is minimised:

$$\Delta = \sqrt{\sum_i \left(V_i - \overline{V}_i\right)^2} \qquad \text{for} \quad i = \{1, \dots, 4\} \tag{4.8}$$

constrained to deflection criteria and exposure factors relating to the maximum stress criterion. The Level-2 optimisation assumes a singular laminate configuration for the entire structure, with a predefined number of layers. As shown in Fig. 4.13, both 8-layered and 48-layered laminates fail to return an error of 0%.

Although the approach of Burgueño and Wu offers a structurally sound and effective approach to the shape and laminate design of FRP structures, it suffers from the concerns raised on the use of lamination parameters (Chapter 4.3.1). Secondly, minimising the strain energy will always make the thickness take on the maximum allowable, which is in conflict with their goal of reducing material use. Third, the Level-2 optimisation is carried out with a predefined number of layers (8 and 48), without mention of the layer thickness. Thus, it is reasonable to believe that different laminate thicknesses are obtained for the two levels. Fourth, the design could be further improved by further division of the geometry, i.e. different laminates in different sections. Finally, the ply angles are small. But, as these are modelled as $\pm\theta°$ stacks, it is a slight improvement from other approaches in terms of manufacturing.

Two-level shape and laminate stacking sequence approach - Tuffaha

Similar to Burgueño and Wu's approach [8], Tuffaha suggested a multi-level framework comprising two levels in his thesis:

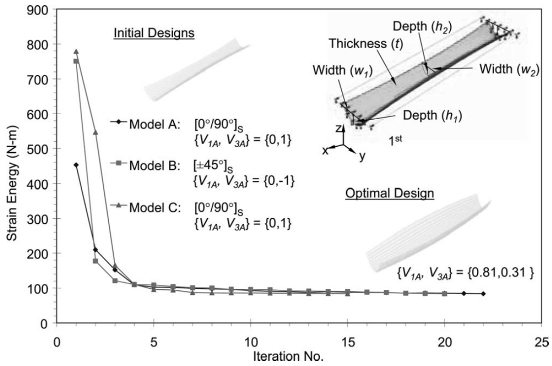

Figure 4.12: Level-1 optimisation for CMB bridges [8].

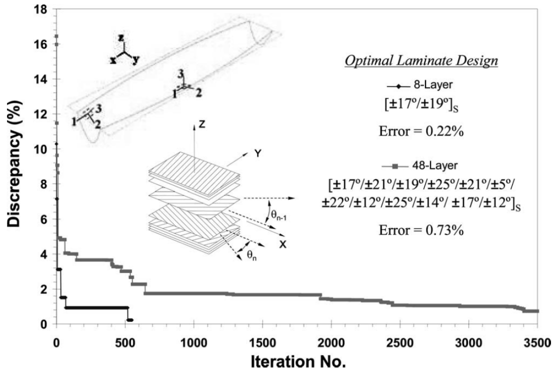

Figure 4.13: Level-2 optimisation of CMB bridges [8].

Level-1 – Stiffness maximisation (strain energy minimisation): find the optimal laminate configuration for a specific geometry.
Level-2 – Weight minimisation: find the optimal shape with regards to the weight of the structure.

In the Level-1 optimisation, the geometry is divided into n sub-spans, each of which can have one out k predefined layups, see Fig. 4.14. Then a brute-force algorithm iterates through the n^k possible combinations. In the Level-2 optimisation, the layups found from the first step are assigned before the mass is minimised, altering the structure's geometry using a genetic algorithm. In addition to key geometric points to alter the geometry, a uniform thickness is used, meaning that all the laminates have the same thickness.

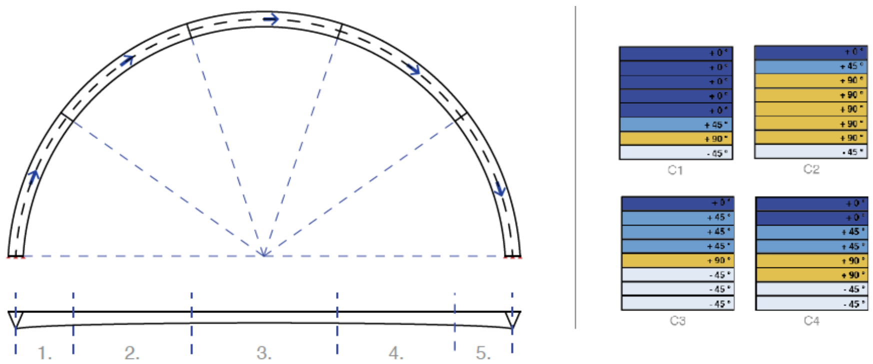

Figure 4.14: Example of the span division and laminate configurations adopted in Tuffaha's Level-1 optimisation [64].

Tuffaha's approach offers a reasonable solution to the shape and lamination stacking optimisation of FRP shell-like structures. However (as he mentions), a possible improvement on the approach includes having different thicknesses for the respective sub-spans and defining different layups for the flat and vertical (or angled) panels. The reasoning for not doing so is based on the added time this would introduce.

Beyond the concerns raised by the author
The geometrical parameters are taken in increments of the first decimal place (i.e. $0.1, 0.2, \ldots, 8.0$) in the Level-2 optimisation. Hence, despite overcoming the inherent difficulty of optimising FRP structures in the first level, the problem remains discrete. Even though this reduces the solution space, using continuous variables (and a gradient-based solver) would likely be beneficial to the computational efficiency of the approach while exploring a greater solution space. Secondly, the thicknesses (in 1 mm increments) of the laminates do not necessarily match the thickness resulting from a laminate configuration. This discrepancy is, however, negligible with regard to the structural response. Third, the permissible thicknesses (lower and upper bounds) are confined between 50 mm and 100 mm, greatly exceeding the recommended maximum laminate thickness of 20 mm.

Though this thesis is not a continuation of the works of Tuffaha, his works are among the inspirations used in the formulation of this report.

Bridging the gap

Although few, there have been made promising contributions to the shape and laminate stacking sequence optimisation of FRP structures. However, improvements can be made to the definition of the panels. For instance, a more dynamical laminate definition can be introduced, similar to the definition in [49]. With this approach, the panels can be configured as hybrid, and the definition of the layers includes the possibility of non-existent plies, ultimately changing the number of layers and the laminate thickness – which in most approaches remains constant. This modelling approach is further discussed in Chapters 5 and 6. Additionally, with the a priori articulation in Chapter 4.2.3, several objectives can be evaluated in a single step. With this, it is possible to capitalise even further on the sustainable benefits of FRP, providing a solution to the challenge engineers are up against: meeting the UN's carbon neutrality goals.

Chapter 4.4. Navigating through the fitness landscape

The fitness landscape of optimisation problems – the solution space obtained for all the possible combinations of the design variables, including the confinements set by the constraints – quickly becomes highly complex, beyond a configuration one can imagine. In fact, if the problem extends beyond two design variables, it is no longer possible to visualise the fitness landscape for all the perturbations of the variables. Figure 4.15 illustrates this discussion. The fitness landscape is obtained for a two-dimensional problem by extruding the point (x_1, x_2) normal to its plane, proportional to the obtained fitness value. Certain functions result in numerous local optima, i.e. peaks and valleys, where the solver can get trapped. Furthermore, narrow peaks are hard to detect due to the sudden change in fitness value. The exploration of these fitness landscapes comprising numerous neighbouring local optima attracts optimisation algorithms like genetic algorithms.

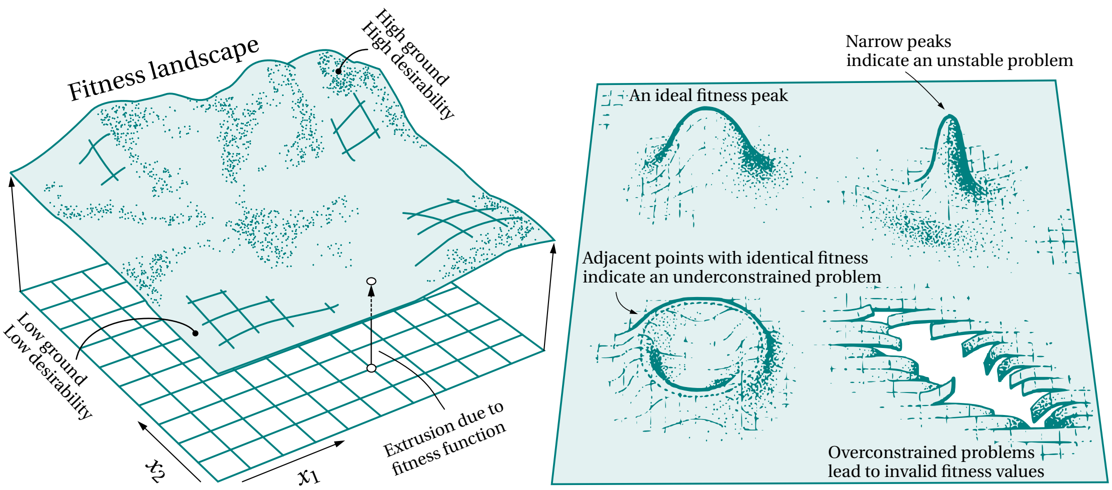

Figure 4.15: Fitness landscapes: (**left**) the relation between a two-dimensional problem and its three-dimensional fitness landscape and (**right**) common fitness landscape topologies. Adapted from [65].

4.4.1. Choosing a solver

The highly non-linear and discrete problems pertaining to the optimisation of FRP rule out the commonly adopted gradient-based solvers. Furthermore, the vast fitness landscapes mean that brute force approaches are inadmissible. It should be noted that the combination of stacking order configurations and geometric variables means that it is unlikely to have a unique global optimum; rather, there will be several global optima. Thus, a proper tool must be selected that explores a large portion of the solution space and, hopefully, can detect these optima.

As Sörensen points out, researchers' "fetish for novelty" has inspired numerous algorithms, which can be seen as a continuous reinvention of the wheel rather than a step forward in the metaheuristic literature [66]. These heuristic approaches are often based on an analogy of some evolutionary processes, such as the *harmony search* (based on the principle of jazz musicians playing together), the *cuckoo search* (inspired by cuckoos laying their eggs in other birds' nests) or the *intelligent water drops* algorithm (inspired by the flow of water to the sea), all with their own set of vocabulary to the describe what essentially are the same concepts. Consequently, the toolbox is becoming increasingly larger, making selecting an adequate tool a problem itself. Nevertheless, without going too much into the details, the following solvers have proved efficient in overcoming the hurdles set forth by the design of composite laminates :

- Simulated Annealing (SA) [48]
- Genetic Algorithm (GA) [67, 68, 69]
- Ant Colony Optimisation (ACO) [70]
- Particle swarm optimisation algorithm [71]
- Artificial Bee Colony (ABC) [72]

Though each of these algorithms presents their favourable qualities, there is generally no single best solver to tackle global optimisation problems. For instance, a delicate property of simulated annealing is that it finds the global optima provided a long enough run-time [45]. Regardless, the algorithms tend to perform well for specific applications. In the topic of FRP, simulated annealing and genetic algorithms are deemed the best performing [71]. Albeit an investigation into the use of different algorithms could benefit the computational efficiency and obtained solution of the proposed framework, the choice of the solver is decided based on availability and simplicity of implementation.

4.4.2. Plug-ins

The framework proposed in this thesis assumes the use of the visual programming language Grasshopper, which runs in the Rhinoceros 3D CAGD application to facilitate the formal exploration of FRP structures. As such, without writing plug-ins for this purpose, the tool is limited to plug-ins natively available in Grasshopper or those available from *food4Rhino* [73]. Table 4.1 compares some of the available plug-ins employing the genetic algorithm, summarising their desirable – and not so desirable – implications.

Table 4.1: The pros and cons of available GA solvers in Grasshopper.

<table>
<tr><th>Plug-in</th><th>Features</th><th>Implications</th></tr>
<tr><td rowspan="2">Galapagos
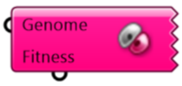</td><td rowspan="2">Single-objective optimisation: genetic algorithm (GA) + Simulated Annealing (SA)</td><td>Advantages:
– Simple, user-friendly interface
– Easy to add variables</td></tr>
<tr><td>Drawbacks:
– Additional steps required to post-process and visualise the solution
– Solution is lost when closing UI</td></tr>
<tr><td rowspan="2">Octopus [74]
</td><td rowspan="2">Multi-objective optimisation: SPEA-2 + HypE</td><td>Advantages:
– Simple, user-friendly interface
– Has input and output plugs allowing for a streamlined workflow</td></tr>
<tr><td>Drawbacks:
– Extensive post-processing required to evaluate solutions at the Pareto front</td></tr>
<tr><td rowspan="2">Wallacei [75]
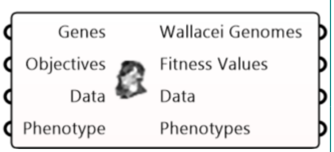</td><td rowspan="2">Multi-objective optimisation: NSGA-2 (non-dominated sorting GA)</td><td>Advantages:
– Easy to connect variables and objectives
– Good means to visualise the solution
– Has input and output plugs allowing for a streamlined workflow</td></tr>
<tr><td>Drawbacks:
– Extensive post-processing required to evaluate solutions at the Pareto front</td></tr>
<tr><td colspan="3">UI = User Interface.</td></tr>
</table>

Though both the Octopus and Wallacei plug-ins offer analysis tools far superior to Galapagos, Galapagos is adopted in this study. Albeit the framework is used to assess a multi-objective problem, a weighted sum approach (Eq. (4.5)) combined with an a priori articulation on the preferences essentially results in a single-objective problem. For the size of the problem, the multi-objective solvers would require a much greater number of function evaluations (due to evaluating different weights of the objectives) accumulating in an undesirable run-time. Furthermore, extensive post-processing would be required to evaluate and weigh the objectives against each other – though it provides better insight. In order to best benefit from the Galapagos plug-in, it is imperative to understand the genetic algorithm and its foundations, as discussed in the following.

4.4.3. Genetic algorithm (GA)

Similar to other heuristic algorithms, genetic algorithms (GAs) are biologically-inspired stochastic solvers based on Darwin's 'survival of the fittest' principle. Presented by Holland in 1975 [76], it mimics the evolutionary processes of a population from one generation to another, facilitated through a set of genetic operators.

As illustrated in Fig. 4.16, the basic genetic algorithm begins by creating a random initial population, in which each candidate solution is called an individual, creature or phenotype. Each individual consists of a chromosome or gene pool representing a design point, containing values for all the design variables of the problem. After evaluating each individual's fitness, a certain portion of the candidates is selected as *parents*, typically selecting the best-performing individuals. Additionally, some of the candidates with lower fitness are chosen as *elite* automatically passed on to the next generation. Children are produced by making random changes to a single parent – *mutation* – or by combining the genes from two parents – *crossover*. The current population is then replaced with the children to form the next generation; thus, the successive populations are called the generations. Then, the algorithm terminates when one or more criteria are met, commonly when:

- the improvement in fitness is less than a given threshold for a consecutive number of generations;
- the number of generations exceeds a specified value; or
- the algorithm exceeds a specific run-time.

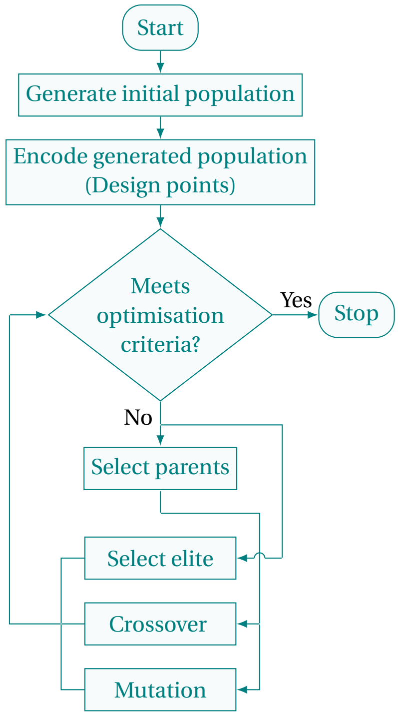

Figure 4.16: The solution process of a typical genetic algorithm. Adapted from [45].

It follows that the quality of the solution and the algorithm's efficiency depends on proper tuning of its operators. A larger population size explores a greater extent of the landscape for each generation; however, the number of iterations grows accordingly. A high proportion of elite children means less variation in the population from generation to generation, making the search less effective. The proportion of children created through crossover aims to retrieve the best qualities of each parent, potentially creating superior children. The remainder of the population is mutated, adding diversity to the population.

The concept on which GAs is based renders them easily understandable and conceptually simple with a wide variety of applications, such as robot trajectory planning, breast cancer detection, and network design [77]. As with any tool, GAs are not perfect, illustrated through an account of their advantages and limitations (Table 4.2):

Table 4.2: Advantages and limitations of GA [47, 71, 77, 78].

Advantages of GA	Limitations of GA
– Able to solve discontinuous, nondifferentiable, stochastic or highly non-linear problems.	– Significant effort might be required in tuning the optimisation options to even find a feasible solution.
– Evaluates multiple possible solutions in a single iteration (generation).	– Relatively slow, especially for simple problems where conventional methods can be applied.
– Can solve single- and multi-objective problems.	– No guarantee of finding the exact global optima.

Chapter 4.5. Sensitivity analysis

An integral part of optimisation problems concerns the determination of the most influential variables, i.e. those having the most significant impact on the objective and constraint functions. To this end, a sensitivity analysis (SA) can be employed to quantify the model's parameters' influence on the system's behaviour. These sensitivity methods can be broadly classified as local and global methods. In short, the former provides a means to understand the direct relationship between an input factor and the model response at a point (or points) in the input parameter space. In the global method, all factors are perturbed at a time, providing a global relationship between factor and model response over the domain of the variables [45, 79]. As global sensitivity analyses are more computationally costly (time-consuming), this thesis's sensitivity analyses are limited to local methods due to time constraints.

A mechanically motivated problem can illustrate the local method considering the bending stress in a cantilevered beam with a rectangular cross-section. The sensitivity of such a problem refers to the amount of change to the system's response when a small change is introduced in an input factor. The bending stress is formulated as

$$\sigma(b,h) = \frac{6Pl}{bh^2} \tag{4.9}$$

where, referring to Fig. 4.17, P is a point load, l is the length; and b and h are the width and height, respectively. The gradient of the bending stress with respect to the width and the height of the cross-section, respectively, are

$$\frac{\partial\sigma}{\partial b} = -\frac{6Pl}{b^2h^2} \tag{4.9a}$$

$$\frac{\partial\sigma}{\partial h} = -\frac{12Pl}{bh^3} \tag{4.9b}$$

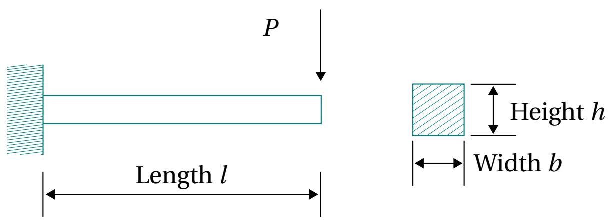

Figure 4.17: Cantilever beam with a square cross-section.

From Eqs. (4.9a) and (4.9b), it is clear that an increase of either the height or the width will amount to reduced stresses. As the cross-section is square ($b = h$), it is two times more effective to increase the height h than the width b to reduce the bending stresses. As the example illustrates, the sensitivity can be easily defined for small dimensions and if the solution space is continuous, allowing the use of gradients, i.e. $\frac{\partial f}{\partial X_i}$. In the case of discrete variables, finite differences should be used, that is, $\frac{\Delta f(\mathbf{x})}{\Delta x_i}$. However, these performance measures can rarely be explicitly expressed in design variables. The function evaluations are carried out numerically through finite element analysis (FEA), meaning that there is no equation to take derivatives of. This concept of local sensitivity analysis will be reiterated in Chapter 7.2; however, the costs and the global warming potential (GWP) related to the constituents will be varied instead – in favour of the design variables.

Chapter 4.6. Conclusion

This chapter answers the following objectives:

O 4.1 What form-finding methods are available that are beneficial to FRP design, and what are their limitations?
O 4.2 What is structural optimisation, and how can it be used to solve the aforementioned limitations?
O 4.3 What specific challenges and potential solutions pertain to the numerical optimisation of FRP structures?

The general form-finding approaches are limited to isotropic materials, introducing the need for a modified approach when aiming to benefit from the tailorable material properties of FRP. Shells of FRP are in favour of a membrane stress state limiting the bending stresses, meaning that the physical principles of Otto and Frei present analogies on which the numerical optimisation procedure could be based.

Although the approach of minimising the strain energy while restricting the mass offers an appreciatable methodology (modified to a sequential procedure by Burgueño and Wu), numerical approaches integrating CAGD and FEM through parametric models can be formulated differently. As will be explained in greater depth in Chapters 5–7, a parametric model simultaneously playing with the geometry and the stacking order can – with the appropriate formulation and implementation of the problem – be used to arrive at economic, sustainable and shape-resistant structures of FRP. Instead of obtaining a stiff structure by minimising the strain energy, limiting the structural response to the appropriate design requirements (e.g. max deflection) will result in a structure that adequately fulfils its purpose. Furthermore, the potential stability problems pertaining to the presented physical and numerical approaches are mitigated by imposing minimal requirements on the buckling behaviour.

While the discrete thicknesses and orientations of FRP laminates and their layers provide potentially beneficial properties, it severely complicates the general form-finding approaches pertaining to isotropic materials. The approach must concurrently consider the geometry and laminate stacking, introducing highly non-linear, discontinuous and discrete optimisation problems, having to be solved by heuristic algorithms such as the genetic algorithm (GA). A parametric definition of the geometry and the stacking order(s) combined with FE analyses offer an integrated approach to explore and optimise complex structures within an easily adjustable and lucid user interface.

5

FRAMEWORK

Chapter 5 introduces the thesis' proposed framework, providing the grounds for the optimisation of a real case bridge in Chapter 6. A method for the concurrent shape and material architecture of structures comprising sandwich panels is presented to optimise this structure. Some key points from the development of the tool are highlighted. Afterwards, the drawbacks of the framework are discussed.

The chapter aims to answer the following:

O 5.1 What optimisation objectives can be efficiently adopted to reach an optimised design?
O 5.2 What are the necessary prerequisites for the optimisation of a structure?
O 5.3 What are the limitations and drawbacks of the framework

Chapter 5.1. Introduction

Chapter objectives

O 5.1 What optimisation objectives can be efficiently adopted to reach an optimised design?

For laminates comprising a singular fibre type, e.g. GFRP, minimising the thickness, mass or volume would be analogous to minimising the cost, as these are virtually linearly proportional relationships. However, for hybrid laminates, a preference for one material over the other must be expressed – for instance, through their cost. Since the costs are defined based on the masses of the constituents and the total composite mass, calculating the environmental impact is straightforward. This practicality led to the introduction of the second objective of this thesis – to minimise the environmental burden. With this, the environmental benefits of employing FRP as a structural material are further increased. At the same time, the costs are reduced, illustrating an effort to increase the popularity of FRP in the civil engineering industry. After all, much of the scepticism towards FRP relates to its relatively high costs.

In hand with the current trends in the building sector and the UN's goal of reaching carbon neutrality by 2050 [80], designers must make fit solutions that comply with the (structural) requirements yet have the best possible impact on the environment. By employing a simplified life cycle assessment (LCA) of the design, one can indicate the environmental burden the product has on the environment. The framework adopts a quantification analogous to a cradle-to-gate approach, covering the raw material extraction and manufacture to the factory exit gate [81]. The assessment is based purely on the climate change impact category, for which the characterisation factor is global warming potential (GWP). The outcome of this category gives the carbon footprint, expressed in terms of CO_2-equivalents ($kgCO_2e$) [82].

Notwithstanding the poor understanding of cost prediction in composites [13], the obvious approach from a design perspective is to minimise the material consumption while aiming to reduce the complexity of the geometry. The recurring costs (for hand layup, Fig. 5.1) are mostly related to locating the plies into the mould (42 %) and assembling to the adjacent structure (29%) [13]. The non-recurring costs are related to design, analysis, tooling, testing, certification and moulding. With an approach aiming to reduce the workload allocated to the design and analysis, the framework proposed herein aspires to reduce the costs related to several aspects of composite structures.

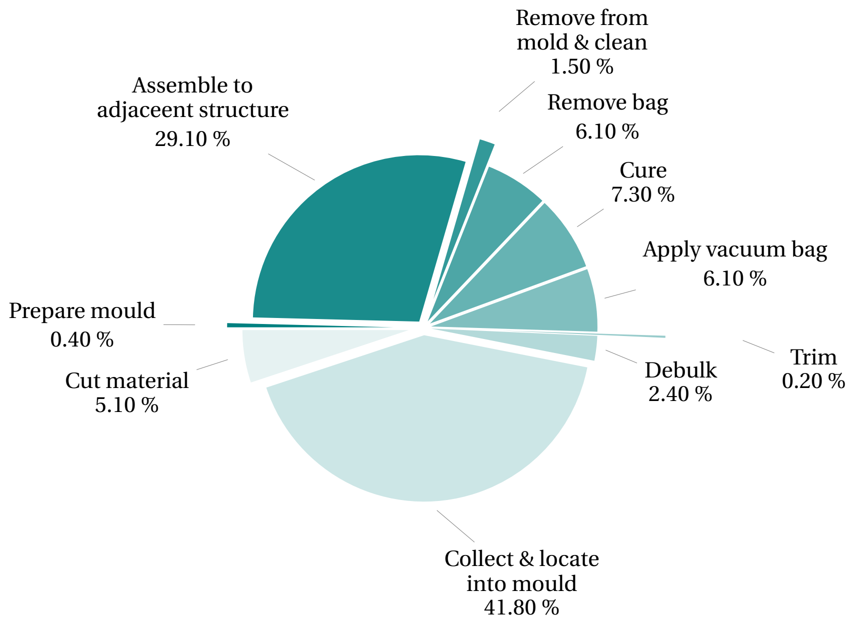

Figure 5.1: Typical processing steps for hand layup and their cost as fractions of total recurring costs. Adapted from [13].

This optimisation model concerns the type of fibre, resin and foam core used to compose the sandwich laminates, meaning that, e.g. additives, fillers and surface treatments are disregarded. Based on these constituents' amounts and the resulting composite mass, one can estimate the allocated cost and carbon footprint by incorporating the appropriate production processes.

The compromise between cost and stiffness introduces a delicate trade-off between the two. A thin laminate typically requires costly CFRP, whereas a thicker laminate of GFRP requires more layers, more resin and a more labour-intensive assembly. A similar relation holds for the stiffness and the carbon footprint. Finding the best configuration is a task fit for the genetic algorithm (GA). Since carbon fibres have higher costs and GWP than glass fibres, the optimal designs concerning both objectives (cost and carbon footprint) will be similar. However, the optimal design concerning costs is not necessarily the optimal design concerning the carbon footprint and vice versa. This intricacy is illustrated in Fig. 7.3. The instability concerns the physical form-finding methods are overcome by introducing stability constraints in the form of a minimum buckling load factor. The use of sandwich panels further improves the local stability, discussed in Chapter 2.3, without compromising the light weight. In short, the proposed framework helps the designer in arriving at a preliminary design which:

- overcomes the stability concerns pertaining to FRP;
- is shape-resistant; and
- is economically and sustainably attractive.

The remainder of this chapter elaborates on the formulation of the intended framework, alongside key points regarding its development and drawbacks.

Chapter 5.2. The proposed framework

Chapter objectives

O 5.2 What are the necessary prerequisites for the optimisation of a structure?

The proposed framework relies on a parametrised geometrical composite model and its panel configurations in the visual programming language Grasshopper running in the Rhinoceros 3D [83] computer-aided design (CAD) application. As illustrated in Fig. 5.3, the optimisation procedure is organised in the following steps:

1. Define a parametric model in Grasshopper and Rhino.
2. Define the in-plane (homogenised) mechanical properties of the panels.
3. Formulate the problem mathematically, defining the design variables and their range, the constraints and the objective function(s).
4. Initialise a genetic algorithm (Galapagos) within Grasshopper and Rhino 3D.
   For each chromosome, until a stopping criterion is met;
   i generate a FE model by computer-aided geometric design; and
   ii evaluate structural responses and the corresponding fitness.
5. Perform a local optimisation in the vicinity of the (near) optimal point found in step 3.
   For each iteration, until a stopping criterion is met;
   i generate a FE model by computer-aided geometric design; and
   ii evaluate structural responses and the corresponding fitness.

The framework assumes two objectives. Nothing prevents adding, removing or changing these – should that be in the designer's interest – as such alterations mainly affect the mathematical formulation. However, one of the objectives should remain, as both articulate a preference between the constituents. The proposed framework is contextualised with a case study on the Klosterøy bridge, where the sections beyond the introduction are organised according to steps the user should follow (see Fig. 5.2).

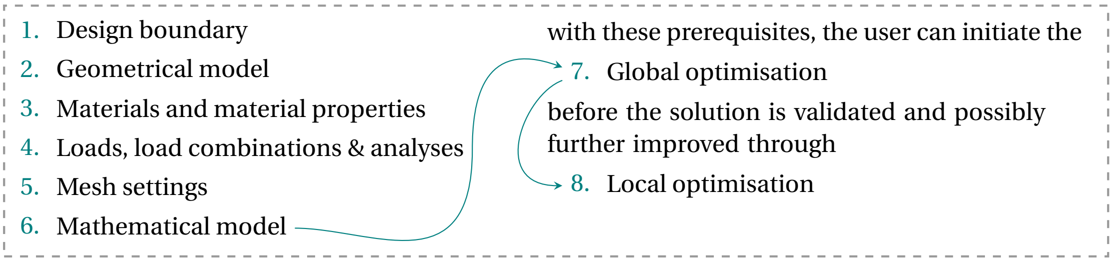

Figure 5.2: The intended steps

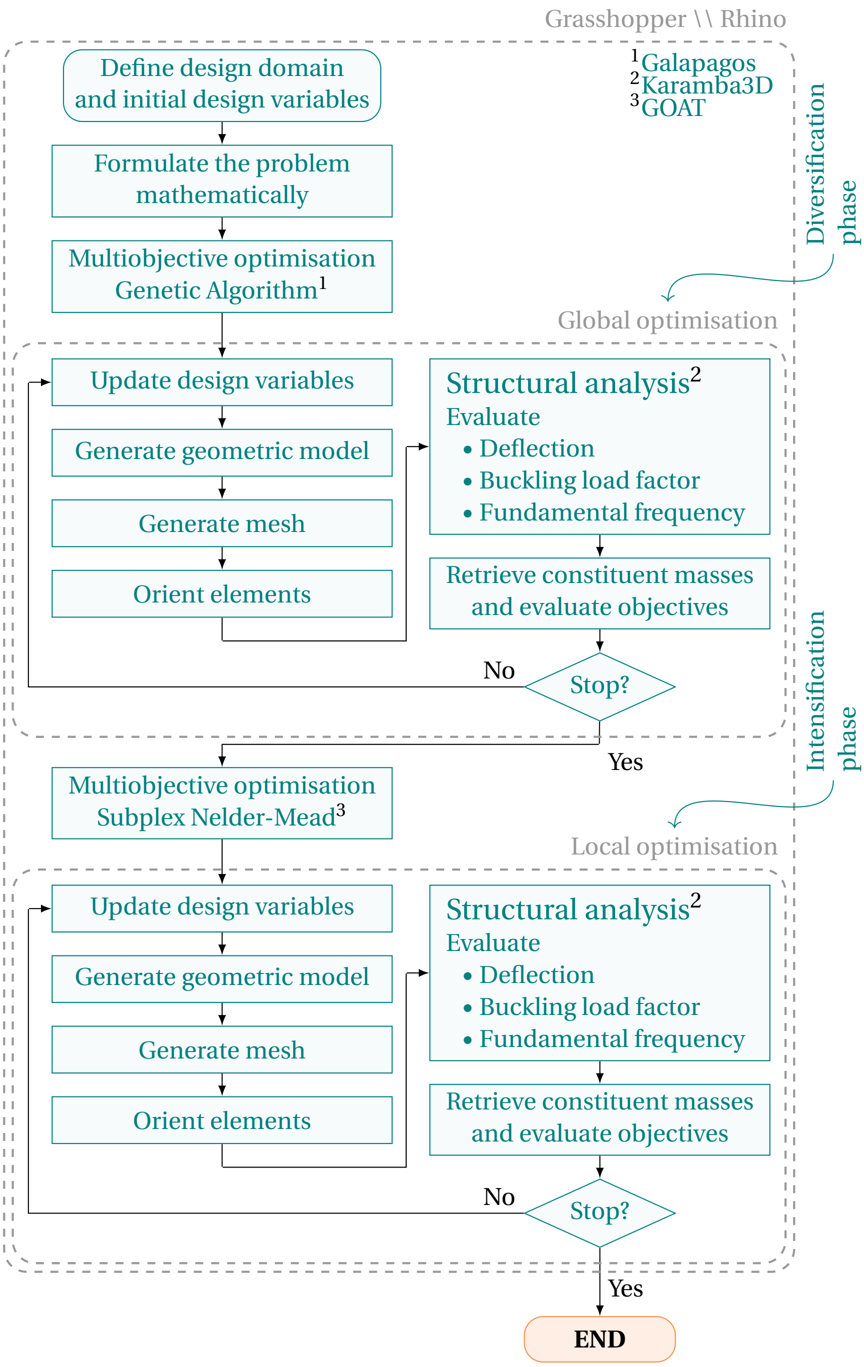

Figure 5.3: The framework procedure. Adapted from Fig. 4.11 [63].

Chapter 5.3. Development of the tool

The development of the tool has been a process of trial and error, requiring several steps of fine-tuning. Before dealing with the sandwich panel configurations that ultimately are the goal of this thesis, more straightforward configurations were investigated – both geometry- and material-wise. Because sandwich panels are monolithic laminates rigidly offset from each other, it is instrumental in defining an approach for designing these face sheets. Then, through minor adjustments to the formulation, a procedure for optimising sandwich panels can be determined.

Appendix C presents the optimisation of a composite girder comprising hybrid laminates, where the possible adoption of five webs mimics the longitudinal stiffeners usually present in semi-monocoque structures. Apart from verifying that the intended approach performs as intended, this investigation led to crucial alterations to the formulation of the problem. Essentially, it was found that stricter constraints have to be introduced on the material side of the problem. Additionally, plies are grouped in pairs, i.e. $0°_2$, $90°_2$ and $\pm 45°$. These alterations ultimately reduce the solution space significantly, enabling a framework including foam cores to overcome the shortcomings of FRP, such as susceptibility to stiffness- and stability issues. Figure 5.4 below summarises the girder optimisation, where a tall and slender cross-section with two webs is obtained in favour of an I-beam with relatively thick panels.

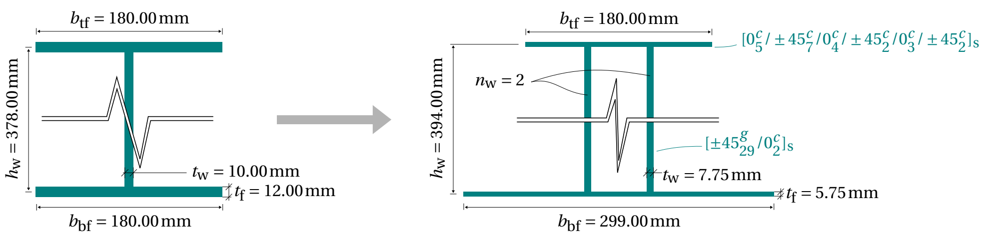

Figure 5.4: From (**left**) initial configuration to (**right**) optimised girder definition: Geometry and laminate specifications.

Chapter 5.4. Drawbacks & limitations

Chapter objectives

O 5.3 What are the limitations and drawbacks of the framework

5.4.1. Modelling limitations

The adoption of Grasshopper and the FE plug-in Karamba poses advantages and drawbacks. The former revolves around the simplicity of a parametric definition of the structure, which can be readily implemented in an optimisation procedure with a relatively fast generation of FE models and consecutive analyses.

The limitations, however, are decisive for the implemented analyses and constraints. It is crucial to remember that "all models are wrong, but some are useful" [84], especially when dealing with complex anisotropic materials. Notably, the various coupling effects discussed in Chapter 3.2.2 – such as extension-bending occurring in unsymmetrical panels – are not captured by the FE plug-in Karamba. Similarly, since stresses and strains in the layers through the thickness are not retrievable, it is not possible to evaluate the strength of the panels according to first ply failure theories (Chapter 3.3). Though such evaluations would be of great help in arriving at optimal designs, appropriate strength must be achieved by adopting appropriate design constraints. To increase the confidence in the structural response affiliated with the obtained solution, the strength of the panels in the (near) optimal design should be verified with software allowing the use of layered properties and appropriate failure theories.

When dealing with panels of considerable thickness, the assumption of plane stress can become erroneous. For thin laminates, the assumption of a linear strain distribution and a plane section usually holds. However, the through-thickness behaviour can significantly change when dealing with sandwich panels. Particularly, the transverse shear deformation may lead to increased deformations and strains which are not captured through regular shell elements. Consequently, the plane does not necessarily remain perpendicular to the middle surface – as assumed with CLT.

The through-thickness shear deformation is analysed for I-beams with flanges having the width $b_f = 100\,\mathrm{mm}$ and webs the height $h_w = 200\,\mathrm{mm}$, where each panel comprises a symmetric definition of `DBLT+PVC H80 20mm+DBLT`. See Appendix D for details on modelling. By doing so, the shear deformation of the core may be properly captured, while the influence of the stiffer face sheets is present. The thickness of 20 mm is based on the minimum core thickness in Chapter 6. From Fig. 5.5, a difference between the modelling approaches of 0.01 mm is found, i.e. a negligible relative difference of 0.07 %. With this in mind, it is concluded that the transverse shear deformation of the sandwich panels can be safely disregarded.

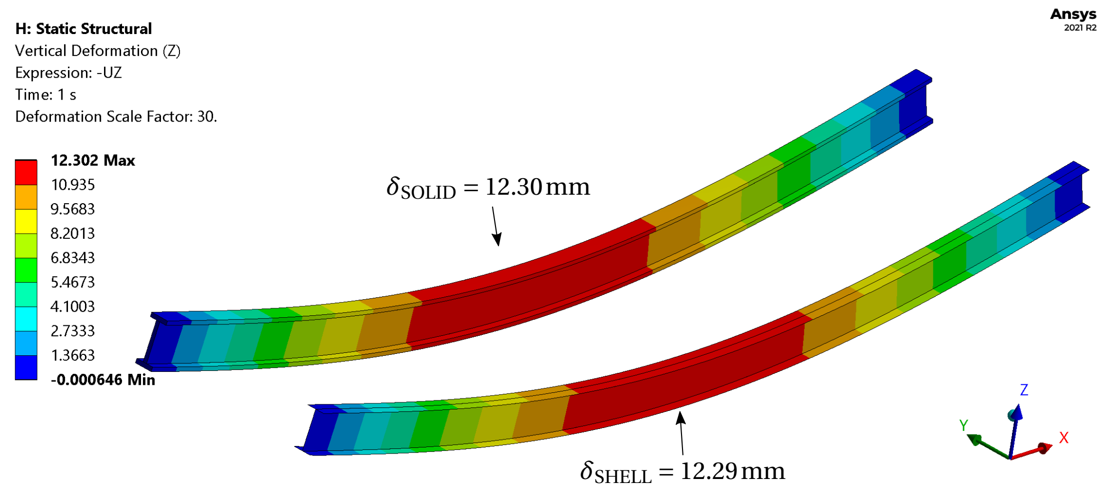

Figure 5.5: Vertical deflection of beams subjected to $q = 1\,\mathrm{kN/m^2}$, modelled with shell and solid elements. Deformation scale: 30.

5.4.2. Evolutionary algorithm limitations

The adoption of Grasshopper's Galapagos plug-in enables formulating optimisation problems with simplicity and visualisation far superior to other software, such as Matlab®. However, its relatively low solution speed is the inherent drawback of the genetic algorithm (GA). On the other, with vast solution spaces and lengthy function evaluations for each iteration (genome) owing to the FE models, it becomes increasingly important to limit the search effectively. As discussed in Chapter 4.4.3, this may result in the solver getting trapped in local optima, failing to reach the global optima. To this end, the optimisation should be initiated from different starting points to gain confidence in the solution and possibly obtain improved results. Further improvement or verification should be implemented through a local optimisation procedure, where the endpoint of the global optimisation procedure is used as the initial point.

Chapter 5.5. Conclusion

The chapter answers the following:

O 5.1 What optimisation objectives can be efficiently adopted to reach an optimised design?
O 5.2 What are the necessary prerequisites for the optimisation of a structure?
O 5.3 What are the limitations and drawbacks of the framework

As opposed to most structural optimisation problems concerning FRP, typically tasked with optimising (maximising) the stiffness, this framework adopts two objectives aiming to minimise both the cost and environmental impact of the structure. To this end, design constraints are introduced to ensure that the structural response meets the requirement and does not impede the safety of the users. Thus the goal is to obtain designs that come at a lower cost and carbon footprint than what common design would lead to.

To meet these objectives, certain prerequisites must be defined. As such, the designer is tasked with defining the scope and an end goal from which a parametric model can be defined. Notably, the design boundary must be defined, including the range of definitions of the variables, boundary conditions, material properties, and the analyses defining the use-case of the structure.

The anisotropic nature of FRP with varying directional properties through each layer suggests that the analyses should use layered orthotropic material properties. However, the adopted FE software is limited to homogenised orthotropic materials, which is deemed an acceptable limitation as the main point of interest is the global behaviour and stiffness of the structure – which again is a consequence of the analysis tool.

6

Validation with real case: Klosterbrua, Skien, Norway

Aiming to develop a framework for the structural form-finding and optimisation of FRP structures, this thesis adopts an approach to concurrently optimise structures' shape and material architecture. To best illustrate the intended procedure, the framework is validated with a real case: the yet-to-be-built Klosterøy bridge in Skien, Norway. This reference project exemplifies an innovative and efficient use-case with composites as the main load-carrying system. A proposed design of the bridge was carried out by the Norwegian engineering firm FiReCo, hereinafter referred to as the 'reference model'.

After introducing the reference project, Chapter 6 traces back to the steps of the optimisation framework. It defines the crucial aspects of the optimisation procedure in general: parameters, variables, geometry generation, mathematical formulation, finite element analysis and algorithms. Then, these concepts are elaborated on for the Klosterøy bridge in particular.

The chapter aims to answer the following:

1. How can a structure be defined to prepare for its optimisation?
2. What are the objectives and design constraints of the optimisation?

Chapter 6.1. Introduction

The Klosterøy bridge in Skien, Norway, is a yet-to-be-built multi-span bridge intended for pedestrian and cycle traffic with a movable composite flap, connecting Jernbanebrygga ("the railway dock") and Klosterøya ("the Monastery island"). The proposed design of the bridge was a collaborative effort between Johs Holt and FiReCo, where FiReCo was responsible for the FRP design. The client's wish to facilitate the passage of ships led to an electro-hydraulic operation system that positions the bridge at a 60° angle at its lifted position. As a novel project requiring a lightweight solution, the Klosterøy bridge, with its composite flap, presents an excellent use-case for composite materials. The bridge is visualised in Fig. 6.1.

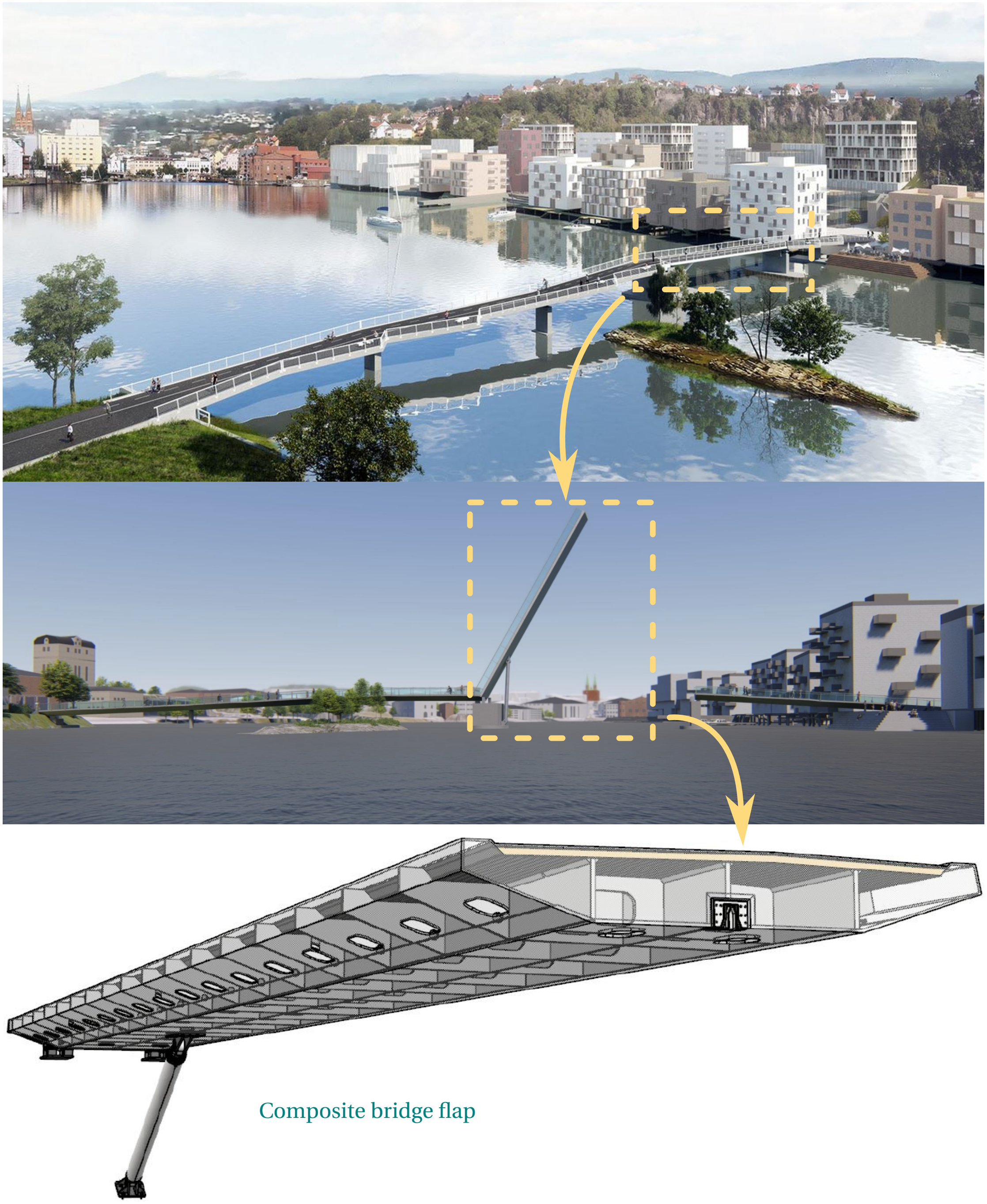

Figure 6.1: Renders of the Klosterøy bridge and its movable composite flap [85, 86, 87]

Chapter 6.2. Framework implementation

The intended steps for the implementation of the framework are reiterated below, to clarify the structure of this chapter. The steps (1) through (4) are covered in Chapters 6.2.2–6.2.5. Then, a section (Chapter 6.3) is dedicated to step (5) – the mathematical model, before the optimisation is initiated in Chapters 6.4.1 and 6.4.2.

1. Design boundary
2. Geometrical model
3. Materials and material properties
4. Loads, load combinations & analyses
5. Mesh settings
6. Mathematical model

with these prerequisites, the user can initiate the

7. Global optimisation

before the solution is validated and possibly further improved through

8. Local optimisation

The intended steps

6.2.1. Design boundary

The first step of the framework involves defining the geometry and its boundaries, designated as the design boundary [45]. The design boundary depends on the client's wishes and practical limitations, typically involving the structure's maximum and minimum spatial geometry; and definition of the support conditions.

Case study: Klosterøybrua

The composite flap considered herein presents one of the spans of the Klosterøy bridge, having to comply with the dimensions of the adjacent spans. The design boundary for the structure is represented through the fixed parameters illustrated in Fig. 6.2. Among the important parameters are its length and point of connection to the cylinder. The end is cut at a 10° angle, resulting in different side lengths of 35905 mm and 34877 mm. The deck width is 5100 mm, while the total width is 5831 mm. As section A-A illustrates, the deck's configuration and the parapets remain constant.

The geometry of the bridge is defined using a global coordinate system, where X, Y and Z refer to the length-direction, width and height, respectively. The supports indicated in Fig. 6.2 restrains against translation in X, Y and Z at the support brackets ($X = 0$) and the bottom of the cylinder. The centre is restrained from translation in Y-direction at its right end, while support plates restrain vertical translation.

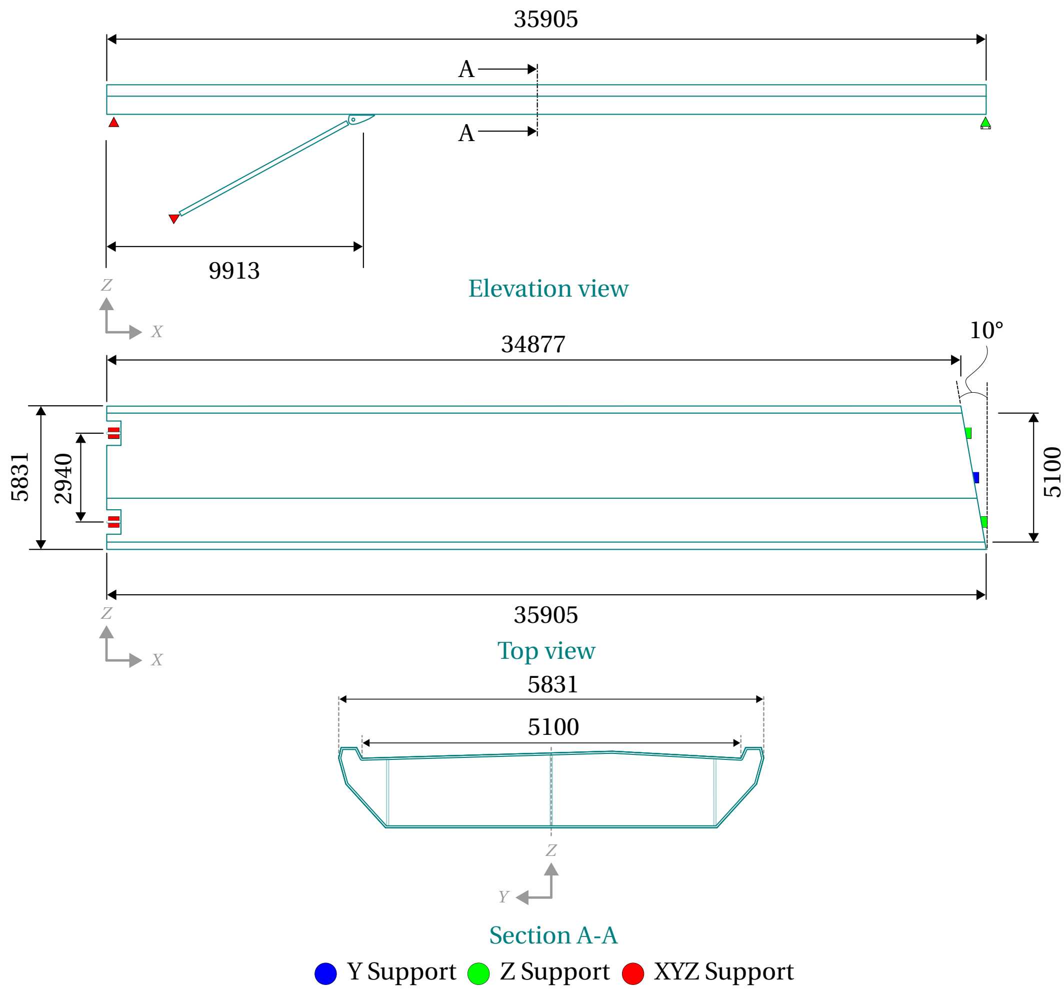

Figure 6.2: Illustration of the bridge geometry and support conditions (not to scale). Section A-A depicts the outline and the constant deck- and parapet configuration.

6.2.2. Geometrical model

Accordant to the workflow in Grasshopper, the geometry is parametrically defined through a set of control points. Depending on the complexity and initial definition of the CAGD model, the mesh is either directly generated from a set of boundary representations (BREPs) or an additional step is required to divide the geometry into panels with identical laminate configurations.

Case study: Klosterøybrua

From cross-section definition to superstructure

Reference points denote the fixed width, measured from the outermost vertices of the parapets. Relative to these parapets, four control points at each end of the bridge define the cross-section(s), which are reduced to two by imposing symmetry (see Fig. 6.3). The control points are defined by their Y- and Z-coordinate, denoted with the subscripts t and b to indicate top and bottom, respectively. Y_{it} (with $i = 1$ referring to $X = 0$ and $i = 2$ to $X = 35905$ mm), is defined relative to the reference point, while Y_{ib} is defined relative to Y_{im}. The top points are vertically offset from the reference points by a distance Z_{it}. Finally, the bottom point is vertically offset from the top points by a distance Z_{ib}. Hence, Y_{it}, Y_{ib}, Z_{it} and Z_{ib} represents the geometrical variables of the optimisation.

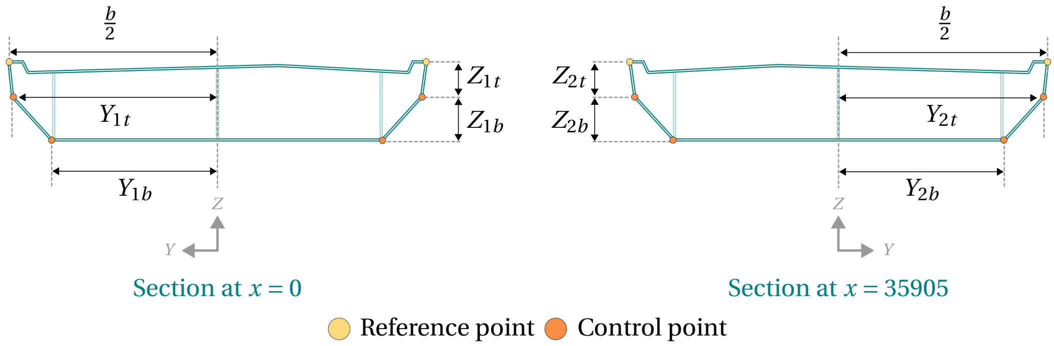

Figure 6.3: Geometric parametric control points. The cross-sections at $X = 0$ and $X = 35905$ are defined through control- and reference points. An 'average' of these sections are created in the middle of the bridge and used for creating a loft defining the exterior shell before the end is cut at a 10° angle. The reference points are constant, while the control points are tweaked to improve the bridge's behaviour.

The flap's structure

Internally, the flap is built up of three longitudinal stiffeners and 16 transverse stiffeners with manholes at a centre-to-centre distance of two meters. These manholes are necessary to accommodate inspection. Similarly, there should be hatches along the bottom exterior for entering the bridge. These are, however, not included in the model.

A steel frame provides the necessary stiffness to accommodate lifting the bridge, i.e. rotating it about the support brackets. The exploded view in Fig. 6.4, generated from the CAGD model, illustrates this configuration.

At $X = 0$, the steel frame has a fixed width of 2940 mm to align with the recesses intended for the support brackets, used as starting points for the longitudinal stiffeners (see Fig. 6.2). The end vertices of the flat part of the bottom shell are used as endpoints of the longitudinal stiffeners, potentially resulting in an angle relative to the unit vector $\hat{x} = \langle 1, 0, 0 \rangle$, giving a fan-like structure. Due to the required structural interaction between the composite and the steel, the steel frame must run parallel to the side panels of the longitudinal stiffeners. Furthermore, the steel frame impedes playing with the definition of the stiffeners; thus, these remain as described (i.e. always 3 longitudinal- and 17 transverse stiffeners). Figure 6.5 illustrates a possible configuration of the flap's stiffeners.

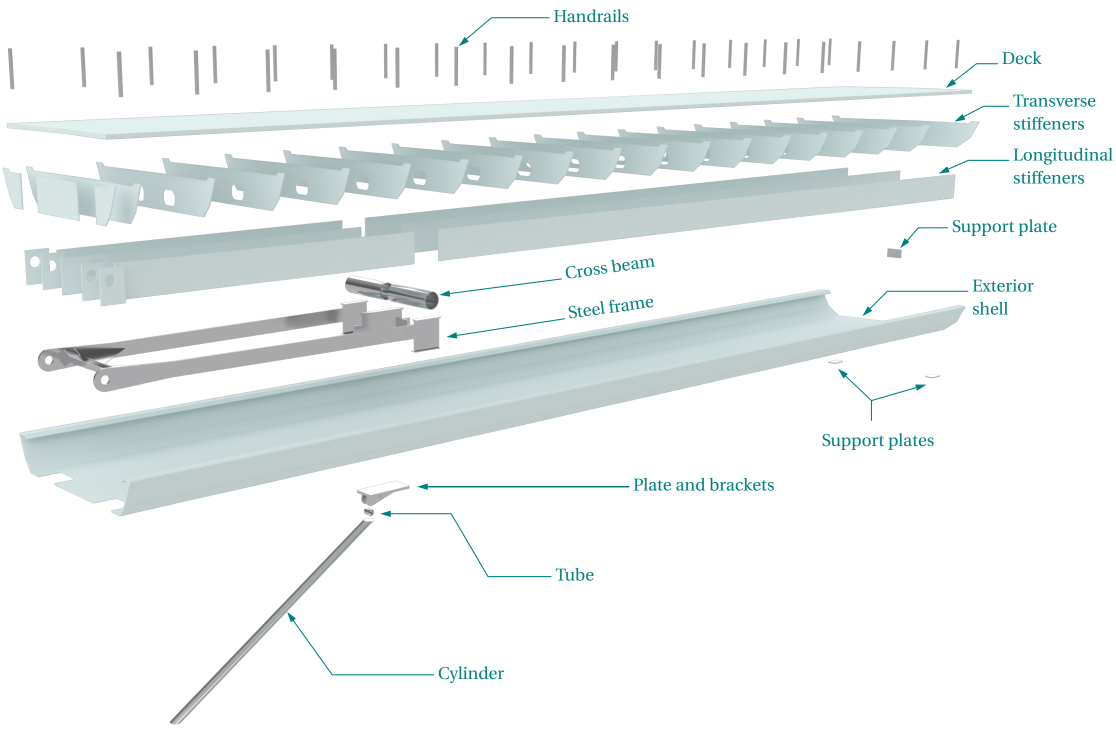

Figure 6.4: Exploded view of the composite flap. Recesses around the support brackets accommodate restraining translation without impeding rotation. The internal transverse stiffeners have manholes accommodating inspection. Zoom to overcome graininess.

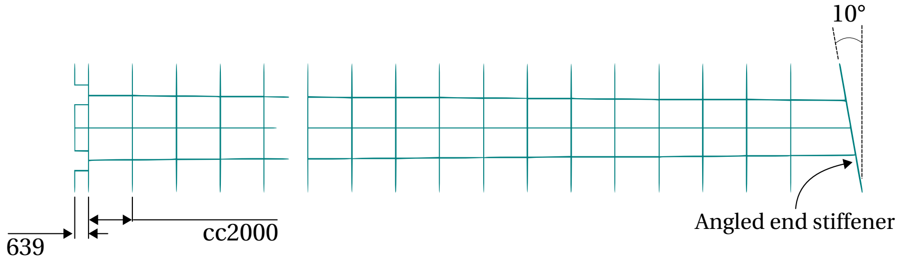

Figure 6.5: Top view of the internal configuration of the composite flap and its stiffeners. Three longitudinal stiffeners and eighteen transverse/angled stiffeners, sixteen of which are internal. The side stiffeners run parallel to the steel frame.

6.2.3. Materials and material properties

The following step involves defining the material composition of the panels. For the laminates, this requires defining the plies' properties and the properties of their constituents, i.e. the resin and fibres properties constituting the plies. In the case of other structural components, such as steel, concrete and so forth, these would naturally have to be provided.

Case study: Klosterøybrua

The bridge's superstructure mainly consists of sandwich panels, which can be built up from hybrid CFRP and GFRP face sheets with intermediate foam cores. Additionally, there are steel components: frame with support brackets, plate and brackets to connect the cylinder to the composite flap, support plates, and handrails.

Steel

The properties of the steel used in the steel frame, support brackets, handrails and support plates are given in Table 6.1.

Table 6.1: Steel (S355) properties

Property	Symbol	Value
Young's modulus [GPa]	E	205
Density [kg/m^3]	ρ	7850
Major Poisson's ratio [-]	ν	0.32
In-plane shear modulus [GPa]	G_{xy}	77

UD plies

To accommodate having hybrid face sheets, UD E-glass fibre reinforced vinylester and UD carbon fibre reinforced vinylester composites are introduced. In order to properly incorporate the defined materials necessary for quantifying the masses of the constituents, the thicknesses of the plies and the mats must be defined. Based on the fibre mass proportion ζ [g/m^2], the mat or ply thicknesses can be obtained from

$$t_{ply} = \frac{\zeta_f}{V_{\mathrm{f}} \cdot \rho_f} \tag{6.1}$$

Unfortunately, different configurations and combinations of the constituents' properties (meaning volume fractions and fibre and resin densities based on recommendations in [16]) fails to approximate the layer thicknesses in the reference model within satisfying error margins. Therefore, the fibres and the resin properties are estimated through an optimisation procedure. Here, the differences in laminate thicknesses between two representative laminates were taken as the objectives to minimise, with fibre densities and fibre volume fractions as optimisation variables (see Appendix E). With the approximated thicknesses, the GFRP and CFRP plies can be described through the properties in Table 6.2.

Fibres and resin

Although the properties of the plies are sufficient in making the model and conducting the structural analyses, it does not facilitate calculating the masses of the constituents nor the corresponding carbon footprint and costs. The constituent properties are also obtained in the above-mentioned optimisation procedure (Appendix E). Note that the mechanical properties such as moduli are not necessary; hence these are not reported; see Table 6.3.

Chopped strand mats (CSM)

The thicknesses of the chopped strand mats and their fibre volume fraction are obtained in Appendix E, while the densities are equal to those of the constituents, E-glass and vinylester resin (Table 6.3). In accordance with the Halpin-Tsai method (Chapter A.2.2), the mechanical properties of the chopped strand mats (CSMs) are calculated, resulting in the properties shown in Table 6.4 assuming in-plane isotropy.

Foam cores

The bridge design uses two foam cores, namely a non-structural PET core for the deck and DIAB's PVC H80 for all other panels (see bottom rows of Table 6.4).

Table 6.2: Ply properties for carbon/vinylester and glass/vinylester, $V_f = 54\%$.

Property	Symbol	Ply	
		E/V[a]	C/V[b]
Young's modulus in fibre direction [GPa]	E_1	42	125
Young's modulus perpendicular to fibre direction [GPa]	E_2	8.5	5.5
In-plane shear modulus [GPa]	G_{12}	3.0	2.0
Density [kg/m^3]	ρ	1910	1500
Major Poisson's ratio [-]	ν	0.26	0.30
Fibre mass proportion [g/m^2]	ζ	800	400
Tensile failure strength, 1-direction [MPa]	X_T	1100	1400
Compressive failure strength, 1-direction [MPa]	X_C	1000	700
Tensile failure strength, 2-direction [MPa]	Y_T	50	25
Compressive failure strength, 2-direction [MPa]	Y_C	150	60
In-plane shear strength [MPa]	S_{12}	60	45
Thickness[c] [mm]	t	0.5789	0.4115

[a]E-glass/Vinylester, [b]Carbon/Vinylester, [c]Approximation from Appendix E.

Table 6.3: Fibre and resin properties, $V_f = 54\%$

Property	Fibre		Resin
	E-glass	Carbon	Vinylester
Density, ρ [kg/m^3]	2570	1790	1200
Placeholder cost [€/kg]	4	30	3
GWP [kgCO_2e/kg]	0.35	25.60	3.79

Conversion factors

The conversion factors account for insecurities and degradation processes that ultimately exacerbate the FRP properties. Considering that the pedestrian traffic is of short-term character and that no specific fatigue cycles are defined for pedestrian bridges, the creep and fatigue-related conversion factors are set to one ($\eta_{cv} = \eta_{cf} = 1$).

Though the live loads are of short-term character, the effects of creep should be investigated in situations where the dead loads may exceed 20-30 % of the live loads.

i Temperature

The Klosterøy bridge has minimum and maximum expected service temperatures (T_s) of $T_{min} = -35°C$ and $T_{max} = 36°C$, respectively. Considering the vinylester resin, PVC foam and the epoxy adhesive, with assumed glass transition temperatures (T_g) of 100°C, 80°C and 100°C, respectively, the governing T_g is 80°C. Consequently, $T_g - 40°C = 40°C > T_s = 36°C$, meaning that $\eta_{ct,SLS} = 1.0$. For ULS, $\eta_{ct,ULS} \equiv 0.9$.

ii Moisture

The surroundings of the bridge position the structure within exposure class II. Hence, $\eta_{cm} = 0.9$.

iii Total conversion factor

Followingly, the two conversion factors to be used in deformations and stability checks are:

- Deformability: $\eta_{c,SLS} = 1.0 \cdot 0.90 = 0.9$
- Stability: $\eta_{c,ULS} = 0.90 \cdot 0.90 = 0.81$

The above conversion factor related to deformability is multiplied with the relevant moduli for deformations and natural frequency analyses. The latter conversion factor is multiplied with the bending equivalent moduli in the stability assessments.

Table 6.4: Properties of the chopped strand mats ($V_f = 30\%$) and foam cores.

	Elasticity modulus [MPa]	Shear modulus [MPa]	Poisson's ratio [-]	Density [kg/m^3]	Thickness* [mm]
CSM					
CSM100	10 900	4 200	0.3	2 570	0.13
CSM300	10 900	4 200	0.3	2 570	0.39
FOAM CORES					
PET 30	12	23	0.32	30	93
PVC H80	85	27	0.4	80	-

*The PVC H80 cores can take on thicknesses readily available from DIAB: 20, 25, 30, 35, 40 mm.

6.2.4. Loads, load combinations & analyses

The loads and their possible combinations are integral to any analysis. The designer should carry out investigations to arrive at the adverse load cases. If not specifically required by the design guidelines (standards), the designer may disregard dead loads in the analyses but accommodate for their effects through precambering the structure (applying an initial curvature).

Case study: Klosterøybrua

Analyses

The analyses conducted in this thesis are chosen to conform to the structural requirements and comfort of the user: (1) linear elastic analyses in serviceability limit state (SLS) calculate the deflection; (2) linear bifurcation analyses in ultimate limit state (ULS) calculate the stability; and (3) natural vibration analyses calculate the fundamental frequency indicating the susceptibility to resonance.

Loads

The bridge is loaded with a uniformly distributed load (UDL) simulating the presence of pedestrians on the deck (Fig. 6.6). The characteristic distributed load can be defined according to EN-1991-2 [88]:

$$q_{fk} = 5 \text{ kN/m}^2 \tag{6.2}$$

Note that this load is used for both SLS and ULS simply due to comparison with the reference model. The use of frequent load combinations ($\psi_{1,1} \cdot q_{fk}$) would result in a more economical design because of the reduced deflection. On the other hand, the stability analyses would likely lead to more conservative material consumption for the critical panels if the buckling load factor were governing.

The modal mass of the structure influences the vibration analyses determining the fundamental frequency of the bridge. As the handrails have no structural significance for the analyses (1) and (2), their presence is accounted for through point masses in (3) – each represented by a mass of 205.6 kg at 2 m intervals (Fig. 6.7).

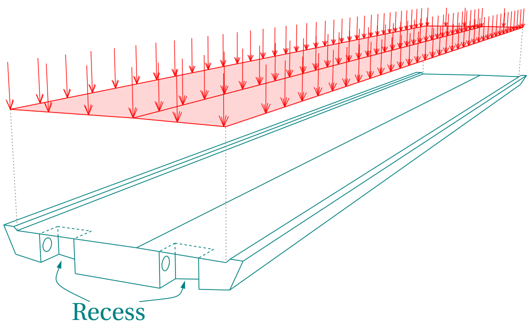

Figure 6.6: Uniformly distributed load $q_{fk} = 5 \text{ kN/m}^2$ applied on the entire deck.

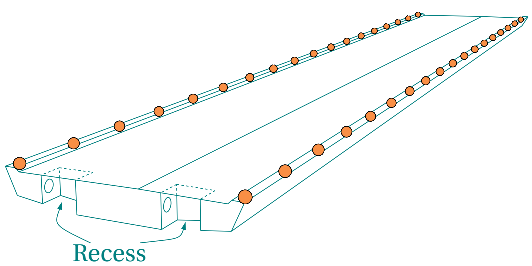

Figure 6.7: Representation of hand rails as point masses of 205.6 kg.

6.2.5. Mesh settings

Element types

The finite element software plug-in Karamba3D [89] uses three element types: truss elements, beam elements and shell elements. The shell elements in Karamba3D are flat 3-noded triangular elements with 12 degrees of freedom (DOFs) that resemble the 'TRIC'-element (see Fig. 6.8) [90, 91, 92]. These elements provide 1) much faster mesh generation than the quad elements, 2) reduce the risk of shear locking, and 3) overcome the complications that quad elements face when discretising dome-like geometries or geometries with holes. Hence, these serve as a good fit for software potentially tasked with evaluating complex shapes. Although the TRIC element originally considers transverse (out-of-plane or through-thickness) shear deformation, the elements in Karamba3D disregard this effect. This conforms with Khirchoff's plate theory and the assumptions for CLT (Chapter 3.2). While the error in this approximation is usually negligible for thin FRP laminates, the through-thickness shear deformation of the sandwich panels adopted in this thesis can prove to be prominent. Therefore, the implications of this assumption and the adopted FE software are investigated, as shown in Chapter 5.4.1. By default, the local x-axis of an element is parallel to the global X-direction, with the face normal depending on the order of the vertices defining the element. For panels where the normal is parallel to the global X-axis, the local x-axis will point in the global Y-direction. See Fig. 6.9. Hence, to conform with the defined convention of this thesis, a step of the element definition concerns the definition of the local axes.

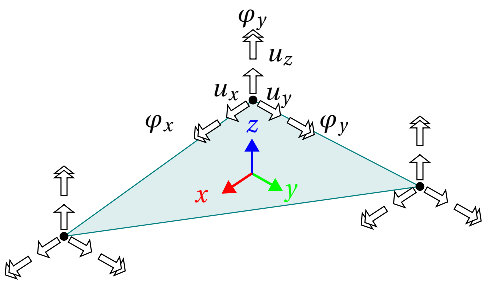

Figure 6.8: Triangular shell element with 12 degrees of freedom. Each node has the translational DOFs u_x, u_y and u_z; and the rotational DOFs φ_x, φ_y and φ_z.

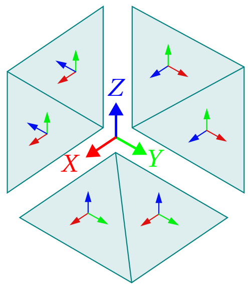

Figure 6.9: Default local axis definition for the elements, depending on the elements' orientation relative to the global axes.

Element size

The computational effort and time expended for each iteration depend heavily on the mesh settings – the bottleneck of the optimisation procedure. The expended time to generate the mesh from the structural geometry and the following structural analyses increases rapidly as the mesh size decreases, introducing the need to find a compromise between the accuracy of the solution and the computational effort.

The choice of element size strictly concerns the definition of the shell elements in the model for which relevant settings to investigate when using Karamba are the mesh resolution (MRes) and edge refinement factor (ERef), collectively ensuring that all the edges and openings are appropriately modelled. Suppose the vertices of the elements do not coincide, which is increasingly more likely with a coarse element size. In that case, there is no structural connection between the elements. Consequently, the model may behave quite unexpectedly and give unreasonable results.

Case study: Klosterøybrua

The adopted mesh settings are defined based on admissible error margins with respect to the structural responses. As shown in Appendix F, a mesh size of 0.3 metres and an edge refinement factor of 0.7 are adopted. This results in an average calculation time of 30 seconds for each iteration, including creating the initial geometry, applying the mesh and executing the structural analyses.

Chapter 6.3. Mathematical model

The following elaborates on the mathematical model, or the mathematical formulation, of the optimisation problem accordant to the typical formulation [93]. After introducing the problem, four basic elements are identified:

i the data;
ii the variables and their range of definition;
iii the set of constraints defining the feasible solutions; and finally
iv the objective functions to minimise.

It is possible to carry out the optimisation without a mathematical formulation. Nevertheless, it is highly convenient to formalise the problem to 1) design the optimisation process, 2) understand the problem and solution, 3) improve the method or solution, and 4) communicate with peers.

6.3.1. Problem introduction

This design problem concerns the minimisation of a weighted sum, Φ, of the carbon footprint $F_1(\mathbf{x})$ and the cost $F_2(\mathbf{x})$ of a composite structure, subject to deflection, fundamental frequency and buckling load factor constraints. Dealing with the mesoscale architecture of the $j \in \{1,\ldots,J\}$ panels each comprising $q \in \{1,\ldots,Q\}$ ply groups and the geometrical layout of the structure described by the variables $\mathbf{y}$, characterises this problem as a concurrent sizing- and shape optimisation problem.

The face sheets of the sandwich panels are defined as hybrid laminates, as the layers may constitute GFRP and CFRP plies. The orientations of each of these ply groups is a set of $\boldsymbol{\theta}$, which may be scaled according to the multiples of the respective ply thickness $\mathbf{T}$ where the reference thickness depends on the ply material $\mathbf{M}$. This approach can be considered an extended mixed-integer programming problem, considering that a ply group may or may not exist. If it exists, it may be scaled according to $\mathbf{T}$. By default, each face sheet's inner and outer layers are defined as CSM plies. Furthermore, a foam core is located at the mid-plane of each panel, offsetting the face sheets from each other proportional to the foam core thickness $\mathbf{h}$. The design variables can therefore be represented as

$$\mathbf{x} = \left[\boldsymbol{\theta}, \mathbf{T}, \mathbf{M}, \mathbf{h}, \mathbf{y}\right]$$

6.3.2. Data

Essential to the evaluation of the objectives are the GWP and cost corresponding to a unit mass of each constituent, the former of which is taken from EUCia EcoCalculator [94], shown in Appendix G.1. The latter is represented through placeholder values per unit kg material, estimated in collaboration with the supervisors.

For the foam core, on the other hand, the costs are provided by DIAB; see Appendix G.2. These foam core costs can be represented through a regression formula:

$$f_{\text{core}}(h_j) = -0.1421 \cdot h_j^2 + 11.588 \cdot h_j \qquad \text{for} \qquad h_j = \{20, 25, \ldots, 40\}\ \text{mm}\ \forall j \tag{6.3}$$

The remainder of the properties are given in Table 6.5. The embodied energy (EE) of the materials are included to illustrate how energy intensive the production of carbon fibres is.

Table 6.5: Environmental impacts and costs associated with materials [94].

	EE [MJ/kg]	**GWP** [$\text{kgCO}_2\text{e/kg}$]	**COST** [€/kg]
Vinylester resin[a]	121.54	3.79	4.00
Carbon fibre[b]	1040.87	48.99	30.00
Glass fibre[c]	36.11	1.81	3.00
CSM[d]	22.85	1.51	-
PVC	72.80	2.86	-

[a]VE Resin (BPA exopy based), [b]Carbon fibre (new), [c]Glass fibre mats, [d]Glass fibre dry chopped strands

In an attempt to quantify the required labour corresponding to increasingly complex geometry, a contribution is added to the cost depending on the total composite mass, namely $c_L = 10.00$ €/kg. Similar holds for the overall carbon footprint, $f_L = 3.55\ \text{kgCO}_2\text{e/kg}$.

6.3.3. Variables and range of definition

The problem variables are divided into those describing the structure's geometrical layout and those describing the material architecture.

Material architectural variables

The sandwich panels are modelled to counter the coupling effects such as extensional-shear ($\mathbf{A}_{16} = \mathbf{A}_{26} = 0$) and the bending-extension coupling ($\mathbf{B} = 0$). Recollecting the discussion in Chapter 3.2.1 and Chapter 3.2, this requires that the panels and their face sheets must be symmetrical and balanced. The former is ensured by mirroring the top face sheet about its center-line, then the resulting face sheet is mirrored about the center-line of the core. To ensure a balanced layup, there must be a layer in $+\theta$ for each layer in $-\theta$, except for 0° and 90°. Consequently, this can automatically be satisfied by discretising +45° and −45° as ply groups of ±45°, effectively reducing the solution space, resulting in three viable orientations. However, the downside of this approach is the mismatch angle between the consecutive plies, which potentially may introduce significant interlaminar stresses.

To allow for hybrid face sheets, two different ply materials, GFRP and CFRP, are incorporated on the orientations side of the variables. Furthermore, to avoid dealing with half-plies, i.e. infeasible thicknesses, the orientations are discretised as:

$$\theta_q \in \left(0_2^c,\ \pm 45^c,\ 90_2^c,\ 0_2^g,\ \pm 45^g,\ 90_2^g\right), \qquad q \in \{1,\dots,Q\} \tag{6.4}$$

where c and g refer to CFRP and GFRP plies, respectively.

Sandwich panel chromosome

By virtue of the symmetric layup the variables describing the sandwich panels can be illustrated by considering a chromosome (Chapter 4.4.3): $X^j_{q,r}$, with $j \in \{1,\dots,J\}$ being the panel index, $q \in \{1,\dots,Q+1\}$ being the ply group index ($2Q$ in total) and the foam core, and $r \in \{1,\dots,3\}$ the properties associated with each ply or foam core. In this thesis $Q = 10$ and $J = 4$ (see Fig. 6.17).

The considered properties will be (a) ply thickness scaling $T_{q,r} = \{0,\dots,1\}$ for $r < 3$ and $T_{q,3} = \{4,\dots,8\}$ where in the case of plies, this factor is constrained by an upper limit of 2, and in the case of the foam, 5 mm is the reference value; (b) orientation $\theta_q = \{0_2°, \pm 45°, 90_2°\}$ encoded as $\theta_q = \{1,2,3\}$, indicating ply stacks of two plies; (c) material $M_q = \{1,2,3\}$ corresponding to CFRP, GFRP and foam. The ply thickness scaling (which at an initial stage was $T_{q,r} = \{0,\dots,2\}$) is limited to 1 to enable a more dynamic exploration of the stacking order and to circumvent having several contiguous plies. Thus, a chromosome representing a sandwich panel has the following shape:

$$X^j_{q,r} = \begin{array}{c} \begin{bmatrix} 1 & 1 & 2 \\ 1 & 2 & 2 \\ 0 & 3 & 2 \\ \vdots & \vdots & \vdots \\ 1 & 2 & 1 \\ 8 & 1 & 3 \end{bmatrix} \end{array} \begin{array}{l} q=1 \\ q=2 \\ q=3 \\ \vdots \\ q=Q \\ q=Q+1 \end{array} \tag{6.5}$$

The chromosome (Eq. (6.5)) indicates that the first ply group is onefold (totally two plies), oriented at 0° and made out of GFRP. The third ply group is absent, while the foam core (last row) will be $5 \cdot 8 = 40$ mm.

The sandwich panel configuration can be visualised by incorporating the stacking notation introduced in Fig. 3.4, as shown in Fig. 6.10. Depending on the chromosome $X^j_{q,r}$, K plies are present. Mirroring these results in face sheets of $2K$ plies, which again are mirrored, resulting in $4K$ plies. These are rigidly offset from each other according to the foam core thickness h^j to form a sandwich panel. Figure 6.11 contextualises the mathematical formulation, illustrating the six (seven – counting the absent) possible configurations of the ply groups.

The material architecture variables alone amounts to a vast solution space (S_{mat}). Each ply group constitutes three orientations, two materials and the thickness scaling amounting to twelve ($3 \cdot 2 \cdot 2 = 12$) combinations for each ply group $q \in \{1,\dots,Q\}$. Thus, the $q \in \{1,\dots,Q\}$ number of ply groups and the f_{c} number of different foam core thicknesses for each panel $j \in \{1,\dots,J\}$ amounts to the following solution space (read: number of combinations):

$$S_{\text{mat}} = \prod_{j=1}^{J} \left(12^Q \cdot f_{\text{c}}\right) \Longrightarrow \left(12^{10} \cdot 5\right)^4 = 9.19 \cdot 10^{45} \text{ combinations.} \tag{6.6}$$

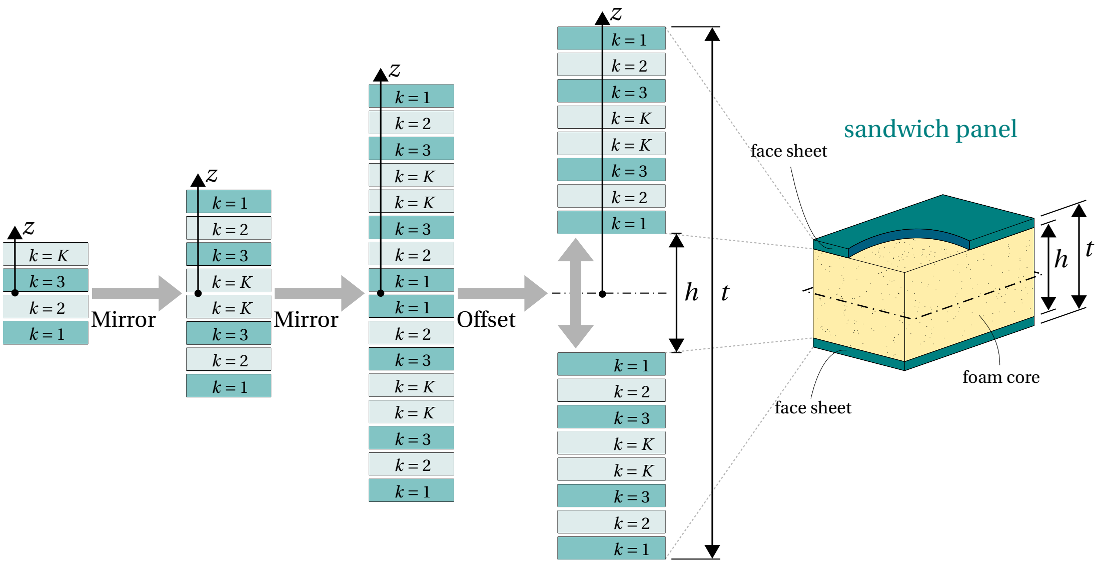

Figure 6.10: Construction of face sheets comprising $2K$ plies, rigidly offset by a distance h, not to scale. Adapted from [60].

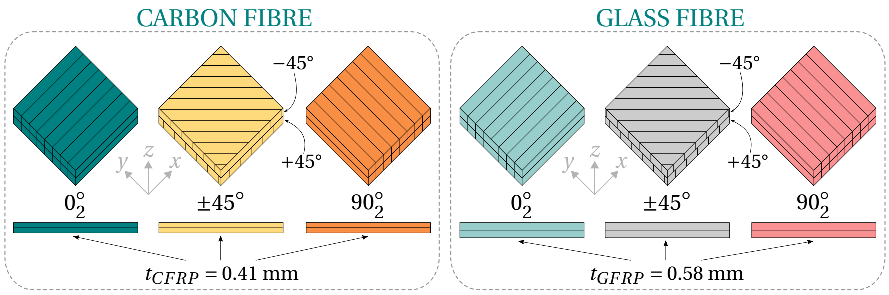

Figure 6.11: Visual representation of plies and ply stacks. Material $M_q = \{1,2,3\}$ and orientation $\theta_q = \{1,2,3\}$. The thicknesses refer to each ply thickness in a ply stack.

Geometrical variables

The geometrical variables' (**y**, Fig. 6.12) range of definition are defined as to (1) prevent sharp angles damaging the fibres during layup, (2) prevent collision between the steel brackets and the external shell, and (3) prevent unrealistic cross-sections. Consequently, the ranges are different for the respective sides (at $X = 0$ and $X = 35905$). The varying fractional digits results from achieving the same initial geometry as the reference model. Decreasing this accuracy, i.e. less fractional digits, can significantly reduce the solution space should the precision be less important. Realistically, the mould precision should not be smaller than 1 mm – depending on the production method of the mould.

Though notably smaller than the material architecture-related search space, the geometrical variables has a significant search space. Y_{1t}, for instance, has a search space of 3001 (see Fig. 6.12). Combined, these variables amount to a search space of $S_{\text{geo}} = 1.97 \cdot 10^{26}$. Thus, the total search space (number of combinations) is $S_{\text{mat}} \cdot S_{\text{geo}} = 1.81 \cdot 10^{72}$, with S_{mat} as defined in Eq. (6.6).

6.3.4. Constraints

The problem constraints relate to the bridge's structural response and the material architecture of each respective panel.

Material architecture-related constraints

Constraints regarding the ply thickness scaling of the ply groups (maximum one time):

$$X^j_{q,1} < 2 \quad \text{for} \quad q = \{1,\dots,Q\},\ j = \{1,\dots,J\} \tag{6.7}$$

Constraints regarding the orientations of the plies:

$$1 \le X^j_{q,2} \le 3 \quad \text{for} \quad q = \{1,\dots,Q\},\ j = \{1,\dots,J\} \tag{6.8}$$

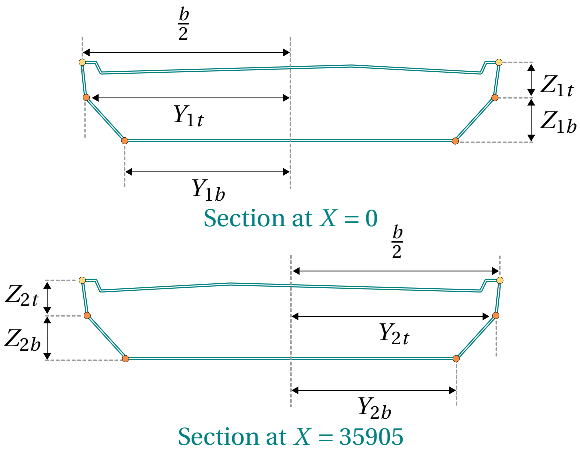

	Variable	Bounds	Unit	S*
$X = 0$	Y_{1t}	0.900 – 1.200	-	301
	Y_{1b}	0.4000 – 0.9000	-	5001
	Z_{1t}	0.6000 – 1.0000	m	4001
	Z_{1b}	0.100 – 1.200	m	1101
$X = 35905$	Y_{2t}	0.300 – 1.200	-	901
	Y_{2b}	0.3000 – 0.9000	-	6001
	Z_{2t}	0.5000 – 1.0000	m	5001
	Z_{2b}	0.100 – 1.200	m	1001

*Search space

Figure 6.12: Geometric variables **y** and their range of definition.

Constraints regarding the foam angle: due to the isotropic material, the orientation is irrelevant; thus, its orientation is fixed to 0°:

$$X^j_{Q+1,2} = 1 \quad \text{for} \quad j = \{1, \ldots, J\} \tag{6.9}$$

Constraints regarding the materials: the ply groups may only comprise the material types 1 or 2, whereas the foam is made of material 3

$$\begin{aligned} X^j_{q,3} &< 3 \quad \text{for} \quad q = \{1, \ldots, Q\},\ j = \{1, \ldots, J\} \\ X^j_{Q+1,3} &= 3 \quad \text{for} \quad j = \{1, \ldots, J\} \end{aligned} \tag{6.10}$$

When a laminate is only composed of ±45 plies, which resulted from the optimisation at an earlier stage (Appendix C), most of the stresses are transferred through interlaminar stresses that the resin must resist. The relatively poor resistance of the resin results in considerable creep, not to mention a highly non-linear stress-strain behaviour. Introducing a minimum amount of fibres in the 0° direction increases axial strain resistance, mitigating the creep concerns. Including a minimum amount of fibres oriented at 90° helps to further reduce the stress variations throughout the laminate, linearising the stress-strain behaviour while ensuring proper load transfer between the adjacent panels. Complying with these requirements leads to the introduction of having a minimum of 12.5 % of fibres in each direction, not considering the stiffness of the respective layers, in hand with the rules of thumb (see Chapter 3.3.6) for FRP designs.

Although the stiffnesses may vary according to the ply material, this is expressed through the total number of plies in each direction, divided by the total number of plies, which is a simplification. Typically, for laminates that are not hybrid, an equal proportion of plies in the different directions translates into equal stiffnesses.

For each face sheet, the total number of plies are

$$K^j = \sum_{q=1}^{Q} (2 \cdot X^j_{q,1}) = 2 \cdot \sum_{q=1}^{Q} X^j_{q,1} \quad \text{for} \quad j = \{1, \ldots, J\} \tag{6.11a}$$

with j referring to the panel. The number of plies in a certain direction is given by

$$K^j_{0°} = K^j_{90°} = 2 \sum_{q=1}^{Q} X^j_{q,1} \quad \text{for} \quad X^j_{q,2=1} \text{ and } X^j_{q,2=3},\ j = \{1, \ldots, J\} \tag{6.11b}$$

i.e. for the orientations 0° and 90°. For plies in the directions +45° and −45°, it holds that

$$K^j_{+45°} = K^j_{-45°} = \sum_{q=1}^{Q} X^j_{q,1} \quad \text{for} \quad X^j_{q,2=2},\ j = \{1, \ldots, J\} \tag{6.11c}$$

As the number of plies in +45° by default equals the number of plies in −45°, we are left with three constraints for each panel j.

$$\frac{K^j_\theta}{K^j} \geq 0.125 \quad \text{for} \quad \theta = \{0, 90, +45, -45\},\ j = \{1, \ldots, J\} \tag{6.11d}$$

Recalling the discussion on practical limitations (Chapter 2.5), one should aim for thicknesses less 20 mm, hence introducing the need for constraints that ensure this.

Including the two layers of CSM sheets positioned at the face sheets' bottom and top surface, one can express this constraint based on Eq. (6.11a). Let t_{fs}^j denote the face sheet thicknesses in panel j and t_q^j for $q \in \{1, \dots, Q\}$ be the ply thicknesses dependent on the selected material of ply group q, then:

$$t_{\text{fs}}^j = 2 \cdot t_{\text{CSM}} + \sum_{q=1}^{Q} (2 \cdot X_{q,1}^j) = 2 \cdot \left(t_{\text{CSM}} + \sum_{q=1}^{Q} X_{q,1}^j \right) \quad \text{for} \quad j = \{1, \dots, J\} \tag{6.12a}$$

leading to:

$$t_{\text{fs}}^j - 20\ \text{mm} \leq 0 \quad \forall j \tag{6.12b}$$

Structural response-related constraints

The constraints concerning the structural response ensure that the bridge will not introduce discomfort for the user in terms of deflections and vibrations while maintaining structural stability by including a minimum buckling load factor. The longest span of the bridge is from the position of the cylinder to the end of the bridge. Cutting the edge at an angle of 10° yields the governing distance $L = 24.6$ m, from which the deflection constraint becomes:

$$\delta(\mathbf{x}) \leq \delta_{max} = \frac{L}{350} \approx 70.29\ \text{mm} \Longrightarrow \delta(\mathbf{x}) - \delta_{max} \leq 0 \tag{6.13}$$

where δ is the greatest deflection among the nodes in the model, and δ_{max} is the maximum allowable deflection. The requirement for the fundamental frequency of the bridge is taken from CUR96, stating that a pedestrian bridge may be considered insensitive to vibrations if its fundamental frequency is greater than 3.40 Hz [95]:

$$\Omega_0(\mathbf{x}) \geq 3.4 \Longrightarrow 3.4 - \Omega_0(\mathbf{x}) \leq 0 \tag{6.14}$$

The constraint concerning the structural stability, quantified by the critical buckling load factor (λ_{cb}), is associated with the first buckling mode of the weakest panel in the structure. As the weakest panel buckles under the loads $N_x\lambda_{cb}$, $N_y\lambda_{cb}$ and $N_{xy}\lambda_{cb}$, the minimum requirement is $\lambda_{cb} \geq 1$. It is recommended to apply a knockdown factor of $\frac{1}{6}$ to account for imperfection sensitivity, based on the ratio between the ultimate load to the critical load [96, 97]. The reciprocal of the knockdown factor expresses a minimum buckling load factor above which the structure can be considered safe from buckling:

$$\lambda_{cb}(\mathbf{x}) \geq 6 \Longrightarrow 6 - \lambda_{cb}(\mathbf{x}) \leq 0 \tag{6.15}$$

6.3.5. Objective functions

The multi-objective optimisation comprises two objectives that depend on the masses of the constituents to concurrently solve the shape and stacking sequence optimisation of the composite structure.

i. Carbon footprint minimisation

The carbon footprint of the structure is expressed as the summation of all the material masses and their respective GWP, plus the total composite mass multiplied by the GWP related to the production process:

$$F_1(\mathbf{x}) = \sum_{s=1}^{S} \rho_s(\mathbf{x}) V_s(\mathbf{x}) f_s(\mathbf{x}) + f_{\text{L}} \cdot m(\mathbf{x}), \tag{6.16}$$

where S is the number of constituent materials, ρ_s, V_s and f_s are the density, volume and GWP for material s, respectively, m is the total composite mass and f_{L} is the environmental impact associated with processing. With the two adopted ply types and CSM mats based on E-glass, $S = 4$, referring to carbon fibre, E-glass fibre, resin and foam core.

ii. Cost minimisation

The total cost of the structure entails a summation of all the materials and their respective masses and costs, plus the labour costs depending on the total composite mass:

$$F_2(\mathbf{x}) = \sum_{s=1}^{S} \rho_s(\mathbf{x}) V_s(\mathbf{x}) c_s(\mathbf{x}) + c_{\text{L}} \cdot m(\mathbf{x}), \tag{6.17}$$

with c_s and c_{L} being the costs associated with material s and labour, respectively.

From multi-objective to single-objective

As the two objectives may differ significantly in value and have different units (€ and $kgCO_2e$), the objectives are normalised with respect to their initial value. Doing so ensures that both objective functions are normalised to ±1 to start with:

$$F_1^*(\mathbf{x}) = \frac{F_1(\mathbf{x})}{F_1(\mathbf{x}^0)} \quad \text{and} \quad F_2^*(\mathbf{x}) = \frac{F_2(\mathbf{x})}{F_2(\mathbf{x}^0)} \tag{6.18}$$

with $\mathbf{x}$ being the vector of design variables, $\mathbf{x}^0$ the vector of design variables at the initial design, while $F_1^*(\mathbf{x})$ and $F_2^*(\mathbf{x})$ refer to Eq. (6.16) and Eq. (6.17), respectively.

The above-normalised objectives are combined into a single-objective optimisation problem. To incorporate the possible constraint violations, this is expressed as a pseudo-objective function, meaning that a penalty is added to the fitness if either of the constraints is violated:

$$\Phi(\mathbf{x}, r_p) = F_1^*(\mathbf{x}) \cdot w_1 + F_2^*(\mathbf{x}) \cdot w_2 + r_p \cdot P(\mathbf{x}), \qquad w_1 + w_2 = 1 \tag{6.19}$$

where r_p is a penalty factor (taken as 1000) to enforce constraint satisfaction, w_1 and w_2 are the weights for the respective objectives, and

$$P(\mathbf{x}) = \sum_{i=1}^{n_c} \left\{\max(0, g_i(\mathbf{x}))\right\}^2, \tag{6.20}$$

with n_c being the number of constraints as introduced in Chapter 6.3.4 and $g_i(\mathbf{x})$ the function value of constraint i, evaluated from the left hand side of the inequalities in Equations (6.11)–(6.15).

Chapter 6.4. Global & local optimisation

The global optimisation method presented herein represents a way to effectively explore as much of the solution space as possible and explore unvisited areas, otherwise known as an explorative or a diversifying search method. The local optimisation focuses on promising regions to converge optimally, usually referred to as exploitation or intensification [98]. Thus to distinguish the search methods at later stages in the report, these are referred to as diversification and intensification [search methods], respectively. Opposite to global optimisation, aimed at effectively exploring as much of the solution space as possible, local optimisation can be seen as an exploitation technique as it focuses on promising regions to converge optimally.

6.4.1. Global optimisation – diversification

As discussed in Chapter 4, genetic algorithms require tuning of their options in order to best perform the optimisation – or even arrive at a feasible solution. Specific to the Galapagos algorithm plug-in, one must first define whether the objective should be minimised or maximised, before tuning the relevant options shown in Table 6.6 and Fig. 6.13(left).

Table 6.6: Galapagos' evolutionary solver options and their description.

Option	Description
Threshold	Optional value below/above which the procedure is terminated
Max stagnant	Number of consecutive generations without improvement – stopping criteria
Population	Population size
Initial boost	Population size multiplier for the first generations – expands the exploration
Maintain	Equivalent to elite children: genomes which automatically are passed to the next generation
Inbreeding	Equivalent to crossover

Case study: Klosterøybrua

Tuning the optimisation options can be a tedious process (see [67]), especially if the calculation of each individual is slow. Depicting the most influential option or operator is not straightforward, usually requiring thorough investigation. Regardless, seeing that Galapagos' default options are similar to those adopted in e.g. [50], the crossover rate (*inbreeding*) and elite portion (*maintain*) are set to 75% and 8%, respectively. The *max stagnant* option is set to 20 generations, which reportedly proved to prevent early stagnation while preventing excessive function evaluations in the vicinity of the optima. Finally, the population size is selected.

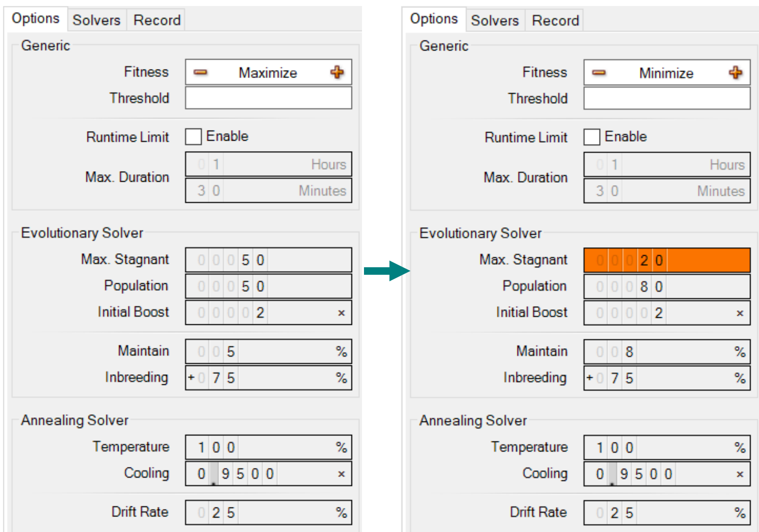

Figure 6.13: Galapagos optimisation options. (**left**) Default and (**right**) adopted options.

Population size

The graphs (Fig. 6.14) illustrate the convergence graphs for different population sizes, initiated at the same point and terminated after 8 hours. Even though the smallest population size (20) evidently returns a better solution sooner, the stochastic nature of GA suggests that this is by luck. Although drawing conclusions from these graphs is somewhat optimistic, a few trends align with the solver's nature. First, small population sizes tend to explore less of the fitness landscape, necessitating numerous generations to improve on the solutions. Hence, a low value of *max stagnant* may result in premature convergence. With an increasing population size, the seeming trend is that a smaller number of generations are required to find better function values. Naturally, more experiments should be conducted to increase confidence in these values. Seeing that all the options arrive at similar fitness values at the eight-hour mark, it is reasonable to choose an intermediate value between 50 and 100, making a compromise between the exploration and the number of function evaluations. Hence, a population size of 80 is adopted.

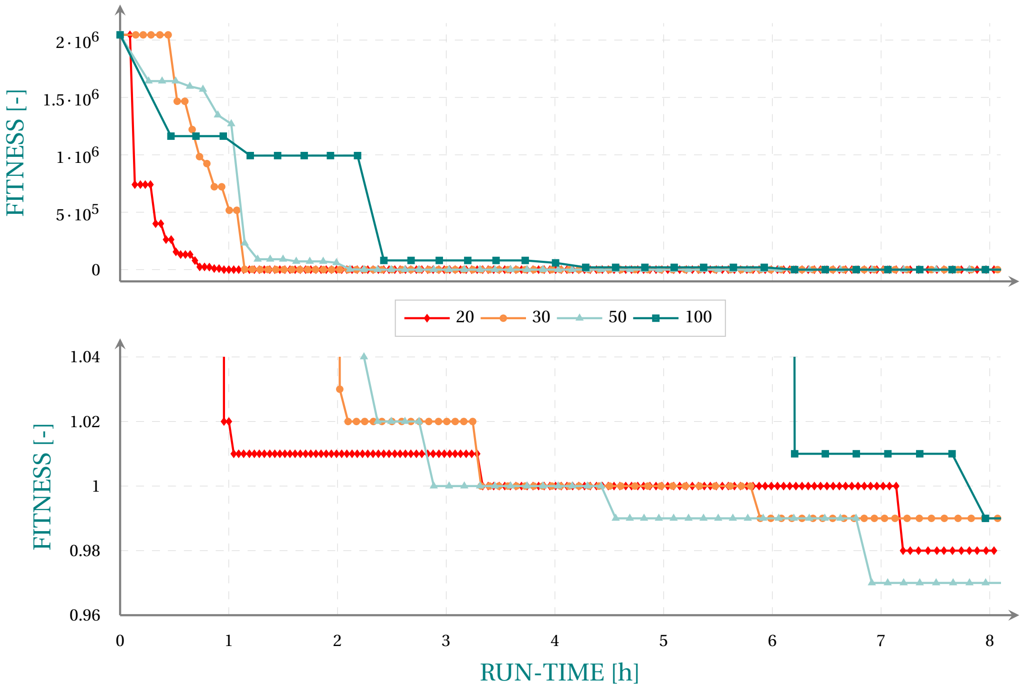

Figure 6.14: Convergence graphs for different population sizes – terminated after 8 hours. Each marker represents one generation.

6.4.2. Local optimisation – intensification

Local optimisation is an important tool in increasing the confidence in the results, seeing that GA merely finds near-optimal points in the vicinity of local extremes. The local intensification can verify whether the solution obtained through the diversifying search is optimal; if not, it can further improve the solution.

Case study: Klosterøybrua

Following the global optimisation carried out with the Galapagos plug-in, further improvement or verification of the solution is realised with the GOAT plug-in [99], making use of its Subplex Nelder-Mead (Sbplx) algorithm [100, 101]. The algorithm is asked to stop when the relative change in objective falls below $1 \cdot 10^{-5}$ (see Fig. 6.15).

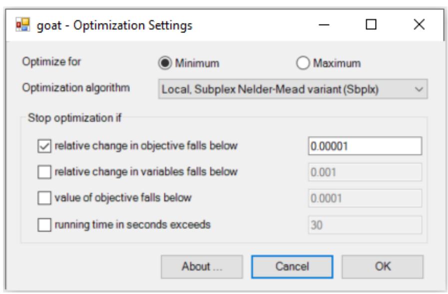

Figure 6.15: GOAT optimisation settings.

The Grasshopper definition (the 'canvas') is shown in Appendix H. For a thorough investigation and perhaps to implement changes or improvements, see the project github repository.

Chapter 6.5. Modelling

The following section elaborates on some important aspects and decisions regarding the modelling of the composite flap. The before-mentioned panel configurations are modelled in the finite element (FE) package Karamba3D [89] as homogenised shells, with in-plane properties calculated with Python and CLT. The lifting cylinder is modelled as a pinned-pinned truss with a constant mass of 4900 kg, meaning that a change in length would change the cross-sectional area. The crossbeam and the pin connecting the cylinder to the lifting brackets are modelled as beam elements. The remaining elements, such as the steel frame components, are modelled with shell elements.

Simplification of the deck structure

An integral part of reducing the computational time translates into reducing the number of finite elements. Apart from performing mesh density analyses, one can achieve this by simplifying parts that are of less significance for the global response of the structure. This case concerns the deck structure, which was originally modelled as a web-stiffened sandwich structure with dissimilar top and bottom face sheets. The web stiffeners were introduced to increase the deck's local resistance, i.e. resistance to concentrated loads. Referring to Fig. 6.16, including these webs would require several small elements without the possibility of including the foam core. The adopted simplification involves a singular unbalanced and nonsymmetrical panel, reducing the calculation time by approximately 90 seconds without compromising the global structural response. Although the deck serves as an interesting optimisation topic, verifying local point loads is outside the scope of this thesis. Furthermore, the lack of solid elements in Karamba3D impedes the inclusion of web-stiffened sandwich panels.

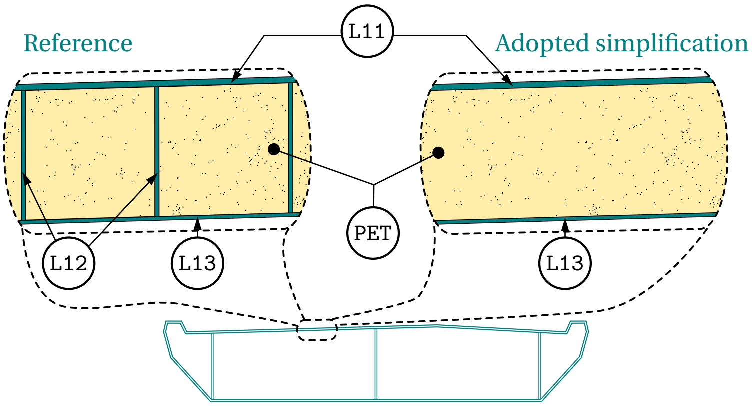

Figure 6.16: Discretisation of the deck configuration from the reference model and the adopted simplification. Description of the laminate codes, e.g. L12, are given in Appendix I.

6.5.1. Panel distribution

Since the design is stiffness-driven and the stresses in the panels are not evaluated during the optimisation procedure, the geometry division can be simplified without being too concerned with stresses arising from connections (local effects). As such, the adoption of $J = 4$ panels with (potentially) unique material architecture is based on the framework's limitations and a goal to reduce the number of variables. The panel groups are (1) transverse stiffeners, (2) longitudinal stiffeners, (3) side panels and (4) bottom panels, as depicted in Fig. 6.17. Naturally, further division of these groups according to, e.g. their X-position could improve the objective values at the cost of a greater computational effort. To better grasp how a panel division could look in the case of evaluating local stresses and more load cases, the panel divisions adopted in the reference model are given in Appendix I.3. For instance, due to thermal effects, the area in the vicinity of the cylinder connection of the bottom panel is rather delicately partitioned (see Chapter I.3.1)

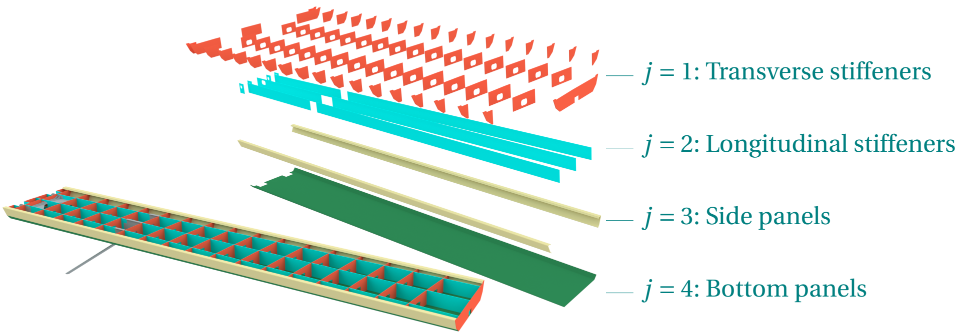

Figure 6.17: The composite flap is divided into $J = 4$ panels. The deck is hidden from the preview.

Chapter 6.6. Analytical solution

Two iterations of an analytical design procedure are performed, defining an initial design to:

- have a notion of what dimensions, panel configurations and structural responses to expect;
- improve the confidence in the results; and
- provide means to quantify the efficiency of the framework.

As such, the analytical solution verifies the numerical results and enables drawing more quantitative conclusions. In Appendix J, the calculations are carried out with the optimisation constraints in mind. By adopting Timoshenko's beam theory [102], the strengths of the panels are verified while capturing the shear deformation of the panels.

The hand calculations lead to the following geometry and structural responses, which are used as an initial point (genome) for the optimisation:

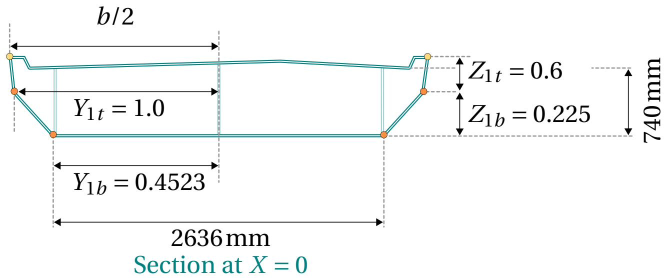

Displacement	50.88	mm
Frequency	4.28	Hz
Buckling	18.51	-
Footprint	314 912.81	$kgCO_2e$
Cost	395 112.69	€

Figure 6.18: Initial geometry and the corresponding structural responses. Symmetry is imposed, such that $Y_{1t} = Y_{2t}$, $Y_{1b} = Y_{2b}$, $Z_{1t} = Z_{2t}$, $Z_{1b} = Z_{2b}$. Note that the illustrated section does not match the imposed variables.

The above geometry portrays a conservatively stiff structure, which is a consequence of all the simplifications and assumptions made when carrying out the analytical solution. Regardless, there is a significant potential to improve the design, seeing that the deflection and buckling resistance greatly exceed the corresponding constraints.

Owing to the stochastic nature of the GA solver, the search is initiated at several starting points, some of which are based on the obtained configurations in Appendix J, Appendix J.4. Specifically, the configuration is used as the initial configuration for creating the Pareto-front in Chapter 7.3.

Chapter 6.7. Conclusion

This chapter answers the following questions:

1. How can a structure be defined to prepare for its optimisation?
2. What are the objectives and design constraints of the optimisation?

As with any structural analysis, the design boundaries must be properly defined. Specifically, one must define the scope and what one would like to answer with the analysis. Then, with a proper plan in mind, the model is set up, defining the geometry, boundary conditions and load cases. Enabling structural optimisation requires the option to alter one or more design variables from one iteration to another. Though several available tools enable such optimisations, these tools are often limited to either focussing on geometrical or material aspects.

In this chapter, a parametrical model is set up to prepare a structural optimisation of the Klosterøy bridge in Norway. Limited to a single load case, the geometrical and material architectural parameters were taken as optimisation variables to concurrently optimise the structure's shape and sizing (material architecture). The steps laid out in the optimisation framework of this thesis to minimise the cost and environmental burden are exemplified with this novel project in mind.

Overcoming the limitations of the adopted FE plug-in requires defining appropriate design constraints, namely, deformation, buckling and fundamental frequency constraints. Furthermore, adequate constraints were introduced on the material side to adhere to rules of thumb when dealing with composite materials. These constraints aim to (1) limit the maximum thickness of the face sheets to prevent issues when wetting out the fibres and (2) ensure adequate stiffness in all directions of the laminates.

7

Results and Post-optimisation

This chapter provides the result of this thesis work. By comparing the obtained solutions with the results pertaining to the analytical solution and the reference model (based on the works of FiReCo), it will be quantified to what extent the framework can be used to improve a design. Furthermore, the sensitivities of the solutions concerning the input parameters (unit cost and global warming potential (GWP)) are investigated. Finally, some of the critical framework limitations are examined using more advanced FE software packages.

After presenting and discussing these results, the author reflects upon choices that could – or should – have been different if what is known at the point of writing was known at the beginning of this thesis work. Then, recommendations and possible future work are laid out.

The chapter aims to answer the following:

1. What is the confidence in the solution?
2. Are the solutions sensitive to changes in the input parameters?
3. Is the framework worthwhile the required effort of setting it up?

Chapter 7.1. Optimality of the solution

As discussed in Chapter 4, the complexity of the problem does not necessarily ensure that the obtained solution is the (global) optimum. The vast solution space, with $1.81 \cdot 10^{72}$ possible combinations, further emphasise the complexity. Therefore, to increase the confidence in the results, the optimisation is initiated from three randomly generated starting points for the configuration $w_1 = 0.8$ and $w_2 = 0.2$. Note that the mathematical formulation uses the initial values of the objectives (Eq. (6.18)). Therefore, the fitness value is not a good indicator of the solution's optimality, as it depends on these initial values. Instead, the objectives should be evaluated individually. Table 7.1 below depicts how these different initial configurations with their related costs and CO_2-equivalents may lead to different solutions (evaluated after the intensification phase). Coincidentally, the best fitness value corresponds to the best objective values.

Table 7.1: Different starting points yield different solutions (for $w_1 = 0.8$ and $w_2 = 0.2$).

Solution	Initial cost [€]	Initial footprint [kgCO$_2$e]	Initial fitness [-]	Optimal cost* [€]	Optimal footprint* [kgCO$_2$e]	Optimal fitness* [-]
1	517 178.268	457 871.757	333 027.344	382 445.548	353 612.805	0.7657
2	621 683.370	517 246.831	351 563.500	352 176.128	311 676.876	0.5954
3	537 865.930	441 812.398	318 751.000	354 578.380	339 219.523	0.7461

The corresponding fitness convergence plots for global diversification and local intensification phases are illustrated in Fig. 7.1, suggesting that the intensification consistently improves on the solution. This means that the diversification merely identifies near-optimal solutions in the vicinity of local optima and that no single global optimum is obtained.

Similarly, Fig. 7.2 shows the global diversification with respect to fitness, carbon footprint and costs, plotted against the number of generations. Feasible solutions (when the fitness is close to or below 1) are found relatively quickly – before the 25th generation.

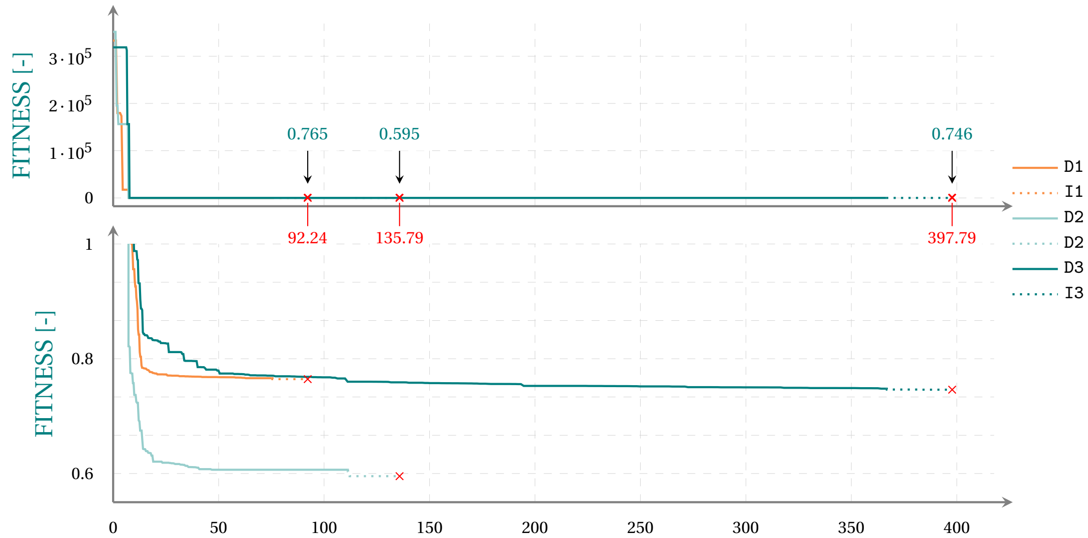

Figure 7.1: Global diversification to local intensification convergence plots, showing the fitness convergence graphs for the configurations in Table 7.1 vs the run-time. The graph depicts the diversification (D)- and intensification (I) phases for solutions 1–3.

Normalisation

Though the discrepancies between the obtained solutions are characteristic of the genetic algorithm, the objective normalisation likely contributes to these disparities. With the simple normalisation method in Eq. (6.18), relative differences between the initial objective values affect the direction in which the algorithm searches, potentially leading to different near-optimal values of the objectives. Technically, altering the value used for normalising the objectives for each optimisation changes the problem definition. Instead, the normalisation should have been done using an average or a non-zero target value. Another viable normalisation approach, which was disregarded as it requires obtaining the maximum and minimum possible value of each objective separately, is to express the i normalised objectives as [57]:

$$F_i^* = \frac{F_i - F_{i,min}}{F_{i,max} - F_{i,min}} \tag{7.1}$$

In certain problems, obtaining $F_{i,max}$ and $F_{i,min}$ is straightforward. However, obtaining these values requires two separate optimisations in more complex cases. Setting each variable to its maximum and minimum value provides good indications. Specific to the problem herein, one could imagine setting the ply thickness scaling factors to 0, which translates to minimal material consumption. Then, however, the ability to invert the structural stiffness matrix is lost, meaning that structural responses cannot be calculated.

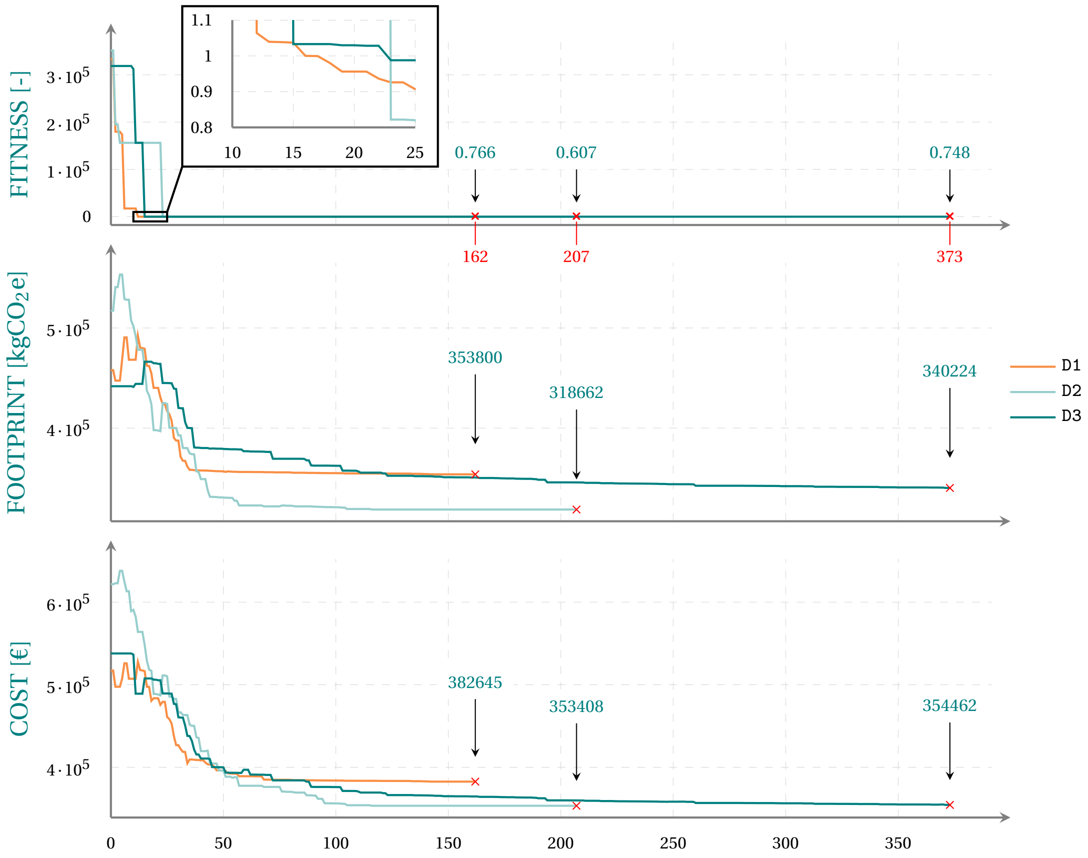

Figure 7.2: Global diversification convergence plots for the three solutions in Table 7.1, illustrating how the (**top**) fitness, (**middle**) carbon footprint and (**bottom**) cost evolves during the global diversification search. D = (global) diversification.

Solution sensitivity

The shape and laminate combinations for the above solution present locally optimum solutions, which are pretty sensitive to alterations of its variables. For instance, by playing with the four laminate specifications, the structural responses change so that one or more structural response-related constraints are violated. Similarly, most alterations of the geometrical variables amount to constraint violations, even when the perturbations remain small.

Such checks should be more thoroughly investigated through proper sensitivity analyses. However, as discussed in the following section, this would amount to too time-consuming investigations – considering the time at hand and the complexity of the problem.

Chapter 7.2. Sensitivity analysis of the input parameters

Sensitivity analysis (SA) enables pinpointing the most influential variables concerning an optimisation problem, as discussed in Chapter 4.5. Here, however, the input parameters concerning the costs and GWP regarding the materials are investigated. Owing to the uncertainties in the adopted placeholder values, especially concerning the costs, the SA is deemed necessary. The foam core costs provided by DIAB are left out of the analysis.

Owing to the costly computation and many optimisation variables, a full SA would be unrealistic within the available time frame. A thorough investigation of this sort would require perturbing all the design variables (several of which are equal). Then, intensification searches should be carried out from these new design points.

In order to provide a representative SA, the material costs and GWPs are perturbed incrementally by 1 %, 5% and 10 %, and repeated in the negative direction (i.e. -1 %, -5 % and 10 %) for *solution 1* in Table 7.1. The procedure is conceptually straightforward. The respective parameters are perturbed by 1 % (and so on) of their original value. This causes an immediate change to the fitness, cost and carbon footprint, essentially presenting a new design point. From this point, a new local intensification is initiated, which is terminated after eight hours.

The effect of perturbing a parameter, i.e. the sensitivity of a performance $\psi(x)$, is commonly evaluated by calculating the corresponding gradient [45]:

$$\frac{\partial \psi}{\partial x} \approx \frac{\psi(x+\Delta x) - \psi(x)}{|\Delta x|} \tag{7.2}$$

However, in this case, the perturbations (Δx) differ by one order of magnitude, meaning that the calculated sensitivities would vary accordingly. Therefore, the sensitivities are calculated by normalising the difference between the new value after the intensification step (recognised by †) and the current value by the current value.

To illustrate how the sensitivities are calculated, consider the second perturbation (column d_2) of the sensitivity matrix regarding the cost of carbon fibres (Table 7.2). Thus, the sensitivity of the fitness due to a 1.5 % increase in the cost of carbon is:

$$\frac{\text{new value} - \text{current value}}{\text{current value}} = \frac{0.759399 - 0.75642}{0.75642} = 0.393\,\% \tag{7.3}$$

Cost sensitivity

From Appendix K.1, it is evident that there are slight changes in the fitness value due to the perturbations. However, as the carbon footprint and the structural responses are equal over most of the perturbations, it is evident that the intensification steps converged to the same solution. The only outlier to these results corresponds to the first perturbation of the carbon fibre cost (i.e. +1 %), for which no improvement on the solution was found. This likely arose because the algorithm used for the intensification is prone to the same pitfalls as the genetic algorithm, meaning there is no guarantee that a better solution can be found – though it evidently exists. The cost sensitivity analysis reveals that a 10 % increase in labour cost amounts to a 0.887 % greater fitness value. Conversely, a 10 % decrease of the same parameter amounts to −0.899 % variation in the fitness value. The next most influential cost parameter concerns carbon fibres.

Global warming potential sensitivity

The outcome of the GWP SA in Appendix K.2 is similar to the cost SA, as the same solutions are obtained, with no difference over the total costs. In this case, however, the variation in fitness value is substantially higher with an increasing GWP for carbon fibres, compared to the remaining GWP parameters. A 10 % variation in the GWP of carbon fibres amounts to approximately a 5.89 % variation in the fitness value.

In terms of constituent materials, the carbon fibres consistently adversely affect the fitness value. At the initiation of the SA, the glass- and carbon fibre masses were 5719 kg and 5264 kg, respectively,

Table 7.2: Sensitivity matrix – Carbon Cost

	Unit	Current value	d_1	d_2	d_3	d_4	d_5	d_6
Original value			30[a]					
Perturbation			1%	5%	10%	−1%	−5%	−10%
Perturbation	€/kg		0.3	1.5	3	−0.3	−1.5	−3
Fitness†	-	7.5642×10^{-1}	7.5698×10^{-1}	7.5940×10^{-1}	7.6242×10^{-1}	7.5578×10^{-1}	7.5336×10^{-1}	7.5034×10^{-1}
Fitness‡	-		7.5698×10^{-1}	7.5940×10^{-1}	7.6242×10^{-1}	7.5577×10^{-1}	7.5336×10^{-1}	7.5034×10^{-1}
Sensitivity	%		7.4004×10^{-2}	3.9335×10^{-1}	7.9269×10^{-1}	-8.5847×10^{-2}	-4.0531×10^{-1}	-8.0465×10^{-1}
Cost†	€	3.7739×10^{5}	3.7893×10^{5}	3.8518×10^{5}	3.9299×10^{5}	3.7581×10^{5}	3.6956×10^{5}	3.6175×10^{5}
Cost‡	€		3.7893×10^{5}	3.8518×10^{5}	3.9299×10^{5}	3.7581×10^{5}	3.6956×10^{5}	3.6175×10^{5}
Sensitivity	%		4.0750×10^{-1}	2.0632×10^{0}	4.1329×10^{0}	-4.2053×10^{-1}	-2.0763×10^{0}	-4.1461×10^{0}
Footprint†	$kgCO_2e$	3.4940×10^{5}	3.4938×10^{5}	3.4938×10^{5}	3.4938×10^{5}	3.4938×10^{5}	3.4938×10^{5}	3.4938×10^{5}
Footprint‡	$kgCO_2e$		3.4938×10^{5}	3.4938×10^{5}	3.4938×10^{5}	3.4938×10^{5}	3.4938×10^{5}	3.4938×10^{5}
Sensitivity	%		-5.7219×10^{-3}	-5.8364×10^{-3}	-5.8364×10^{-3}	-5.8364×10^{-3}	-5.8364×10^{-3}	-5.8364×10^{-3}
Deflection†	mm	7.0234×10^{1}	7.0278×10^{1}	7.0279×10^{1}	7.0279×10^{1}	7.0279×10^{1}	7.0279×10^{1}	7.0279×10^{1}
Deflection‡	mm		7.0278×10^{1}	7.0284×10^{1}	7.0284×10^{1}	7.0284×10^{1}	7.0284×10^{1}	7.0284×10^{1}
Sensitivity	%		6.1970×10^{-2}	7.0734×10^{-2}	7.0734×10^{-2}	7.0734×10^{-2}	7.0734×10^{-2}	7.0734×10^{-2}
Frequency†	Hz	4.0821×10^{0}	4.0779×10^{0}	4.0783×10^{0}	4.0783×10^{0}	4.0783×10^{0}	4.0783×10^{0}	4.0783×10^{0}
Frequency‡	Hz		4.0779×10^{0}	4.0774×10^{0}	4.0774×10^{0}	4.0774×10^{0}	4.0774×10^{0}	4.0774×10^{0}
Sensitivity	%		-1.0299×10^{-1}	-1.1556×10^{-1}	-1.1556×10^{-1}	-1.1556×10^{-1}	-1.1556×10^{-1}	-1.1556×10^{-1}
Buckling factor†	-	1.1237×10^{1}	1.1157×10^{1}	1.1156×10^{1}	1.1156×10^{1}	1.1156×10^{1}	1.1156×10^{1}	1.1156×10^{1}
Buckling factor‡	-		1.1157×10^{1}	1.1162×10^{1}	1.1162×10^{1}	1.1162×10^{1}	1.1162×10^{1}	1.1162×10^{1}
Sensitivity	%		-7.1238×10^{-1}	-6.7331×10^{-1}	-6.7331×10^{-1}	-6.7331×10^{-1}	-6.7331×10^{-1}	-6.7331×10^{-1}

[a] [€/kg], †immediate value, ‡value after new intensification phase.

meaning quite similar amounts. Thus, it is not surprising that percentage-wise increments of the carbon fibre-related parameters are decisive, especially since the carbon fibre cost and GWP are notably greater than the remaining constituents.

The GWP and cost SAs revealed that changes to the global warming potential influence the solution the most, irrespective of whether the parameters are decreased or increased. Though this result is a consequence of the initially high GWP of carbon fibres, it suggests that the solution, fortunately, is not subject to market conditions (changes to material costs). However, the SAs are based on an intensification- rather than a diversification approach. Would that be the case (while also having greater confidence in obtaining a global optimal solution for each run), one could more confidently conclude that the solution is less subject to market conditions. In that case, the overall costs and carbon footprints could vary, but the structural configuration should remain the same.

Not only is the solution highly subject to variations in the carbon fibre GWP, the value itself is reportedly unstable. For instance, the two available values from the EuCIA calculator are 38.95 $kgCO_2e/kg$ and 48.99 $kgCO_2e/kg$ (the latter – and newest – of which is adopted in this work), suggesting that the parameter can fluctuate by 25 % [94]. Since its adoption in this work, no change has been reported to the GWP of carbon fibres.

Chapter 7.3. Pareto front

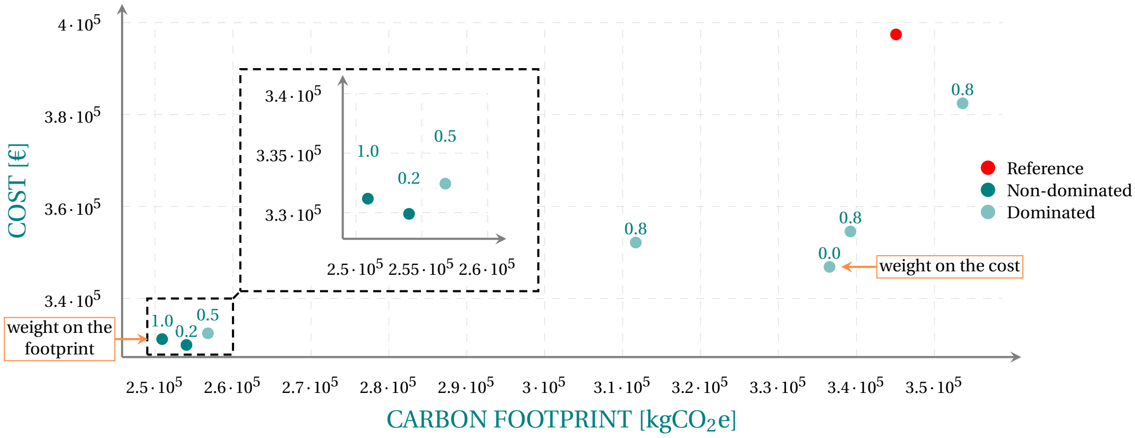

Figure 7.3: Pareto-front, showing the relation between the objectives as the weights w_1 and w_2 varies. The tag above each marker indicates the value of w_1. The solutions from Table 7.1 with $w_1 = 0.8$ are included. The objective values corresponding to the reference solutions are indicated in red.

Some characteristic points of the Pareto front are sought after by varying the weights of the objectives to gain better insight into the multi-objective optimisation problem. Reiterating that $w_1 + w_2 \equiv 1.0$, the extremes can be obtained for $w_1 = 1.0$ and $w_1 = 0.0$, illustrating the cases when all the weight is on the carbon footprint and the cost, respectively. Furthermore, intermediate points are obtained, helping to visualise the relationship between the values of the objectives depending on their respective weights. Note that when $w_1 = 1.0$ ($w_2 = 0$) and $w_2 = 1.0$ ($w_1 = 0$), the objectives are not normalised.

As is apparent from the plot of the Pareto-front (Fig. 7.3), there is unfortunately little correlation between the weights and the obtained solutions. As indicated in Fig. 4.7, one would expect a correlation between the weights and the solution such that an increasing value of w_1 amounts to a decreasing carbon footprint. While several points follow this trend, the wide scatter indicates that the points pertaining to $w_1 = 0.0$, $w_1 = 0.5$ and $w_1 = 0.8$ are dominated solutions, meaning that these solutions represent points where the solver got trapped in local optimum. The solution related to $w_1 = 0.5$ is a good solution in comparison to the remaining dominated points.

The only points that seem to follow the expected trend are those conforming to $w_1 = 1.0$ and $w_1 = 0.2$, representing the best solutions concerning the carbon footprint and the cost, respectively. If the objectives were strictly conflicting, and the remainder of the solutions did not get trapped in local optimum points, these would likely have been located along an exponential-like curve going through the points for $w_1 = 0.2$ and $w_1 = 1.0$. Even though the objectives are somewhat dependent on each other (not strictly conflicting due to dependence on the constituent masses), it is reasonable to expect such a trend. Then, all the points would fit inside the zoomed-in region of the plot.

Concluding whether a solution is a global optimum (or non-dominated when speaking of the Pareto-front) is not something one can do with the utmost confidence. To confidently know whether this is the case, one would have to go through all the combinations using a brute-force approach, which for the current problem definition would require $1.73 \cdot 10^{66}$ years of constant computing to evaluate all combinations, with an average of 30 seconds per iteration. This is obviously not a plausible approach. Therefore, the conclusion that certain points are non-dominated is drawn based on the expected exponential-like trend of the Pareto-front.

Chapter 7.4. Comparison of the solutions

The design points in the presented Pareto-front (Fig. 7.3) and *solution 2* in Table 7.1 are further investigated herein. Specifically, the structural responses are presented for all the solutions. Then the non-dominated solutions are more thoroughly investigated. A collection of all the results are provided in Appendix M.

Structural responses

Figure 7.4 outlines the structural responses, constituent masses and corresponding objective values, indicating that all the obtained solutions outperform the analytical solution – except for the $w_1 = 0.0$ configuration. For the analysed load case and design requirements, adequate stiffness can be obtained through the predominant use of GFRP, which is generally advantageous to achieving a more environmentally friendly structure. The combination of deflection- and material architecture-related constraints seem to play the biggest role in the solutions, as the deflection constraint is (close to) active for all solutions. This, in combination with a minimum laminate thickness – indirectly required from the constraint Eq. (6.11a) – ensure a natural frequency and buckling resistance exceeding the respective constraints.

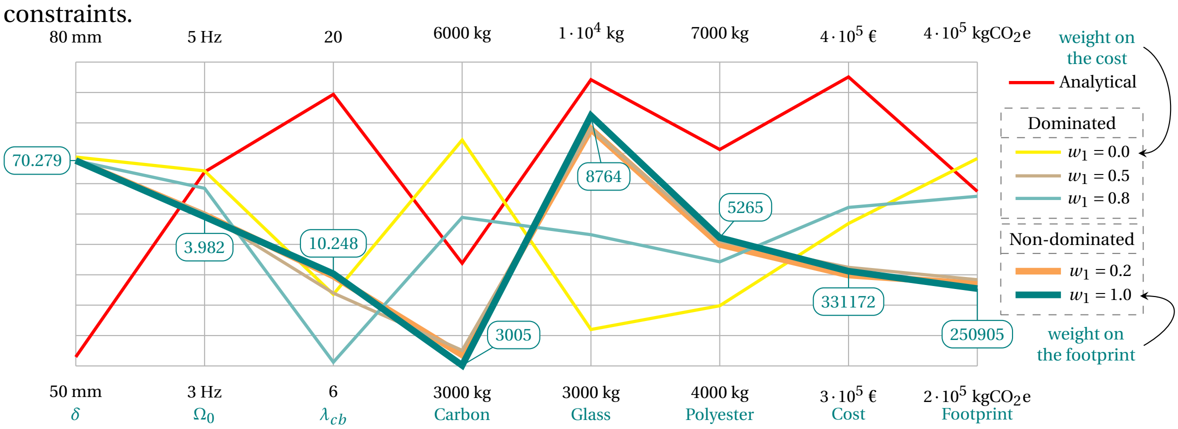

Figure 7.4: Structural responses, masses of the constituents, and the corresponding objective values for the various solutions. The indicated values correspond to the non-dominated solution with $w_1 = 1.0$ (and $w_2 = 0.0$).

However, for the configuration $w_1 = 0.0$, the deflection marginally exceeds the corresponding constraint $\delta_{max} = 72.29$ mm. This was a consequence of not normalising the objectives, meaning that the adopted penalty factor of $r_p = 1000$ did not suffice in restricting the solution space. The penalty factors commonly are incrementally increased (usually by a factor of 10 – or even 1000 – depending on the problem) with the previously obtained solution as the initial point to slowly arrive at good solutions [45]. However, such investigations are too time-consuming for the problem at hand. With less restrictions provided by r_p, the fitness landscape is effectively larger, resulting in a significantly longer run-time before a stopping criterion is met – at which point the solution suffers from large constraint violations. Nonetheless, with a deflection of 70.62 mm, small adjustments to the design are necessary to satisfy the constraints. After all, the framework is intended as a preliminary design tool. Without altering the penalty factor r_p, the $w_1 = 1.0$ configuration successfully arrives at a feasible solution – though at a run-time which significantly exceeds that of the other configurations. The convergence plots in Appendix L illustrates this discussion.

Geometry and sandwich panel configurations

Arguably, the two most influential parts of the bridge are the deck and the bottom panel, collectively acting as a stress couple to provide most of the stiffness. Necessarily, to obtain proper stiffness, the bottom panel should thus either be wide and thin or narrow and thick. The best solution is an example of the latter, with the bottom panel specification shown in Fig. 7.5. The remaining panel configuration for the $J = 4$ panel divisions (Fig. 6.17) are summarised in Appendix M, Fig. M.1. Because all the panels have the same core thickness (20 mm), only the face sheet configurations above their respective centerline are given.

The non-dominated solutions presents laminates with equal face sheets everywhere but for the bottom panels, which is related to the corresponding geometries. This agrees with the expected specifications, as the (close to) vertical panels have the ±45° layers close to the surface, followed by $90_2°$, translating to panels with a high shear- and transverse (vertical) stiffness. The $w_1 = 1.0$ configuration, for instance, has the stiffer plies further away from the centre, presenting a panel with a slightly greater bending stiffness than the $w_1 = 0.2$ configuration.

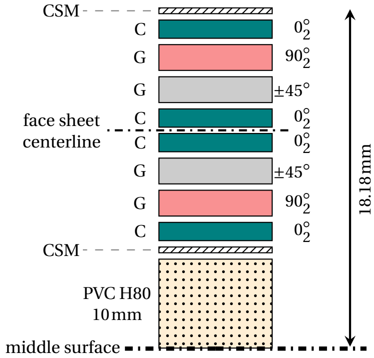

Figure 7.5: The material architecture for the bottom panels resulting from the optimisation with $w_1 = 1.0$ and $w_2 = 0$. The total panel thickness is 36.37 mm. G and C refer to GFRP and CFRP plies, respectively, in accordance with Fig. 6.11.

Figure 7.6: The face sheet specifications for the $J = 4$ panel configurations.

Weight	Transverse stiffeners	Longitudinal stiffeners	Side panels	Bottom panels
$w_1 = 0.2$	G ±45° G 90°_2 G 0°_2	G ±45° G 90°_2 G 0°_2	G ±45° G 90°_2 G 0°_2	G ±45° G 90°_2 C 0°_2 C 0°_2
$w_1 = 1.0$	G ±45° G 90°_2 G 0°_2	G ±45° G 90°_2 G 0°_2	G ±45° G 90°_2 G 0°_2	C 0°_2 G 90°_2 G ±45° C 0°_2

With the rather lenient structural requirements, numerous combinations of shapes and sizings (material architecture) can satisfy the imposed requirements. As the requirements become more stringent, the feasible solution space will be reduced accordingly. The geometrical variables (Fig. 7.7) and the corresponding cross-sections at $X = 0$ and $X = L$ (Fig. 7.8) illustrate a wide range of possible shapes.

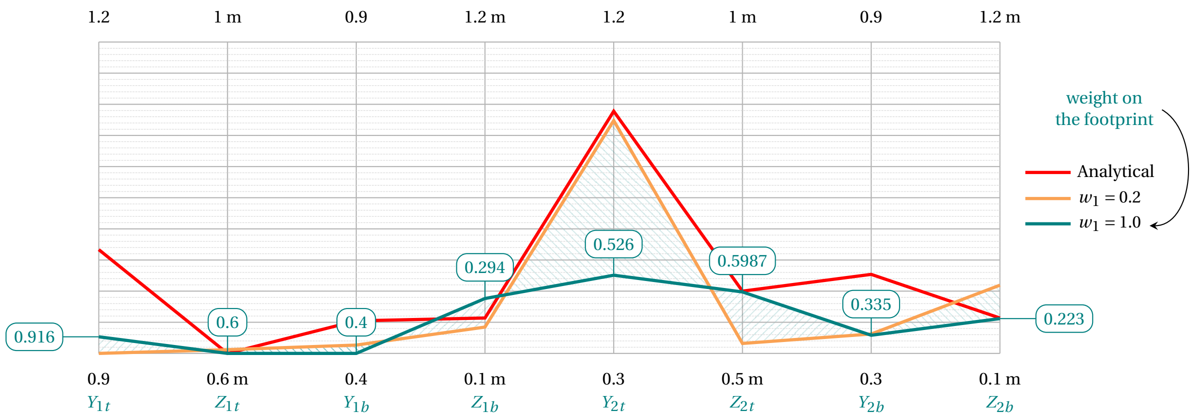

Figure 7.7: Geometrical variable values for the analytical and (near) optimal solutions ($w_1 = 1.0$ and $w_1 = 0.2$).

Focused on the non-dominated solutions it is likely that the remainder of the solutions would comprise laminates equal to those of either the $w_1 = 1.0$ or $w_1 = 0.2$ configurations, with cross sections intermediate of the two solutions. The shaded regions in Fig. 7.8 represent a range of cross sections which likely would be the outcome of the remainder the solutions, were they not trapped in local optima.

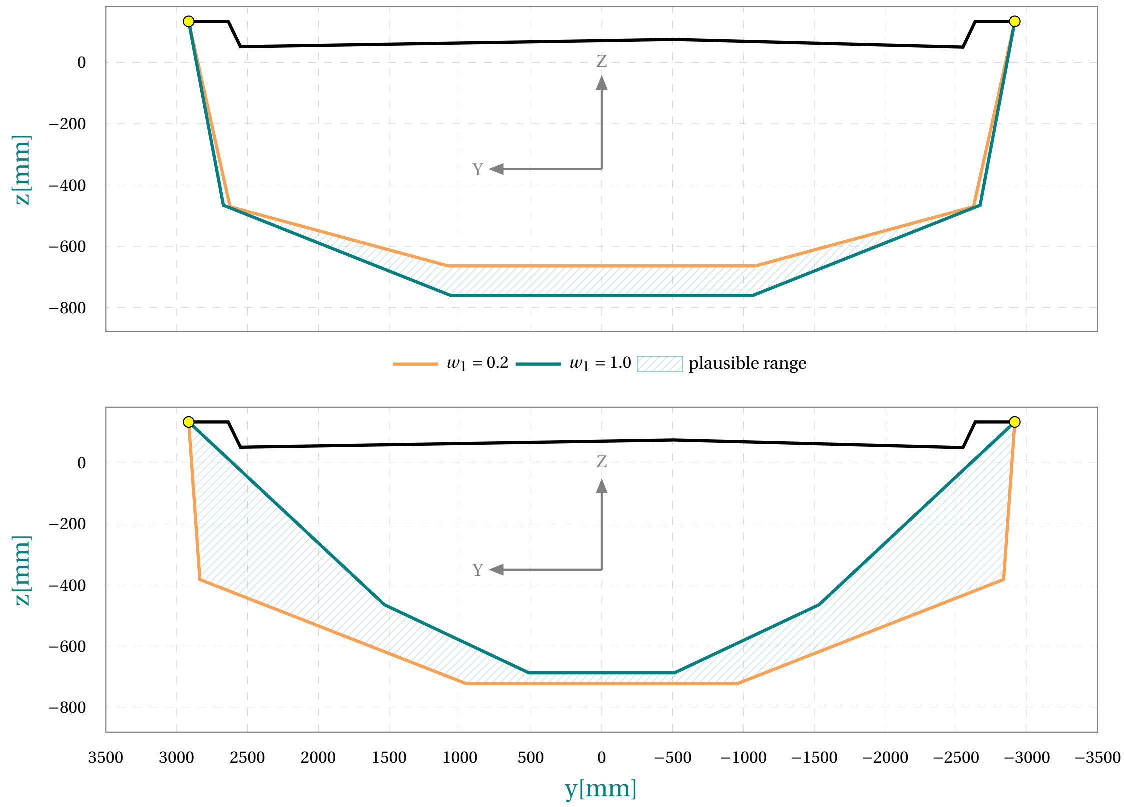

Figure 7.8: Cross-sections for the solutions at (**top**) $X = 0$ and (**bottom**) $X = L$ before the geometry is cut a 10° angle. The shaded areas suggest plausible configurations for the remainder of the solutions.

Chapter 7.5. Comparison with the reference model

In order to quantify the efficiency of the framework, the obtained solutions are compared to the objective values pertaining to the reference model (disregarding constraint violations) and the analytically obtained solution. The objective values corresponding to the reference model are obtained by modelling the structure in Karamba and calculating the values through the Grasshopper script (Appendix H).

Before comparisons can be made, the deformations are compared as shown in Fig. 7.9. The discrepancy of 5 mm is acceptable since the reference model has a slightly stiffer deck, different boundary conditions, and further improved stiffness through layered material properties that somewhat increases the lever arm for the stiffest plies. Furthermore, the adopted geometrical layout is read from technical drawings, which may amount to different heights of certain components. Appendix I indicates the panel distributions and respective material architectures.

Regarding the reference model, it might be overly optimistic to conclude that the structure scores much better with respect to the objectives, as its design is based on different requirements – most of which are strength-related. This concerns local reinforcement due to connections and thermal load cases, not to mention analyses of the bridge in its lifted position. As discussed earlier, however, the deck configuration remains the same.

Relative difference

The non-dominated solutions (Fig. 7.3) are compared to the analytical- and reference solutions in Fig. 7.10. Evidently, the $w_1 = 1.0$-configuration present a design with a 27.3 % lower carbon footprint than the reference solution. Similarly, the $w_1 = 0.2$-configuration has a cost which is 17 % lower than that of the reference solution.

Disregarding the infeasible solution, the "worst" solution (the top right point in the Pareto-plot, Fig. 7.3) presents a relative reduction of the cost of 3.8 %, however at a carbon footprint which is 2.5 % worse. This is a consequence of the randomly chosen initial points shown in Table 7.1.

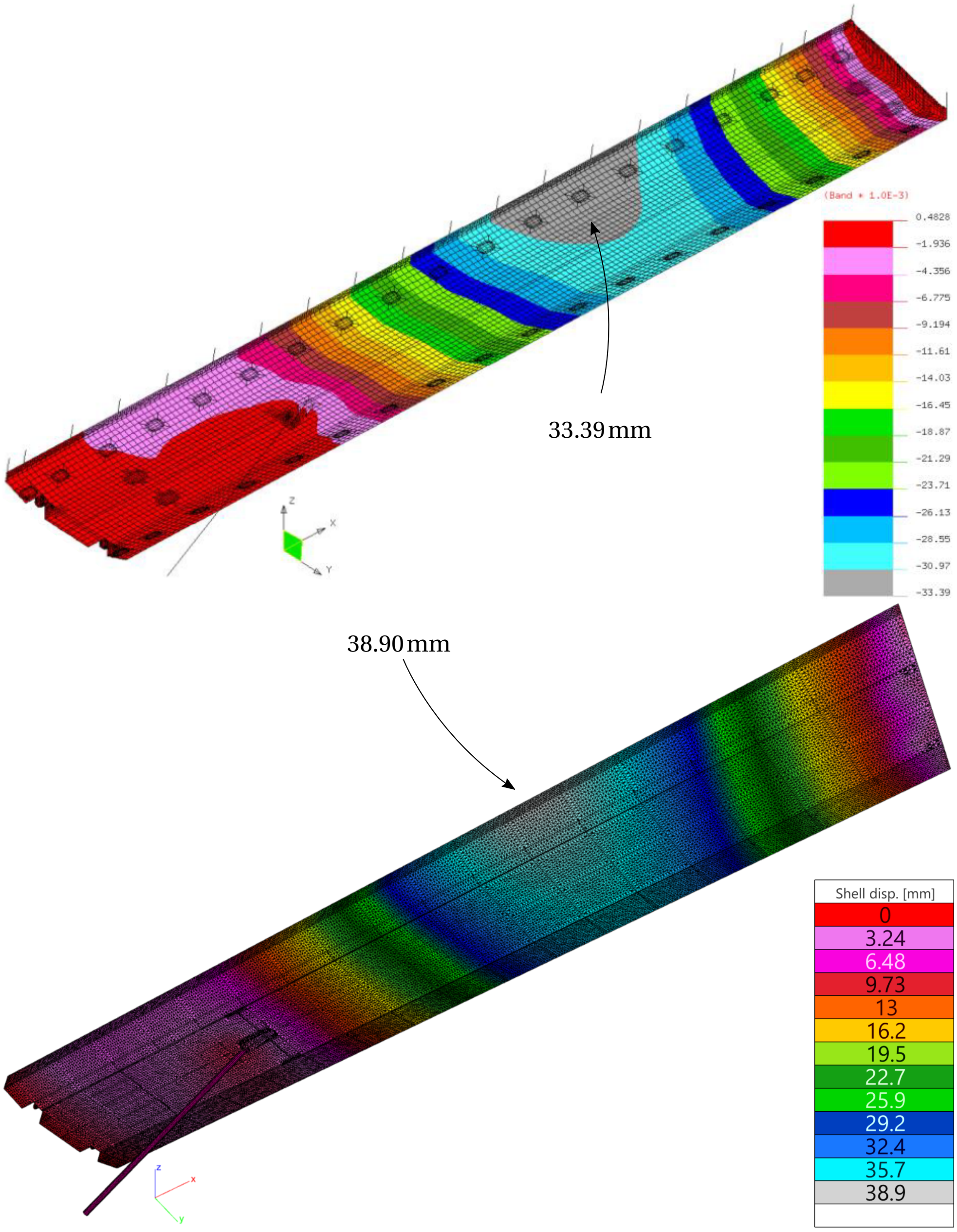

Figure 7.9: Comparison of vertical deflections between the reference model (**top**) and the same shape and material configuration adopted in Karamba (**bottom**), subjected to 5 kN/m^2 uniformly distributed across the deck.

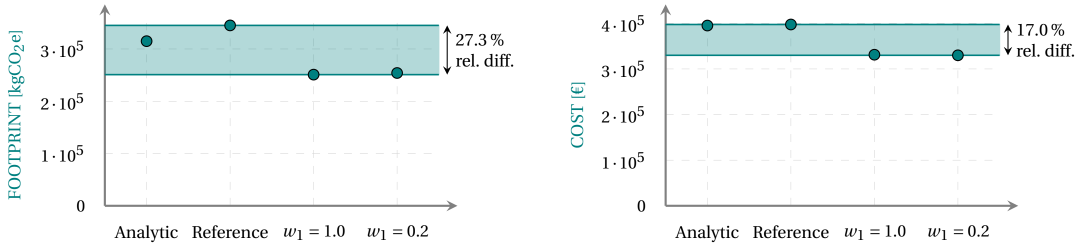

Figure 7.10: The carbon footprint (**left**) and cost (**right**) pertaining to the analytical-, reference- and non-dominated solutions.

Chapter 7.6. Post-optimality and production

The use of the Karamba plug-in limits the laminate definition to using the middle surface of the elements. In reality, however, especially when manufacturing using VARTM, the first layer in the stack defines the A-surface, meaning the external surface that would usually face outward due to its smooth finish. Structurally, this does not necessarily amount to erroneous behaviour if the actual middle surface aligns with the one assumed in the numerical model. Nonetheless, the calculated constituent masses are slightly off with the implemented middle-to-middle surface approach. Realistically, each edge of the internal stiffeners should be offset inwards to account for the half-thickness of the external shell – to ensure that the parts fit together. On the other hand, seeing that the deck and exterior structure likely would be formed through two separate moulds, the stiffeners would have to be glued and laminated to the B-surface of the exterior after curing. Accounting for the material necessary to ensure proper cooperation between the components, the overall calculated material consumption is likely off by a negligible amount.

Different moulds were not considered in the framework, which is usually considered one of the highest non-recurring costs [13]. The investigated geometry does not have symmetric load conditions or initial geometry, which invites asymmetrical geometry. Following the assumption that the deck and bottom shell (exterior) are cast separately and that the longitudinal stiffeners are continuous, several moulds are required for the transverse stiffeners. Regardless of the production method, the transverse stiffeners alone would require $2(16 \times 2) = 64$ core pieces, as suggested by the various geometries in Fig. 7.11. Casting these on glass tables using VARTM allows for the creation of flat sandwich panels with smooth surfaces, which must be glued and laminated (by hand lay-up) to the exterior shell and longitudinal stiffeners.

Chapter 7.7. Verification and validation

Much like one would have to verify whether one's order of pancakes smells, feels and looks as expected, the tool verification concerns whether the imposed specifications and assumptions (such as design constraints and calculations) are satisfactory. A part of this verification includes controlling the calculations and confirming whether the structural behaviour correctly captures the material layup. Then, after verifying the (FE) model, its accuracy in representing the real model is validated. Finally, the structure's strength is checked against well-known strength criteria, indicating whether the structure fares well concerning first-ply failure (FPF) and core failure.

7.7.1. Verification

In order to have a satisfactory tool, the parametric model must behave according to the specifications and assumptions. This was a rather tedious procedure, considering the numerous combinations ($S_{\text{geo}} = 1.97 \cdot 10^{26}$), making it impossible to go through all combinations of geometrical variables. After several runs and alterations, the parametric model was considered verified when the resulting structure no longer caused errors in evaluating the objective function (which could fail, for instance, if the steel frame and the surrounding FRP panels were not connected). When comparing the structural response with the reference model (see Chapter 7.5) and analytical calculations (see Appendix J), deflection discrepancies of 5.5 and 23.3 mm, respectively, were found. Both deviations are deemed acceptable, with the latter owing to several simplifications implemented in the hand calculations.

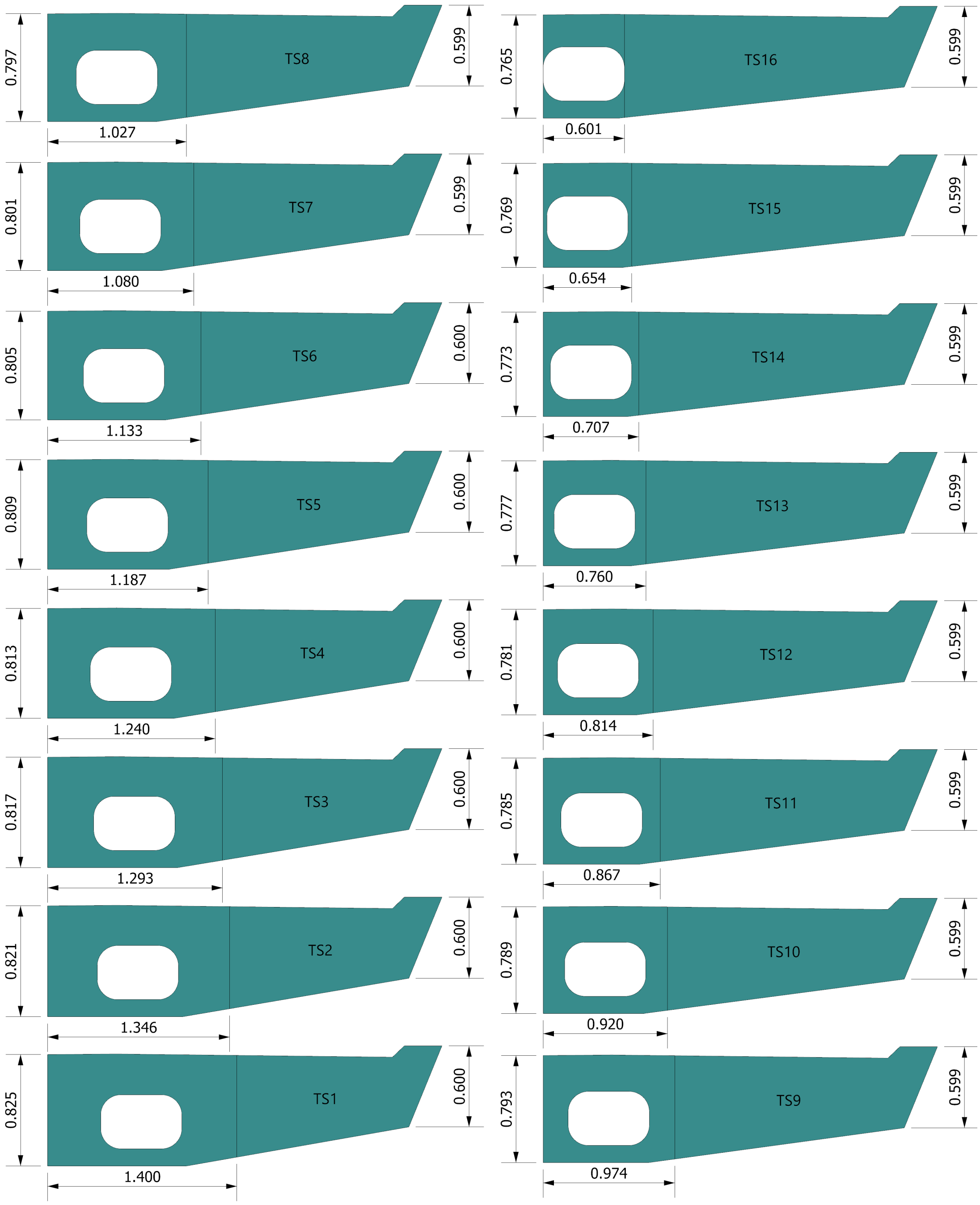

Figure 7.11: The 16 internal transverse stiffeners pertaining to the $w_1 = 1.0$ configuration. Left: TS1–TS8, right: TS9–TS16. Units in meters, scale: 1 : 50.

7.7.2. Validation

The limitations of Karamba invite validation procedures through FE software adopting layered material properties. To this end, *solution 2* indicated in Table 7.1 is used as input in Ansys®, ensuring the structural integrity and responses match.

Comparison and control of structural responses

The structural responses obtained with Karamba are compared with the outcome of a similar analysis conducted in Ansys®. This check can be relatively easily performed since the geometry generated through Grasshopper can be saved as a `.stp` file. Then, with Ansys Spaceclaim®, minor geometrical alterations are introduced; before generating the mesh, applying laminate specifications, and defining proper boundary conditions. The FE model and boundary conditions in Ansys® are covered in Appendix N.1, followed by a comparison of responses in Appendix N.2. The responses are close to identical, validating that the homogenised properties correctly capture the laminate behaviour. However, Ansys® reports a lower buckling resistance than the analytical and numerical solutions initially suggest. The difference is due to stress concentrations in the connection between the longitudinal stiffener and the steel frame.

Framework validation

Next to validating the structural responses, the results prove that the framework operates according to its intention. Even with a randomised initial point, improved design are obtained. Considering the size of the solution space, such a feat is not a guarantee. Nonetheless, the results suggest that the adopted settings and configurations are reasonable (see Chapter 6.4.1). However, as will be discussed in the last chapter, there are several adjustments one could implement in order to improve the confidence in framework, in turn increasing the probability of finding a (better) solution.

7.7.3. Control of strength

Following the structural response evaluation, the structure's resistance against first-ply failure (Tsai-Wu) and core failure is presented in Appendix N.3. As the FPF plot (Fig. 7.12) indicates, the areas of high utilisation are quite local. Moreover, FPF is dominated by matrix damage, which one generally can allow if the affected area is small, as the stresses can redistribute to the surrounding fibres. This assumption should, however, be aligned with the load's expected occurrence and return period. Typically, the indicated locations are prone to local reinforcements, which would have been a topic in later design stages of the composite flap. Regardless, the control suggests that the stiffness-driven design and optimisation tool arrives at solutions that fare well with regard to strength requirements.

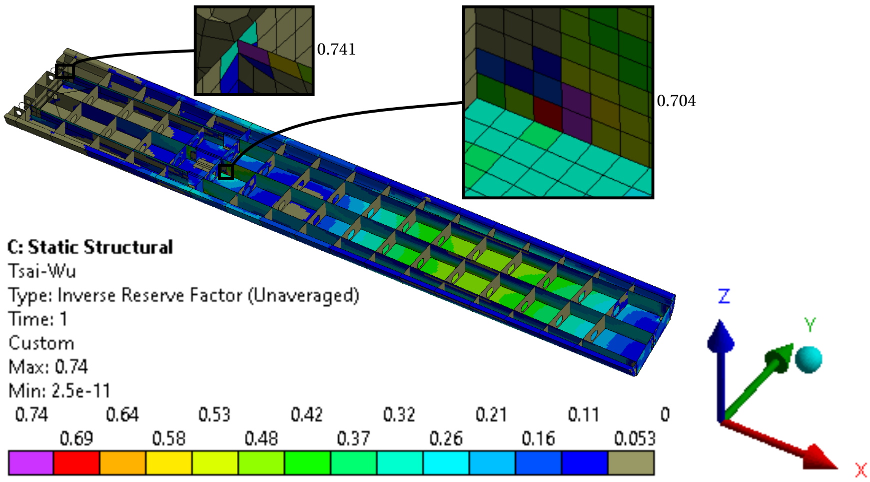

Figure 7.12: Verification of FPF through the Tsai-Wu criterion. Greatest utilisation of 0.741.

Chapter 7.8. Conclusion

This chapter answers the following questions:

1. What is the confidence in the solution?
2. Are the solutions sensitive to changes in the input parameters?
3. Is the framework worthwhile the required effort of setting it up?

In hand with the limitations of the genetic algorithms, the presented solutions suggest that no single global optimum has been found. While this impairs the confidence in the result(s), substantial cost- and carbon footprint reductions of 17 % and 27.3 %, respectively, were found. Albeit these improvements are based on slightly different design criteria from the reference model and fewer load cases, it presents a design which performs adequately concerning the strength requirements for the load case investigated in Ansys®.

The sensitivity analysis (SA) proved that the solution is relatively insensitive to perturbations of the unit costs, suggesting that the solution is not subject to market conditions. However, the solution is highly subject to global warming potential (GWP) variations, with a sensitivity of 5.9 % to a 10 % difference in the GWP of carbon fibre. Since the solutions after the intensification phase converged to the same solution, it can be concluded that solution 1 was sub-optimal, meaning it was merely a near-optimal local optimum.

The downside of parametric models is the required initial effort to create them, often used as an argument against their implementation. However, minor configurations are necessary to prepare it for another project once such a model is created. Perhaps, more importantly, is the optimisation procedure itself. As the results proved, the run-time varies between one to slightly more than three weeks, which in certain cases exceeds the time at hand – for instance, in the early stages of concept phases or preliminary designs, where estimates are of greater interest than accurate descriptions. Even considering the solution with the fastest time until convergence (typically the dominated solutions), significant improvement was found. However, it is far from a global optimum, which is considered to be in the vicinity of the left-most points in the Pareto-front (Fig. 7.3). Note, however, that one cannot with certainty say how far a solution is from a global optimum without knowing the exact point. The complexity of the problem can be reduced by adopting geometrical variables with a discontinuous range of definitions to reduce the required effort significantly.

In the following chapter, the key findings are presented along with discussions and reflections concerning the research's main topic, before concluding with recommendations and proposed future work/investigations.

DISCUSSIONS

This thesis aimed to investigate the feasibility of adopting FRP in the main load-carrying system of bridges and create a framework for the preliminary design of these employing monocoque structures. The following research question was laid out:

> "What is the potential cost- and carbon footprint reduction in monocoque FRP bridges when a numerical optimisation approach is adopted, and what is required for its implementation?"

To answer this question, a literature review was carried out to present and describe the basic elements of FRP, defining appropriate mechanical properties for the material. The final chapter of the literature review concerns structural optimisation and form-finding, presenting recent advancements in the field and pinpointing their deficiency.

Chapter 5 presents the optimisation tool, adopting theory from the preceding chapter, aiming to arrive at an approach filling some of the gaps in the numerical optimisation of FRP structures.

The developed tool employs the CAGD software Rhino®and its parametric interface, Grasshopper®. After defining a parametric definition for the geometry and the anisotropic material properties of the panels that make up the composite bridge, the structure is analysed through the FEM plug-in Karamba. Then, the genetic algorithm plug-in Galapagos iterates through a vast number of designs, evaluating constraint violations until it meets a stopping criterion. Next, further improvement is searched for through an intensification phase (local optimisation). As such, the proposed framework can be used to concurrently optimise composite bridges' shape and material architecture while minimising their cost and environmental burden, presenting a multi-objective optimisation approach for the preliminary design of said structures.

The framework is intended for designing internally stiffened monocoque structures and is an extension of approaches in the literature in that it employs sandwich panels and can adopt hybrid face sheets (GFRP or CFRP). Accordingly, it overcomes FRP's poor stiffness and stability and assists in obtaining lightweight and buckling-resistant solutions that are aesthetically elegant and require less maintenance than conventional structural concepts. To showcase the potential of the optimisation framework, the yet-to-be-built single-leaf bascule Klosterøy bridge in Skien, Norway, was investigated, validating the tool with a real case. General lessons from the modelling procedure and reflections on parametric design and form-finding can be drawn from this investigation, discussed in the following.

1. Key findings

The conducted case study found that the carbon footprint and cost could be significantly reduced from the original values. Correspondingly, the mass is decreased because these factors are functions of the constituent masses (fibres, resin and foam cores). It was investigated whether one of the first outcomes (designs) satisfied the strength requirements, the outcome of which suggests the stiffness-driven design often withstands the occurring stresses. The following represents the key findings of the study.

Cost- and carbon footprint reduction

- With reference to the composite bridge designed by FiReCo, the carbon footprint is reduced by 27.4% when all weight is on the first objective ($w_1 = 1.0$). Similarly, when $w_1 = 0.2$ (and $w_2 = 0.8$), the cost is reduced by 17%.

Solution sensitivity

- The solution is practically insensitive to market conditions. The sensitivity analyses on the input parameters revealed that a 5% increase in the unit cost of carbon fibre amounts to a 4% increase in the total cost.

Implementation requirements

- It took approximately two months to make the parametric model that can be used to design a simple bridge. A new, simple bridge design can be prepared for optimisation in anything between two hours and a week. Then, without further adjustments to the algorithm and the mathematical formulation, the optimisation study would take approximately a week. A more complex design would use the same general setup. New design details (such as further divisions of the bottom panels) can be developed and implemented within two days.

Reflections and recommendations concerning these findings are presented in the succeeding sections.

2. Reflections

Following the literature review, the optimisation framework is defined for concurrent geometry and material architecture optimisation. Chapter 5 introduces the framework itself with its optimisation objectives, followed by Chapter 6 exemplifying appropriate definitions of parameters (read: geometrical variables) and design constraints, before Chapter 7 presents the results of this study.

2.1. On the significance of the findings and its impact on existing knowledge

The research findings presented in this study carry great potential in enhancing the design of composite structures, as the tool may serve as valuable to researchers and practitioners. Ideally, the presented approach can be implemented in preliminary design stages to widen the explorative phase, arriving at cost-efficient bridges with low carbon footprints. Importantly, by implementing FE plug-ins, accurate geometry evaluations are considered rather than analytical estimates and simplifications. Moreover, the adopted optimisation constraints and admissible sandwich panel configurations overcome some of the major challenges faced by the composite design community, namely relatively poor stiffness and stability. As such, the framework extends beyond approaches concerned with isotropic materials while allowing optimising free-form structures utilising the in-plane strength and stiffness of FRP laminates. Ultimately, the findings suggest that the framework serves as an essential step in convincing sceptical stakeholders concerned with the costs and otherwise not-so-well-documented features of FRP.

2.2. On the limitations of the framework

Most of the framework limitations are consequences of simplifications implemented to reduce the computational effort and the adopted modelling tools available within Grasshopper and Rhino. Importantly, the FE model is limited to tetrahedral elements, notoriously known to appear stiffer due to increased occurrences and probabilities of shear-locking. However, the verification through a second FE software – Ansys®– proved that the structural response suggested by Karamba is less stiff than when modelling with quadrilateral quadratic elements. Even with smaller elements and a significantly greater number of nodes, the global stiffness appears greater. Moreover, shell elements are generally recommended when modelling thin panels, as the assumptions of plane stress can become erroneous, and the through-thickness shear deformation may be severe. Nonetheless, the brief investigation discussed in Chapter 5.4.1 suggests that the behaviour of the panels is correctly captured for the thicknesses in question (all solutions suggest core thicknesses of 20 mm).

The required run-time is possibly the framework's greatest shortcoming, causing structural designers to refrain from adopting it in real cases concerned with time-constraints. However, by using more powerful computers, this issue can be circumvented. The adopted encoding permits a multitude of different genomes (in terms of the material architecture – layup) that essentially are the same. This is a consequence of the ply thickness scaling (taken as present vs absent plies). Limiting the ply thickness scaling to the outermost plies, perhaps reducing the admissible number of plies, would be an efficient improvement. Further reflections and improvements in this regard are discussed in the section concerning future work.

The normalisation of the pseudo-objective function depends on the initial configuration. As such, it prevents comparing of solutions solely based on their fitness value, perhaps making these comparisons less intuitive. Consequently, the two objective values must be considered rather than one singular value. Beyond the complications it causes for the post-processing, it requires adjustments when setting up the optimisation procedure if any parameters (read: optimisation variables) are changed. Forgetting to do so may lead to faulty fitness function values and poor solution quality.

Nonetheless, the desire to implement a parametric model for the structural optimisation of a composite structure should be a decision where the required time to configure the model and run analyses should be carefully weighed against the typically iterative design process. Especially interesting are cases where the shape and the laminate specifications are concurrently optimised, where the potential gain of such an approach is significant. In cases where the structural shape is predefined due to design constraints or use, the solution space can be substantially reduced, making the optimisation only concerned with the materials and, consequently, more effective. In either case, such approaches enable an automatic generation and evaluation of a magnitude of possible solutions – which perhaps would never have been even considered – dependent on the parametric definition.

2.3. On the validation with a real case

The Klosterøy bridge is an innovative project that calls for a lightweight solution, making it an ideal candidate for utilizing composite materials. While steel bascule bridges already exist, their heavy weight necessitates large-scale drive trains, making alternative solutions more desirable. In this regard, a monocoque composite sandwich flap is a more suitable choice, especially considering the challenges faced by current counterparts. For example, steel solutions may incorporate an orthotropic steel deck (OSD), which has been found to be prone to significant fatigue complications [103]. Additionally, the combined use of a bituminous pavement and steel can introduce thermal forces that may pose problems and increase service costs.

On the parametric modelling of the Klosterøy bridge

Before defining an optimisation problem for the Klosterøy bridge, a tedious effort was put into generating a representative parametric model. For a generic bridge-like structure, this is a relatively straightforward process. However, several components and sections have specific locations and positions for this design, making generating the parametric model time-consuming (see Appendix I). When the relevant parts had been included, the next step was to achieve similar structural responses as FiReCo reported, gaining confidence in the modelling. However, since the parametric model was generated based on technical drawings, the structural responses – deflections in particular – were off by more than 40 mm, indicating that the geometry or laminate definitions were improperly defined. The latter uncertainty was diminished through an optimisation procedure to obtain proper ply thicknesses (Appendix E). Even after this stage, some discrepancies were present, at which point it was deemed necessary to start the optimisation procedure.

The early stages of these optimisations revealed that certain combinations of the parameters resulted in a loss of structural integrity, i.e. situations where the components were no longer working in synergy. Though quick initial checks rule out these issues, the $2.00 \cdot 10^{26}$ possible combinations of the geometrical variables precluded this option. With the adopted Grasshopper definition, loss of structural integrity means that the fitness value of the current genome cannot be calculated (due to null values). These erroneous configurations could be corrected by programming the solver to treat null values as zero – i.e. the best possible fitness – and paying attention to the solution process. Had the author realised this earlier, a substantial amount of time would have been spared.

The investigated load cases and configuration of the bridge, namely a UDL on the bridge deck in its closed position under SLS paired with linear bifurcation and modal analyses, are rather primitive. Among interesting possible inclusions, one could imagine considering the lifting mechanism's capacity vs. the composite's weight. Dynamic effects on the structure due to wind loads would also be an interesting inclusion. Generally, lower cross-sections are more aerodynamic and less affected by wind. This may have a great impact on the support in an elevated position, not to mention the composite connected to it.

On the outcome

Although the run-time in some instances far exceeds what one has available, the results prove that considerable cost- and emission savings can be found.

The material definition and the adhering constraints require that the face sheets, by default, must be relatively thick (5.2 mm and 7.2 mm for CFRP and GFRP, respectively). Allowing for thinner face sheets essentially allows for less material consumption, in turn requiring that the structure must obtain its stiffness through the shape. This could further lower the cost and environmental impact. On the other hand, the deflections adhering to the different solutions were found to be extremely close to the respective constraint, meaning that the stiffness is quite optimal (in the sense that small changes to either variable would result in constraint violations).

The run-time combined with the time constraints concerning this thesis work prevented obtaining confidence in the solutions' optimality. Increasing the confidence would require restarting the optimisation from the same initial configuration numerous times, which is heavily time-consuming. Similarly, having more solutions converging to points expected to make out the Pareto-front would be beneficial in depicting the solutions' dependency on the weight of the objectives. Nevertheless, the few good solutions obtained can be used to express deficiencies in the other solutions.

2.4. On integration with existing literature and theories

The case study's limitations were in line with the previous work by Burgueno and Wu [8], demonstrating that the optimisation of shape and material in a structure comprising anisotropic material properties is susceptible to considerable obstacles. Namely, the discrete and highly non-linear solution space, requiring efficient global optimisation algorithms such as the genetic algorithm. The findings suggest that a single-step approach for the numerical optimisation of FRP bridges is feasible, though an intensification step is desirable. For instance, Burgueno and Wu's two-step approach implies one laminate in level 1 (optimising the shape and the lamination parameters), which may not be theoretically possible to construct in level 2 (minimising lamination parameter discrepancies). Thus, their outcome is not necessarily the global optimum when considering the possible combinations of shape and material configurations. Instead, concurrently optimising the shape and material architecture will lead to combinations which benefit from both parameter sets, leading to structures with high global stiffnesses. However, the vast solution space amounts to run times that are not desirable. It demonstrates the effectiveness of using genetic algorithms as a tool to optimize the fibre orientations in composite laminates and provides insights into the potential improvements in structural stiffness and strength that can be achieved through such optimization strategies. The use of other algorithms can be envisioned, though their implementation in Grasshopper may not be straightforward, depending on the available plug-ins or programming proficiency of the designer.

3. Future work and recommendations

The framework's limitations suggest areas in which it can be improved along with topics fit for further investigation, some of which concern strength assessment and efficiency improvements.

3.1. Assessing the strength

After the initiation of this research, Karamba has been updated to include an orthotropic failure criterion, namely the Tsai-Wu criterion. Though implementing this criterion in Grasshopper and Rhino is limited to a homogenised orthotropic material – meaning that layer-wise failures cannot be assessed – it invites an exciting addition to the current framework. Reiterating the framework's disregard for stress evaluation (concerned with SLS), implementing such a failure criterion would significantly improve the framework's value in the preliminary design stage. Note that each evaluation would add a constraint to the problem formulation. This would decrease the feasible design space while increasing the complexity of the function evaluations, in turn increasing the computational effort. On the other hand, greater insight of this kind can significantly reduce the required tuning in the later stages of the design. A possible approach for its implementation would be to define orthotropic stress limits for the laminates based on the in-plane elastic moduli and strain limits provided in, e.g. JRC [16], similar to the approach adopted in the hand calculations (see Appendix J.3). Bear in mind that the support conditions in Karamba could introduce singularities or stress concentrations, which should be carefully accounted for in the script to prevent obtaining overly conservative laminates.

A more intriguing approach would be to scope the panel strains and curvatures to each layer through the thickness by means of CLT, enabling assessing the laminates' strength against appropriate in-plane failure criteria on a ply-by-ply basis.

3.2. Reducing the solution space

The current solutions space (read: number of combinations) depends on the $q \in \{1,\ldots,Q\}$ number of ply groups, the f_c number of different foam core thicknesses and $j \in \{1,\ldots,J\}$ the number of panels with (possibly) unique layups. Thus, the total number of material architectural-related combinations amount to $S_{\text{mat}} = \prod_{j=1}^{J}\left(12^{Q}\cdot f_c\right) = \left(12^{10}\cdot 5\right)^4 = 9.19\cdot 10^{45}$ combinations (see Eq. (6.6)).

With able engineering judgement, several values can be adjusted locally or even overall. For instance, $q = Q = 10$ represents a total face sheet thickness close to 20 mm. Such thicknesses are rarely necessary and are generally advised against (see Chapter 3.3.6). With this in mind, or through a simplified optimisation procedure, one could reduce the maximum admissible number of layers and foam core thicknesses, consequently reducing the solution space. For instance, the longitudinal- and transverse stiffeners may be limited to GFRP panels, with $Q_1 = Q_2 = 4$. Such an adjustment would reduce the material architectural-related solution space to

$$S_{\text{mat}} = \left(6^4\cdot 5\right)^2\cdot\left(12^{10}\cdot 5\right)^2 = 4.02\cdot 10^{30}\ \text{combinations.}$$

The solution space is still of a size beyond imagination. Naturally, further improvements on the size of the solution space can be envisioned, for instance, concerning the number of different foam core thicknesses, f_c.

3.3. Implementation in a real project

Certain adjustments should be incorporated to implement the framework in a real project. First, key load cases should be determined, especially those expected to govern the design. Then, to prevent having stress concentrations decisive for the overall material architecture of the panels, the division into panels should be determined appropriately. Otherwise, shear and moment concentrations (typically near supports) would define the panels, resulting in overly conservative and costly structures.

Secondly, one should seek to set up the model using symmetry conditions, which, to some extent, limits the possible geometries. Nonetheless, the model size is halved (or quartered), naturally decreasing the computational effort. Note, however, that the natural mode shapes may not be symmetrical, which should be carefully investigated. Non-symmetrical load cases further prohibit this implementation. Then the mesh may be refined in regions prone to stress concentrations, better capturing geometrical details.

Third, the material architecture-related variables should be aligned with regular production processes and readily available reinforcement mats. Typically, unidirectional (UD, 0°), double-biased (DB, ±45°), longitudinal-transverse (LT, $0°, 90°$), and DBLT ($0°, +45°, 90°, -45°$) mats are used, rather than the random order of orientations in this thesis. Then, if only the UD mats are allowed to take on GFRP or CFRP (all other mats taken as GFRP), the total combinations for each ply group are reduced from 12 to 6, drastically decreasing the solution space considering the exponential terms in discussed in the previous section. Moreover, ply drops and reinforcement overlaps should be incorporated. This is, strictly speaking, not necessary to implement in the optimisation procedure, as the implementation of overlaps will increase global stiffness while decreasing abrupt stiffness changes. Such checks should, however, be carried out before finalising the project.

Fourth, in order to present solutions to stakeholders, it would be lucrative to present more accurate numbers in terms of costs and carbon footprint. The latter is obtained from relevant sources, but the costs can be more accurately modelled. In doing so, one could reach out to manufacturers for a better approximate estimate of labour costs proportional to, e.g. the expended material. Perhaps, one could be able to account for complex geometries and the increased need for cutting and overlaps, amounting to more labour and material consumption.

3.4. Adopting other FE software

The framework can be linked with other software. Several plugins are readily available through Food4Rhino, although the parametric definition of a structure comprising anisotropic laminates may not be straightforward. In the development of the tool, such an approach was developed for Sofistik, enabling to capture of the layered material properties and different couplings, not limited to homogenised properties. Though its implementation was discarded since Karamba's mesher faced fewer problems and was generally more effective, with appropriate packages and software installed, running analyses in Sofistik with the Grasshopper script should be straightforward (unsuppress the appropriate group of components, see the github repository).

3.5. Vehicular bridges

At the onset of this thesis, the intention was to create an optimisation framework applicable to vehicular composite bridges. However, due to easier access to reference data (the Klosterøy bridge), the focus was aimed at pedestrian bridges. Nevertheless, a promising and extremely interesting extension of the presented framework would be to adjust it and use it for vehicular bridges. Then, in order to increase the stability and compressive resistance, a hybrid closed composite box girder with an overlying concrete deck could make for a promising starting point, perhaps based on the works of Siwoski [6].

4. Conclusion

The findings suggest that the cost and carbon footprint can be reduced by 27.4% and 17%, respectively, with reference to FiReCo's design. However, considering the implemented simplifications and limitations, it can not be guaranteed that the outcome satisfies all the design constraints and requirements which present themselves from the tender. Nevertheless, with the defined optimisation constraints, it has been proved that the suggested approach allows for considerable cost- and emission reductions. As such, the framework can be handy in convincing stakeholders concerned with the relatively high costs of composite structures. Nevertheless, much of the scepticism stems from (in the eyes of the stakeholders) too few representations of composite in the built environment showcasing its potential.

The framework successfully bridges a gap concerning the numerical optimisation of composite structures. Importantly, the developed programming approach allows for *possibly* absent plies (varying laminate thicknesses) and hybrid laminates (GFRP and CFRP), all the while utilising free-form in FRP, trying to utilise on the material's strength and overcoming its weaknesses. Thus, it serves as an important mean to meeting the UN's carbon neutrality goals. However, significant improvement should be implemented in order to improve the framework's efficiency and the optimality of – and the confidence in – the solutions.

Main Report Bibliography

[1] L. Blaga, J. D. Santos, R. Băncilă and S. T. Amancio-Filho, 'Friction riveting (fricriveting) as a new joining technique in gfrp lightweight bridge construction', *Construction and Building Materials*, vol. 80, pp. 167–179, 2015.

[2] P. Górriz, A. Bansal, C. Paulotto, S. Primi and I. Calvo, 'Composite solutions for construction sector', in *Case Study of Innovative Projects*, B. L. Moya, M. D. S. de Gracia and L. F. Mazadiego, Eds., Rijeka: IntechOpen, 2017, ch. 3. DOI: 10.5772/intechopen.68964.

[3] M. Drissi-Habti, 'Smart composites for durable infrastructures—importance of structural health monitoring (shm)', in *Advances in FRP Composites in Civil Engineering*, Springer, 2011, pp. 264–267.

[4] I. Paeglite, J. Smirnovs and A. Paeglitis, 'Traffic load effects on dynamic bridge performance', 2016, pp. 2364–2369. [Online]. Available: https://www.scopus.com/inward/record.uri?eid=2-s2.0-85000925934&partnerID=40&md5=74631bb904fd257113a99c7656968c8d.

[5] P. B. Potyrała, *Use of fibre reinforced polymer composites in bridge construction. State of the art in hybrid and all-composite structures*, 2011. [Online]. Available: https://core.ac.uk/download/pdf/41803742.pdf.

[6] T. Siwowski, M. Rajchel, D. Kaleta and L. Wlasak, 'The first polish road bridge made of frp composites', *Structural Engineering International*, vol. 27, pp. 308–314, May 2017. DOI: 10.2749/101686617X14881932436339.

[7] T. Keller, 'Multifunctional and robust composite material structures for sustainable construction', in *Advances in FRP Composites in Civil Engineering*, L. Ye, P. Feng and Q. Yue, Eds., Berlin, Heidelberg: Springer Berlin Heidelberg, 2011, pp. 20–25, ISBN: 978-3-642-17487-2.

[8] R. Burgueño and J. Wu, 'Membrane-based forms for innovative FRP bridge systems through structural optimization', *Journal of Composites for Construction*, vol. 10, no. 5, pp. 453–461, 2006.

[9] American Composites Manufacturers Association. 'What are composites?' (2021), [Online]. Available: http://compositeslab.com/composites-101/what-are-composites/ (visited on 01/02/2022).

[10] T. Ngo, 'Introduction to composite materials', *Composite and Nanocomposite Materials From Knowledge to Industrial Applications*, 2020. DOI: 10.5772/intechopen.91285.

[11] F. Campbell, *Structural Composite Materials*. ASM International, 2010, ISBN: 9781615031405.

[12] C. T. Herakovich, *Mechanics of Fibrous Composites*. New York, NY: John Wiley & Sons, 1998, ISBN: 9780471106364.

[13] C. Kassapoglou, *Design and analysis of composite structures: with applications to aerospace structures*. John Wiley & Sons, 2013.

[14] K. Chawla, 'Glass fibers', in *Encyclopedia of Materials: Science and Technology*, K. J. Buschow *et al.*, Eds., Oxford: Elsevier, 2001, pp. 3541–3545, ISBN: 978-0-08-043152-9. DOI: 10.1016/B0-08-043152-6/00630-6.

[15] D. Zenkert, *The Handbook of Sandwich Construction*. Engineering Materials Advisory Services, 1997, ISBN: 9780947817961.

[16] L. Ascione *et al.*, 'Prospect for new guidance in the design of FRP', Institute for the Protection and the Security of the Citizen, Standard EUR 27666 EN, Draft, 2017. [Online]. Available: https://ec.europa.eu/jrc/en/publication/eur-scientific-and-technical-research-reports/prospect-new-guidance-design-frp.

[17] Prince-Lund Engineering. 'Properties of aramid fibers'. (2021), [Online]. Available: https://www.princelund.com/aramid-fibers.html (visited on 01/02/2022).

[18] R. Nijssen, *Composite materials: an introduction*. Inholland University of Applied Sciences Netherlands, 2015. [Online]. Available: https://compositesnl.nl/wp-content/uploads/2020/02/branded-book-toray-advanced-composites.pdf.

[19] J. L. Clarke, *Structural design of polymer composites: Eurocomp design code and background document*. CRC Press, 2003.

[20] S. Gudmundsson, 'Chapter 5 - Aircraft structural layout', in *General Aviation Aircraft Design*, S. Gudmundsson, Ed., Boston: Butterworth-Heinemann, 2014, pp. 97–131, ISBN: 978-0-12-397308-5. DOI: 10.1016/B978-0-12-397308-5.00005-2.

[21] J. Smits, 'Fiber-reinforced polymer bridge design in the Netherlands: Architectural challenges toward innovative, sustainable, and durable bridges', *Engineering*, vol. 2, no. 4, pp. 518–527, 2016, ISSN: 2095-8099. DOI: 10.1016/J.ENG.2016.04.004.

[22] AM Structures. 'Foryd harbour bridge'. (2022), [Online]. Available: https://www.amstructures.com/portfolio/foryd-harbour-bridge/ (visited on 04/02/2022).

[23] CTS Bridges. 'FRP bridges installed by helicopter - Scotland'. (2022), [Online]. Available: https://www.externalworksindex.co.uk/entry/131828/CTS-Bridges/FRP-bridges-installed-by-helicopter-Scotland/ (visited on 05/02/2021).

[24] Ir. Jan Peeters, *Lecture slides in FRP Structures - from boats and airplanes to bridges*, Sep. 2018.

[25] International Transport Forum. 'National regulations and practices in international road transport: Weights and dimensions: The netherlands'. (2021), [Online]. Available: https://www.itf-oecd.org/road-transport-group/weights-and-dimensions/netherlands (visited on 04/02/2022).

[26] R. M. Jones, *Mechanics of composite materials*. CRC press, 1998, ISBN: 9781560327127.

[27] C. York, 'Unified approach to the characterization of coupled composite laminates: Benchmark configurations and special cases', *Journal of Aerospace Engineering*, vol. 23, no. 4, pp. 219–242, 2010.

[28] S. W. Tsai and E. M. Wu, 'A general theory of strength for anisotropic materials', *Journal of composite materials*, vol. 5, no. 1, pp. 58–80, 1971.

[29] C. H. Wang and C. N. Duong, 'Chapter 2 - failure criteria', in *Bonded Joints and Repairs to Composite Airframe Structures*, C. H. Wang and C. N. Duong, Eds., Oxford: Academic Press, 2016, pp. 21–45, ISBN: 978-0-12-417153-4. DOI: 10.1016/B978-0-12-417153-4.00002-5.

[30] M. Hinton, P. Soden and A.-S. Kaddour, *Failure criteria in fibre reinforced polymer composites: the world-wide failure exercise*. Elsevier, 2004, ISBN: 978-0-08-044475-8. DOI: 10.1016/B978-0-080-44475-8.X5000-8.

[31] N. P. Vedvik. 'TMM4175 Polymer Composites [course website]'. (2021), [Online]. Available: https://folk.ntnu.no/nilspv/TMM4175/index.html (visited on 21/12/2021).

[32] G. H. Staab, 'Lamina failure theories', in *Laminar Composites (Second Edition)*, G. H. Staab, Ed., Second Edition, Butterworth-Heinemann, 2015, pp. 139–187, ISBN: 978-0-12-802400-3. DOI: 10.1016/B978-0-12-802400-3.00005-2.

[33] Z. Hashin, 'Failure Criteria for Unidirectional Fiber Composites', *Journal of Applied Mechanics*, vol. 47, no. 2, pp. 329–334, Jun. 1980, ISSN: 0021-8936. DOI: 10.1115/1.3153664.

[34] A. Puck and H. Schürmann, 'Failure analysis of frp laminates by means of physically based phenomenological models', *Composites Science and Technology*, vol. 58, no. 7, pp. 1045–1067, 1998, ISSN: 0266-3538. DOI: 10.1016/S0266-3538(96)00140-6.

[35] C. G. Davila, P. P. Camanho and C. A. Rose, 'Failure criteria for frp laminates', *Journal of Composite Materials*, vol. 39, no. 4, pp. 323–345, 2005. DOI: 10.1177/0021998305046452.

[36] K.-U. Bletzinger and E. Ramm, 'Structural optimization and form finding of light weight structures', *Computers & Structures*, vol. 79, no. 22, pp. 2053–2062, 2001, ISSN: 0045-7949. DOI: 10.1016/S0045-7949(01)00052-9.

[37] D. Veenendaal and P. Block, 'An overview and comparison of structural form finding methods for general networks', *International Journal of Solids and Structures*, vol. 49, no. 26, pp. 3741–3753, 2012. DOI: 10.1016/j.ijsolstr.2012.08.008.

[38] L. Glaeser, *The work of Frei Otto*. The Museum of Modern Art, 1972, ISBN: 0870703322. [Online]. Available: https://assets.moma.org/documents/moma_catalogue_2662_300299029.pdf.

[39] J. Y. Chi and R. d. O. Pauletti, 'An outline of the evolution of pneumatic structures', in *II Simposio Latinoamericano de Tensoestructuras, Caracas*, 2005. [Online]. Available: https://www.researchgate.net/publication/228655700_An_outline_of_the_evolution_of_pneumatic_structures#fullTextFileContent.

[40] H. Isler, 'Concrete shells derived from experimental shapes', *Structural Engineering International*, vol. 4, no. 3, pp. 142–147, 1994.

[41] R. Burgueño and J. Wu, 'An integrated approach to shape and laminate stacking sequence optimization of free-form FRP shells', *Computer Methods in Applied Mechanics and Engineering*, vol. 195, no. 33, pp. 4106–4123, 2006, ISSN: 0045-7825. DOI: 10.1016/j.cma.2005.07.015.

[42] J. Wu, '[excerpt from] shape and laminate optimization of fiber-reinforced-polymer structures', Ph.D. dissertation, Michigan State University, 2004. [Online]. Available: https://www.proquest.com/openview/a540f3f73e11825ef1850903e9e311e6/1.

[43] P. W. Christensen and A. Klarbring, *An introduction to structural optimization*. Springer Science & Business Media, 2008, vol. 153.

[44] M. P. Bendsoe and O. Sigmund, *Topology optimization: theory, methods, and applications*. Springer Science & Business Media, 2003, ISBN: 978-3-642-07698-5.

[45] K.-H. Chang, *Design theory and methods using CAD/CAE: The computer aided engineering design series*. Academic Press, 2014, ISBN: 978-0-12-398512-5.

[46] neosGuide. 'Types of optimization problems'. (2020), [Online]. Available: https://neos-guide.org/optimization-tree (visited on 14/02/2022).

[47] O. Kramer, 'Genetic algorithms', in *Genetic algorithm essentials*, Springer, 2017.

[48] M. Akbulut and F. O. Sonmez, 'Design optimization of laminated composites using a new variant of simulated annealing', *Computers & structures*, vol. 89, no. 17-18, pp. 1712–1724, 2011.

[49] A. R. M. Rao and P. Shyju, 'A meta-heuristic algorithm for multi-objective optimal design of hybrid laminate composite structures', *Computer-Aided Civil and Infrastructure Engineering*, vol. 25, no. 3, pp. 149–170, 2010.

[50] Ş. Karakaya and Ö. Soykasap, 'Natural frequency and buckling optimization of laminated hybrid composite plates using genetic algorithm and simulated annealing', *Structural and Multidisciplinary Optimization*, vol. 43, no. 1, pp. 61–72, 2011.

[51] R. Koide and M. Luersen, 'Maximization of fundamental frequency of laminated composite cylindrical shells by ant colony algorithm', *Journal of Aerospace Technology and Management*, vol. 5, pp. 75–82, Mar. 2013. DOI: 10.5028/jatm.v5i1.233.

[52] R. Koide, G. França and M. Luersen, 'An ant colony algorithm applied to lay-up optimization of laminated composite plates', *Latin American Journal of Solids and Structures*, vol. 10, pp. 491–504, May 2013. DOI: 10.1590/S1679-78252013000300003.

[53] J. F. Davalos, P. Qiao and E. J. Barbero, 'Multiobjective material architecture optimization of pultruded FRP I-beams', *Composite Structures*, vol. 35, no. 3, pp. 271–281, 1996.

[54] P. Qiao, J. F. Davalos and E. J. Barbero, 'Design optimization of fiber reinforced plastic composite shapes', *Journal of composite materials*, vol. 32, no. 2, pp. 177–196, 1998.

[55] L. A. Schmit and B Farshi, 'Optimum laminate design for strength and stiffness', *International Journal for Numerical Methods in Engineering*, vol. 7, no. 4, pp. 519–536, 1973.

[56] Y. Ohta, 'Genetic algorithms for optimization of laminated composite cylindrical shells', in *8th Symposium on Multidisciplinary Analysis and Optimization*, 2000, p. 4939.

[57] F. S. Almeida and A. Awruch, 'Design optimization of composite laminated structures using genetic algorithms and finite element analysis', *Composite structures*, vol. 88, no. 3, pp. 443–454, 2009.

[58] S. W. Tsai and N. J. Pagano, 'Invariant properties of composite materials', AIR FORCE MATERIALS LAB WRIGHT-PATTERSON AFB OH WRIGHT-PATTERSON AFB, Tech. Rep., 1968. [Online]. Available: https://apps.dtic.mil/sti/pdfs/AD0668761.pdf.

[59] H. Fukunaga and G. N. Vanderplaats, 'Stiffness optimization of orthotropic laminated composites using lamination parameters', *AIAA journal*, vol. 29, no. 4, pp. 641–646, 1991.

[60] G. H. Silva and Y. Meddaikar, 'Lamination parameters for sandwich and hybrid material composites', *AIAA Journal*, vol. 58, no. 10, pp. 4604–4611, 2020.

[61] R. Z. G. Bohrer and I. Y. Kim, 'Concurrent topology and stacking sequence optimization of composite laminate plates using lamination parameters', *Composite Structures*, vol. 276, p. 114 556, 2021, ISSN: 0263-8223. DOI: 10.1016/j.compstruct.2021.114556.

[62] J. Andersson and G. Good, 'Parametric analysis and stiffness optimisation of FRP pedestrian bridges: Optimisation of hybrid fibre compositions and fibre angles in serviceability limit state', M.S. thesis, Chalmers University of Technology, Gothenburg, Sweden, Oct. 2017. [Online]. Available: https://odr.chalmers.se/bitstream/20.500.12380/250990/1/250990.pdf.

[63] R. Burgueño and J. Wu, 'An uncoupled approach to shape and laminate optimization of FRP membrane and shell structures', in *Structures Congress 2005: Metropolis and Beyond*, 2005, pp. 1–6. DOI: 10.1061/40753(171)110.

[64] M. Tuffaha, 'Form-finding framework for FRP shells: A multi-step structural optimization tool for preliminary FRP designs', M.S. thesis, TU Delft, Delft, The Netherlands, Oct. 2019. [Online]. Available: http://resolver.tudelft.nl/uuid:26451229-0bec-4629-8adf-b13d9d41cbe3.

[65] D. Rutten, 'Galapagos: On the logic and limitations of generic solvers', *Architectural Design*, vol. 83, no. 2, pp. 132–135, 2013.

[66] K. Sörensen, 'Metaheuristics—the metaphor exposed', *International Transactions in Operational Research*, vol. 22, no. 1, pp. 3–18, 2015.

[67] R. L. Riche and R. T. Haftka, 'Optimization of laminate stacking sequence for buckling load maximization by genetic algorithm', *AIAA journal*, vol. 31, no. 5, pp. 951–956, 1993.

[68] M. Walker and R. E. Smith, 'A technique for the multiobjective optimisation of laminated composite structures using genetic algorithms and finite element analysis', *Composite structures*, vol. 62, no. 1, pp. 123–128, 2003.

[69] M. K. Apalak, M. Yildirim and R. Ekici, 'Layer optimisation for maximum fundamental frequency of laminated composite plates for different edge conditions', *Composites Science and Technology*, vol. 68, no. 2, pp. 537–550, 2008.

[70] M Abachizadeh and M Tahani, 'An ant colony optimization approach to multi-objective optimal design of symmetric hybrid laminates for maximum fundamental frequency and minimum cost', *Structural and Multidisciplinary Optimization*, vol. 37, no. 4, pp. 367–376, 2009.

[71] Z. K. Awad, T. Aravinthan, Y. Zhuge and F. Gonzalez, 'A review of optimization techniques used in the design of fibre composite structures for civil engineering applications', *Materials & Design*, vol. 33, pp. 534–544, 2012.

[72] M. K. Apalak, D. Karaboga and B. Akay, 'The artificial bee colony algorithm in layer optimization for the maximum fundamental frequency of symmetrical laminated composite plates', *Engineering Optimization*, vol. 46, no. 3, pp. 420–437, 2014.

[73] McNeel Europe. 'food4Rhino: Apps for Rhino and Grasshopper'. (2022), [Online]. Available: https://www.food4rhino.com/en.

[74] R. Vierlinger, 'Multi objective design interface', M.S. thesis, Technischen Universität Wien, Wien, Austria, Apr. 2013. DOI: 10.13140/RG.2.1.3401.0324.

[75] M. Makki, M. Showkatbakhsh and Y. Song. 'An evolutionary multi-objective optimization and analytic engine for grasshopper 3d'. (2022), [Online]. Available: https://www.wallacei.com/ (visited on 17/02/2022).

[76] J. H. Holland, *Adaptation in natural and artificial systems: an introductory analysis with applications to biology, control, and artificial intelligence*. MIT press, 1992.

[77] S.N.Sivanandam and S.N.Deepa, *Introduction to Genetic Algorithms*. Heidelberg, Berlin: Springer, 2008, ISBN: 978-3-540-73189-4.

[78] The MathWorks, Inc., *Global optimization toolbox: User's guide*, version 4.5 (R2021a), 2021. [Online]. Available: https://nl.mathworks.com/help/gads/.

[79] M Nogal and A Nogal, 'Sensitivity method for extreme-based engineering problems', *Reliability Engineering & System Safety*, vol. 216, p. 107 997, 2021. DOI: 10.1016/j.ress.2021.107997.

[80] European Commission. 'Going climate-neutral by 2050'. (2019), [Online]. Available: https://op.europa.eu/en/publication-detail/-/publication/92f6d5bc-76bc-11e9-9f05-01aa75ed71a1 (visited on 23/09/2021).

[81] PwC. 'Life cycle assessment of cfgf – continuous filament glass fibre products'. (2016), [Online]. Available: https://www.glassfibreeurope.eu/wp-content/uploads/2016/11/LCA-report-CFGF-products_20161031_PwC.pdf (visited on 10/04/2021).

[82] C. Hill and A. Norton, *LCA database of environmental impacts to inform material selection process*, 2018. [Online]. Available: https://ec.europa.eu/research/participants/documents/downloadPublic?documentIds=080166e5c240650f&appId=PPGMS.

[83] R. McNeel *et al.*, 'Rhinoceros 3D, (Version 7.0) [Software]', *Robert McNeel & Associates, Seattle, WA*, 2010.

[84] G. E. P. Box, 'Statistics as a catalyst to learning by scientific method part ii—a discussion', *Journal of Quality Technology*, vol. 31, no. 1, pp. 16–29, 1999. DOI: 10.1080/00224065.1999.11979890.

[85] Johs Holt AS. 'Klaffebru i Skien'. (2022), [Online]. Available: http://www.johsholt.no/prosjekt/klaffebru/ (visited on 14/02/2022).

[86] R. K. Joki and T. Heggenhougen. 'The DACOMAT project speeded up their career'. (2020), [Online]. Available: https://www.sintef.no/projectweb/dacomat/news-and-events/the-dacomat-project-speeded-up-their-career/ (visited on 22/01/2022).

[87] FiReCo, *Personal communication*.

[88] *EN 1991-2 Eurocode 1: Actions on structures - Part 2: Traffic loads on bridges*, EN, Brussels: CEN, 2003.

[89] C. Preisinger, 'Linking structure and parametric geometry', *Architectural Design*, vol. 83, no. 2, pp. 110–113, 2013.

[90] J. Argyris, L. Tenek and L. Olofsson, 'Tric: A simple but sophisticated 3-node triangular element based on 6 rigid-body and 12 straining modes for fast computational simulations of arbitrary isotropic and laminated composite shells', *Computer Methods in Applied Mechanics and Engineering*, vol. 145, no. 1, pp. 11–85, 1997, ISSN: 0045-7825. DOI: 10.1016/S0045-7825(96)01233-9.

[91] J. Argyris, M. Papadrakakis, C. Apostolopoulou and S. Koutsourelakis, 'The tric shell element: Theoretical and numerical investigation', *Computer Methods in Applied Mechanics and Engineering*, vol. 182, no. 1, pp. 217–245, 2000, ISSN: 0045-7825. DOI: 10.1016/S0045-7825(99)00094-8.

[92] C. Preisinger, *Karamba3D: Parametric engineering*, version 1.3.1, 2018.

[93] E. Castillo, A. J. Conejo, P. Pedregal, R. Garcia and N. Alguacil, *Building and solving mathematical programming models in engineering and science.* John Wiley & Sons, 2011.

[94] A. Scheepens, A. van der Flier, A. Romeo-Hall and R. Veugen. 'Eco impact calculator for for composites (Version 1.4) [Software]'. (2021-4), [Online]. Available: https://ecocalculator.eucia.eu/ (visited on 01/02/2022).

[95] CROW, 'Vezelversterkte kunststoffen in bouwkundige en civieltechnische draagconstructies', CROW, Standard CRW AA96:2019, 2019. [Online]. Available: https://www.crow.nl/publicaties/vezelversterkte-kunststoffen-in-bouwkundige-en-civ.

[96] P. Hoogenboom, *Reader for the course CIE4143: Shell Analysis, Theory and Application*, 2021.

[97] V. Weingarten, E. Morgan and P. Seide, 'Elastic stability of thin-walled cylindrical and conical shells under combined internal pressure and axial compression', *AIAA Journal*, vol. 3, no. 6, pp. 1118–1125, 1965.

[98] F. Glover, 'Tabu search—part I', *ORSA Journal on computing*, vol. 1, no. 3, pp. 190–206, 1989.

[99] Rechenraum GmbH. 'goat: Free optimization solver component for Rhino's Grasshopper'. (2022), [Online]. Available: https://www.rechenraum.com/en/goat.html.

[100] Steven G. Johnson. 'The NLopt nonlinear-optimization package'. (2022), [Online]. Available: https://github.com/stevengj/nlopt (visited on 14/03/2022).

[101] T. H. Rowan, 'Functional stability analysis of numerical algorithms', Ph.D. dissertation, The University of Texas at Austin, 1990.

[102] S. Timoshenko, *Vibration problems in engineering*. New York, NY: D. Van Nostrand Company, Inc, 1937, pp. 337–338.

[103] Q. Zhang, Y. Bu and Q. Li, 'Review on fatigue problems of orthotropic steel bridge deck', *China Journal of Highway and Transport*, vol. 30, no. 3, pp. 14–30, 2017.

Appendices Bibliography

[1] J. C. Halpin and J. L. Kardos, 'The Halpin-Tsai equations: A review', *Polymer Engineering & Science*, vol. 16, no. 5, pp. 344–352, 1976.

[2] C. T. Herakovich, *Mechanics of Fibrous Composites*. New York, NY: John Wiley & Sons, 1998, ISBN: 9780471106364.

[3] L. Ascione *et al.*, 'Prospect for new guidance in the design of FRP', Institute for the Protection and the Security of the Citizen, Standard EUR 27666 EN, Draft, 2017. [Online]. Available: https://ec.europa.eu/jrc/en/publication/eur-scientific-and-technical-research-reports/prospect-new-guidance-design-frp.

[4] S. W. Tsai and N. J. Pagano, 'Invariant properties of composite materials', AIR FORCE MATERIALS LAB WRIGHT-PATTERSON AFB OH WRIGHT-PATTERSON AFB, Tech. Rep., 1968. [Online]. Available: https://apps.dtic.mil/sti/pdfs/AD0668761.pdf.

[5] R. Z. G. Bohrer and I. Y. Kim, 'Concurrent topology and stacking sequence optimization of composite laminate plates using lamination parameters', *Composite Structures*, vol. 276, p. 114 556, 2021, ISSN: 0263-8223. DOI: 10.1016/j.compstruct.2021.114556.

[6] H. Fukunaga and G. N. Vanderplaats, 'Stiffness optimization of orthotropic laminated composites using lamination parameters', *AIAA journal*, vol. 29, no. 4, pp. 641–646, 1991.

[7] K. Yamazaki, 'Two-level optimization technique of composite laminate panels by genetic algorithms', in *37th Structure, Structural Dynamics and Materials Conference*, 1996, p. 1539.

[8] H. FUKUNAGA, 'Netting theory and its application to optimum design of laminated composite plates and shells', in *29th Structures, Structural Dynamics and Materials Conference*, 1988, p. 2332.

[9] ANSYS Inc, *ANSYS Composite PrepPost User's Guide*, 2013. [Online]. Available: https://www.academia.edu/25099111/ANSYS_Composite_PrepPost_Users_Guide.

[10] The MathWorks, Inc., *Optimization toolbox: User's guide*, version 9.1 (R2021a), 2021. [Online]. Available: https://nl.mathworks.com/help/optim/.

[11] C. Preisinger, 'Linking structure and parametric geometry', *Architectural Design*, vol. 83, no. 2, pp. 110–113, 2013.

[12] A. Scheepens, A. van der Flier, A. Romeo-Hall and R. Veugen. 'Eco impact calculator for for composites (Version 1.4) [Software]'. (2021-4), [Online]. Available: https://ecocalculator.eucia.eu/ (visited on 01/02/2022).

[13] L. P. Kollár, 'Local buckling of fiber reinforced plastic composite structural members with open and closed cross sections', *Journal of Structural Engineering*, vol. 129, no. 11, pp. 1503–1513, 2003.

[14] C. Kassapoglou, *Design and analysis of composite structures: with applications to aerospace structures*. John Wiley & Sons, 2013.

[15] ANSYS, Inc. 'Ansys (Version R 2021 R2) [Software]'. (2022), [Online]. Available: https://www.ansys.com/.

[16] Łukasz Skotny. 'Why is a triangular element stiffer?' (21 February 2019), [Online]. Available: https://enterfea.com/why-is-a-triangular-element-stiffer/ (visited on 22/05/0022).

Appendices

Appendix A Unidirectional and mat ply properties

The material properties of composites can be defined making use of the micromechanical properties of the constituents, and their relation expressed through the fibre volume fraction V_f. The following discussion presents two methods for determining the lamina properties, the *Rule of Mixtures* method and the *Halpin-Tsai* method [1]. The shortcomings of the *Rule of Mixtures* method, i.e. the difficulties and inaccuracies associated with predicting the elastic properties of a UD lamina using mathematical closed form solutions, prompted the introduction of a semi-empirical relationship. Among the available theories, the Halpin-Tsai method stands out as the most popular and widely used relationships.

A.1. The Rule of Mixtures method

The elastic properties of UD lamina can be defined by assuming that fibres and resin either act in series or in parallel.

Firstly, the volume fractions are defined such that

$$V_f + V_m = 1 \Longleftrightarrow V_m = (1 - V_f) \tag{A.1}$$

where the subscripts f and m refer to the fibre and the resin matrix, respectively. From Eq. (A.1) the upper bound of the composite modulus can be defined assuming that the constituents act in parallel as

$$E \leq E_f V_f + E_m (1 - V_f) \tag{A.2}$$

Making use of the compliance, it can be proved the the lower bound of the apparent Young's modulus follows [2]:

$$\begin{aligned} \frac{1}{E} &= \frac{V_f}{E_f} + \frac{(1 - V_f)}{E_m} \\ E &\geq \frac{E_f E_m}{V_f E_m + (1 - V_f) E_m} \end{aligned} \tag{A.3}$$

Obviously, the Poisson's ratio and the density can be expressed using the *Rule of Mixtures* as:

$$\nu_{12} = \nu_f V_f + \nu_m (1 - V_f) \quad \text{and} \quad \rho = \rho_f V_f \rho_m (1 - V_f), \tag{A.4}$$

respectively. In the above equations, any expression for the required modulus can be promptly substituted. Consider for example the shear modulus of the composite:

$$\frac{1}{G_{12}} = \frac{V_f}{G_f} + \frac{(1 - V_f)}{G_m}$$

The above presented set of equations, the *Rule of Mixtures*, is relatively approximate, yet it adequately predicts the longitudinal modulus.

A.2. The Halpin-Tsai method

Overcoming the shortcomings of the *Rule of Mixtures* cannot easily be achieved through closed form mathematical solutions and purely mechanical considerations. The following set of equations are based on the slightly modified Halpin-Tsai equations from the JRC 2017 draft document for UD plies and mat plies, such as CSM [3].

A.2.1. UD PLIES

$$E_1 = \left[E_m + \left(E_{f1} - E_m\right)\cdot V_f\right]\cdot \varphi_{UD} \tag{A.5}$$

$$E_2 = \left[\frac{\left(1+\xi_2\eta_2 V_f\right)}{\left(1-\eta_2 V_f\right)}\cdot E_m\right]\cdot \varphi_{UD} \tag{A.6}$$

$$G_{12} = \left[\frac{\left(1+\xi_G\eta_G V_f\right)}{\left(1-\eta_G V_f\right)}\cdot G_m\right]\cdot \varphi_{UD} \tag{A.7}$$

$$\nu_{12} = \nu_m - \left(\nu_m - \nu_f\right)\cdot V_f \tag{A.8}$$

where:

$$\text{for } E_2: \quad \eta_2 = \frac{\left(\frac{E_{f2}}{E_m} - 1\right)}{\left(\frac{E_{f2}}{E_m} + \xi_2\right)}, \quad \xi_2 = 2; \qquad \text{for } G_{12}: \quad \eta_G = \frac{\left(\frac{G_f}{G_R} - 1\right)}{\left(\frac{G_f}{G_R} + \xi_G\right)}, \quad \xi_G = 1. \tag{A.9}$$

in which φ_{UD} is an empirical reduction factor, $\varphi_{UD} = 0.97$.

A.2.2. MAT PLIES

In conformity with Eqs. (A.5)–(A.9), the properties of mat plies, such as CSM mats, can be defined by introducing Manera's equations and the empirical reduction factor $\varphi_{mat} = 0.91$ [3]:

$$\begin{aligned} E_1 = E_2 &= \left[\frac{\left(U_1+U_4\right)\cdot\left(U_1-U_4\right)}{U_1}\right]\cdot\varphi_{mat} \\ G_{12} &= \left[\frac{\left(U_1-U_4\right)}{2}\right]\cdot\varphi_{mat} \\ \nu_{12} &= \frac{U_4}{U_1} \end{aligned} \tag{A.10}$$

in which

$$\begin{aligned} U_1 &= \frac{3C_{11}+3C_{22}+2C_{12}+4C_{66}}{8} \\ U_4 &= \frac{C_{11}+C_{22}+6C_{12}-4C_{66}}{8} \\ C_{11} &= \frac{E_{1UD}}{1-\nu_{12UD}^2\cdot\frac{E_{2UD}}{E_{1UD}}} \\ C_{22} &= \frac{E_{2UD}}{1-\nu_{12UD}^2\cdot\frac{E_{2UD}}{E_{1UD}}} \\ C_{12} &= \frac{\nu_{12UD}\cdot E_{1UD}}{1-\nu_{12UD}^2\cdot\frac{E_{2UD}}{E_{1UD}}} \\ C_{66} &= G_{21UD} \end{aligned} \tag{A.11}$$

Appendix B Lamination parameters

B.1. Lamination parameters

In 1968 Tsai and Pagano [4] introduced LPs as trigonometric functions of the ply orientations, expressing the stiffness tensor of laminated composite as a linear function of the material invariants [5]. This derivation allows to explain the section properties of any laminate based on 12 lamination parameters and 1 laminate thickness.

There are 4 lamination parameters corresponding to each of the **A**, **B** and **D** matrices, thus ξ_i^A, ξ_i^B and ξ_i^D for $i \in (1,2,3,4)$ refer to the in-plane, coupling, and out-of-plane section stiffness properties of the laminate, respectively. For laminates consisting of N layers, the lamination parameters are defined as the integral of the layer orientations over the thickness z, which can be conveniently evaluated from the summations in Table B.1 below.

Table B.1: Lamination parameters [4, 5]

In-plane	Coupling	Out-of-plane
$\xi_1^A = \sum_{k=1}^{N} cos(2\theta_k)(z_k - z_{k-1})$	$\xi_1^B = \frac{1}{2}\sum_{k=1}^{N} cos(2\theta_k)(z_k^2 - z_{k-1}^2)$	$\xi_1^D = \frac{1}{3}\sum_{k=1}^{N} cos(2\theta_k)(z_k^3 - z_{k-1}^3)$
$\xi_2^A = \sum_{k=1}^{N} sin(2\theta_k)(z_k - z_{k-1})$	$\xi_2^B = \frac{1}{2}\sum_{k=1}^{N} sin(2\theta_k)(z_k^2 - z_{k-1}^2)$	$\xi_2^D = \frac{1}{3}\sum_{k=1}^{N} sin(2\theta_k)(z_k^3 - z_{k-1}^3)$
$\xi_3^A = \sum_{k=1}^{N} cos(4\theta_k)(z_k - z_{k-1})$	$\xi_3^B = \frac{1}{2}\sum_{k=1}^{N} cos(4\theta_k)(z_k^2 - z_{k-1}^2)$	$\xi_3^D = \frac{1}{3}\sum_{k=1}^{N} cos(4\theta_k)(z_k^3 - z_{k-1}^3)$
$\xi_4^A = \sum_{k=1}^{N} sin(4\theta_k)(z_k - z_{k-1})$	$\xi_4^B = \frac{1}{2}\sum_{k=1}^{N} sin(4\theta_k)(z_k^2 - z_{k-1}^2)$	$\xi_4^D = \frac{1}{3}\sum_{k=1}^{N} sin(4\theta_k)(z_k^3 - z_{k-1}^3)$

Focusing on symmetrical laminates such that the coupling matrix $\mathbf{B} = 0$, allows defining the membrane **A** and bending **D** stiffness terms as[5]:

$$\begin{aligned}
\mathbf{A} &= T\left(U_E\mathbf{I}_E + U_G\mathbf{I}_G + \xi_1^A U_{\Delta C}\mathbf{I}_1 + \xi_2^A U_{\Delta C}\mathbf{I}_2 + \xi_3^A U_{\nu C}\mathbf{I}_3 + \xi_4^A U_{\nu C}\mathbf{I}_4\right) \\
\mathbf{D} &= \frac{T^3}{3}\left(U_E\mathbf{I}_E + U_G\mathbf{I}_G + \xi_1^D U_{\Delta C}\mathbf{I}_1 + \xi_2^D U_{\Delta C}\mathbf{I}_2 + \xi_3^D U_{\nu C}\mathbf{I}_3 + \xi_4^D U_{\nu C}\mathbf{I}_4\right)
\end{aligned} \tag{B.1}$$

in which T is the laminate thickness and:

$$\begin{aligned}
&\mathbf{I}_E = [I_E] = \begin{bmatrix} 1 & 1 & 0 \\ 1 & 1 & 0 \\ 0 & 0 & 0 \end{bmatrix} \quad
\mathbf{I}_G = [I_G] = \begin{bmatrix} 0 & -2 & 0 \\ -2 & 0 & 0 \\ 0 & 0 & 1 \end{bmatrix} \quad
\mathbf{I}_1 = [I_1] = \begin{bmatrix} 1 & 0 & 0 \\ 0 & -1 & 0 \\ 0 & 0 & 0 \end{bmatrix} \\
&\mathbf{I}_2 = [I_2] = \frac{1}{2}\begin{bmatrix} 0 & 0 & 1 \\ 0 & 0 & 1 \\ 1 & 1 & 0 \end{bmatrix} \quad
\mathbf{I}_3 = [I_3] = \begin{bmatrix} 1 & -1 & 0 \\ -1 & 1 & 0 \\ 0 & 0 & -1 \end{bmatrix} \quad
\mathbf{I}_4 = [I_4] = \begin{bmatrix} 0 & 0 & 1 \\ 0 & 0 & -1 \\ 1 & -1 & 0 \end{bmatrix}
\end{aligned} \tag{B.2}$$

In Eq. (B.1), U_E, U_G,$U_{\Delta C}$ and $U_{\nu C}$ are the stiffness invariants:

$$\begin{aligned}
U_E &= \frac{1}{8}\left(3\overline{Q}_{11} + 3\overline{Q}_{22} + 2\overline{Q}_{12} + 4\overline{Q}_{66}\right) \qquad & U_G &= \frac{1}{8}\left(\overline{Q}_{11} + \overline{Q}_{22} - \overline{Q}_{12} + 4\overline{Q}_{66}\right) \\
U_{\Delta C} &= \frac{1}{2}\left(\overline{Q}_{11} - \overline{Q}_{22}\right) & U_{\nu C} &= \frac{1}{8}\left(\overline{Q}_{11} + \overline{Q}_{22} - 2\overline{Q}_{12} - 4\overline{Q}_{66}\right)
\end{aligned} \tag{B.3}$$

where the reduced stiffnesses $\overline{\boldsymbol{Q}}_{ij}$ for UD lamina are defined as in Eq. (3.1). From Eq. (B.3) and Eq. (B.1) it is obvious that the membrane and bending matrices can be easily expressed for a given laminate configuration. However, expressing **A** and **D** purely based on the continuous LP is not straight forward when it comes to hybrid layups, or even sandwich panels, due to the inconstant values of the $\overline{Q}_{ij}$.

Simplified expressions for LPs

The expressions in Eqs. (B.1)–(B.3) can be simplified further by only considered symmetrical balanced laminates, and assuming that the coupling terms D_{16} and D_{26} can be neglected, resulting in a total of four LPs with their corresponding relation to the stiffness matrix **A** and **D**:

$$\begin{aligned}
\mathbf{A} &= T\left(U_E\mathbf{I}_E + U_G\mathbf{I}_G + \xi_1^A U_{\Delta C}\mathbf{I}_1 + \xi_2^A U_{\Delta C}\mathbf{I}_2 + \cancel{\xi_3^A U_{\nu C}\mathbf{I}_3} + \cancel{\xi_4^A U_{\nu C}\mathbf{I}_4}\right)\\
&= T\left(U_E\mathbf{I}_E + U_G\mathbf{I}_G + \xi_1^A U_{\Delta C}\mathbf{I}_1 + \xi_2^A U_{\Delta C}\mathbf{I}_2\right)\\
\mathbf{D} &= \frac{T^3}{3}\left(U_E\mathbf{I}_E + U_G\mathbf{I}_G + \xi_1^D U_{\Delta C}\mathbf{I}_1 + \xi_2^D U_{\Delta C}\mathbf{I}_2 + \cancel{\xi_3^D U_{\nu C}\mathbf{I}_3} + \cancel{\xi_4^D U_{\nu C}\mathbf{I}_4}\right)\\
&= \frac{T^3}{3}\left(U_E\mathbf{I}_E + U_G\mathbf{I}_G + \xi_1^D U_{\Delta C}\mathbf{I}_1 + \xi_2^D U_{\Delta C}\mathbf{I}_2\right)
\end{aligned} \tag{B.4}$$

$$\mathbf{I}_E = \begin{bmatrix} 1 & 1 & 0\\ 1 & 1 & 0\\ 0 & 0 & 0\end{bmatrix} \qquad \mathbf{I}_G = \begin{bmatrix} 0 & -2 & 0\\ -2 & 0 & 0\\ 1 & -1 & 0\end{bmatrix} \qquad \mathbf{I}_1 = \begin{bmatrix} 1 & 0 & 0\\ 0 & -1 & 0\\ 0 & 0 & 0\end{bmatrix} \qquad \mathbf{I}_2 = \frac{1}{2}\begin{bmatrix} 0 & 0 & 1\\ 0 & 0 & 1\\ 1 & 1 & 0\end{bmatrix} \tag{B.5}$$

$$\begin{aligned}
U_E &= \frac{1}{8}\left(3\bar{Q}_{11} + 3\bar{Q}_{22} + 2\bar{Q}_{12} + 4\bar{Q}_{66}\right)\\
U_G &= \frac{1}{8}\left(\bar{Q}_{11} + \bar{Q}_{22} - \bar{Q}_{12} + 4\bar{Q}_{66}\right)\\
U_{\Delta C} &= \frac{1}{2}\left(\bar{Q}_{11} - \bar{Q}_{22}\right)
\end{aligned} \tag{B.6}$$

B.1.1. Feasible region for lamination parameters

One of the main goals in any optimisation problem, is to reduce the number of variables and the design space to a minimum. To this end, in relation to LPs, it is effective to define symmetrical and balanced laminates, in which the shear/extension coupling and bending coupling vanishes. Furthermore, neglecting the bending/twisting ($D_{16} = D_{26} = 0$) coupling leads to:

$$\xi_2^A = \xi_4^A = \xi_4^D = \xi_4^D = 0$$

allowing to express **A** and **D** from 2 LPs each. Considering that the LPs are bound by the values -1 and 1,

$$-1 \le \xi_i^j \le 1, \qquad i = 1,2,\ldots 4, \qquad j = A, B, D \tag{B.7}$$

the feasible regions of the in-plane and out-of-plane LPs, respectively, can be defined [6, 7]:

$$\begin{aligned}
(\xi_1^A)^2 - \xi_2^A + 1 \le 0, \qquad (\xi_2^A) \le 1\\
(\xi_1^D)^2 - \xi_2^D + 1 \le 0, \qquad (\xi_2^D) \le 1
\end{aligned} \tag{B.8}$$

meaning that $(\xi_1^A)^2 \le \xi_2^A$ and $\xi_2^A \le 1$ are the constraints for in-plane LPs, while $(\xi_1^D)^2 \le \xi_2^D$ and $\xi_2^D \le 1$ are the constraints for out-of-plane LPs.

Figure B.1 illustrates the relation between the in-plane LPs ξ_1^A and ξ_2^B and the ply orientations of two laminates, and the feasible region of their LPs. Equation (B.8) defines the allowable combination domain, indicated in red. Points $P(\xi_1, \xi_2)$ along this parabola ($\xi_2 = \xi_1^2$) refer to ply stacks of $[+\theta°/-\theta°]$. For instance, $P(1,0)$ corresponds to a 0° laminate, $P(-1,0)$ corresponds to a 90° laminate, and $P(0,-1)$ corresponds to a [±45°] laminate, indicated by the coloured triangle.

Relation between in-plane and out-of-plane LPs

The relation between the in-plane and out-of-plane parameters was established in [8], and further simplified in [6]. In brief: a point $P(\xi_1^A, \xi_2^A)$ translates to a feasible region in the $\xi_1^D - \xi_2^D$-plane, divided into 4 regions (see Fig. B.1).

The following expressions shows the relation between ξ_E, ξ_1^D and ξ_2^D, resulting in the point (ξ_1^D, ξ_2^D) which corresponds to $E^\dagger$ and $G^\dagger$ as (ξ_E, ξ_E^2) moves along the parabola. (ξ_E, ξ_E^2) corresponds to E for $0 \le \alpha \le \angle APD$ and G for $\angle APD \le \alpha \le \pi$. Thus, the boundaries of the regions $I - IV$ are expressed as follows:

$$\xi_2^D = \frac{\xi_2^A - \xi_E^2}{\xi_1^A - \xi_E}\xi_1^D + \frac{\xi_1^A \xi_E - \xi_2^A}{\xi_1^A - \xi_E}\xi_E \tag{B.9a}$$

where **Region I** ....

$$\left(-1 \leq \xi_E \leq \frac{\xi_1^A - \xi_2^A}{1-\xi_1^A}\right)$$
$$\xi_1^D = \xi_E + \frac{1}{\xi_1^A - \xi_E}\frac{\left((\xi_1^A)^2 - 2\xi_1^A\xi_E + \xi_E^2\right)^3}{\left(\xi_2^A - 2\xi_1^A\xi_E + \xi_E^2\right)^2} \tag{B.9b}$$

Region II ....

$$\left(\frac{\xi_1^A - \xi_2^A}{1-\xi_1^A} \leq \xi_E \leq \frac{\xi_1^A + \xi_2^A}{1+\xi_1^A}\right)$$
$$\xi_1^D = \xi_E + \frac{\left(\xi_2^A - \xi_E^2\right)^2}{\left(1-\xi_E^2\right)^2}\left(\xi_1^A - \xi_E\right) \tag{B.9c}$$

Region III..

$$\left(-1 \leq \xi_E \leq \frac{\xi_1^A - \xi_2^A}{1-\xi_1^A}\right)$$
$$\xi_1^D = \xi_E + \left(\xi_1^A - \xi_E\right)\left[1 + \frac{\xi_2^A - (\xi_1^A)^2}{\xi_2^A - 2\xi_1^A\xi_E + \xi_E^2} + \left(\frac{\xi_2^A - (\xi_1^A)^2}{\xi_2^A - 2\xi_1^A\xi_E + \xi_E^2}\right)^2\right] \tag{B.9d}$$

Region IV..

$$\left(\frac{\xi_1^A - \xi_2^A}{1-\xi_1^A} \leq \xi_E \leq \frac{\xi_1^A + \xi_2^A}{1+\xi_1^A}\right)$$
$$\xi_1^D = \xi_E + \frac{\left(1-\xi_E^2\right)\left(\xi_1^A - \xi_E\right)}{\xi_2^A - \xi_E^2}\left[1 - \left(\frac{1-\xi_2^A}{1-\xi_E^2}\right)^3\right] \tag{B.9e}$$

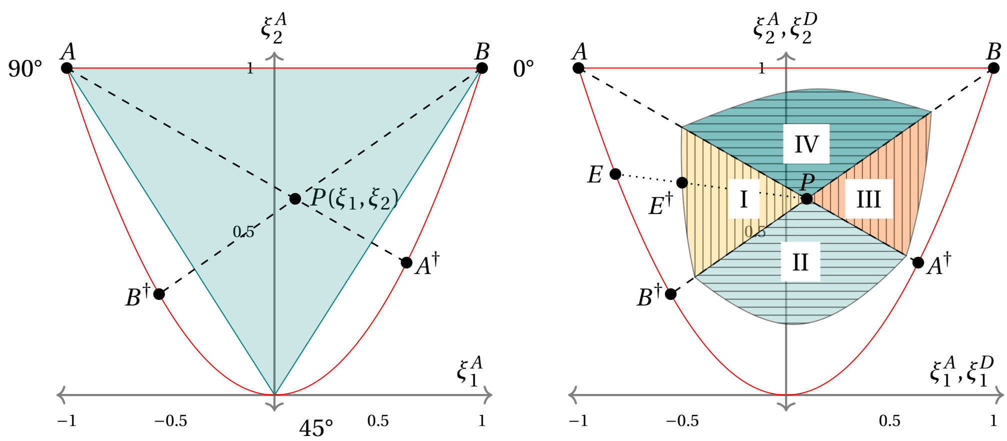

Figure B.1: (**left**) The feasible region for the in-plane lamination parameters corresponding to a laminate comprising 0°, 90° and ±45° orientations; and (**right**) the feasible region for the out-of-plane LPs for a specific point $P(\xi_1^A, \xi_2^A)$.

Appendix C Beam optimisation – Development of the tool

C.1. Optimisation of composite beam

C.1.1. System and data

To gain confidence and a better understanding of the intended approach, a single step multi-objective optimisation procedure is performed on a composite girder subjected to loads and boundary conditions as shown in Fig. C.1, in addition to gravity of $1g$.

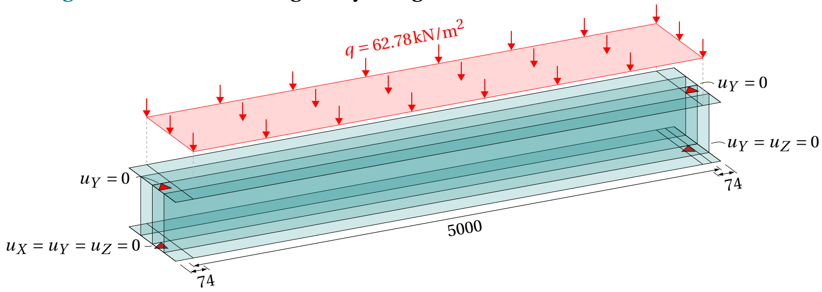

Figure C.1: A composite girder with support widths of 74 mm, span of $L = 5$ m subjected to $q = 62.78\,\mathrm{kN/m^2}$. Not to scale.

The adopted material properties are listed in Table C.1. These ply properties are derived based on the Rule of Mixtures (Appendix A.1), the resulting properties of which are shown in the two rightmost columns. The adopted constituent costs and GWPs are shown in the two bottom rows. Furthermore, the labour cost and GWP related to the composite assembly are taken as $c_L = 10.00\,€/\mathrm{kg}$ and $f_L = 0.57\ \mathrm{kgCO_2e/kg}$, respectively. Note that a different f_L is adopted in Chapter 6.

Table C.1: Fibre and resin properties and the related ply properties, $V_f = 55\%$ [3]

	Fibre		Resin	Ply	
	E-glass	Carbon	Polyester	E/P[a]	C/P[b]
Longitudinal modulus, E_1 [GPa]	73.1	238	3.5	40.55	128.52
Transverse modulus, E_2 [GPa]	73.1	15	3.5	12.86	7.56
Density, ρ [kg/m^3]	2570	1790	1200	1954	1525
Major Poisson's ratio, ν_{12} [-]	0.238	0.30	0.38	0.30	0.34
Shear modulus, G_{12} [GPa]	30	50	1.35	3.96	4.16
Thickness, t [mm]	-	-	-	0.125	0.125
Placeholder cost [€/kg]	3	30	4	-	-
GWP [$\mathrm{kgCO_2e/kg}$]	1.78	48.99	3.79	-	-

[a]E-glass/Polyester, [b]Carbon/Polyester

C.1.2. Variables

Geometrical parameters and variables

The top flange has a fixed breadth, analogous to the deck width in bridge design. The parameters describing the geometrical layout of the girder are shown in Fig. C.2, where the breadth of the bottom flange (b_{bf}), number of webs (n_{w}) and web height (h_{w}) are taken as the geometrical optimisation variables $\mathbf{y}$. The webs are evenly spaced within the breadth of the top flange, according to n_{w}. Therefore, the intermediate spacing c_{w} between the webs decreases with an increasing number of webs:

$$c_{\mathrm{w}} = (60, 45, 36, 30)\ \mathrm{mm} \qquad \forall \left\{c_{\mathrm{w}} \mid 2 \le n_{\mathrm{w}} \le 5\right\}$$

Consequently, only when an odd number of webs are selected the middle web is located along the centre of the flanges (see Fig. C.2).

Panel chromosome

The variables describing the panels can be illustrated through a chromosome: $X^j_{q,r}$, with $j \in \{1,2\}$ being the panel index, $q \in \{1,\ldots,Q\}$ being the ply group index (2Q in total), and $r \in \{1,\ldots,3\}$ being the

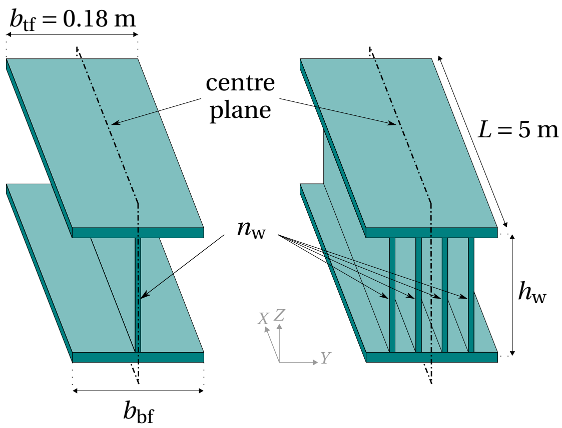

Variable	Bounds	Unit	Range
b_{bf}	[0.120, 0.300]	m	181
h_w	[0.150, 0.400]	m	251
n_w	$\{1, 2, \ldots, 5\}$	–	5

Figure C.2: Geometrical parameters and variables of the composite girder illustrating two arbitrary configurations.

properties associated with each ply. Here, $J = 2$ and $Q = 20$, where $j = 1$ and $j = 2$ refer to flanges and webs, respectively. The considered properties will be (a) ply thickness scaling $T_q = \{0, \ldots, 4\}$; (b) orientation $\theta_q = \{0°, \pm 45°, 90°\}$ encoded as $\theta_q = \{1, 2, 3\}$, where in the case $\theta_q = 2$, the ply thicknesses are halved; (c) material $M_q = \{1, 2\}$ corresponding to CFRP and GFRP. Hence, a chromosome representing a laminate has the following shape:

$$X^j_{q,r} = \begin{array}{cc} \begin{bmatrix} 1 & 1 & 1 \\ 1 & 2 & 2 \\ \vdots & \vdots & \vdots \\ 2 & 3 & 2 \end{bmatrix} & \begin{array}{c} q = 1 \\ q = 2 \\ \vdots \\ q = Q \end{array} \end{array} \tag{C.1}$$

The above chromosome (Eq. (C.1)) represents a laminate where the outermost ply group presents one layer oriented at 0° made of CFRP; and the innermost ply group is twofold, oriented at ±45° and made of GFRP.

C.1.3. Constraints

Material architecture-related constraints

Constraints regarding the ply thickness scaling of the ply groups (maximum five times):

$$X_{q,1} < 6 \quad \text{for} \quad q = \{1, \ldots, Q\} \tag{C.2}$$

Constraints regarding the orientation of the plies:

$$1 \leq X_{q,2} \leq 3 \quad \text{for} \quad q = \{1, \ldots, Q\} \tag{C.3}$$

Constraints regarding the materials – may only comprise material 1 or 2:

$$X_{q,3} < 3 \quad \text{for} \quad q = \{1, \ldots, Q\} \tag{C.4}$$

A maximum panel thickness of 20 mm is assured from the definition of variables, meaning that the thickness of panel j (t_j) is restricted to:

$$t_j = (2 \cdot 0.125)\ \text{mm} \cdot \sum_{q=1}^{Q} \left(X_{q,1}\right) \leq 20\,\text{mm} \quad \text{for} \quad j = \{1, 2\} \tag{C.5}$$

Structural response-related constraints

The structural response-related constraints are similar to those applicable for the bridge considered in Chapter 6, with a maximum deflection of:

$$\delta(\mathbf{x}) \leq \delta_{max} = \frac{L}{350} \approx 14.29\,\text{mm}, \tag{C.6}$$

a minimum fundamental frequency:

$$\Omega_0(\mathbf{x}) \geq 3.4\,\text{Hz}, \tag{C.7}$$

and a somewhat arbitrarily chosen buckling factor:

$$\delta_{cb}(\mathbf{x}) \geq 2.5. \tag{C.8}$$

C.1.4. Objective functions

The objectives, cost (F_1) and carbon footprint (F_2), are normalised with respect to their initial values, then combined to a pseudo-objective function (see Chapter 6.3.5 for further elaboration):

$$\boxed{F_1(\mathbf{x}) = \sum_{s=1}^{S} \rho_s(\mathbf{x}) V_s(\mathbf{x}) c_s(\mathbf{x}) + c_{\mathrm{L}} \cdot m(\mathbf{x})} \qquad \boxed{F_2(\mathbf{x}) = \sum_{s=1}^{S} \rho_s(\mathbf{x}) V_s(\mathbf{x}) f_s(\mathbf{x}) + f_{\mathrm{L}} \cdot m(\mathbf{x})}$$
$$\downarrow \qquad\qquad\qquad\qquad\qquad\qquad \downarrow$$
$$\boxed{F_1^*(\mathbf{x}) = \frac{F_1(\mathbf{x})}{F_1(\mathbf{x}^0)}} \qquad\qquad \boxed{F_2^*(\mathbf{x}) = \frac{F_2(\mathbf{x})}{F_2(\mathbf{x}^0)}} \tag{C.9}$$
$$\Phi(\mathbf{x}, r_p) = \boxed{F_1^*(\mathbf{x})} \cdot w_1 + \boxed{F_2^*(\mathbf{x})} \cdot w_2 + r_p \cdot P(\mathbf{x}), \qquad w_1 + w_2 = 1$$

where r_p (= 10000) is a penalty factor to enforce constraint satisfaction, w_1 (= 0.2) and w_2 (= 0.8) are the weights for the respective objectives.

C.2. Results & Discussion

The obtained solution is compared with an initial design to better quantify the improvement in the design. The initial geometry is taken as a GFRP I-beam, with anisotropic symmetric flanges and webs having the compositions $[0^g_{70\%}/+45^g_{10\%}/90^g_{10\%}/-45^g_{10\%}]_s$ and $[0^g_{35\%}/+45^g_{25\%}/90^g_{15\%}/-45^g_{25\%}]_s$, respectively. The geometry and the laminate configurations for the designs are shown in Fig. C.3, with further comparison of their corresponding features provided in Fig. C.4. Notably, excessive deflection and weak buckling resistance for the initial design amount to a high fitness value due to the penalties.

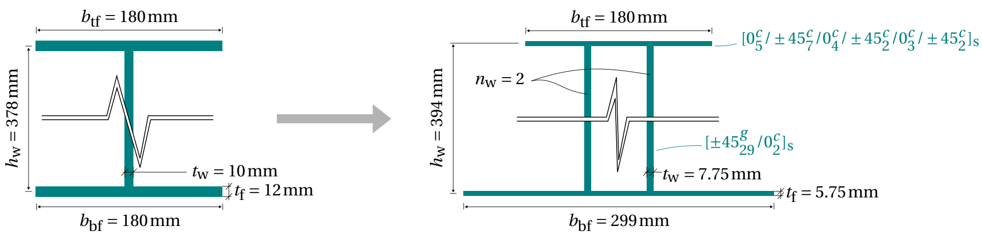

Figure C.3: From (**left**) initial configuration to (**right**) optimised girder definition: Geometry and laminate specifications.

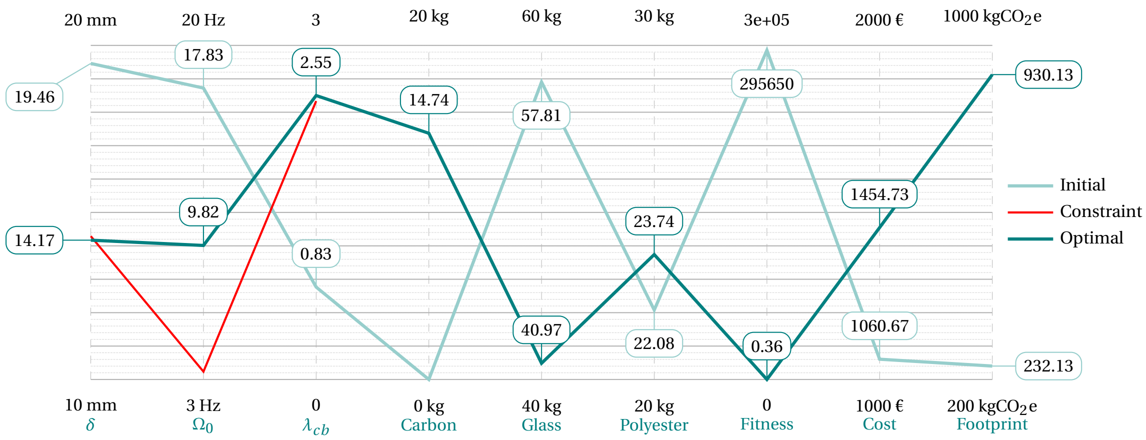

Figure C.4: Structural responses, masses of the constituents, and the corresponding objective values for the initial and optimal design.

Laminate specifications

With no specific requirement on the material architecture or structure of the laminates, the solution suggest laminates with high levels of contiguity and little diversity. The high portion of double biased (DB) mats in the flanges is immediately surprising, as it diminishes the stiffness of the beam. However, the governing buckling mode is buckling of the webs due to the support reactions. Thus, the flange configuration has transverse/shear stiffness to restrain rotation of the webs, ultimately decreasing the webs' buckling length. Double biased (DB) mats in the webs are expected, owing to the dominant shear that must be carried, in addition to the governing buckling mode, which is countered by ±45° reinforcement close to the surface.

Optimality of the solution

The most obvious result of the optimisation, is an increased cost and carbon footprint, owing to the initial solution infeasible, having insufficient stiffness and buckling resistance. Evidently, the deflection and buckling load factor are close to their constraint values, whereas the stiffness ensures that fundamental frequency easily exceeds the criterion. Any attempt to change the configurations, e.g. removing a ply or changing the material of a ply, makes the solution infeasible, confirming that the solution is a local optimum. However, applying the initial laminate specifications to the same geometry, satisfies the constraints with a much lower fitness value, meaning that the obtained solution is a consequence of premature convergence as the solver got stuck in a local optimum and failed to reach a global one. Apart from increasing the population size and modifying other optimisation options, one can overcome such issues by implementing adequate constraints. For this reason, several constraints on the material architecture are introduced in Chapter 6.

Adjustments

The element type and analyses fail to capture an important feature of FRP, namely that insufficient transverse stiffness in the flanges would lead to them folding about the webs, which can be prominent in non-linear analyses. Consequently, to overcome this phenomenon, additional constraints on the material architecture are introduced in Chapter 6, namely a minimum of 12.5 % fibres in each direction. This also helps to overcome non-linear stress behaviour and undesirable creep effects, discussed in Chapter 3.3.6

This investigation is not intended to serve as an example of a geometry that can be easily assembled, judging by the possibility to have 5 closely spaced webs. However, by introducing sandwich cores in the intermediate gaps, one can obtain desired geometry, while further increasing the buckling resistance of the cross-section. For the obtained geometry, a foam core of 60.00 mm – 7.75 mm = 52.25 mm would be necessary.

Appendix D Shell vs solid elements

The following illustrates the modelling of two 5 m long composite girders to compare the use of shell and solid shell elements, illustrating whether the influence of transverse shear is critical for moderately thick sandwich cores. With quadratic SHELL281 elements, ANSYS' ACP module offers the creation of a solid model based on the thicknesses of the laminates. In doing so, the shell elements are extruded appropriately, before these are divided through the thickness to represent a solid element model comprising SOLID186 elements [9].

As illustrated in Fig. D.2, an average element size of 10.00 mm is adopted. Furthermore, four elements are used through the thickness of the cores, whereas the DBLT mats are modelled using a singular element. For these analyses, the material properties are taken as represented in Table 6.2, using conversion factors adhering to SLS. Each DBLT mat consist of 4 layers of the GFRP plies, each having $\frac{1}{4}$ of its thickness. Thus, each total panel thickness is 21.158 mm.

The boundary conditions are illustrated in Fig. D.1, where restraints along the bottom flange edges represent pinned- and roller supports. A node at each top edge of the webs is restrained in Y-direction. The beams are subjected to a uniformly distributed load of $q = 1\,\mathrm{kN/m^2}$, applied to the top flange.

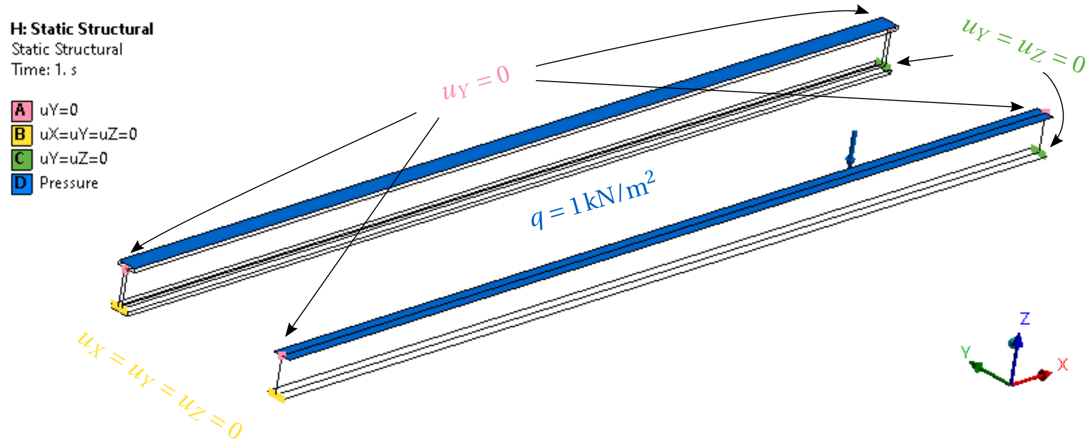

Figure D.1: The loads and boundary conditions adopted for the I-beams.

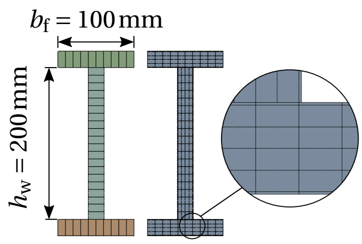

Figure D.2: Cross sections illustrating the thickness and mesh for the shell (**left**) and the solid (**right**) model. 4 elements are used through the thickness of the cores, while a singular element is used through the DBLT mat.

Appendix E Approximation of the ply thicknesses

E.1.1. Problem introduction

Initial estimates and configurations of the consituents' properties were assumed based on indications given in [3]. However, these configurations failed to correctly approximate the thicknesses of the laminates given in the reference model (designed by FiReCo). Therefore, instead of making numerous guesses, an optimisation problem was introduced, with which the aim is to define appropriate properties of the constituents such that the discrepancies between laminate thicknesses in the reference model and those in this thesis' model are reduced. This step is necessary in order to correctly evaluate the response and the masses of the different materials.

The structure follows the general elements of an optimisation problem: (1) the data, (2) the variables and their range of definition, (3) the constraints, and (4) the objective function to optimise.

To solve this problem, Matlab's® algorithm `fminimax` is used, which addresses the problem of minimising the maximum of a set of nonlinear functions, expressed as a goal attainment problem with goals of 0 and weights of 1 [10]:

$$\min_{x} \max_{i} \left(\frac{F_i(\mathbf{x}) - g_i}{w_i} \right)$$

with g referring to 'goal' and w to 'weight'. The optimisation options are taken as default, except that: the constraint tolerance is set to $1 \cdot 10^{-9}$, the step tolerance is set to $1 \cdot 10^{-9}$, and a central finite difference type is selected.

E.1.2. Data

The relevant ply properties are shown in Table E.1, which is a reduced version of Table 6.2. Note that the CSM100 and CSM300 mats constitute E-glass fibres and have the fibre mass proportions 100 g/m^2 and 300 g/m^2, respectively.

The layup of the two selected reference laminates are shown in Table E.2, where 'LT' refers to longitudinal-transverse (0°, 90°) and 'DB' refers to double-biased (±45°), and 'c' indicates CFRP plies of carbon/vinylester:

Table E.1: Ply properties for carbon/vinylester and glass/vinylester.

Property	**Symbol**	**Ply**	
		E/V[a]	C/V[b]
Density [kg/m^3]	ρ	1910	1500
Fibre mass proportion [g/m^2]	ζ	800	400

[a]E-glass/Vinylester, [b]Carbon/Vinylester

Table E.2: Reference laminates and their thicknesses.

Notation	**Layup**	**Thickness**
L12	CSM300 + 3DB + 2LT	3.2 mm
L23	CSM100 + 6DBc + CSM100	2.7 mm

The thicknesses of the respective layers/mats follow from the relevant fibre mass proportion ζ, fibre volume fraction V_f and density ρ:

$$t_{ply/mat} = \frac{\zeta}{V_f \cdot \rho} \tag{E.1}$$

where the fibre volume fraction for CSM differs from UD plies.

E.1.3. Variables and range of definition

The variables and their range:

$$\begin{aligned}
\text{E-glass fibre density [kg/m}^3\text{]:} &\quad 2500 \le x_1 \le 2600 \\
\text{Carbon fibre density [kg/m}^3\text{]:} &\quad 1700 \le x_2 \le 1800 \\
\text{Resin density [kg/m}^3\text{]:} &\quad 1000 \le x_3 \le 1200 \\
\text{Fibre volume fraction [-]:} &\quad 0.52 \le x_4 \le 0.54 \\
\text{Fibre volume fraction CSM [-]:} &\quad 0.2 \le x_5 \le 0.3
\end{aligned}$$

where the difference in fibre volume fraction for the UD plies and CSM mats owes to difficulties in achieving greater fibre volume fraction than 0.3 for CSM.

E.1.4. Constraints

There are two nonlinear equality constraints, as the resulting densities of the plies must correspond to those in Table E.1. The density of a ply follows from

$$\rho_f \cdot V_f + \rho_r \cdot (1 - V_f) \qquad \text{or equivalently} \qquad x_i \cdot x_4 + x_3 \cdot (1 - x_4) \qquad \text{for } i = 1, 2$$

hence the constraints read

$$x_1 \cdot x_4 + x_3 \cdot (1 - x_4) - 1910 = 0 \tag{E.2}$$

$$x_2 \cdot x_4 + x_3 \cdot (1 - x_4) - 1500 = 0 \tag{E.3}$$

E.1.5. Objective functions

There are two objectives, as the goal is to minimise the discrepancies between thicknesses of the reference laminates and those resulting from the optimisation. Table E.2 indicates the preferred thicknesses, and the stacking configuration. The thicknesses of the CSM300, CSM100, E-glass/vinylester and carbon/vinylester plies are, respectively, as follows:

$$t_{CSM300}(x_1, x_5) = \frac{300}{x_1 \cdot x_5} \cdot 10^3 \text{ mm} \tag{E.4a}$$

$$t_{CSM100}(x_1, x_5) = \frac{100}{x_1 \cdot x_5} \cdot 10^3 \text{ mm} \tag{E.4b}$$

$$t_{EV}(x_1, x_4) = \frac{800}{x_1 \cdot x_4} \cdot 10^3 \text{ mm} \tag{E.4c}$$

$$t_{CV}(x_2, x_4) = \frac{400}{x_2 \cdot x_4} \cdot 10^3 \text{ mm} \tag{E.4d}$$

from which the two objectives to minimise can be defined as:

$$F_1(\mathbf{x}) = \left(\frac{300}{x_1 \cdot x_5} + 5 \cdot \frac{800}{x_1 \cdot x_4} \right) \cdot 10^3 - 3.2 \, mm \tag{E.5}$$

$$F_2(\mathbf{x}) = \left(\frac{100}{x_1 \cdot x_5} + 6 \cdot \frac{400}{x_2 \cdot x_4} \right) \cdot 10^3 - 2.7 \, mm \tag{E.6}$$

E.1.6. Solution

The best found solution, i.e. the solution obtained when the constraints are satisfied to within the constraint tolerance and the size of the current search direction is less than twice the value of the step size tolerance, amounts to:

$$F_1(\mathbf{x}^*) = 0.0851 \qquad \text{and} \qquad F_2(\mathbf{x}^*) = 0.0296 \tag{E.7}$$

where $\mathbf{x}^*$ is the vector of 'optimal' design variables: $\mathbf{x}^* = [2559.3, 1147.8, 1800, 0.3, 0.54]^T$, expressed in terms material properties in Table E.3. The resulting thicknesses of the plies and laminates are given in Table E.4.

Table E.3: Densities and volume fractions to use for Klosterøybrua in Chapter 6

Variable	Property	Value	Unit
x_1	ρ_{GFRP}	2559.3	kg/m^3
x_2	ρ_{CFRP}	1800.0	kg/m^3
x_3	$\rho_{\mathrm{vinylester}}$	1147.8	kg/m^3
x_4	$V_{\mathrm{f,CSM}}$	0.3	-
x_5	V_{f}	0.54	-

Table E.4: Mat thicknesses corresponding to the properties in Table E.3 calculated with Eq. (E.1), and the resulting laminate thicknesses.

Type	Thickness acc. Eq. (E.1) [mm]
GFRP	0.5789
CFRP	0.4115
CSM100	0.1302
CSM300	0.3907

Laminate	Thickness [mm]	Error [%]
L12	3.2851	2.67
L23	2.7296	1.10

Appendix F Mesh Density Analysis

The mesh density analysis is an important step in making a compromise between computational power and efficiency. As the bottleneck of the optimisation procedure relies heavily on the time expended to generate the mesh and execute the analyses, it is paramount to arrive at a reasonable configuration when it comes to the chosen mesh size.

For this investigation, the parameters *mesh resolution* and *edge refinement factor* are varied, which collectively make sure that all the edges and openings are properly modelled. In Karamba, the mesh size is labelled **MRes**, depicting a target size which the software tries to achieve. The edge refinement, **ERef**, is a multiplication factor for the mesh size that determines the target edge length of faces at BREP-boundaries [11]. Naturally, lower values of both result in a greater number of nodes and more expensive calculations.

If the vertices of two neighbouring elements do not meet, i.e. identical vertices, there is no structural connection between them ensuing from a poor mesh configuration. Consequently, the structure may behave strangely and give unreasonable results.

Let $E_i \in (0.3, 0.35, ...0.85)$ denote the edge refinement factor, and $M_j \in (0.1, 0.15, ...1.0)$ m the mesh resolution. By iterating through E_i for M_j, a satisfactory compromise can be found. The decision is based on the computational time and the corresponding structural response, and their error. In this regard, no preference or order of importance is defined for the responses.

A mean error is calculated corresponding to all the possible configurations, by evaluating the average per response. The error for each individual response is obtained by considering the mean value of the for all values obtained when $M_1 = 0.1$ m. Then, the best (lowest) mean error is found for each M_j.

The plots in Fig. F.1 and Fig. F.2 illustrate how the computational time and mean error depend on the mesh size, respectively. For each mesh size, the corresponding best edge refinement factor is selected, indicated by the different colours. The 'calculation time' refer to one iteration of the entire script, i.e.:

1. Generate BREPs defining the geometry
2. Create mesh of the geometry
3. Conduct structural analyses
   - Linear analysis, Linear Bifurcation Analysis (buckling), Natural Frequency Analysis

where (2) and (3) are of interest, as (1) remains constant.

The error does not follow a linear pattern, as can be seen in the differences when $MRes$ goes from $MRes = 0.25$ to $MRes = 0.3$ (Fig. F.2). As visualised through the plots and in the table below, the configuration $MRes = 0.3$ m and $ERef = 0.7$ result in an error of 3.1 %, which is deemed appropriate.

Table F.1: Mesh density analysis showing the model's dependence on mesh size and edge refinement.

Mesh size resolution [m]	Edge refinement factor	Number of Elements	Number of Nodes	Time [ms]	Buckling factor	Deflection [mm]	Natural frequency [Hz]	Error [%]
10.00	0.40	168806	78071	75.73	20.84	37.78	4.32	0.16
15.00	0.60	68786	31660	42.83	20.63	38.07	4.36	0.14
20.00	0.65	37891	17026	34.28	20.25	37.20	4.52	0.96
25.00	0.70	24957	11007	30.15	21.54	36.54	4.55	3.32
30.00	0.70	18637	8111	27.48	22.11	36.90	4.71	2.11
35.00	0.60	16643	7114	26.99	21.97	36.39	4.73	2.57
40.00	0.70	11686	4906	25.03	19.53	36.39	4.51	2.47
45.00	0.75	9321	3908	23.88	18.70	36.68	4.66	3.56
50.00	0.75	7935	3305	23.77	19.18	36.35	4.72	2.46
55.00	0.60	8723	3600	24.32	18.54	36.51	4.68	2.86
60.00	0.55	8445	3461	25.03	20.41	35.81	4.69	3.06
65.00	0.45	9752	3915	24.13	25.09	35.81	4.54	3.01
70.00	0.45	8690	3502	23.02	21.35	35.57	4.70	4.13
75.00	0.40	9510	3822	24.18	25.75	35.26	4.55	3.54
80.00	0.55	6359	2569	23.77	20.94	35.18	4.95	3.48
85.00	0.35	9632	3856	24.57	24.86	35.29	4.55	3.48
90.00	0.35	8620	3467	25.15	21.14	34.96	4.72	4.17
95.00	0.30	9747	3922	24.74	21.98	35.03	4.55	4.40
100.00	0.30	9514	3812	27.28	25.99	34.84	4.55	5.02

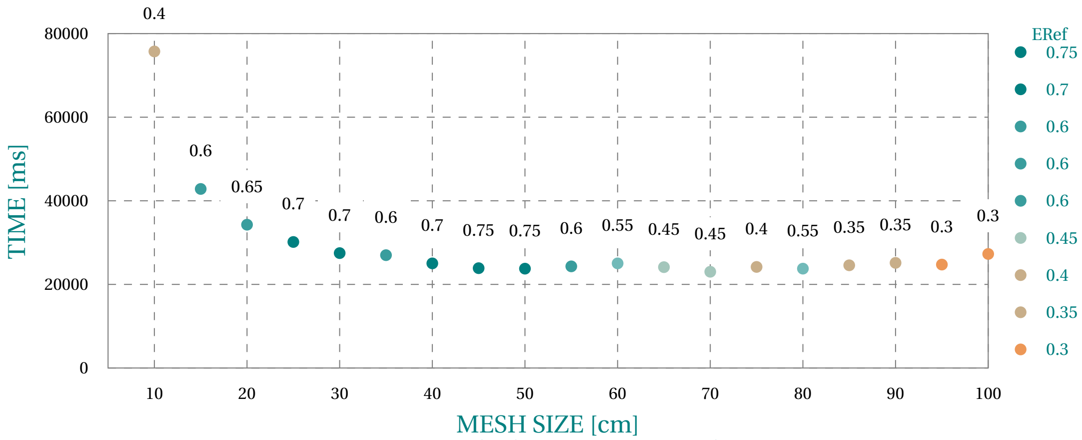

Figure F.1: Calculation time vs mesh size.

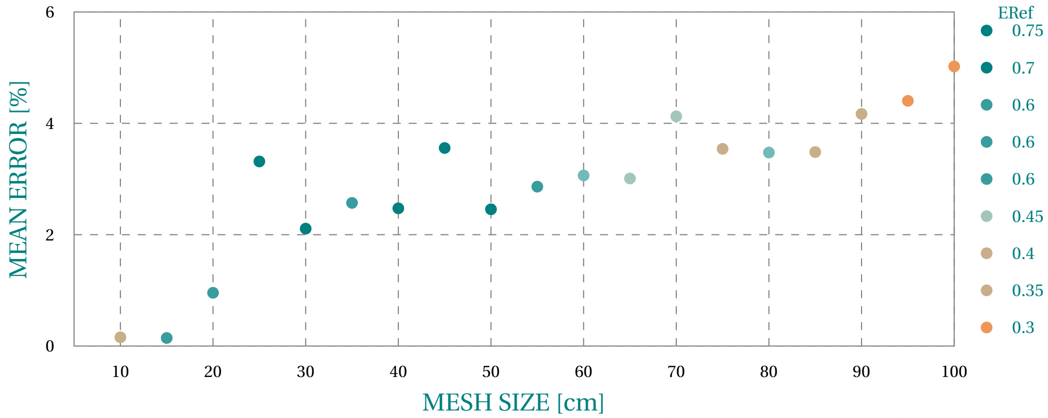

Figure F.2: Mean error vs mesh size. MRes = 30 cm depicts the chosen value.

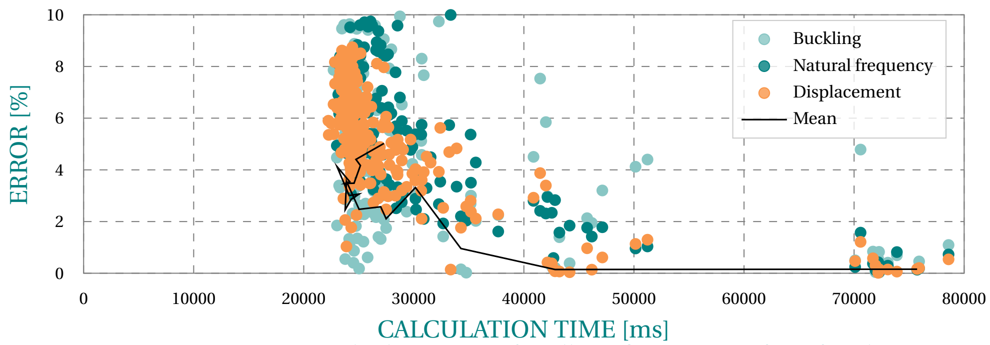

Figure F.3: Error vs calculation time for all configurations of ERef and MRes.

Figure F.3 shows the error corresponding to each response, plotted for all configurations of E_i and M_j, limited to an error of 10 %. The black line illustrates the mean error of the responses. As shown, the buckling load factor fluctuates the most among the configurations, while also having the greatest contribution to the mean error. Though it seem to converge around 45 seconds (negligible improvement beyond this point), the error of 2% at 27 seconds serves as a good compromise. In the case of 200 generations with a population size of 80, a ten seconds increase in calculation time amounts to a of almost two days (44.4 hours).

Appendix G Cost and global warming potentials

G.1. Constituent costs and global warming potential

Global warming potential

Since access to LCA databases is hindered by subscription fees, the environmental data is taken from EUCia EcoCalculator [12]. Retrieving the environmental impacts for the adopted materials is done as follows from the online software, resulting in the values shown in Table G.1, where EE refers to the embodied energy: EE

1. Define a product with a net weight of 1 kg.
2. Do not include any conversion process, i.e. only consider the materials' contribution.
3. For all constituents, calculate the carbon footprint of 1 kg material.
4. Finally, add a conversion process to obtain the contribution from the selected manufacturing process.

Albeit the intended processing method is VARTM, or vacuum infusion, a GWP relating to processing is assumed considering pultrusion. Hence, from step (4), the global warming potential related to the labour is $f_L = 3.55\ \mathrm{kgCO_2e/kg}$.

Costs

The adopted costs are derived from estimates provided by the supervisors, and represent placeholder values per unit kg material. Noting that the foam costs are presented in Appendix G.2, the remaining values are given in the rightmost column of Table G.1. The CSM-mats are made of E-glass, thus no explicit cost is reported.

Table G.1: Environmental impacts and costs associated with materials [12].

	EE [MJ/kg]	GWP [$\mathrm{kgCO_2e/kg}$]	COST [€/kg]
Vinylester resin[a]	121.54	3.79	4.00
Carbon fibre[b]	1040.87	48.99	30.00
Glass fibre[c]	36.11	1.81	3.00
CSM[d]	22.85	1.51	-
PVC	72.80	2.86	-

[a]VE Resin (BPA exopy based), [b]Carbon fibre (new), [c]Glass fibre mats, [d]Glass fibre dry chopped strands

G.2. Costs of foam core

For the foam cores used in this thesis, the assumed properties and costs correspond to those provided by Diab. This company was originally founded in Sweden in the 50's, and has ever since gain traction world wide.

The costs provided by the Norwegian sales unit of Diab are shown in Table G.2 below, indicating thicknesses of 20, 30 and 40 mm[1]. These costs include cutting, handling and packaging, and do not follow a linear distribution.

Table G.2: Costs of various PVC foam panels.

Article no.	**Article**	**Cost** [NOK/m^2]	**Cost*** [€/m^2]
1008020	H80 20 PSC 2440x1220	101.32	9.97
1008030	H80 30 PSC 2440x1220	557.00	54.82
1008040	H80 40 PSC 2440x1220	724.00	71.26

*Calculated with the exchange rate 10.16 (NOK) to 1 (€).

From the given costs, a reference value is calculated for each 5 mm increment between 20 and 40 mm, i.e. $\{20, 25, \ldots, 40\}$, based on a polynomial regression. The result are shown in Fig. G.1. It follows that the adopted costs are approximations, purely based on the unit cost per square meter. More accurate approximations should consider cutting of the mats, as this would likely introduce waste.

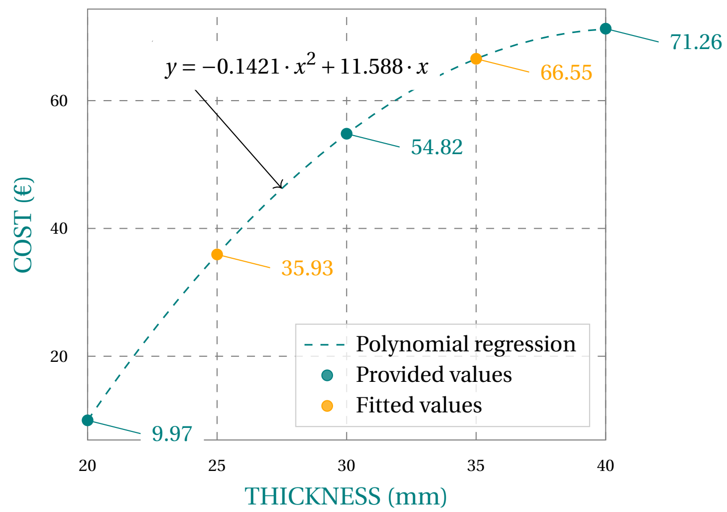

Figure G.1: Cost of PVC H80 panels.

[1] (Diab Group®, personal communication, Dec 13, 2021)

Appendix H Grasshopper definition – the Klosterøy bridge

H.1. Canvas definition with simplifications

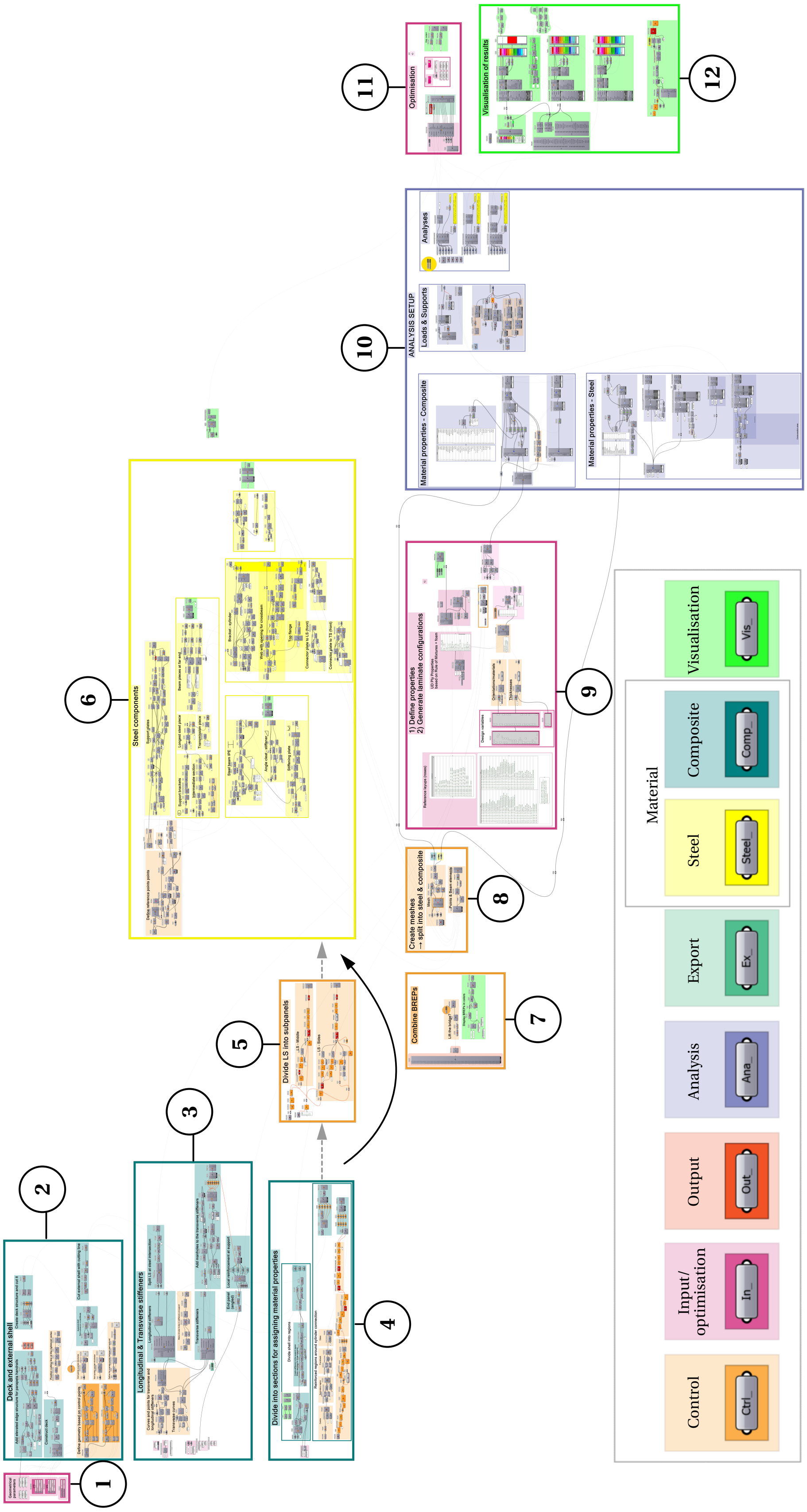

Figure H.1: The Grasshopper canvas illustrating the parametric definition of the Klosterøy bridge. The adopted colour scheme helps to orient within the graphical programming interface. Zoom to see details.

The Grasshopper definition in Fig. H.1 is simplified to help clarify the flow of the script. Generally, Grasshopper definitions go strictly from left to right; however, some modification is required to squeeze the definition into a readable figure. The definition can be split into 12 distinct groups or steps.

Some of these steps are visualised in Fig. H.2. (11) controls the geometrical parameters[1] in (1), which defines the control points from which a loft is created, defining the exterior shell, before the end is cut at an angle. In (3), the longitudinal and transverse stiffeners are added. (4) divides the exterior shell in three: a bottom piece, sides/diagonals, and the top/verticals. (5) introduces further optional divisions, accordant to FiReCo's reference model. In (6) the steel components are created, before all the BREPs are combined in (7). A mesh is created from the surface elements in (8). In (9), the costs and constituent properties are defined, while sandwich panels are created – controlled by (11) – and their in-plane properties calculated through CLT. The analyses are prepared in (10), defining supports and loads; and quite importantly, the composite panels are oriented according to the right-hand rule. Finally, the structural responses can be visualised in (12).

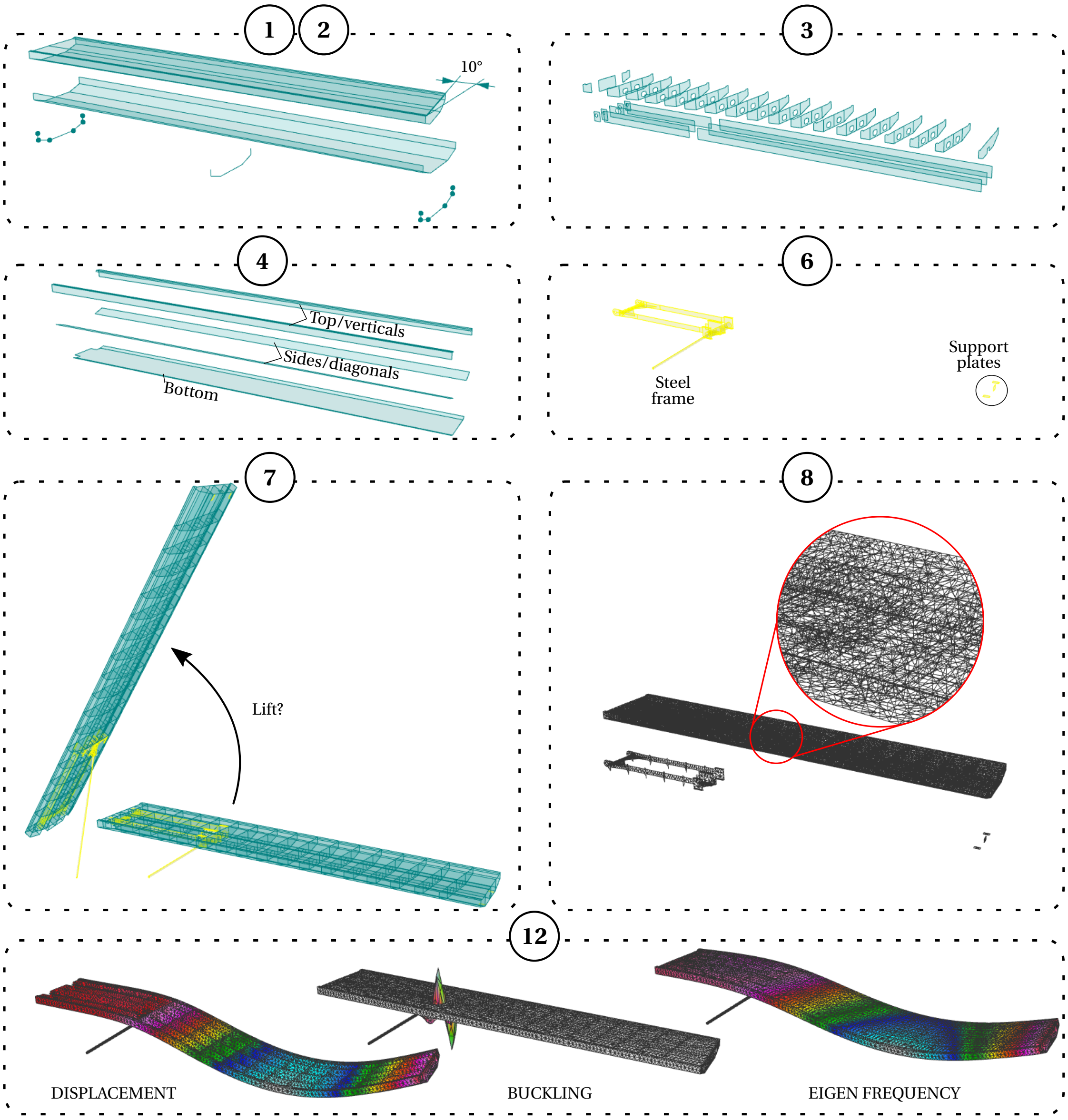

Figure H.2: Visual representation of what the groups in Fig. H.1 result in, emphasising important groups.

[1] variables

Appendix I Laminate codes and description

I.1. Laminate codes, reinforcement and panel roses

The following appendix describes the adopted reinforcement notations, illustrating some of the configurations to further clarify the scheme. First, the reinforcements and core qualities are described in Table I.1 and Table I.2, respectively.

Table I.1: Reinforcement

Code	Description
CSM100	100 g/m^2 CSM E-glass
CSM300	300 g/m^2 CSM E-glass
DB	800 g/m^2 E-glass
DBLT	800 g/m^2 E-glass
LT	800 g/m^2 E-glass
DBc	400 g/m^2 Carbon
Lc	800 g/m^2 Carbon

DB = double-biased, LT = longitudinal-transverse, c = carbon

Table I.2: Core qualities

Code	Description
K1	PVC H80 (DIAB)
K2	PET
K3	DBLT Single skin laminate

K3 is originally used in composite-to-steel connections to increase the bearing strength.

A collection of important face sheet configurations (laminates) are given in Table I.3, wherein the ply and mat thickness are taken from Appendix E, Table E.4. The stacking order is described chronologically from the outside, inwards towards the core of the panel. In practise, woven mats are used in favour of stacked UD layers. However, for modelling purposes, the layers herein are discretised ply by ply, including the appropriate amount of resin (see visualisation of a DB mat below).

Table I.3: Laminate notations with their corresponding stacking order and laminate thickness

Notation	Stacking order (towards core)	Thickness [mm]
L11	CSM300 + 4(9Lc+DB) + 2LT + DB	18.51
L12	CSM300 + 3DB + 2LT	3.29
L13	2LT + DB + CSM300	2.13

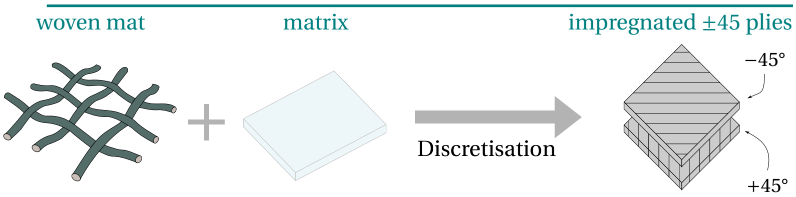

Roses

In order to systematically keep track of common laminates, roses are used to indicate their layup. The rose (Fig. I.1) below represents the adopted deck configuration of the Klosterøy bridge, where the L11 laminate (with CSM closest to the surface) is the top face sheet, and the L13 laminate is the bottom face sheet, with CSM closest to the interior of the bridge. These are offset from each other by a K2-quality core (PET), with a thickness of 93 mm.

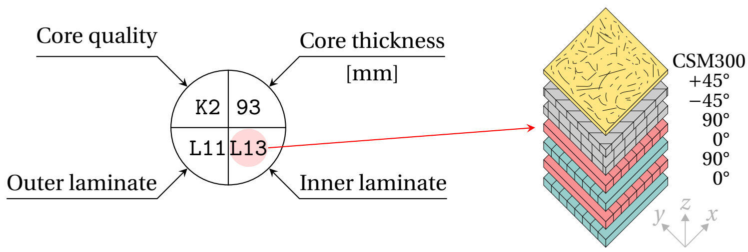

Figure I.1: Rose describing a panel configuration. This example illustrates the adopted simplification of the bridge deck, with a 93 mm thick PET core. The L13 face sheet is illustrated.

I.2. Laminate codes – Reference model

Table I.4: Laminate notations with their corresponding stacking order and laminate thickness

Location	Notation	Stacking order (towards core)	Thickness [mm]
Deck	L11	CSM300 + 4(9Lc+DB) + 2LT + DB	18.51
	L12	CSM300 + 3DB + 2LT	3.29
	L13	2LT + DB + CSM300	2.13
Stiffeners	L20	CSM100 + 4DB + CSM100	2.58
	L21	CSM100 + 8DB + CSM100	4.89
	L22	CSM100 + 10DB + CSM100	6.05
	L23	CSM100 + 6DBc + CSM100	2.73
	L24	CSM100 + 12DBc + CSM100	5.20
Bottom	L30	CSM300 + 4DB + CSM100	2.84
	L31	CSM100 + 4DB + CSM100	2.58
	L32	CSM300 + 2DB + 12Lc + DB + 12Lc + DB + CSM100	12.71
	L33	CSM100 + DB + 12Lc + DB + 12Lc + 2DB + CSM100	12.45
	L34	CSM300 + DB + 4Lc + DB + 4Lc + DB + CSM100	2.26
	L35	CSM100 + DB + 4Lc + DB + 4Lc + DB + CSM100	2.00
	L36	CSM300 + 2DB + 8Lc + DB + 8Lc + DB + CSM100	2.84
	L37	CSM100 + DB + 8Lc + DB + 8Lc + 2DB + CSM100	2.58
	L38	CSM300 + 5DB + 12Lc + DB + 12Lc + DB + CSM100	4.57
	L39	CSM100 + DB + 12Lc + DB + 12Lc + 5DB + CSM100	4.31
Bottom	L40	CSM300 + 5DB + 18Lc + DB + 18Lc + 5DB + CSM100	21.70
	L41	CSM100 + DB + 18Lc + DB + 18Lc + 5DB + CSM100	19.13
	L42	CSM300 + 7DB + 12DBLT + CSM100	11.52
	L43	CSM100 + 7DB + 12DBLT + CSM100	11.26
	L44	CSM300 + 4DB	2.71
Sides	L50	CSM300 + 4DB + CSM100	2.84

I.3. Panel configurations – Reference model

The divisions and configurations of the various panels as adopted in the reference model are illustrated herein. Through comparison with the adopted element model, the simplification is clarified further. As mentioned, the reasoning behind these simplifications comes from stress analyses considerations that are not implemented, specifically thermal-, joint- and connection analyses. The laminate notations are provided in Appendix I.2, Table I.4.

I.3.1. Exterior shell

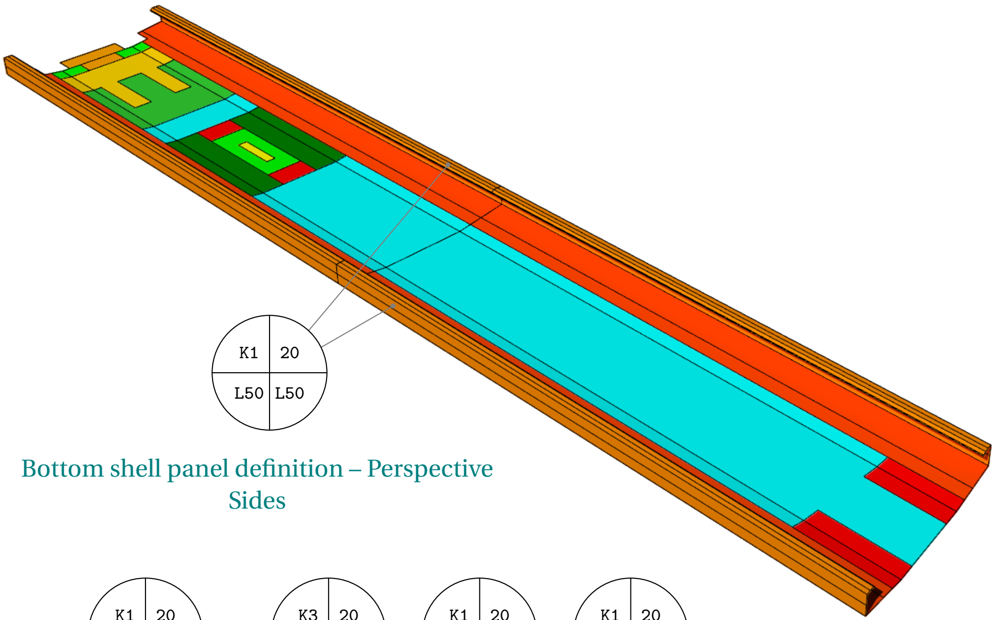

Bottom shell panel definition – Perspective
Sides

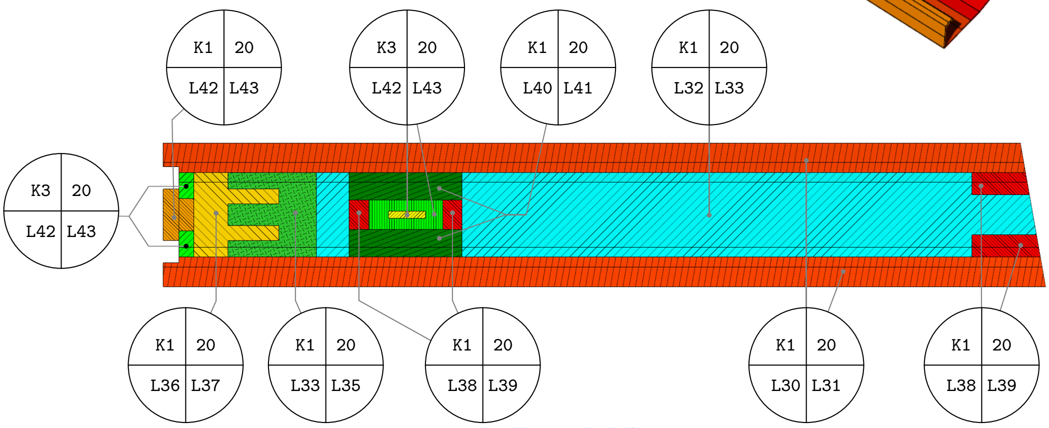

Bottom shell panel definition – Top View

I.3.2. Transverse Stiffeners

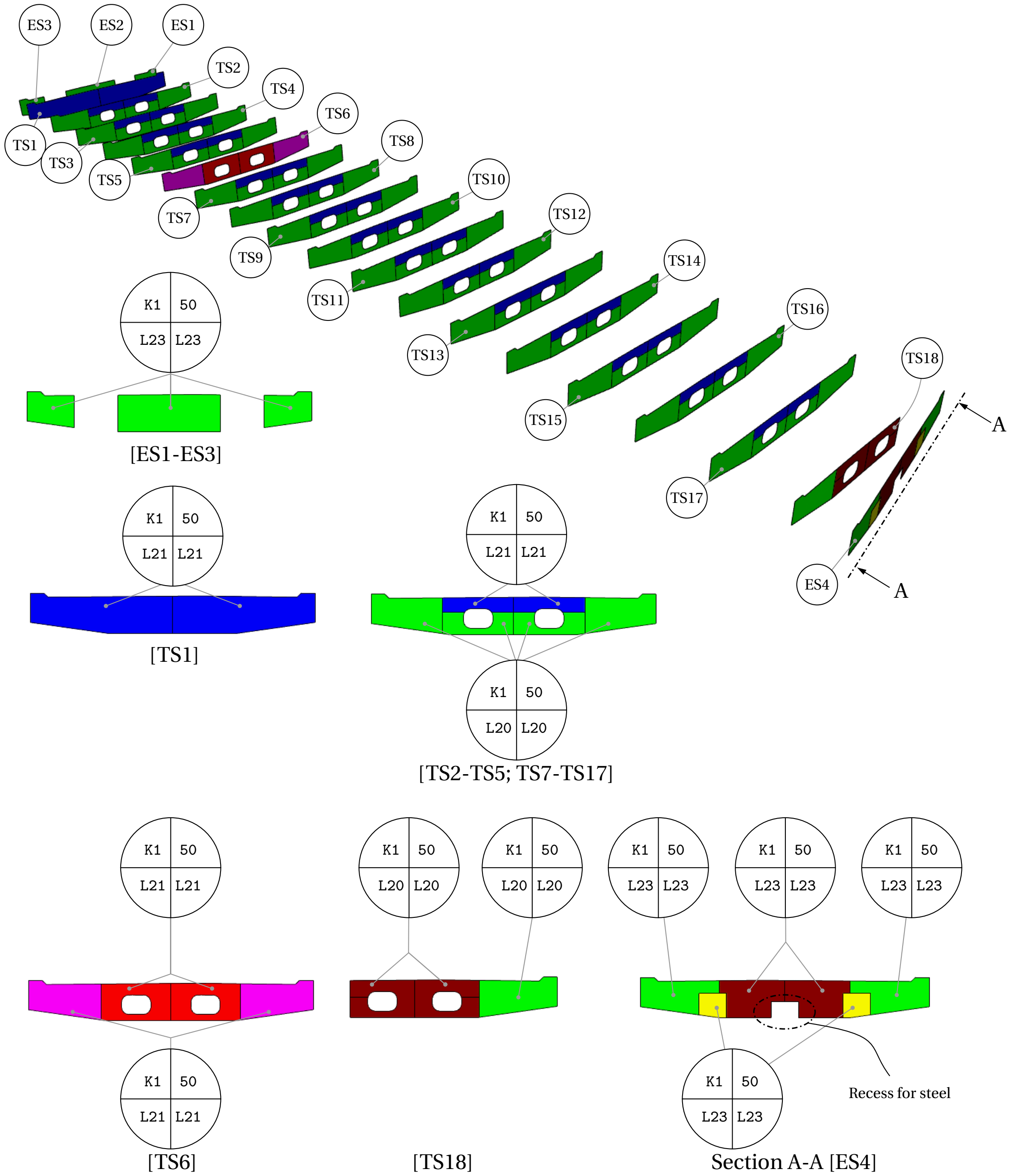

I.3.3. Longitudinal stiffeners

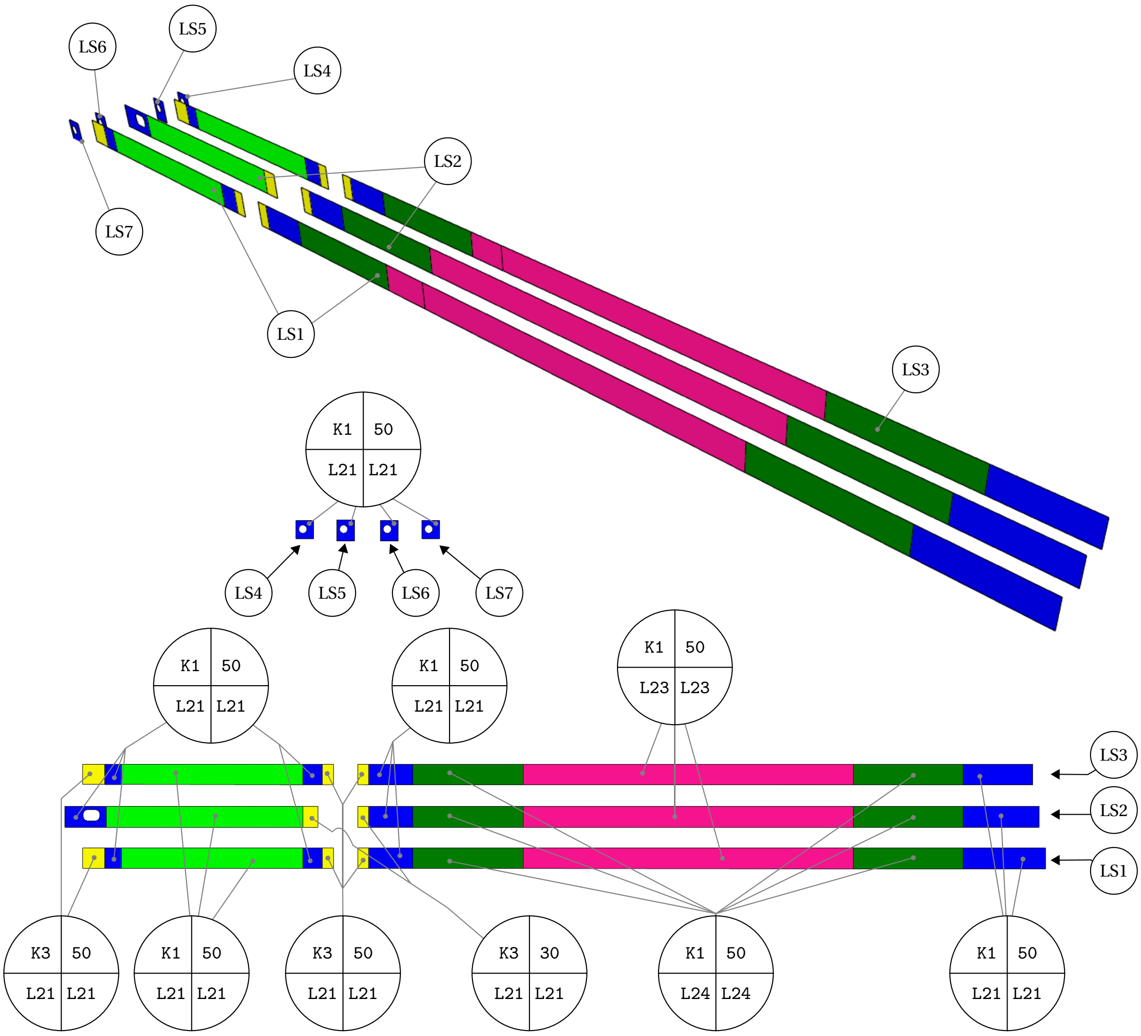

Appendix J Analytical solution – The Kloster bridge

J.1. Derivation of beam equations – Timoshenko beam theory (Maple)

The bridge structure is discretized as a continous beam comprising the spans L_1 and L_2 ($L_1 \neq L_2$).

The following derivation illustrates how to obtain the beam equations for such beams, assuming constant properties of the cross-section.

Two ODEs are needed for each subspan:

1) for $x = 0$ to $x = L_1$:

```
> ODE1 := EI * diff(phi1(x),x$2) - GA * (diff(w1(x),x) + phi1(x)) = 0: ODE1;
```

$$EI\left(\frac{d^2}{dx^2}\,\phi 1(x)\right) - GA\left(\frac{d}{dx}\,w1(x) + \phi 1(x)\right) = 0 \tag{1}$$

```
> ODE2 := GA * (diff(w1(x),x$2) + diff(phi1(x),x)) = -q: ODE2;
```

$$GA\left(\frac{d^2}{dx^2}\,w1(x) + \frac{d}{dx}\,\phi 1(x)\right) = -q \tag{2}$$

2) for $x = L_1$ to $x = L_2$:

```
> ODE3:= EI * diff(phi2(x),x$2)- GA * (diff(w2(x),x) + phi2(x)) = 0: ODE3;
```

$$EI\left(\frac{d^2}{dx^2}\,\phi 2(x)\right) - GA\left(\frac{d}{dx}\,w2(x) + \phi 2(x)\right) = 0 \tag{3}$$

```
> ODE4:= GA *(diff(w2(x),x$2) + diff(phi2(x),x)) = -q: ODE4;
```

$$GA\left(\frac{d^2}{dx^2}\,w2(x) + \frac{d}{dx}\,\phi 2(x)\right) = -q \tag{4}$$

Solve ODEs

```
> solution := dsolve({ODE1,ODE2,ODE3,ODE4},{w1(x),phi1(x),w2(x),phi2(x)}): assign
  (solution):
> w1 := w1(x): phi1 := phi1(x): w2 := w2(x): phi2 := phi2(x):
> gamma__1 := diff(w1,x) + phi1: kappa1 := diff(phi1,x): gamma__2 := diff(w2,x)+
  phi2: kappa2 := diff(phi2,x):
> V1 := GA * gamma__1: M1 := EI * kappa1: V2 := GA * gamma__2: M2 := EI * kappa2:
```

Boundary and interface conditions

> zero displacement and moment:

```
  x := 0: eq1 := w1=0: eq2 := M1=0:
```

> zero displacement and moment:

```
  x := (L__K): eq3 := w2=0: eq4 := M2=0:
```

> zero displacement, equal moment, equal rotation:

```
  x := L__1: eq5 := w1=0: eq6 := w2=0: eq7 := M1=M2: eq8 := phi1=phi2:
```

Next, we solve for the displacement, bending moments etc..

```
> solution := solve({eq1,eq2,eq3,eq4,eq5,eq6,eq7,eq8},{_C1,_C2,_C3,_C4,_C5,_C6,
  _C7,_C8}): assign(solution): x := 'x':
```

Displacement fields

```
> w__1(x) = simplify(w1);
```

$$w_1(x) = \frac{1}{24\,GA\left(-\frac{L_1\left(L_1-L_K\right)GA}{3}+EI\right)EI}\left(q\left(x-L_1\right)\left(-\frac{\left(L_1-L_K\right)\left(\frac{L_1^3}{2}+\left(\frac{x}{2}-\frac{3\,L_K}{2}\right)L_1^2+\left(x-\frac{L_K}{2}\right)\left(x-L_K\right)L_1+\frac{x\,L_K^2}{2}\right)GA^2}{3}+EI\left(3\,L_1^2+\left(-x-4\,L_K\right)L_1+x^2\right)GA-12\,EI^2\right)x\right) \tag{5}$$

```
> w__2(x) = simplify(w2);
```

$$w_2(x) = \frac{1}{24\,GA\left(-\frac{L_1\left(L_1-L_K\right)GA}{3}+EI\right)EI}\left(q\left(x-L_1\right)\left(x-L_K\right)\left(-\frac{\left(\frac{L_1^3}{2}+\left(\frac{x}{2}-\frac{L_K}{2}\right)L_1^2+\left(x^2-\frac{3}{2}\,x\,L_K-\frac{1}{2}\,L_K^2\right)L_1-\left(x-\frac{3\,L_K}{2}\right)x\,L_K\right)L_1\,GA^2}{3}+\left(3\,L_1^2+\left(-x-L_K\right)L_1+x^2-x\,L_K-L_K^2\right)EI\,GA-12\,EI^2\right)\right) \tag{6}$$

Bending moments

```
> M__1(x) = simplify(M1);
```

$$M_1(x) = -\frac{12\,q\left(\frac{GA\,L_1^3}{12}-\frac{GA\left(x-\frac{L_K}{2}\right)L_1^2}{3}+\left(\frac{L_K\left(x-L_K\right)GA}{3}-EI\right)L_1+\frac{GA\,L_K^3}{12}+EI\,x\right)x}{-8\,GA\,L_1^2+8\,GA\,L_1\,L_K+24\,EI} \tag{7}$$

```
> M__2(x) = simplify(M2);
```

$$M_2(x) = -\frac{12\,q\left(x-L_K\right)\left(\frac{GA\,L_1^3}{12}-\frac{GA\left(x+\frac{L_K}{4}\right)L_1^2}{3}+\left(\frac{\left(x-\frac{L_K}{4}\right)L_K\,GA}{3}-EI\right)L_1+EI\,x\right)}{-8\,GA\,L_1^2+8\,GA\,L_1\,L_K+24\,EI} \tag{8}$$

Shear forces

```
> V__1(x) =(V1);
```

$$V_1(x) = GA\left(\frac{q\left(-GA\,L_1^3-2\,GA\,L_K\,L_1^2+4\,GA\,L_1\,L_K^2-GA\,L_K^3+12\,EI\,L_1\right)}{8\,GA\left(-GA\,L_1^2+GA\,L_1\,L_K+3\,EI\right)}-\frac{q\,x}{GA}\right) \tag{9}$$

```
> V__2(x) = (V2);
```

$$V_2(x) = GA\left(\frac{q\left(-GA\,L_1^3-3\,GA\,L_K\,L_1^2+5\,GA\,L_1\,L_K^2+12\,EI\,L_1+12\,EI\,L_K\right)}{8\,GA\left(-GA\,L_1^2+GA\,L_1\,L_K+3\,EI\right)}-\frac{q\,x}{GA}\right) \tag{10}$$

J.2. Assumptions and properties

Klosterøybrua Analytical Solution

The calculations carried out in the following serves as a verification of the numerical results (FEA). It also helps to quantify how the optimisation not only simplifies the design procedure, but how it efficiently can improve the design.

The calculations coincide with the constraints defined in the thesis, aiming to make a design that at least meets the deflection and buckling requirements. The latter is quantified by means of critical stresses, and not evaluated against a single buckling load factor (λ_{cr}). Reiterating these constraints:

1. Deflection constraint: $\delta \le \frac{L}{350}$
2. Buckling constraint: $\lambda_{cr} \ge 6$

The fundamental frequency is rather complicated to determine analytically owing the complex geometry. It is thus disregarded.

Furthermore, each laminate (face sheet) must have at least 12.5% of fibres oriented at each direction, i.e. at least 12.5 % orientated at 0°, 45°, 90° and - 45°.

Assumptions

Although several assumptions are made as they appear applicable throughout this calculation sheet, it will be assumed that:

- the deck structure is flat and no (longitudinal) curvature is present;
- the loaded area is the width between the parapets and hand rails;
- only the vertical uniformly distributed load $q_{fk} := 5kPa$ (EN 1991-2) is present;
- the panels may comprise carbon/vinylester, glass/vinylester with a PVC foam core;
- the cross section is made by vacuum infusion and a fibre volume fraction of $V_f := 54\%$ is achieved;
- the cross-section is constant, neglecting the transverse stiffeners with intermediate spacings;
- shear lag can be disregarded; and
- the contribution of the steel frame can be neglected.

Conversion factors:

The conversion factors are calculated in accordance with the JRC 2017 draft document. No specific conversion factors related to creep effects are considered.

Influence of fatigue:

No specific fatigue load cycles are defined for footbridges according to EN 1991-2.

$\eta_{cf} := 1.0$

Influence of moisture:

The surroundings of the bridge position the structure within exposure class II:

$\eta_{cm} := 0.9$

Thermal influence:

The service temperature is in the range: $T_{min} := -35$ $T_{max} := 36$

Glass transition temperatures (°C):

$T_{g.resin} := 100$ $T_{g.PVC} := 80$ $T_{g.epoxy} := 100$

$T_g := min\left(T_{g.resin}, T_{g.PVC}, T_{g.epoxy}\right) = 80 \quad °C$

For verification of deformability:

$$\eta_{ct.SLS} := \left| \begin{array}{l} 1.0 \quad if \quad T_{max} < T_g - 40 \\ 0.9 \quad if \quad T_g - 40 < T_{max} < T_g - 20 \end{array} \right. = 1$$

1/15

For verification of strength and stability:

$\eta_{ct.ULS} := 0.9$ $\eta_{ct.stab} := \eta_{ct.ULS}$

Overall conversion factor:

$\eta_{c.SLS} := \eta_{ct.SLS} \cdot \eta_{cm} \cdot \eta_{cf} = 0.9$ $\eta_{c.ULS} := \eta_{ct.ULS} \cdot \eta_{cm} \cdot \eta_{cf} = 0.81$

Partial safety factors:

The partial safety factors are defined according to Tables 2.1 and 2.2 of the JRC (2017) document. JRC states that the quality corresponds to $V_x < 0.1$ if vacuum infusion is used.

The UD plies have material properties which are derived from test. These are then used to determine the laminate properties through classical lamination theory (CLT). Therefore,

$\gamma_{M1} := 1.15$ material properties derived from tests + CLT

Conditions	ULS (strength)	Local stability	Global stability
Production processes and properties of FRP with $V_x \leq 0.10$	1.35	1.5	1.35

ULS Strength

$\gamma_{M2} := 1.35$

$\gamma_{M.str} := \gamma_{M1} \cdot \gamma_{M2} = 1.553$

Local stability

$\gamma_{M2} := 1.5$

$\gamma_{M.loc} := \gamma_{M1} \cdot \gamma_{M2} = 1.725$

Global stability

$\gamma_{M2} := 1.35$

$\gamma_{M.glo} := \gamma_{M1} \cdot \gamma_{M2} = 1.553$

Note that the numerical results are obtained disregarding partial factors. Therefore, for comparison, they will not be implemented.

Material and geometrical properties

It is assumed that the loaded area of the deck does not include the parapets or the elevated side structure to which the handrails are connected. The deck is assumed to be perfectly flat. Some of these parameters are taken from the FE model.

$b_{deck} := 5.0997m$

The end of the bridge is cut at angle of 10 degrees, resulting in different side lengths:

$L_{right\_side} := 35.8405m$ $cut\_angle := 10deg$

$L_{left\_side} := L_{right\_side} - b_{deck} \cdot tan(cut\_angle) = 34.941\ m$

As a further simplification, disregarding the possible torsional effects of the cut end, the length is of the bridge is taken as the average of the two sides.

$$L_K := \frac{L_{right\_side} + L_{left\_side}}{2} = 35.391\ m$$

K denotes Klosterøybrua

Assuming that the beam can be considered as continuous, neglecting the contribution of the internal steel frame from x=0 to the connection to the cylinder. It is also assumed that the cylinder provides an infinitely stiff support, i.e. no deflection. The centre of the cylinder support is approximately at $X_{syl} := 9.9137 \cdot m$. This results in two sub spans:

$$L_1 := \frac{X_{syl}}{L_K} \cdot L_K = 9.914\ m \qquad L_2 := L_K - L_1 = 25.477\ m \qquad L_f := \frac{L_1}{L_K} = 0.28$$

2/15

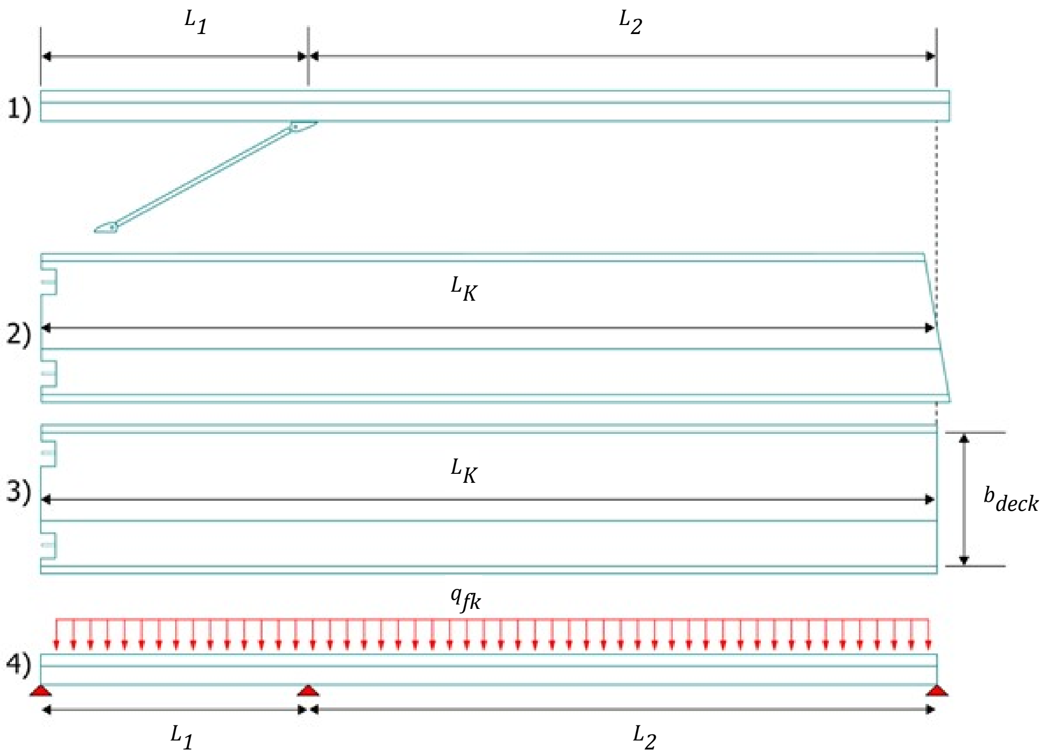

1) Elevation view. 2) Top view. 3) Simplified geometry. 4) Bridge discretized as beam.

Densities:

$\rho_{glass} := 2559.259 \frac{kg}{m^3}$ $\quad \rho_{carbon} := 1800 \frac{kg}{m^3}$ $\quad \rho_{resin} := 1147.826 \frac{kg}{m^3}$

$\rho_{EV} := 1970 \frac{kg}{m^3}$ E-glass/vinylester $\quad \rho_{CV} := 1500 \frac{kg}{m^3}$ Carbon/vinylester $\quad \rho_{PVC} := 80 \frac{kg}{m^3}$ Foam

$\rho_{carbon} \cdot V_f + \rho_{resin} \cdot (1 - V_f) = 1500 \frac{kg}{m^3}$ $\quad \rho_{glass} \cdot V_f + \rho_{resin} \cdot (1 - V_f) = 1910 \frac{kg}{m^3}$

E-glass/Vinylester ply properties

$E_{1.EV} := 42GPa$ $\quad E_{2.EV} := 8.5GPa$ $\quad G_{12.EV} := 3GPa$ $\quad t_{EV} := 0.578871201158 \cdot mm$

$\nu_{12.EV} := 0.26$ $\quad \nu_{21.EV} := \nu_{12.EV} \frac{E_{2.EV}}{E_{1.EV}} = 0.053$ $\quad t_{CSM} := 0.13024602026 \cdot mm$

Carbon/Vinylester ply properties

$E_{1.CV} := 125GPa$ $\quad E_{2.CV} := 5.5GPa$ $\quad G_{12.CV} := 2GPa$ $\quad t_{CV} := 0.411522633745mm$

$\nu_{12.CV} := 0.3$ $\quad \nu_{21.CV} := \nu_{12.CV} \frac{E_{2.CV}}{E_{1.CV}} = 0.013$

3/15

J.3. First iteration

First iteration

The buckling resistance of shear-dominated panels is in favour of +-45 plies close to the surface. With this in mind, the first iteration assumes symmetrical panels with core thicknesses of 20 mm and face sheets with the following configurations:

DB = +45/-45

Longitudinal Stiffener (LS):	CSM100 + DB + 90° + 90° + 0° + 0°	$t = 4.891 \cdot mm$
Transverse Stiffener (LS):	CSM100 + DB + 90° + 90° + 0° + 0°	$t = 4.891 \cdot mm$
Bottom shell (bs):	CSM100 + DB + 90° + 90° + 0°c + 0°c + 0°c + 0°c	$t = 8.184 \cdot mm$

Where e.g. 90° refer to a GFRP ply, and 90°c refer to a CFRP ply, oriented at 90°.

The remainder of the exterior (the diagonal/vertical part) are taken equivalently to the LS configuration.

Bottom shell face sheet

LS/TS/Sides face sheet

In-plane properties of <u>SANDWICH DECK</u>

The sandwich deck with a PET foam core has the following properties (derived through CLT):

$$\begin{pmatrix} E_{1.deck} \\ E_{2.deck} \\ G_{12.deck} \end{pmatrix} := \begin{pmatrix} 16460.115 \\ 1793.23 \\ 713.353 \end{pmatrix} \cdot MPa \qquad \nu_{12.deck} := 0.337 \qquad t_{deck} := 113.637 \cdot mm \qquad \rho_{deck} := 318.332 \cdot kg \cdot m^{-3}$$

↑membrane equivalent properties↑ ↓bending equivalent properties↓

$$\begin{pmatrix} E_{1.b.deck} \\ E_{2.b.deck} \\ G_{12.b.deck} \end{pmatrix} := \begin{pmatrix} 36333.868 \\ 3912.582 \\ 1512.297 \end{pmatrix} \cdot MPa \qquad \begin{pmatrix} D_{11.deck} \\ D_{12.deck} \\ D_{22.deck} \\ D_{66.deck} \end{pmatrix} = \begin{pmatrix} 4.496 \times 10^{9} \\ 1.607 \times 10^{8} \\ 4.842 \times 10^{8} \\ 1.849 \times 10^{8} \end{pmatrix} \cdot N \cdot mm$$

$$\nu_{12.b.deck} := 0.332$$

In-plane properties of <u>BOTTOM SHELL</u>

$$\begin{pmatrix} E_{1.bs} \\ E_{2.bs} \\ G_{12.bs} \end{pmatrix} := \begin{pmatrix} 25723.757 \\ 8643.932 \\ 2306.351 \end{pmatrix} \cdot MPa \qquad \nu_{12.bs} := 0.233 \qquad t_{bs} := 36.367 \cdot mm$$

$$\begin{pmatrix} E_{1.b.bs} \\ E_{2.b.bs} \\ G_{12.b.bs} \end{pmatrix} := \begin{pmatrix} 46711.802 \\ 15980.111 \\ 4318.445 \end{pmatrix} \cdot MPa \qquad \nu_{12.b.bs} := 0.235 \qquad \rho_{bs} := 824.517 \cdot kg \cdot m^{-3}$$

$$\begin{pmatrix} D_{11.bs} \\ D_{12.bs} \\ D_{22.bs} \\ D_{66.bs} \end{pmatrix} = \begin{pmatrix} 1.908 \times 10^{8} \\ 1.535 \times 10^{7} \\ 6.529 \times 10^{7} \\ 1.731 \times 10^{7} \end{pmatrix} \cdot N \cdot mm$$

4/15

In-plane properties of LONGITUDINAL STIFFENERS

$$\begin{pmatrix} E_{1.LS} \\ E_{2.LS} \\ G_{12.LS} \end{pmatrix} := \begin{pmatrix} 8915.537 \\ 8915.537 \\ 2458.307 \end{pmatrix} \cdot MPa \qquad \nu_{12.LS} := 0.229 \qquad t_{LS} := 34.414 \cdot mm$$

$$\begin{pmatrix} E_{1.b.LS} \\ E_{2.b.LS} \\ G_{12.b.LS} \end{pmatrix} := \begin{pmatrix} 16875.208 \\ 16992.706 \\ 4743.163 \end{pmatrix} \cdot MPa \qquad \nu_{12.b.LS} := 0.231 \qquad \rho_{LS} := 841.348 \cdot kg \cdot m^{-3}$$

$$\begin{pmatrix} D_{11.LS} \\ D_{12.LS} \\ D_{22.LS} \\ D_{66.LS} \end{pmatrix} = \begin{pmatrix} 6.056 \times 10^{7} \\ 1.406 \times 10^{7} \\ 6.098 \times 10^{7} \\ 1.611 \times 10^{7} \end{pmatrix} \cdot N \cdot mm$$

Panel strengths according to to JRC

JRC suggests to use 1.2% and 1.6% ultimate strains for the longitudinal and transverse; and shear strength of laminates.

$\sigma_{1.bs} := E_{1.bs} \cdot 1.2\% = 308.685 \cdot MPa$ $\qquad \sigma_{1.deck} := E_{1.deck} \cdot 1.2\% = 197.521 \cdot MPa$

$\sigma_{2.bs} := E_{2.bs} \cdot 1.2\% = 103.727 \cdot MPa$ $\qquad \sigma_{2.deck} := E_{2.deck} \cdot 1.2\% = 21.519 \cdot MPa$

$\tau_{12.bs} := G_{12.bs} \cdot 1.6\% = 36.902 \cdot MPa$ $\qquad \tau_{12.deck} := G_{12.deck} \cdot 1.6\% = 11.414 \cdot MPa$

Cross-section properties

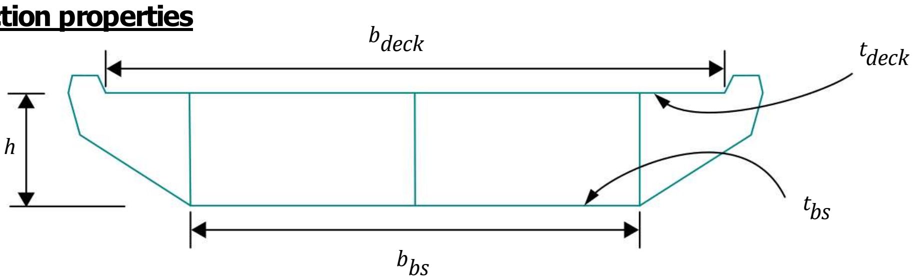

Some important cross-sectional parameters

Not to scale

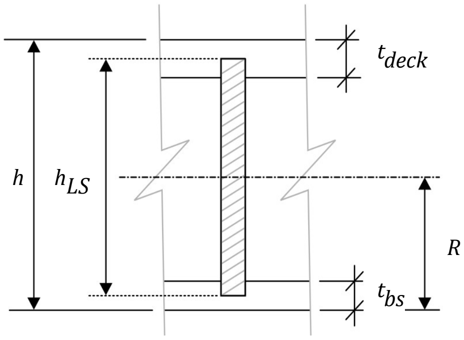

Estimated geometrical parameter for the first iteration:

$h_{LS} := 740mm$ height of longitudinal stiffener $\qquad b_{bs} := 4000mm$ bs=bottom shell

In Karamba, the distance between the deck and bottom shell is equivalent to the height of the stiffeners (see illustration above). Therefore, the total height h is:

$$h := h_{LS} + \frac{t_{deck}}{2} + \frac{t_{bs}}{2} = 815.002 \cdot mm \qquad \frac{h}{2} = 407.501 \cdot mm$$

Neutral axis

The neutral axis is located at

$$\bar{y} = \frac{\sum_j EAy_j}{\sum_j EA_j}$$ where y is distance from the centre of area j to the bottom ($y = 0$)

$y_{bs} := \frac{t_{bs}}{2} = 18.183 \cdot mm \qquad y_{deck} := h - \frac{t_{deck}}{2} = 758.183 \cdot mm \qquad y_{LS} := \frac{h_{LS} + t_{bs}}{2} = 388.183 \cdot mm$

$A_{bs} := b_{bs} \cdot t_{bs} = 1.455 \times 10^5 \cdot mm^2 \qquad A_{deck} := b_{deck} \cdot t_{deck} = 5.795 \times 10^5 \cdot mm^2$ areas

$A_{LS} := t_{LS} \cdot h_{LS} = 2.547 \times 10^4 \cdot mm^2$ area of a single stiffener

$sum\_EAy := A_{bs} \cdot E_{1.bs} \cdot y_{bs} + 3A_{LS} \cdot E_{1.LS} \cdot y_{LS} + A_{deck} \cdot E_{1.deck} \cdot y_{deck} = 7.565 \times 10^{12} \cdot N \cdot mm$

$sum\_EA := A_{bs} \cdot E_{1.bs} + 3 \cdot A_{LS} \cdot E_{1.LS} + A_{deck} \cdot E_{1.deck} = 1.396 \times 10^{10} N$

$y := \frac{sum\_EAy}{sum\_EA} = 541.804 \cdot mm \qquad R := y$

$E_{1.best} := max(E_{1.bs}, E_{1.deck}, E_{1.LS}) = 2.572 \times 10^4 \cdot MPa$

$\beta_1 := \frac{E_{1.best}}{E_{1.bs}} = 1 \qquad \beta_2 := \frac{E_{1.best}}{E_{1.deck}} = 1.563 \qquad \beta_3 := \frac{E_{1.best}}{E_{1.LS}} = 2.885$ stiffness ratio

Second moment of Inertia

$$I_y := \frac{1}{\beta_1}\left[\frac{b_{bs} \cdot t_{bs}^3}{12} + A_{bs} \cdot \left(R - \frac{t_{bs}}{2}\right)^2\right] + \frac{1}{\beta_2} \cdot \left[\frac{b_{deck} \cdot t_{deck}^3}{12} + A_{deck} \cdot \left(h - \frac{t_{deck}}{2} - R\right)^2\right] \ldots$$
$$+ \frac{3}{\beta_3} \cdot \left[t_{LS} \cdot \frac{\left(R - \frac{t_{bs}}{2}\right)^3}{12} + \left[t_{LS} \cdot \left(R - \frac{t_{bs}}{2}\right)\right] \cdot \left(\frac{R - \frac{t_{bs}}{2}}{2}\right)^2\right] \ldots$$
$$+ \frac{3}{\beta_3} \cdot \left[t_{LS} \cdot \frac{(h - 0.5 \cdot t_{deck} - R)^3}{12} + \left[t_{LS} \cdot (h - 0.5 \cdot t_{deck} - R)\right] \cdot \left(\frac{h - 0.5 \cdot t_{deck} - R}{2}\right)^2\right]$$

$I_y = 5.949 \times 10^{10} \cdot mm^4$

$W_{y.top} := \frac{I_y}{h - R} = 2.178 \times 10^8 \cdot mm^3 \qquad W_{y.bot} := \frac{I_y}{R} = 1.098 \times 10^8 \cdot mm^3$

The equivalent stiffnesses are thus (assuming that all the shear is taken by the longitudinal stiffeners):

$EI := \eta_{c.SLS} \cdot E_{1.best} \cdot I_y = 1.377 \times 10^6 \cdot kN \cdot m^2 \qquad EI = 1.377 \times 10^{15} \cdot N \cdot mm^2$

$A_v := h_{LS} \cdot t_{LS} \cdot 3 = 7.64 \times 10^4 \cdot mm^2$ shear area $\qquad GA_v := \eta_{c.SLS} \cdot G_{12.LS} \cdot A_v = 1.69 \times 10^5 \cdot kN$

6/15

Loads and load combinations

The loads are taken as prescribed by Johs Holt and/or as described in EN 1991.
For the live load deflection, the contribution of the dead load is disregarded, as this should be accommodated by an initial curvature.

$q_{fk} = 5 \cdot \frac{kN}{m^2}$ $\qquad q_{dead} := 1000 \frac{kN}{m}$ $\qquad \gamma_q := 1.0$ $\qquad \psi_1 := 0.7$

$q_{SLS.fr} := \left(0 \cdot q_{dead} + \psi_1 \cdot q_{fk}\right) \cdot b_{deck} = 17.849 \cdot \frac{kN}{m}$

Differential equation expressing deflection

The expression for the the bridge's displacement field is derived in the Maple-script: Appendix J.1

Let L_1 be the location of the intermediate support, L_K the total length, x the point of interest, and q (= $q_{fk} \cdot b_{deck}$) a line load, then the displacement at a point x can be visualised as:

$GA = 1.69 \times 10^5$ kN $\qquad q = 25.498 \frac{kN}{m}$ $\qquad EI = 1.377 \times 10^6 \ kN \cdot m^2$

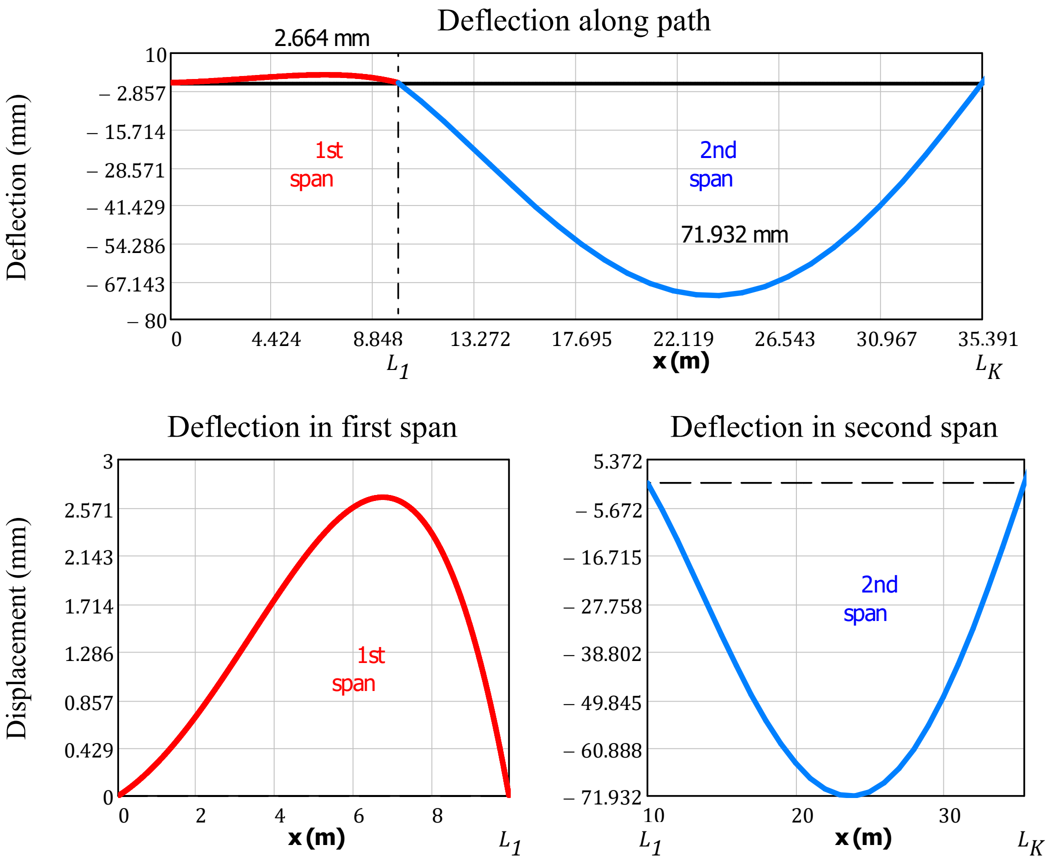

Note different ranges on the y-axes

The deflection is within the feasible limit: $\qquad \delta = 71.932 \cdot mm \quad < \quad \frac{L_2}{350} = 72.792 \cdot mm$

7/15

Differential equation expressing bending moment

It is expected that the maximum bending moments are over the intermediate support and approximately in the middle of the second span. The bending moment before the cylinder is not of interest, as the second field includes the peak in field 1.

Moment in field 2 (x = L_1 .. L_K):

$$M2(x2) := -\frac{-12\cdot(x2-L_K)\cdot\left[\left(\frac{GA\cdot L_1^{\,3}}{12}\right)-\frac{\left(x2+\frac{L_K}{4}\right)\cdot GA\cdot L_1^{\,2}}{3}+\left[\frac{\left(x2-\frac{L_K}{4}\right)\cdot L_K\cdot GA}{3}-EI\right]\cdot L_1+EI\cdot x2\right]\cdot q}{-8\cdot GA\cdot L_1^{\,2}+8\cdot GA\cdot L_1\cdot L_K+24\cdot EI}$$

$x_{max} = 24.866\,m$ coordinate for max sagging moment

$M2(L_1) = 1.438\times10^3\cdot kN\cdot m$ $\quad M2(x_{max}) = -1.412\times10^3\cdot kN\cdot m$

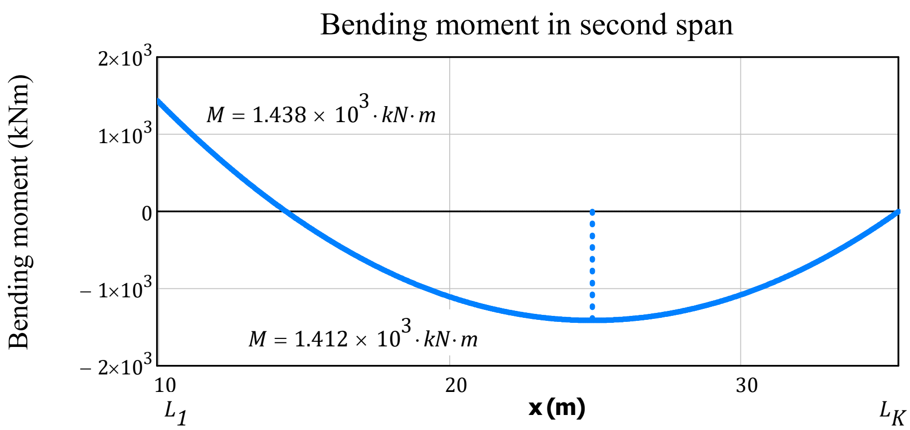

Tension has negative sign

Differential equation expressing shear force

The shear force is simply the derivative of the bending moment, resulting in the following graph

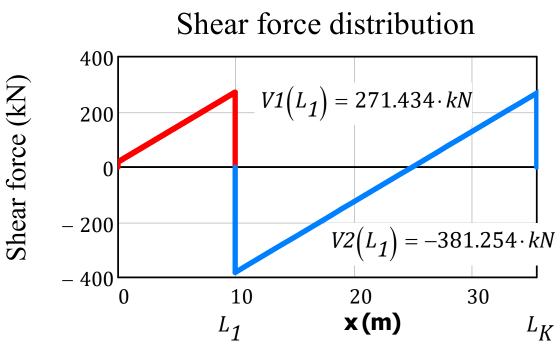

$V1(L_1) = 0.271\,\frac{1}{N}\cdot kN$

The reaction force is equal to the difference in shear forces:

$V1(0) = 18.649\cdot kN$ $\quad V1(L_1) = 271.434\cdot kN$

$V2(L_1) = -381.254\cdot kN$ $\quad V2(L_K) = 268.376\cdot kN$

$V_{Ed.L1} := |V1(L_1)| + |V2(L_1)| = 652.7\cdot kN$

Cross-section resistances

Verification of bending resistance

It is assumed that the panels have equal compressive and tensile strengths, i.e. $f_{d.t} = f_{d.c}$.

The strengths of the top flange (deck) and the bottom flange (bottom shell) is then:

$$f_{d.deck} := \eta_{c.ULS} \cdot \frac{\sigma_{1.deck}}{\gamma_{M.str}} = 103.055 \cdot MPa \qquad f_{d.bs} := \eta_{c.ULS} \cdot \frac{\sigma_{1.bs}}{\gamma_{M.str}} = 161.053 \cdot MPa$$

The maximum stress due to bending - in span

$$M_{sagging} := \left|M2\left(x_{max}\right)\right| = 1.412 \times 10^3 \cdot kN \cdot m$$

$$\sigma_{bot} := \frac{M_{sagging}}{W_{y.bot}} = 12.862 \cdot MPa \qquad \sigma_{top} := \frac{M_{sagging}}{W_{y.top}} = 6.486 \cdot MPa \qquad UC := \frac{\sigma_{bot}}{f_{d.bs}} = 0.08$$

The maximum stress due to bending - over support

$$M_{hogging} := \left|M2\left(L_1\right)\right| = 1.438 \times 10^3 \cdot kN \cdot m \qquad \sigma_{bot.sup} := \frac{M_{hogging}}{W_{y.bot}} = 13.095 \cdot MPa$$

$$\sigma_{top.sup} := \frac{M_{hogging}}{W_{y.top}} = 6.603 \cdot MPa \qquad UC := max\left(\frac{\sigma_{bot.sup}}{f_{d.bs}}, \frac{\sigma_{top.sup}}{f_{d.deck}}\right) = 0.081$$

Verification of shear resistance

In the final model, a steel frame substitutes the longitudinal stiffeners at the intermediate support. However, as a conservative assumption, it is assumed that the longitudinal stiffeners transfer the shear. The shear force is taken as the reaction force.

$$\tau_{12.LS} := E_{1.LS} \cdot 1.6\% = 142.649 \cdot MPa \qquad A_V = 7.64 \times 10^4 \cdot mm^2$$

$$f_{d.V} := \eta_{c.ULS} \cdot \frac{\tau_{12.LS}}{\gamma_{M.str}} = 74.425 \cdot MPa \qquad V_{Rd} := A_V \cdot f_{d.V} = 5.686 \times 10^3 \cdot kN \qquad UC := \frac{V_{Ed.L1}}{V_{Rd}} = 0.115$$

Local stability of the cross section due to bending

For the buckling verification, one should make use of the centre-to-centre distances of the panels. The length of the longitudinal stiffeners remain the same, whereas the the widths for both deck and bottom are taken as b_f (see below). As a conservative assumption, an equivalent hollow section is considered.

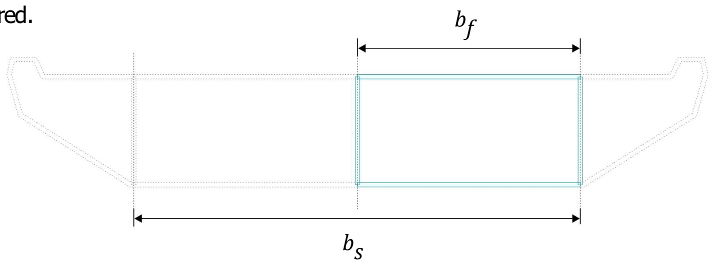

$$b_f := \frac{b_{bs}}{2} = 2000 \cdot mm \qquad h_{LS} = 740 \cdot mm$$

9/15

The bending equivalent properties for the respective panels are determined according to CLT:

$$\begin{pmatrix} D_{11.deck} \\ D_{12.deck} \\ D_{22.deck} \\ D_{66.deck} \end{pmatrix} = \begin{pmatrix} 4.496 \times 10^{6} \\ 1.607 \times 10^{5} \\ 4.842 \times 10^{5} \\ 1.849 \times 10^{5} \end{pmatrix} J \qquad \begin{pmatrix} D_{11.bs} \\ D_{12.bs} \\ D_{22.bs} \\ D_{66.bs} \end{pmatrix} = \begin{pmatrix} 1.908 \times 10^{5} \\ 1.535 \times 10^{4} \\ 6.529 \times 10^{4} \\ 1.731 \times 10^{4} \end{pmatrix} \cdot J \qquad \begin{pmatrix} D_{11.LS} \\ D_{12.LS} \\ D_{22.LS} \\ D_{66.LS} \end{pmatrix} = \begin{pmatrix} 6.056 \times 10^{4} \\ 1.406 \times 10^{4} \\ 6.098 \times 10^{4} \\ 1.611 \times 10^{4} \end{pmatrix} J$$

$J = 10^{3} N \cdot mm$

Local verification of the bottom shell according to Kassapoglou

General formulas on plate buckling assumes infinitely long plates, i.e. plates where the length is 5 times greater than the width. Since the plate in question has a small aspect ratio (AR<5), the buckling resistance is verified through the theory of Prof. Kassapoglou (2013).
With an intermediate spacing of 2 m between the transverse stiffeners, its (buckling) length is taken as:

$l_{bs.buck} := 2m = 2000 \cdot mm$ $\quad a := l_{bs.buck}$ length $\quad b := b_f = 2000 \cdot mm$ width

$AR := \frac{a}{b} = 1$ aspect ratio

$$m_b := \begin{vmatrix} 3 & if & AR \geq 2.5 \\ 2 & if & AR < 2.5 \\ 1 & if & 0.6 \leq AR \leq 1.5 \\ AR & if & AR < 0.6 \end{vmatrix} = 1 \qquad m_b = 1$$

number of half sines

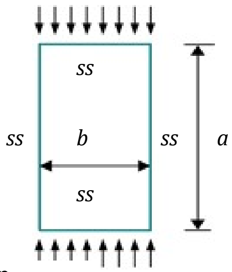

In addition to the m_b in the direction of the load, it assumed that $n_b = 1$ in the direction transverse to the applied load. The theory assumes that the plate is loaded in axial direction, meaning that no transformation is necessary.

$D_{11} := D_{11.bs} = 1.908 \times 10^{8} \cdot N \cdot mm$ $\qquad D_{12} := D_{12.bs} = 1.535 \times 10^{7} \cdot N \cdot mm$

$D_{22} := D_{22.bs} = 6.529 \times 10^{7} \cdot N \cdot mm$ $\qquad D_{66} := D_{66.bs} = 1.731 \times 10^{7} \cdot N \cdot mm$

$$N_o := \frac{\pi^2 \cdot \left[D_{11} \cdot m_b^{\,4} + 2 \cdot \left(D_{12} + 2 \cdot D_{66}\right) \cdot m_b^{\,2} \cdot AR^2 + D_{22} \cdot (AR)^4 \right]}{a^2 \cdot m_b^{\,2}} = 878.531 \cdot \frac{N}{mm}$$

critical buckling load

$f_{k.cr} := \frac{N_o}{t_{bs}} = 24.157 \cdot MPa$ critical buckling stress $\qquad t_{bs} = 36.367 \cdot mm$

$f_{d.cr} := \eta_{c.ULS} \cdot \frac{f_{k.cr}}{\gamma_{M.loc}} = 11.343 \cdot MPa$

$\sigma_{Ed} := \sigma_{bot.sup} = 13.095 \cdot MPa$ $\qquad UC := \frac{\sigma_{Ed}}{f_{d.cr}} = 1.154$

the panel is clamped inbetween to steel plates at the point of greatest compression, thus high UC could be OK.

The buckling load factor (λ) indicates the factor by which the loads can be increased to induce buckling. As the numerical response is calculated without taking into consideration the partial safety factors, we can distinguish between an analytical value and the corresponding expected value to obtain numerically (FEM).

$$\lambda := \left(\frac{\sigma_{Ed}}{f_{d.cr}}\right)^{-1} = 0.866 \qquad \lambda := \left[\frac{\sigma_{Ed}}{\left(\eta_{c.ULS} \cdot f_{k.cr}\right)}\right]^{-1} = 1.494$$

analytical $\qquad$ "numerical"

The buckling factor is inferior to the criterion

10/15

Local stability of the cross section due to reaction forces - x = L_K

The main load carrying components have insufficient resistance against buckling.
Next, we verify whether the transverse stiffeners have sufficient buckling resistance, again making use Kassapoglou's theories.

The end of the bridge rests on steel plates. For this verification, these are assumed to be perfectly rectangular. The width of these plates (in y-direction) is assumed to be the area of load introduction. Next, we assume that the stress spreads at an 45° angle through the bottom shell.

$b_{plate} := 295mm$ $\quad b_{eff.TS} := b_{plate} + 2 \cdot t_{bs} = 367.734 \cdot mm$ $\quad h_{TS} := h_{LS}$

$a := h_{TS}$ Length $\quad b := b_{eff.TS}$ Width $\quad AR := \frac{a}{b} = 2.012$ aspect ratio

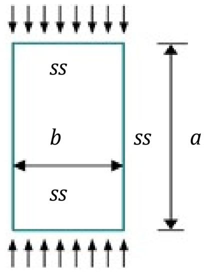

$$m_b := \begin{cases} 3 & if \quad AR \geq 2.5 \\ 2 & if \quad AR < 2.5 \\ 1 & if \quad 0.6 \leq AR \leq 1.5 \\ AR & if \quad AR < 0.6 \end{cases} = 2$$ number of half sines

The theory assumes that the plate is loaded in axial direction. Thus, the D_{ij} entries must be transformed (rotated 90°).

$D_{11} := D_{22.TS} = 6.098 \times 10^{7} \cdot N \cdot mm$ $\quad D_{12} := D_{12.TS} = 1.406 \times 10^{7} \cdot N \cdot mm$

$D_{22} := D_{11.TS} = 6.056 \times 10^{7} \cdot N \cdot mm$ $\quad D_{66} := D_{66.TS} = 1.611 \times 10^{7} \cdot N \cdot mm$

$$N_o := \frac{\pi^2 \cdot \left[D_{11} \cdot m_b^{\,4} + 2 \cdot \left(D_{12} + 2 \cdot D_{66}\right) \cdot m_b^{\,2} \cdot AR^2 + D_{22} \cdot (AR)^4\right]}{a^2 \cdot m_b^{\,2}} = 1.563 \times 10^{4} \cdot \frac{N}{mm}$$ critical buckling load

$f_{k.cr} := \frac{N_o}{t_{TS}} = 454.081 \cdot MPa$ $\quad t_{TS} = 34.414 \cdot mm$ $\quad$ critical buckling stress

$f_{d.cr} := \eta_{c.ULS} \cdot \frac{f_{k.cr}}{\gamma_{M.loc}} = 213.221 \cdot MPa$

Assuming that the shear is carried equally by the two middle pieces of the transverse stiffener:

$V_{Ed} := \frac{V2(L_K)}{2} = 134.188 \cdot kN$ $\quad \sigma_{Ed} := \frac{V_{Ed}}{b \cdot t_{TS}} = 10.603 \cdot MPa$ $\quad UC := \frac{\sigma_{Ed}}{f_{d.cr}} = 0.05$

At x = L_1 $\quad$ Either longitudinal or transverse stiffeners can buckle (same case holds for both)

$V_{Ed} := \frac{V_{Ed.L1}}{2} = 326.344 \cdot kN$ $\quad \sigma_{Ed} := \frac{V_{Ed}}{b \cdot t_{TS}} = 25.787 \cdot MPa$ $\quad UC := \frac{\sigma_{Ed}}{f_{d.cr}} = 0.121$

$\lambda_{ana} := \left(\frac{\sigma_{Ed}}{f_{d.cr}}\right)^{-1} = 8.268$ $\quad \lambda_{num} := \left(\frac{\sigma_{Ed}}{f_{k.cr} \cdot \eta_{c.ULS}}\right)^{-1} = 14.263$

11/15

J.4. Second iteration

Second Iteration

From the first iteration, with $h_{LS} = 740 \cdot mm$ and $b_{bs} = 4000 \cdot mm$, the deflection is just below the constraint $\delta_{max} = 72.792 \cdot mm$. The buckling constraint, however, is not satisfied.

There are two approaches to achieve $\lambda_{cr} > 6$ for the governing panel (bottom shell adjacent to the intermediate support):

1. Decrease the width of the panel (change geometry)
2. Increase the flexural stiffness of the panel (change material architecture)

Both of these changes are introduced.

New geometry

The number of half sines (m_b) greatly affects the buckling resistance. Therefore, a width is selected resulting in 2 two half sines:

$h_{LS} := 740mm$ $\qquad$ $b_{bs} = 4000 \cdot mm \rightarrow\rightarrow \quad b_{bs} := 2660mm$

$$h := h_{LS} + \frac{t_{deck}}{2} + \frac{t_{bs}}{2} = 815.002 \cdot mm \qquad \frac{h}{2} = 407.501 \cdot mm$$

New panel definition of the bottom shell

Seeing that the global stiffness scantily satisfies the criterion, the other panels remain unchanged. The new face sheet configuration of the bottom shell is as follows:

CSM100 + DB + 2(90°) + 4(0°c)	$t = 8.184 \cdot mm$	old
CSM100 + DB + 4(0°c) + 2(90°) + DB + 4(0°c) + 2(90°)	$t = 13.791 \cdot mm$	new

where the 12.5 % criterion with 2 plies in each group require and increased number of the DB and 90° plies as well (DB is modelled as +45 and -45 plies).

In-plane properties of BOTTOM SHELL

membrane-equivalent

$$\begin{pmatrix} E_{1.bs} \\ E_{2.bs} \\ G_{12.bs} \end{pmatrix} := \begin{pmatrix} 38143.967 \\ 8930.643 \\ 3176.227 \end{pmatrix} \cdot MPa \qquad \nu_{12.bs} := 0.313 \qquad t_{bs} := 47.583 \cdot mm$$

bending-equivalent

$$\begin{pmatrix} E_{1.b.bs} \\ E_{2.b.bs} \\ G_{12.b.bs} \end{pmatrix} := \begin{pmatrix} 60225.676 \\ 14191.535 \\ 5116.618 \end{pmatrix} \cdot MPa \qquad \nu_{12.b.bs} := 0.316 \qquad \rho_{bs} := 1023.633 \cdot kg \cdot m^{-3}$$

$$\begin{pmatrix} D_{11.bs} \\ D_{12.bs} \\ D_{22.bs} \\ D_{66.bs} \end{pmatrix} = \begin{pmatrix} 5.538 \times 10^{8} \\ 4.129 \times 10^{7} \\ 1.305 \times 10^{8} \\ 4.594 \times 10^{7} \end{pmatrix} \cdot N \cdot mm$$

Neutral axis

$$y_{bs} := \frac{t_{bs}}{2} = 23.791 \cdot mm \qquad y_{deck} := h - \frac{t_{deck}}{2} = 758.183 \cdot mm \qquad y_{LS} := \frac{h_{LS} + t_{bs}}{2} = 393.791 \cdot mm$$

$A_{bs} := b_{bs} \cdot t_{bs} = 1.266 \times 10^{5} \cdot mm^{2}$ $\qquad$ $A_{deck} := b_{deck} \cdot t_{deck} = 5.795 \times 10^{5} \cdot mm^{2}$ areas

$A_{LS} := t_{LS} \cdot h_{LS} = 2.547 \times 10^{4} \cdot mm^{2}$ area of a single stiffener

$$sum\_EAy := A_{bs} \cdot E_{1.bs} \cdot y_{bs} + 3A_{LS} \cdot E_{1.LS} \cdot y_{LS} + A_{deck} \cdot E_{1.deck} \cdot y_{deck} = 7.615 \times 10^{12} \cdot N \cdot mm$$

12/15

$sum\_EA := A_{bs} \cdot E_{1.bs} + 3 \cdot A_{LS} \cdot E_{1.LS} + A_{deck} \cdot E_{1.deck} = 1.505 \times 10^{10} \, N$

$y := \dfrac{sum\_EAy}{sum\_EA} = 506.07 \cdot mm$ $\qquad R := y$

$E_{1.best} := max(E_{1.bs}, E_{1.deck}, E_{1.LS}) = 3.814 \times 10^4 \cdot MPa$

$\beta_1 := \dfrac{E_{1.best}}{E_{1.bs}} = 1$ $\qquad \beta_2 := \dfrac{E_{1.best}}{E_{1.deck}} = 2.317$ $\qquad \beta_3 := \dfrac{E_{1.best}}{E_{1.LS}} = 4.278$ stiffness ratio

Second moment of Inertia

$I_y = 5.353 \times 10^{10} \cdot mm^4$ $\qquad W_{y.top} := \dfrac{I_y}{h - R} = 1.733 \times 10^8 \cdot mm^3$ $\qquad W_{y.bot} := \dfrac{I_y}{R} = 1.058 \times 10^8 \cdot mm^3$

The equivalent stiffnesses are thus (assuming that all the shear is taken by the longitudinal stiffeners):

$EI := \eta_{c.SLS} \cdot E_{1.best} \cdot I_y = 1.838 \times 10^6 \cdot kN \cdot m^2$ $\qquad EI = 1.838 \times 10^{15} \cdot N \cdot mm^2$

$A_v := h_{LS} \cdot t_{LS} \cdot 3 = 7.64 \times 10^4 \cdot mm^2$ shear area $\qquad GA_v := \eta_{c.SLS} \cdot G_{12.LS} \cdot A_v = 1.69 \times 10^5 \cdot kN$

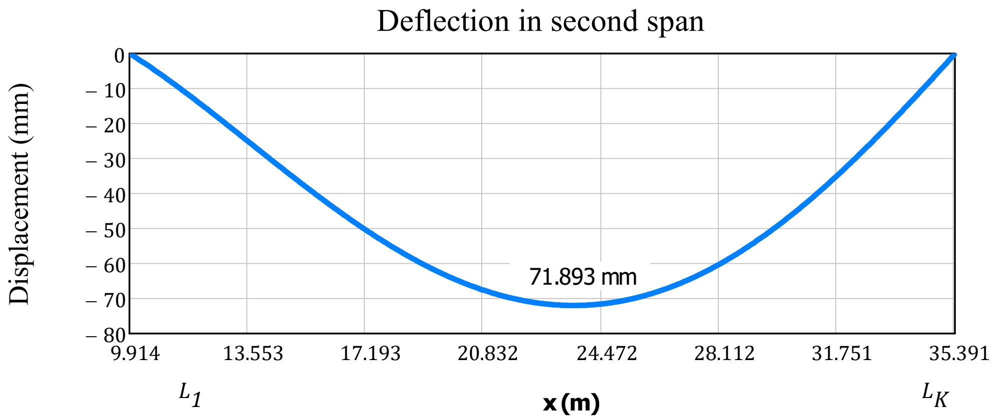

Local verification of the bottom shell according to Kassapoglou

$l_{bs.buck} := 2m = 2000 \cdot mm$ $\qquad a := l_{bs.buck}$ length $\qquad b := \dfrac{b_{bs}}{2} = 1330 \cdot mm$ width

$AR := \dfrac{a}{b} = 1.504$ aspect ratio

$$m_b := \begin{cases} 3 & \text{if } AR \geq 2.5 \\ 2 & \text{if } AR < 2.5 \\ 1 & \text{if } 0.6 \leq AR \leq 1.5 \\ AR & \text{if } AR < 0.6 \end{cases} = 2$$

number of half sines

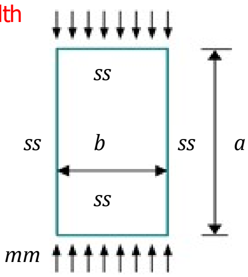

$D_{11} := D_{11.bs} = 5.538 \times 10^8 \cdot N \cdot mm$ $\qquad D_{12} := D_{12.bs} = 4.129 \times 10^7 \cdot N \cdot mm$

$D_{22} := D_{22.bs} = 1.305 \times 10^8 \cdot N \cdot mm$ $\qquad D_{66} := D_{66.bs} = 4.594 \times 10^7 \cdot N \cdot mm$

$$N_o := \frac{\pi^2 \cdot \left[D_{11} \cdot m_b^{\,4} + 2 \cdot \left(D_{12} + 2 \cdot D_{66}\right) \cdot m_b^{\,2} \cdot AR^2 + D_{22} \cdot (AR)^4\right]}{a^2 \cdot m_b^{\,2}} = 7.363 \times 10^3 \cdot \frac{N}{mm}$$

critical buckling load

13/15

$f_{k.cr} := \frac{N_o}{t_{bs}} = 154.738 \cdot MPa$ critical buckling stress $t_{bs} = 47.583 \cdot mm$

$f_{d.cr} := \eta_{c.ULS} \cdot \frac{f_{k.cr}}{\gamma_{M.loc}} = 72.66 \cdot MPa$ $\sigma_{Ed} := \sigma_{bot.sup} = 13.095 \cdot MPa$ $UC := \frac{\sigma_{Ed}}{f_{d.cr}} = 0.18$

$\lambda := \left(\frac{\sigma_{Ed}}{f_{d.cr}}\right)^{-1} = 5.549$ $\lambda := \left[\frac{\sigma_{Ed}}{(\eta_{c.ULS} \cdot f_{k.cr})}\right]^{-1} = 9.572$ > 6 $OK!$

The defined panel configurations and geometrical parameters are introduced as the initial values of the variables in the optimisation problem.

With $Y_{1t} := 1.000$, $Z_{1t} := 0.6000$, $Y_{1b} = 0.422$ and $Z_{1b} = 0.255 \cdot mm$; and $Y_{2t} = Y_{1t}$, $Z_{2t} = Z_{1t}$, $Y_{2b} = Y_{1b}$ and $Z_{2b} = Z_{1b}$, the initial geometry becomes:

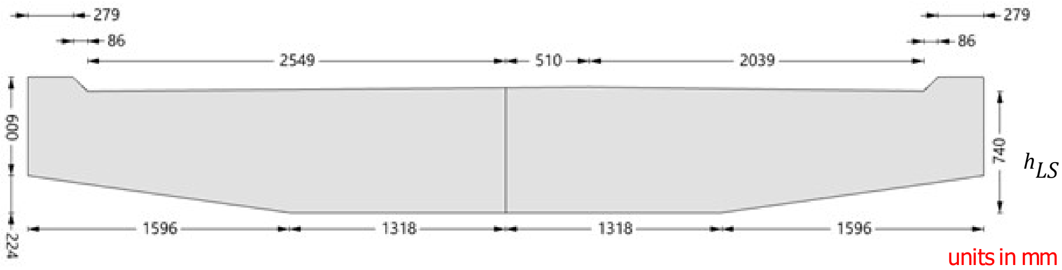

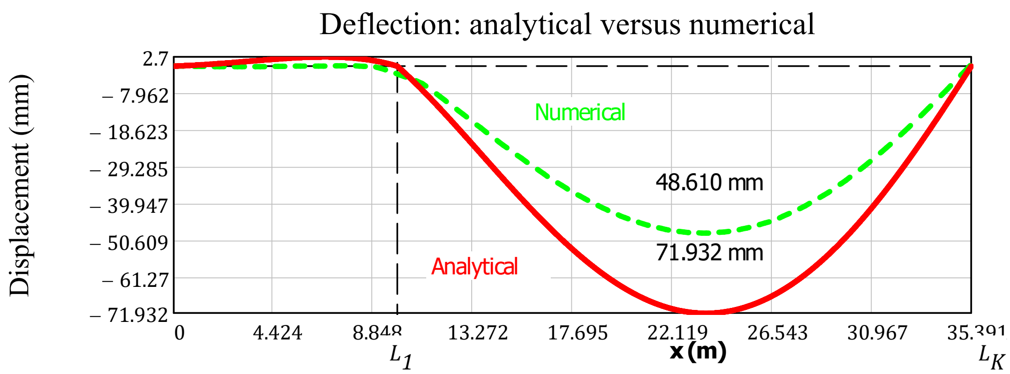

The FE model behaves much stiffer due to the steel frame (from $x = 0$ to $x = L_1$) and the inclusion of the transverse stiffeners and the remainder of the exterior shell. The cylinder deforms slightly, in addition to rotation about this point, resulting in nonzero values in $x = L_1$. The difference between the numerical (green line, measured along the bottom shell at $Y = 0$) and analytical solution (red) exemplifies this.

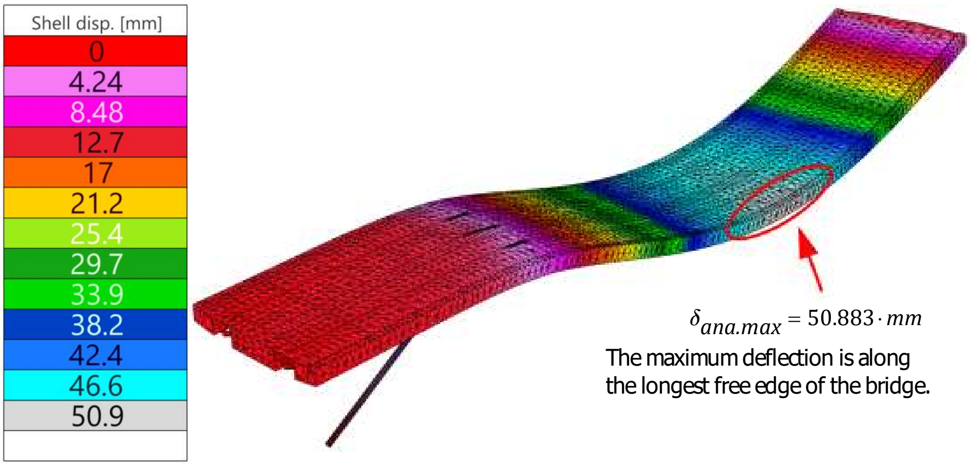

$\delta_{ana.max} = 50.883 \cdot mm$

The maximum deflection is along the longest free edge of the bridge.

Naturally, with all the simplifications adopted herein, the element model will have greater stiffness and better buckling performance owing to interaction between the elements providing rotational stiffness along the edges. Furthermore, the maximum compression is not acting uniformly on the plate.

The governing buckling shape coincides with the analytical solution, seeing that the bottom shell is the governing case. The shape, however, is different. The differences are owing to:

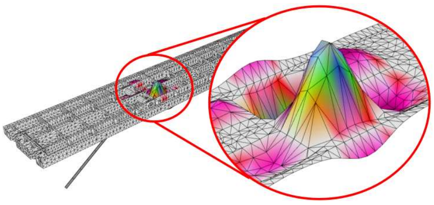

- greater rotational stiffness along the edges
- less compression - the greatest compression is where the steel bracket is clamped to bottom shell
- steel frame resists most of the load

$\lambda_{cr.numerical} = 18.514$ vs. $\lambda_{cr.analytical} = 9.572$

The aspect ratio suggested that the shape would follow two half sines ($m_b = 2$). The numerical solution, however, does not agree with this assumption. This discrepancy is likely owing to greater rotational restraint along the edges (pinned connection was assumed). It is also likely that the ranges for the aspect ratios and the corresponding value of m is not as rigid as the theory suggest. With $AR = 1.504$ one could as well assume that $m_b := 1$ - seeing that expressions that decrease in accuracy close to the upper and lower ranges of definition.

References - see also *Appendices Bibliography*

[13] Kollár, L. P. (2003). Local buckling of fiber reinforced plastic composite structural members with open and closed cross sections. Journal of Structural Engineering, 129(11), 1503-1513.

[14] Kassapoglou, C. (2013). Design and analysis of composite structures: with applications to aerospace structures (2nd ed., Ser. Aerospace series). Wiley.

Appendix K Sensitivity analysis

The tables herein show the sensitivity analysis conducted for *solution 1*, listed in Table 7.1. All tables have the same structure, where

current value	=	value obtained after the diversification and intensification for *solution 1* ;
perturbation	=	change of parameter, given in percentage and its new value; and
immediate value	=	the immediately obtained value due to the perturbation of a parameter.

If there are differences in the maximum and minimum value of all the entries in the *Sensitivity* rows, these cells are colored red and blue to indicate the maximum and minimum values, respectively.

K.1. Cost sensitivity

Table K.1: Sensitivity matrix – Carbon Cost

	Unit	Current value	d_1	d_2	d_3	d_4	d_5	d_6
Original value			30[a]					
Perturbation			1%	5%	10%	−1%	−5%	−10%
Perturbation	€/kg		0.3	1.5	3	−0.3	−1.5	−3
Fitness[†]	-	7.5642×10^{-1}	7.5698×10^{-1}	7.5940×10^{-1}	7.6242×10^{-1}	7.5578×10^{-1}	7.5336×10^{-1}	7.5034×10^{-1}
Fitness[‡]	-		7.5698×10^{-1}	7.5940×10^{-1}	7.6242×10^{-1}	7.5577×10^{-1}	7.5336×10^{-1}	7.5034×10^{-1}
Sensitivity	%		7.4004×10^{-2}	3.9335×10^{-1}	7.9269×10^{-1}	-8.5847×10^{-2}	-4.0531×10^{-1}	-8.0465×10^{-1}
Cost[†]	€	3.7739×10^{5}	3.7893×10^{5}	3.8518×10^{5}	3.9299×10^{5}	3.7581×10^{5}	3.6956×10^{5}	3.6175×10^{5}
Cost[‡]	€		3.7893×10^{5}	3.8518×10^{5}	3.9299×10^{5}	3.7581×10^{5}	3.6956×10^{5}	3.6175×10^{5}
Sensitivity	%		4.0750×10^{-1}	2.0632×10^{0}	4.1329×10^{0}	-4.2053×10^{-1}	-2.0763×10^{0}	-4.1461×10^{0}
Footprint[†]	$kgCO_2e$	3.4940×10^{5}	3.4938×10^{5}	3.4938×10^{5}	3.4938×10^{5}	3.4938×10^{5}	3.4938×10^{5}	3.4938×10^{5}
Footprint[‡]	$kgCO_2e$		3.4938×10^{5}	3.4938×10^{5}	3.4938×10^{5}	3.4938×10^{5}	3.4938×10^{5}	3.4938×10^{5}
Sensitivity	%		-5.7219×10^{-3}	-5.8364×10^{-3}	-5.8364×10^{-3}	-5.8364×10^{-3}	-5.8364×10^{-3}	-5.8364×10^{-3}
Deflection[†]	mm	7.0234×10^{1}	7.0278×10^{1}	7.0279×10^{1}	7.0279×10^{1}	7.0279×10^{1}	7.0279×10^{1}	7.0279×10^{1}
Deflection[‡]	mm		7.0278×10^{1}	7.0284×10^{1}	7.0284×10^{1}	7.0284×10^{1}	7.0284×10^{1}	7.0284×10^{1}
Sensitivity	%		6.1970×10^{-2}	7.0734×10^{-2}	7.0734×10^{-2}	7.0734×10^{-2}	7.0734×10^{-2}	7.0734×10^{-2}
Frequency[†]	Hz	4.0821×10^{0}	4.0779×10^{0}	4.0783×10^{0}	4.0783×10^{0}	4.0783×10^{0}	4.0783×10^{0}	4.0783×10^{0}
Frequency[‡]	Hz		4.0779×10^{0}	4.0774×10^{0}	4.0774×10^{0}	4.0774×10^{0}	4.0774×10^{0}	4.0774×10^{0}
Sensitivity	%		-1.0299×10^{-1}	-1.1556×10^{-1}	-1.1556×10^{-1}	-1.1556×10^{-1}	-1.1556×10^{-1}	-1.1556×10^{-1}
Buckling factor[†]	-	1.1237×10^{1}	1.1157×10^{1}	1.1156×10^{1}	1.1156×10^{1}	1.1156×10^{1}	1.1156×10^{1}	1.1156×10^{1}
Buckling factor[‡]	-		1.1157×10^{1}	1.1162×10^{1}	1.1162×10^{1}	1.1162×10^{1}	1.1162×10^{1}	1.1162×10^{1}
Sensitivity	%		-7.1238×10^{-1}	-6.7331×10^{-1}	-6.7331×10^{-1}	-6.7331×10^{-1}	-6.7331×10^{-1}	-6.7331×10^{-1}

[a] [€/kg], [†]immediate value, [‡]value after new intensification phase.

Table K.2: Sensitivity matrix – Glass Cost

	Unit	Current value	d_1	d_2	d_3	d_4	d_5	d_6
Original value			3^a					
Perturbation			1%	5%	10%	−1%	−5%	−10%
Perturbation	€/kg		0.03	0.15	0.3	−0.03	−0.15	−0.3
Fitness†	-	7.5642×10^{-1}	7.5645×10^{-1}	7.5672×10^{-1}	7.5706×10^{-1}	7.5631×10^{-1}	7.5604×10^{-1}	7.5570×10^{-1}
Fitness‡	-		7.5645×10^{-1}	7.5672×10^{-1}	7.5706×10^{-1}	7.5631×10^{-1}	7.5604×10^{-1}	7.5570×10^{-1}
Sensitivity	%		3.0365×10^{-3}	3.9105×10^{-2}	8.4190×10^{-2}	-1.4998×10^{-2}	-5.1066×10^{-2}	-9.6151×10^{-2}
Cost†	€	3.7739×10^{5}	3.7755×10^{5}	3.7825×10^{5}	3.7913×10^{5}	3.7719×10^{5}	3.7649×10^{5}	3.7561×10^{5}
Cost‡	€		3.7755×10^{5}	3.7825×10^{5}	3.7913×10^{5}	3.7719×10^{5}	3.7649×10^{5}	3.7561×10^{5}
Sensitivity	%		4.0152×10^{-2}	2.2709×10^{-1}	4.6077×10^{-1}	-5.3318×10^{-2}	-2.4026×10^{-1}	-4.7394×10^{-1}
Footprint†	$kgCO_2e$	3.4940×10^{5}	3.4938×10^{5}	3.4938×10^{5}	3.4938×10^{5}	3.4938×10^{5}	3.4938×10^{5}	3.4938×10^{5}
Footprint‡	$kgCO_2e$		3.4938×10^{5}	3.4938×10^{5}	3.4938×10^{5}	3.4938×10^{5}	3.4938×10^{5}	3.4938×10^{5}
Sensitivity	%		-5.8364×10^{-3}	-5.8364×10^{-3}	-5.8364×10^{-3}	-5.8364×10^{-3}	-5.8364×10^{-3}	-5.8364×10^{-3}
Deflection†	mm	7.0234×10^{1}	7.0279×10^{1}	7.0279×10^{1}	7.0279×10^{1}	7.0279×10^{1}	7.0279×10^{1}	7.0279×10^{1}
Deflection‡	mm		7.0284×10^{1}	7.0284×10^{1}	7.0284×10^{1}	7.0284×10^{1}	7.0284×10^{1}	7.0284×10^{1}
Sensitivity	%		7.0734×10^{-2}	7.0734×10^{-2}	7.0734×10^{-2}	7.0734×10^{-2}	7.0734×10^{-2}	7.0734×10^{-2}
Frequency†	Hz	4.0821×10^{0}	4.0783×10^{0}	4.0783×10^{0}	4.0783×10^{0}	4.0783×10^{0}	4.0783×10^{0}	4.0783×10^{0}
Frequency‡	Hz		4.0774×10^{0}	4.0774×10^{0}	4.0774×10^{0}	4.0774×10^{0}	4.0774×10^{0}	4.0774×10^{0}
Sensitivity	%		-1.1556×10^{-1}	-1.1556×10^{-1}	-1.1556×10^{-1}	-1.1556×10^{-1}	-1.1556×10^{-1}	-1.1556×10^{-1}
Buckling factor†	-	1.1237×10^{1}	1.1156×10^{1}	1.1156×10^{1}	1.1156×10^{1}	1.1156×10^{1}	1.1156×10^{1}	1.1156×10^{1}
Buckling factor‡	-		1.1162×10^{1}	1.1162×10^{1}	1.1162×10^{1}	1.1162×10^{1}	1.1162×10^{1}	1.1162×10^{1}
Sensitivity	%		-6.7331×10^{-1}	-6.7331×10^{-1}	-6.7331×10^{-1}	-6.7331×10^{-1}	-6.7331×10^{-1}	-6.7331×10^{-1}

[a] [€/kg], †immediate value, ‡value after new intensification phase.

Table K.3: Sensitivity matrix – Resin Cost

	Unit	Current value	d_1	d_2	d_3	d_4	d_5	d_6
Original value			4^a					
Perturbation			1%	5%	10%	−1%	−5%	−10%
Perturbation	€/kg		0.04	0.2	0.4	−0.04	−0.2	−0.4
Fitness†	-	7.5642×10^{-1}	7.5646×10^{-1}	7.5679×10^{-1}	7.5719×10^{-1}	7.5630×10^{-1}	7.5597×10^{-1}	7.5557×10^{-1}
Fitness‡	-		7.5646×10^{-1}	7.5678×10^{-1}	7.5719×10^{-1}	7.5630×10^{-1}	7.5597×10^{-1}	7.5557×10^{-1}
Sensitivity	%		4.7577×10^{-3}	4.7711×10^{-2}	1.0140×10^{-1}	-1.6719×10^{-2}	-5.9672×10^{-2}	-1.1336×10^{-1}
Cost†	€	3.7739×10^{5}	3.7758×10^{5}	3.7842×10^{5}	3.7947×10^{5}	3.7716×10^{5}	3.7632×10^{5}	3.7527×10^{5}
Cost‡	€		3.7758×10^{5}	3.7842×10^{5}	3.7947×10^{5}	3.7716×10^{5}	3.7632×10^{5}	3.7527×10^{5}
Sensitivity	%		4.9073×10^{-2}	2.7170×10^{-1}	5.4998×10^{-1}	-6.2239×10^{-2}	-2.8486×10^{-1}	-5.6314×10^{-1}
Footprint†	$kgCO_2e$	3.4940×10^{5}	3.4938×10^{5}	3.4938×10^{5}	3.4938×10^{5}	3.4938×10^{5}	3.4938×10^{5}	3.4938×10^{5}
Footprint‡	$kgCO_2e$		3.4938×10^{5}	3.4938×10^{5}	3.4938×10^{5}	3.4938×10^{5}	3.4938×10^{5}	3.4938×10^{5}
Sensitivity	%		-5.8364×10^{-3}	-5.8364×10^{-3}	-5.8364×10^{-3}	-5.8364×10^{-3}	-5.8364×10^{-3}	-5.8364×10^{-3}
Deflection†	mm	7.0234×10^{1}	7.0279×10^{1}	7.0279×10^{1}	7.0279×10^{1}	7.0279×10^{1}	7.0279×10^{1}	7.0279×10^{1}
Deflection‡	mm		7.0284×10^{1}	7.0284×10^{1}	7.0284×10^{1}	7.0284×10^{1}	7.0284×10^{1}	7.0284×10^{1}
Sensitivity	%		7.0734×10^{-2}	7.0734×10^{-2}	7.0734×10^{-2}	7.0734×10^{-2}	7.0734×10^{-2}	7.0734×10^{-2}
Frequency†	Hz	4.0821×10^{0}	4.0783×10^{0}	4.0783×10^{0}	4.0783×10^{0}	4.0783×10^{0}	4.0783×10^{0}	4.0783×10^{0}
Frequency‡	Hz		4.0774×10^{0}	4.0774×10^{0}	4.0774×10^{0}	4.0774×10^{0}	4.0774×10^{0}	4.0774×10^{0}
Sensitivity	%		-1.1556×10^{-1}	-1.1556×10^{-1}	-1.1556×10^{-1}	-1.1556×10^{-1}	-1.1556×10^{-1}	-1.1556×10^{-1}
Buckling factor†	-	1.1237×10^{1}	1.1156×10^{1}	1.1156×10^{1}	1.1156×10^{1}	1.1156×10^{1}	1.1156×10^{1}	1.1156×10^{1}
Buckling factor‡	-		1.1162×10^{1}	1.1162×10^{1}	1.1162×10^{1}	1.1162×10^{1}	1.1162×10^{1}	1.1162×10^{1}
Sensitivity	%		-6.7331×10^{-1}	-6.7331×10^{-1}	-6.7331×10^{-1}	-6.7331×10^{-1}	-6.7331×10^{-1}	-6.7331×10^{-1}

[a] [€/kg], †immediate value, ‡value after new intensification phase.

Table K.4: Sensitivity matrix – Labour Cost

	Unit	Current value	d_1	d_2	d_3	d_4	d_5	d_6
Original value			10[a]					
Perturbation			1%	5%	10%	−1%	−5%	−10%
Perturbation	€/kg		0.1	0.5	1	−0.1	−0.5	−1
Fitness†	-	7.5642×10^{-1}	7.5706×10^{-1}	7.5976×10^{-1}	7.6313×10^{-1}	7.5570×10^{-1}	7.5300×10^{-1}	7.4962×10^{-1}
Fitness‡	-		7.5705×10^{-1}	7.5976×10^{-1}	7.6313×10^{-1}	7.5570×10^{-1}	7.5300×10^{-1}	7.4962×10^{-1}
Sensitivity	%		8.3326×10^{-2}	4.4055×10^{-1}	8.8708×10^{-1}	-9.5287×10^{-2}	-4.5251×10^{-1}	-8.9905×10^{-1}
Cost†	€	3.7739×10^{5}	3.7912×10^{5}	3.8610×10^{5}	3.9484×10^{5}	3.7562×10^{5}	3.6864×10^{5}	3.5990×10^{5}
Cost‡	€		3.7912×10^{5}	3.8610×10^{5}	3.9484×10^{5}	3.7562×10^{5}	3.6863×10^{5}	3.5990×10^{5}
Sensitivity	%		4.5629×10^{-1}	2.3078×10^{0}	4.6222×10^{0}	-4.6946×10^{-1}	-2.3210×10^{0}	-4.6353×10^{0}
Footprint†	$kgCO_2e$	3.4940×10^{5}	3.4938×10^{5}	3.4938×10^{5}	3.4938×10^{5}	3.4938×10^{5}	3.4938×10^{5}	3.4938×10^{5}
Footprint‡	$kgCO_2e$		3.4938×10^{5}	3.4938×10^{5}	3.4938×10^{5}	3.4938×10^{5}	3.4938×10^{5}	3.4938×10^{5}
Sensitivity	%		-5.8364×10^{-3}	-5.8364×10^{-3}	-5.8364×10^{-3}	-5.8364×10^{-3}	-5.8364×10^{-3}	-5.8364×10^{-3}
Deflection†	mm	7.0234×10^{1}	7.0279×10^{1}	7.0279×10^{1}	7.0279×10^{1}	7.0279×10^{1}	7.0279×10^{1}	7.0279×10^{1}
Deflection‡	mm		7.0284×10^{1}	7.0284×10^{1}	7.0284×10^{1}	7.0284×10^{1}	7.0284×10^{1}	7.0284×10^{1}
Sensitivity	%		7.0734×10^{-2}	7.0734×10^{-2}	7.0734×10^{-2}	7.0734×10^{-2}	7.0734×10^{-2}	7.0734×10^{-2}
Frequency†	Hz	4.0821×10^{0}	4.0783×10^{0}	4.0783×10^{0}	4.0783×10^{0}	4.0783×10^{0}	4.0783×10^{0}	4.0783×10^{0}
Frequency‡	Hz		4.0774×10^{0}	4.0774×10^{0}	4.0774×10^{0}	4.0774×10^{0}	4.0774×10^{0}	4.0774×10^{0}
Sensitivity	%		-1.1556×10^{-1}	-1.1556×10^{-1}	-1.1556×10^{-1}	-1.1556×10^{-1}	-1.1556×10^{-1}	-1.1556×10^{-1}
Buckling factor†	-	1.1237×10^{1}	1.1156×10^{1}	1.1156×10^{1}	1.1156×10^{1}	1.1156×10^{1}	1.1156×10^{1}	1.1156×10^{1}
Buckling factor‡	-		1.1162×10^{1}	1.1162×10^{1}	1.1162×10^{1}	1.1162×10^{1}	1.1162×10^{1}	1.1162×10^{1}
Sensitivity	%		-6.7331×10^{-1}	-6.7331×10^{-1}	-6.7331×10^{-1}	-6.7331×10^{-1}	-6.7331×10^{-1}	-6.7331×10^{-1}

[a] [€/kg], † immediate value, ‡ value after new intensification phase.

K.2. Global warming potential (GWP) sensitivity

Table K.5: Sensitivity matrix – Carbon GWP

	Unit	Current value	d_1	d_2	d_3	d_4	d_5	d_6
Original value			48.99[a]					
Perturbation			1%	5%	10%	−1%	−5%	−10%
Perturbation	$kgCO_2e/kg$		0.4899	2.4495	4.899	−0.4899	−2.4495	−4.899
Fitness†	-	7.5642×10^{-1}	7.6084×10^{-1}	7.7867×10^{-1}	8.0095×10^{-1}	7.5192×10^{-1}	7.3409×10^{-1}	7.1181×10^{-1}
Fitness‡	-		7.6084×10^{-1}	7.7867×10^{-1}	8.0095×10^{-1}	7.5192×10^{-1}	7.3409×10^{-1}	7.1181×10^{-1}
Sensitivity	%		5.8328×10^{-1}	2.9403×10^{0}	5.8867×10^{0}	-5.9524×10^{-1}	-2.9523×10^{0}	-5.8986×10^{0}
Cost†	€	3.7739×10^{5}	3.7737×10^{5}	3.7737×10^{5}	3.7737×10^{5}	3.7737×10^{5}	3.7737×10^{5}	3.7737×10^{5}
Cost‡	€		3.7737×10^{5}	3.7737×10^{5}	3.7737×10^{5}	3.7737×10^{5}	3.7737×10^{5}	3.7737×10^{5}
Sensitivity	%		-6.5832×10^{-3}	-6.5832×10^{-3}	-6.5832×10^{-3}	-6.5832×10^{-3}	-6.5832×10^{-3}	-6.5832×10^{-3}
Footprint†	$kgCO_2e$	3.4940×10^{5}	3.5193×10^{5}	3.6214×10^{5}	3.7489×10^{5}	3.4683×10^{5}	3.3663×10^{5}	3.2387×10^{5}
Footprint‡	$kgCO_2e$		3.5193×10^{5}	3.6214×10^{5}	3.7489×10^{5}	3.4683×10^{5}	3.3663×10^{5}	3.2387×10^{5}
Sensitivity	%		7.2430×10^{-1}	3.6448×10^{0}	7.2955×10^{0}	-7.3597×10^{-1}	-3.6565×10^{0}	-7.3072×10^{0}
Deflection†	mm	7.0234×10^{1}	7.0279×10^{1}	7.0279×10^{1}	7.0279×10^{1}	7.0279×10^{1}	7.0279×10^{1}	7.0279×10^{1}
Deflection‡	mm		7.0284×10^{1}	7.0284×10^{1}	7.0284×10^{1}	7.0284×10^{1}	7.0284×10^{1}	7.0284×10^{1}
Sensitivity	%		7.0734×10^{-2}	7.0734×10^{-2}	7.0734×10^{-2}	7.0734×10^{-2}	7.0734×10^{-2}	7.0734×10^{-2}
Frequency†	Hz	4.0821×10^{0}	4.0783×10^{0}	4.0783×10^{0}	4.0783×10^{0}	4.0783×10^{0}	4.0783×10^{0}	4.0783×10^{0}
Frequency‡	Hz		4.0774×10^{0}	4.0774×10^{0}	4.0774×10^{0}	4.0774×10^{0}	4.0774×10^{0}	4.0774×10^{0}
Sensitivity	%		-1.1556×10^{-1}	-1.1556×10^{-1}	-1.1556×10^{-1}	-1.1556×10^{-1}	-1.1556×10^{-1}	-1.1556×10^{-1}
Buckling factor†	-	1.1237×10^{1}	1.1156×10^{1}	1.1156×10^{1}	1.1156×10^{1}	1.1156×10^{1}	1.1156×10^{1}	1.1156×10^{1}
Buckling factor‡	-		1.1162×10^{1}	1.1162×10^{1}	1.1162×10^{1}	1.1162×10^{1}	1.1162×10^{1}	1.1162×10^{1}
Sensitivity	%		-6.7331×10^{-1}	-6.7331×10^{-1}	-6.7331×10^{-1}	-6.7331×10^{-1}	-6.7331×10^{-1}	-6.7331×10^{-1}

[a] [$kgCO_2e/kg$], † immediate value, ‡ value after new intensification phase.

Table K.6: Sensitivity matrix – Glass GWP

	Unit	Current value	d_1	d_2	d_3	d_4	d_5	d_6
Original value			1.81[a]					
Perturbation			1%	5%	10%	−1%	−5%	−10%
Perturbation	$kgCO_2e/kg$		0.0181	0.0905	0.181	−0.0181	−0.0905	−0.181
Fitness†	-	7.5642×10^{-1}	7.5656×10^{-1}	7.5727×10^{-1}	7.5815×10^{-1}	7.5620×10^{-1}	7.5549×10^{-1}	7.5460×10^{-1}
Fitness‡	-		7.5656×10^{-1}	7.5727×10^{-1}	7.5815×10^{-1}	7.5620×10^{-1}	7.5549×10^{-1}	7.5460×10^{-1}
Sensitivity	%		1.7491×10^{-2}	1.1138×10^{-1}	2.2873×10^{-1}	-2.9452×10^{-2}	-1.2334×10^{-1}	-2.4069×10^{-1}
Cost†	€	3.7739×10^{5}	3.7737×10^{5}	3.7737×10^{5}	3.7737×10^{5}	3.7737×10^{5}	3.7737×10^{5}	3.7737×10^{5}
Cost‡	€		3.7737×10^{5}	3.7737×10^{5}	3.7737×10^{5}	3.7737×10^{5}	3.7737×10^{5}	3.7737×10^{5}
Sensitivity	%		-6.5832×10^{-3}	-6.5832×10^{-3}	-6.5832×10^{-3}	-6.5832×10^{-3}	-6.5832×10^{-3}	-6.5832×10^{-3}
Footprint†	$kgCO_2e$	3.4940×10^{5}	3.4948×10^{5}	3.4989×10^{5}	3.5040×10^{5}	3.4928×10^{5}	3.4887×10^{5}	3.4837×10^{5}
Footprint‡	$kgCO_2e$		3.4948×10^{5}	3.4989×10^{5}	3.5040×10^{5}	3.4928×10^{5}	3.4887×10^{5}	3.4837×10^{5}
Sensitivity	%		2.3246×10^{-2}	1.3958×10^{-1}	2.8499×10^{-1}	-3.4919×10^{-2}	-1.5125×10^{-1}	-2.9666×10^{-1}
Deflection†	mm	7.0234×10^{1}	7.0279×10^{1}	7.0279×10^{1}	7.0279×10^{1}	7.0279×10^{1}	7.0279×10^{1}	7.0279×10^{1}
Deflection‡	mm		7.0284×10^{1}	7.0284×10^{1}	7.0284×10^{1}	7.0284×10^{1}	7.0284×10^{1}	7.0284×10^{1}
Sensitivity	%		7.0734×10^{-2}	7.0734×10^{-2}	7.0734×10^{-2}	7.0734×10^{-2}	7.0734×10^{-2}	7.0734×10^{-2}
Frequency†	Hz	4.0821×10^{0}	4.0783×10^{0}	4.0783×10^{0}	4.0783×10^{0}	4.0783×10^{0}	4.0783×10^{0}	4.0783×10^{0}
Frequency‡	Hz		4.0774×10^{0}	4.0774×10^{0}	4.0774×10^{0}	4.0774×10^{0}	4.0774×10^{0}	4.0774×10^{0}
Sensitivity	%		-1.1556×10^{-1}	-1.1556×10^{-1}	-1.1556×10^{-1}	-1.1556×10^{-1}	-1.1556×10^{-1}	-1.1556×10^{-1}
Buckling factor†	-	1.1237×10^{1}	1.1156×10^{1}	1.1156×10^{1}	1.1156×10^{1}	1.1156×10^{1}	1.1156×10^{1}	1.1156×10^{1}
Buckling factor‡	-		1.1162×10^{1}	1.1162×10^{1}	1.1162×10^{1}	1.1162×10^{1}	1.1162×10^{1}	1.1162×10^{1}
Sensitivity	%		-6.7331×10^{-1}	-6.7331×10^{-1}	-6.7331×10^{-1}	-6.7331×10^{-1}	-6.7331×10^{-1}	-6.7331×10^{-1}

[a] [$kgCO_2e/kg$], † immediate value, ‡ value after new intensification phase.

Table K.7: Sensitivity matrix – Resin GWP

	Unit	Current value	d_1	d_2	d_3	d_4	d_5	d_6
Original value			3.79[a]					
Perturbation			1%	5%	10%	−1%	−5%	−10%
Perturbation	$kgCO_2e/kg$		0.0379	0.1895	0.379	−0.0379	−0.1895	−0.379
Fitness†	-	7.5642×10^{-1}	7.5673×10^{-1}	7.5848×10^{-1}	7.5986×10^{-1}	7.5603×10^{-1}	7.5464×10^{-1}	7.5290×10^{-1}
Fitness‡	-		7.5673×10^{-1}	7.5848×10^{-1}	7.5986×10^{-1}	7.5603×10^{-1}	7.5464×10^{-1}	7.5290×10^{-1}
Sensitivity	%		3.9989×10^{-2}	2.7213×10^{-1}	4.5371×10^{-1}	-5.1950×10^{-2}	-2.3583×10^{-1}	-4.6567×10^{-1}
Cost†	€	3.7739×10^{5}	3.7737×10^{5}	3.7737×10^{5}	3.7737×10^{5}	3.7737×10^{5}	3.7737×10^{5}	3.7737×10^{5}
Cost‡	€		3.7737×10^{5}	3.7737×10^{5}	3.7737×10^{5}	3.7737×10^{5}	3.7737×10^{5}	3.7737×10^{5}
Sensitivity	%		-6.5832×10^{-3}	-6.5832×10^{-3}	-6.5832×10^{-3}	-6.5832×10^{-3}	-6.5832×10^{-3}	-6.5832×10^{-3}
Footprint†	$kgCO_2e$	3.4940×10^{5}	3.4958×10^{5}	3.5059×10^{5}	3.5137×10^{5}	3.4918×10^{5}	3.4839×10^{5}	3.4739×10^{5}
Footprint‡	$kgCO_2e$		3.4958×10^{5}	3.5059×10^{5}	3.5137×10^{5}	3.4918×10^{5}	3.4839×10^{5}	3.4739×10^{5}
Sensitivity	%		5.1122×10^{-2}	3.3876×10^{-1}	5.6375×10^{-1}	-6.2795×10^{-2}	-2.9063×10^{-1}	-5.7542×10^{-1}
Deflection†	mm	7.0234×10^{1}	7.0279×10^{1}	7.0279×10^{1}	7.0279×10^{1}	7.0279×10^{1}	7.0279×10^{1}	7.0279×10^{1}
Deflection‡	mm		7.0284×10^{1}	7.0284×10^{1}	7.0284×10^{1}	7.0284×10^{1}	7.0284×10^{1}	7.0284×10^{1}
Sensitivity	%		7.0734×10^{-2}	7.0734×10^{-2}	7.0734×10^{-2}	7.0734×10^{-2}	7.0734×10^{-2}	7.0734×10^{-2}
Frequency†	Hz	4.0821×10^{0}	4.0783×10^{0}	4.0783×10^{0}	4.0783×10^{0}	4.0783×10^{0}	4.0783×10^{0}	4.0783×10^{0}
Frequency‡	Hz		4.0774×10^{0}	4.0774×10^{0}	4.0774×10^{0}	4.0774×10^{0}	4.0774×10^{0}	4.0774×10^{0}
Sensitivity	%		-1.1556×10^{-1}	-1.1556×10^{-1}	-1.1556×10^{-1}	-1.1556×10^{-1}	-1.1556×10^{-1}	-1.1556×10^{-1}
Buckling factor†	-	1.1237×10^{1}	1.1156×10^{1}	1.1156×10^{1}	1.1156×10^{1}	1.1156×10^{1}	1.1156×10^{1}	1.1156×10^{1}
Buckling factor‡	-		1.1162×10^{1}	1.1162×10^{1}	1.1162×10^{1}	1.1162×10^{1}	1.1162×10^{1}	1.1162×10^{1}
Sensitivity	%		-6.7331×10^{-1}	-6.7331×10^{-1}	-6.7331×10^{-1}	-6.7331×10^{-1}	-6.7331×10^{-1}	-6.7331×10^{-1}

[a] [$kgCO_2e/kg$], † immediate value, ‡ value after new intensification phase.

Table K.8: Sensitivity matrix – Labour GWP

	Unit	Current value	d_1	d_2	d_3	d_4	d_5	d_6
Original value			3.55[a]					
Perturbation			1%	5%	10%	−1%	−5%	−10%
Perturbation	$kgCO_2e/kg$		0.0355	0.1775	0.355	−0.0355	−0.1775	−0.355
Fitness†	-	7.5642×10^{-1}	7.5746×10^{-1}	7.6180×10^{-1}	7.6721×10^{-1}	7.5530×10^{-1}	7.5096×10^{-1}	7.4554×10^{-1}
Fitness‡	-		7.5746×10^{-1}	7.6180×10^{-1}	7.6721×10^{-1}	7.5530×10^{-1}	7.5096×10^{-1}	7.4554×10^{-1}
Sensitivity	%		1.3726×10^{-1}	7.1023×10^{-1}	1.4264×10^{0}	-1.4922×10^{-1}	-7.2219×10^{-1}	-1.4384×10^{0}
Cost†	€	3.7739×10^{5}	3.7737×10^{5}	3.7737×10^{5}	3.7737×10^{5}	3.7737×10^{5}	3.7737×10^{5}	3.7737×10^{5}
Cost‡	€		3.7737×10^{5}	3.7737×10^{5}	3.7737×10^{5}	3.7737×10^{5}	3.7737×10^{5}	3.7737×10^{5}
Sensitivity	%		-6.5832×10^{-3}	-6.5832×10^{-3}	-6.5832×10^{-3}	-6.5832×10^{-3}	-6.5832×10^{-3}	-6.5832×10^{-3}
Footprint†	$kgCO_2e$	3.4940×10^{5}	3.5000×10^{5}	3.5248×10^{5}	3.5558×10^{5}	3.4876×10^{5}	3.4628×10^{5}	3.4318×10^{5}
Footprint‡	$kgCO_2e$		3.5000×10^{5}	3.5248×10^{5}	3.5558×10^{5}	3.4876×10^{5}	3.4628×10^{5}	3.4318×10^{5}
Sensitivity	%		1.7165×10^{-1}	8.8159×10^{-1}	1.7690×10^{0}	-1.8332×10^{-1}	-8.9326×10^{-1}	-1.7807×10^{0}
Deflection†	mm	7.0234×10^{1}	7.0279×10^{1}	7.0279×10^{1}	7.0279×10^{1}	7.0279×10^{1}	7.0279×10^{1}	7.0279×10^{1}
Deflection‡	mm		7.0284×10^{1}	7.0284×10^{1}	7.0284×10^{1}	7.0284×10^{1}	7.0284×10^{1}	7.0284×10^{1}
Sensitivity	%		7.0734×10^{-2}	7.0734×10^{-2}	7.0734×10^{-2}	7.0734×10^{-2}	7.0734×10^{-2}	7.0734×10^{-2}
Frequency†	Hz	4.0821×10^{0}	4.0783×10^{0}	4.0783×10^{0}	4.0783×10^{0}	4.0783×10^{0}	4.0783×10^{0}	4.0783×10^{0}
Frequency‡	Hz		4.0774×10^{0}	4.0774×10^{0}	4.0774×10^{0}	4.0774×10^{0}	4.0774×10^{0}	4.0774×10^{0}
Sensitivity	%		-1.1556×10^{-1}	-1.1556×10^{-1}	-1.1556×10^{-1}	-1.1556×10^{-1}	-1.1556×10^{-1}	-1.1556×10^{-1}
Buckling factor†	-	1.1237×10^{1}	1.1156×10^{1}	1.1156×10^{1}	1.1156×10^{1}	1.1156×10^{1}	1.1156×10^{1}	1.1156×10^{1}
Buckling factor‡	-		1.1162×10^{1}	1.1162×10^{1}	1.1162×10^{1}	1.1162×10^{1}	1.1162×10^{1}	1.1162×10^{1}
Sensitivity	%		-6.7331×10^{-1}	-6.7331×10^{-1}	-6.7331×10^{-1}	-6.7331×10^{-1}	-6.7331×10^{-1}	-6.7331×10^{-1}

[a] [$kgCO_2e/kg$], †immediate value, ‡value after new intensification phase.

Appendix L Improvement on the analytical solution

The graphs herein represent the convergence graphs for the optimisations where the analytical solution presented in Appendix J and Chapter 6.6 is taken as the initial point. Four cases are investigated with the weights on objective one, i.e. the carbon footprint (w_1), taken as 1.0, 0.5, 0.2 and 0.0.

For the configurations $w_1 = 0.0$ and $w_1 = 1.0$, the objectives were not normalised, resulting in fitness values of several orders of magnitude greater than the remaining configurations. Hence, the convergence[1] plots for the configurations $w_1 = 1.0$ and $w_1 = 0.0$ are presented in Fig. L.1, whereas the configurations $w_1 = 0.2$ and $w_1 = 0.5$ are presented in Fig. L.2. Notice the run-time for the $w_1 = 1.0$-configuration which is almost thrice that of the $w_1 = 0.0$-configuration (Fig. L.1).

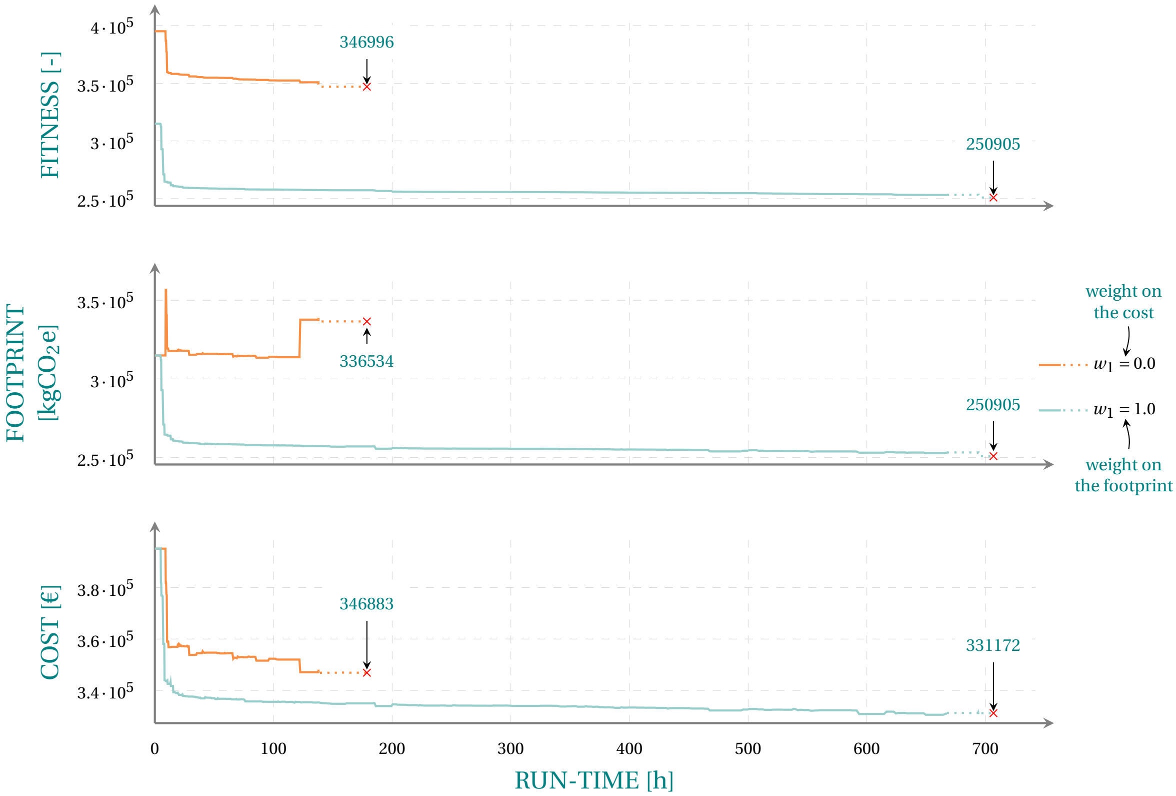

Figure L.1: Fitness convergence plot (**top**) for the configurations $w_1 = 1.0$ and $w_1 = 0.0$. The corresponding carbon footprint (**middle**) and cost are shown (**bottom**).

[1] here convergence refers to when a stopping criteria is met

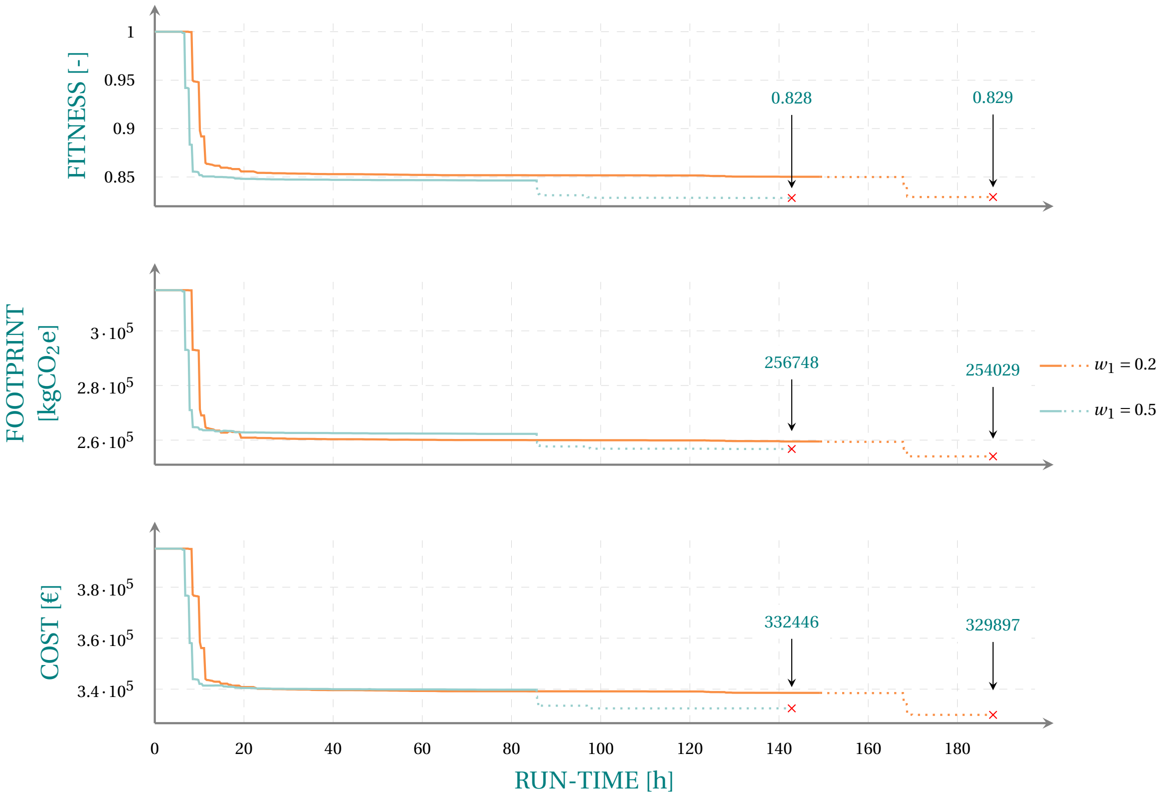

Figure L.2: Fitness convergence plots (**top**) for the configurations $w_1 = 0.2$ and $w_1 = 0.5$. The corresponding carbon footprint (**middle**) and cost are shown (**bottom**).

Appendix M Comparisons of the solutions

The cross-sections and laminates corresponding to the configurations illustrated in Fig. 7.4 are presented herein.

M.1. Layups

Figure M.1: The face sheet specifications for the $J = 4$ panel configurations.

Weight	Transverse stiffeners	Longitudinal stiffeners	Side panels	Bottom panels
$w_1 = 0.0$	C 90°_2 G 0°_2 G $\pm45^\circ$	C 0°_2 G $\pm45^\circ$ C 90°_2	C 0°_2 G $\pm45^\circ$ C 90°_2	C 0°_2 C 90°_2 C $\pm45^\circ$
$w_1 = 0.2$	G $\pm45^\circ$ G 90°_2 G 0°_2	G $\pm45^\circ$ G 90°_2 G 0°_2	G $\pm45^\circ$ G 90°_2 G 0°_2	G $\pm45^\circ$ G 90°_2 C 0°_2 C 0°_2
$w_1 = 0.5$	G $\pm45^\circ$ G 90°_2 G 0°_2	G $\pm45^\circ$ G 90°_2 G 0°_2	G $\pm45^\circ$ G 90°_2 G 0°_2	G $\pm45^\circ$ C 0°_2 G 90°_2 C 0°_2
$w_1 = 0.8$	C 90°_2 G $\pm45^\circ$ G 0°_2	C 90°_2 G $\pm45^\circ$ C 0°_2	C $\pm45^\circ$ G 0°_2 C 90°_2	C 90°_2 G $\pm45^\circ$ G 0°_2
$w_1 = 1.0$	G $\pm45^\circ$ G 90°_2 G 0°_2	G $\pm45^\circ$ G 90°_2 G 0°_2	G $\pm45^\circ$ G 90°_2 G 0°_2	C 0°_2 G 90°_2 G $\pm45^\circ$ C 0°_2

Combining these panel specifications (Fig. M.1) with the shapes (Fig. M.3), the variations over the panel configurations in Fig. M.1 makes more sense. For instance, the section at $X = L$ for $w_1 = 0.8$ suggest that more of the load transfer goes along the exterior, resulting in stiffer plies near the surface. While the outcome makes sense structurally, it should be reiterated that the combination of shape and material architecture likely is the result of premature convergence – a rather suboptimal solution. The $w_1 = 0.0$ configuration failed to converge to a feasible solution, reflected through the panels that differ significantly from the structures with similar shapes.

M.2. Cross-sections

The geometrical variables are indicated in Fig. M.2, with the corresponding cross-sections at $X = 0$ and $X = L$ given in Fig. M.3.

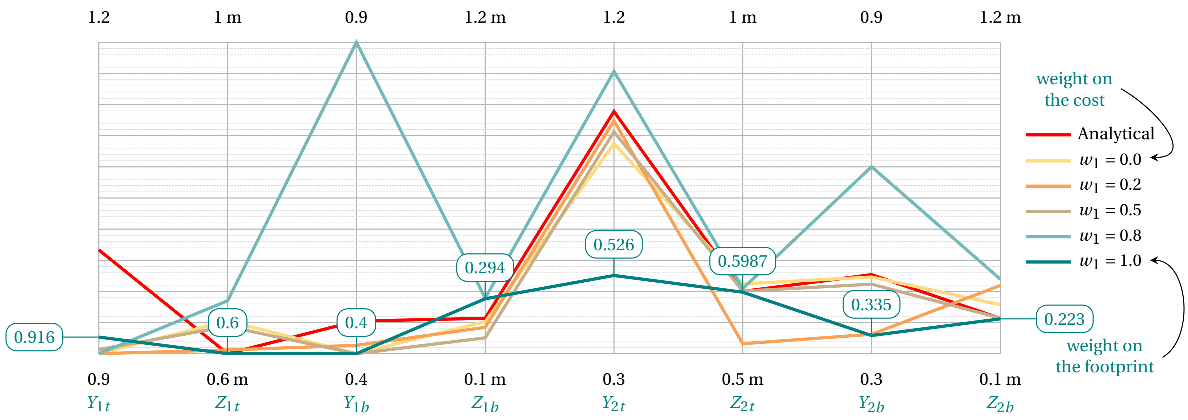

Figure M.2: Geometrical variable values for the analytical and optimal solutions presented in Fig. 7.3.

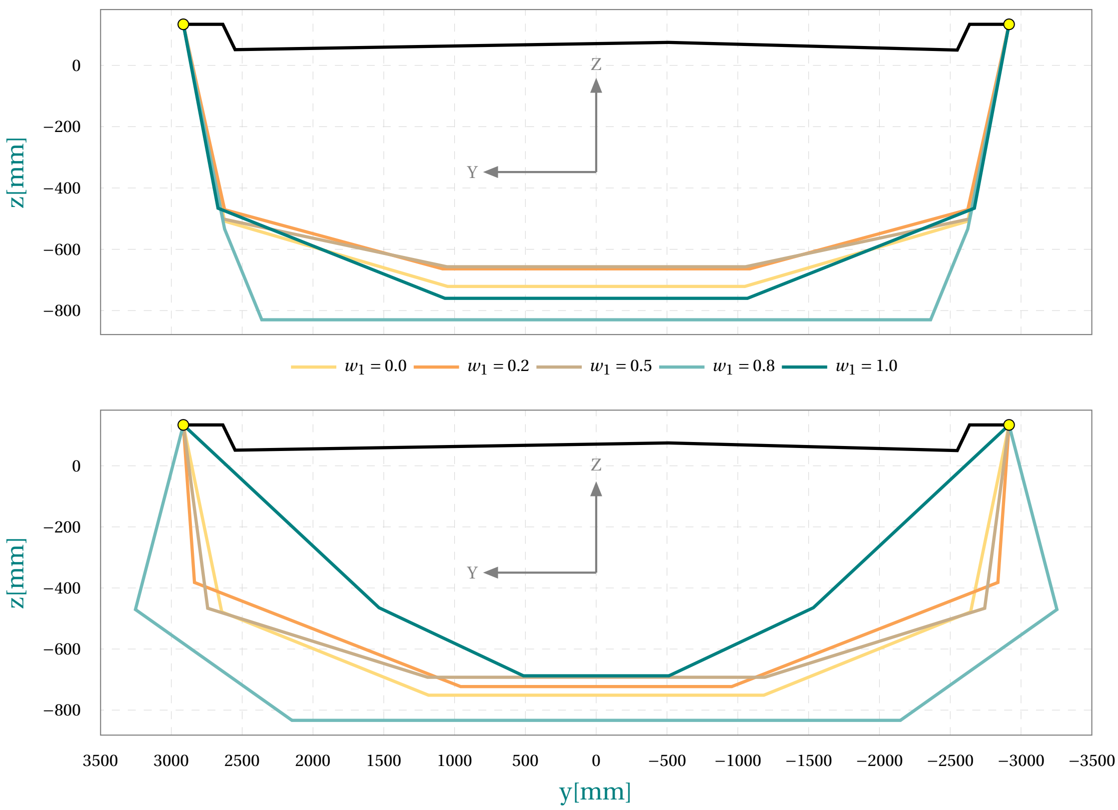

Figure M.3: Cross-sections for the solutions at (**top**) $X = 0$ and (**bottom**) $X = L$ before the geometry is cut a 10° angle.

Appendix N Ansys® verification

The analyses presented here verify the obtained solution from the optimisation procedure in Chapter 6. Specifically, the solution corresponding to row 2 of Table 7.1 and its pertaining geometry is investigated in Ansys® [15] and compared with the response of the Karamba model.

N.1. Modelling

The following analyses make use of 2D shell elements ('SHELL 181') with 2nd order (quadratic) interpolation and an automatically generated mesh with an element size of 100.00 mm.

Material properties

The adopted properties are given in Tables 6.1, 6.2 and 6.4. The appropriate moduli are multiplied by $\eta_{\mathrm{c,SLS}} = 0.9$ for deformation analyses, and $\eta_{\mathrm{c,ULS}} = 0.81$ for strength analyses. Furthermore, the lacking strengths properties are defined using JRC's strain- and shear strain limits [3], respectively:

$$\varepsilon_{\mathrm{f1}} = \varepsilon_{\mathrm{f2}} = 1.2\,\% \qquad \text{and} \qquad \gamma_{\mathrm{f12}} = 1.6\,\%.$$

Element orientation

The structural response relies heavily upon a proper definition of the laminates and their fibre orientations. Hence, appropriate orientations must be defined for the respective panels, see Fig. N.1, where the deck- and the panels on the right side are hidden from the preview. To account for a draping-like effect during lay-up, the normals of the side panels face inwards (although insignificant with symmetric panels).

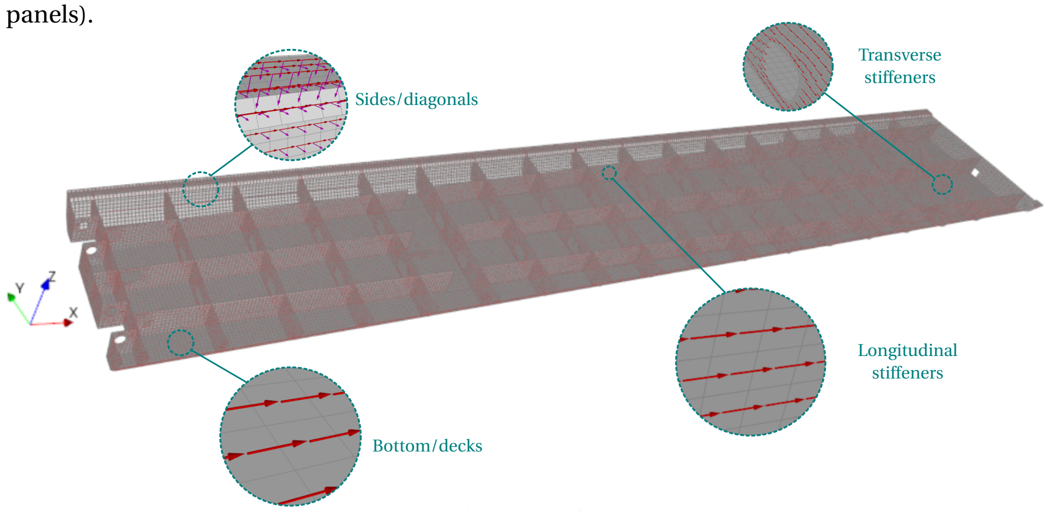

Figure N.1: 0° direction and normals for the side/diagonal panels.

Supports & boundary conditions

The boundary conditions are modelled by making use of 'remote displacements', allowing to constrain points, edges and surfaces to a point rigidly. The internal perimeters of the brackets (X1R, X1L) are restrained in X, Y and Z. The side steel plates (X3R, X3L) are restrained in Z, while the translation in Y is restrained for the middle plate (X3M). The endpoint of the cylinder (X2) is restrained in X, Y, and Z. See Fig. N.2. As such, the constraints are different from the Karamba model, as it only allows for constraining nodes.

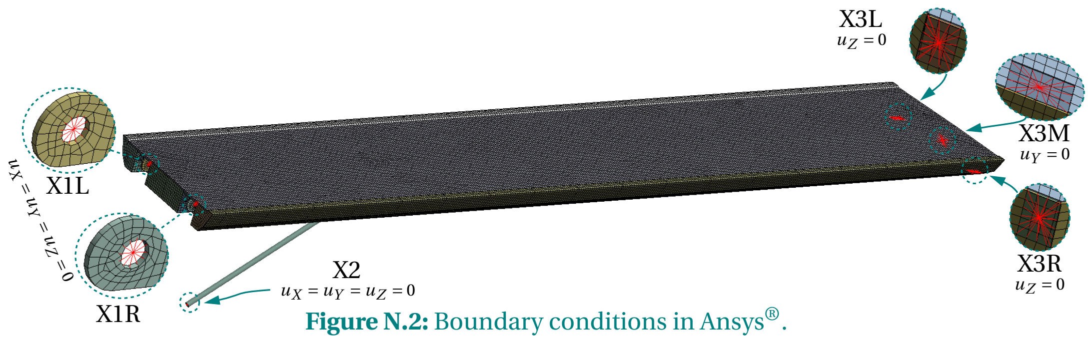

Figure N.2: Boundary conditions in Ansys®.

N.2. Ansys® vs Karamba – comparison of structural responses

Figures N.3–N.5 illustrate the structural responses (deformation, first mode of vibration and first buckling mode) for the two models; and the similarities and discrepancies between them.

Deformation

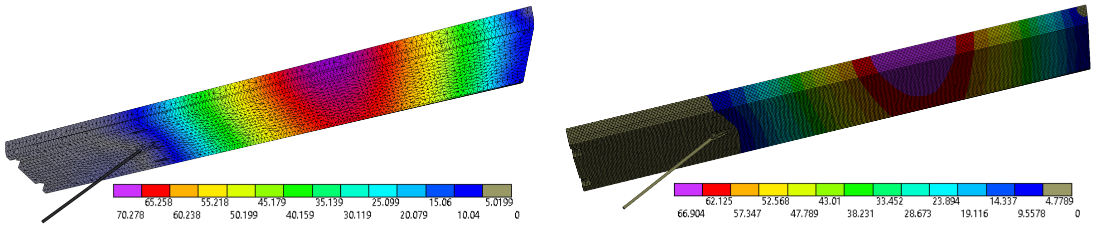

Figure N.3: Total deformations: $\delta^{\text{KARAMBA}} = 70.28\,\text{mm}$ and $\delta^{\text{ANSYS}} = 66.90\,\text{mm}$. (**left**) Karamba, (**right**) Ansys®.

Vibrations – Fundamental frequency

Karamba automatically scales the deformation in vibration analyses such that the greatest deformation becomes unity (1.00 m), with the contour displaying absolute values of deformations. Scaling the deformations appropriately reveals that both models display similar fundamental modes of vibration, namely a vertical bending/torsional mode.

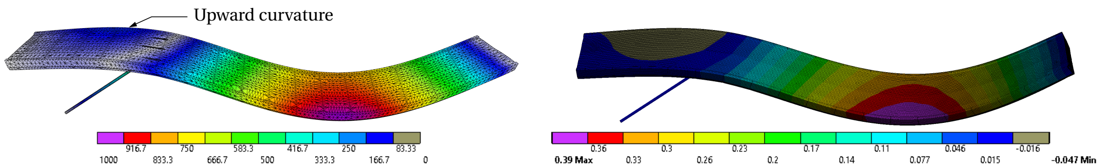

Figure N.4: The first mode of vibration: $\Omega_0^{\text{KARAMBA}} = 4.17\,\text{Hz}$ and $\Omega_0^{\text{ANSYS}} = 4.25\,\text{Hz}$.
(**left**) Karamba, deformation scale: 4; (**right**) Ansys®, deformation scale: 1029.8. Unit: mm.

Stability – Buckling load factor

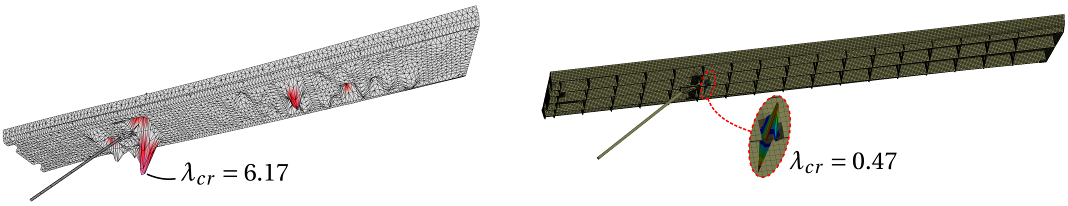

Figure N.5: The first buckling modes: $\lambda_{cr}^{\text{KARAMBA}} = 6.17$ and $\lambda_{cr}^{\text{ANSYS}} = 0.47$. (**left**) Karamba, (**right**) Ansys®. The bottom panel is hidden in the **right** figure.

Evidently, the Ansys® element model has similar behaviour to the Karamba model, despite differences in layered properties, quad elements, and support conditions. Even though triangular elements are known to behave stiffer than quadrilateral elements [16], the Ansys® model acts stiffer, owing to a slightly greater lever arm for the top face sheet in the deck. Discrepancies in buckling behaviour ($\lambda_{cr}^{\text{KARAMBA}} = 6.17$ vs $\lambda_{cr}^{\text{ANSYS}} = 0.68$) is a consequence of stress concentrations around the steel-to-composite connection, introducing buckling of the longitudinal stiffener. This is in contrast to the analytical- and numerical Karamba solution, both suggesting that the bottom panel in the vicinity of the cylinder connection would buckle.

N.3. Strength verification

A ULS strength analysis is carried out to investigate the strength of the different sandwich panels against the Tsai-Wu criterion (introduced in Chapter 3.3) and shear failure of the core. The material partial factors $\gamma_{M1} = 1.15$, $\gamma_{M2,str,fs} = 1.35$ and $\gamma_{M2,str,core} = 1.5$ are taken from JRC [3]. With $\gamma_Q = 1.5$, the uniformly distributed load reads:

$$q_{ULS} = 5.00\,\mathrm{kN/m^2} \cdot \gamma_Q = 7.50\,\mathrm{kN/m^2} \tag{N.1}$$

Evaluating the *inverse reserve factor* in Ansys® is equivalent to finding the exposure factors $f_{E,TW}$ (Eq. (3.15)) and $f_{E,MS}$ (Eq. (3.16)). Introducing weighting factors (WF), a satisfactory strength can be reported if the *inverse reserve factor* ≤ 1.0, with

$$\mathrm{WF_{fs}} = \left(\frac{\eta_{c,ULS}}{\gamma_{M,str,fs}}\right)^{-1} = 1.92 \qquad \text{and} \qquad \mathrm{WF_{core}} = \left(\frac{\eta_{c,ULS}}{\gamma_{M,str,core}}\right)^{-1} = 2.13 \tag{N.2}$$

for the face sheets and cores, respectively.

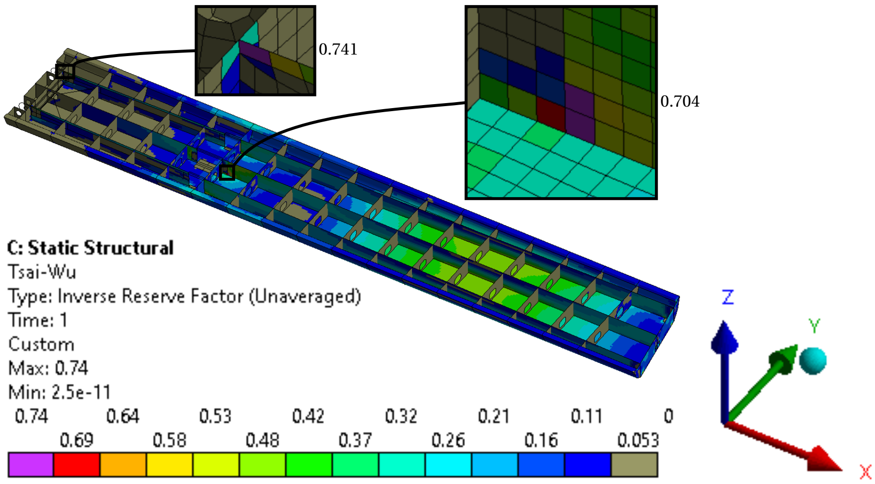

Figure N.6: Greatest Tsai-Wu factor: 0.741.

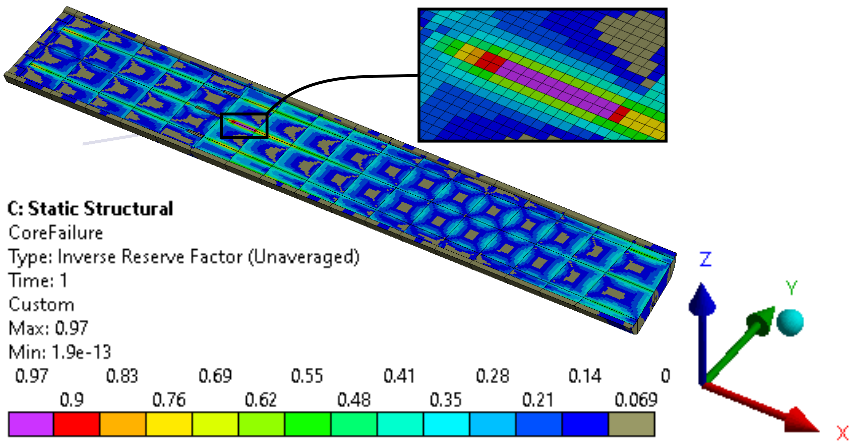

Figure N.7: Maximum core failure factor: 0.967

The panels satisfy the strength criteria, with locally high utilisation due to stress concentrations because of sudden stiffness variations. In Fig. N.6, high utilisation occurs in the steel-to-longitudinal stiffener connection around the cylinder, coinciding with the governing location for buckling.

High utilisation of the core above the middle flange of the steel frame (see Fig. N.7) is a consequence of the modelling, seeing that the surfaces overlap. Nonetheless, the steel frame acts as an intermediate support in the transverse direction of the deck, giving rise to shear forces. Including web stiffeners in the deck – which are left out of these analyses – will increase the stiffness and alleviate these local stresses to some extent.

N.4. Conclusion

Based on the presented results, the following conclusions can be drawn:

- The structural responses agree well with each other when evaluating the deflections and vibrations for the models using homogenised and layered properties, respectively.
- Poor buckling resistance for the Ansys® model is a consequence of stress concentrations.
- The constraints ensure that the structure becomes adequately stiff, meeting the strength requirements (for the investigated load case).